Laboratory Investigations of the Thermal and Non-Thermal Processing of Condensed Aromatic Hydrocarbons in the Interstellar Medium

John David Thrower

Submitted for the degree of Doctor of Philosophy

Heriot-Watt University

School of Engineering and Physical Sciences

August 2009

ABSTRACT

The thermal and non-thermal desorption of C_6H_6 has been investigated as a model for the behaviour of other aromatic hydrocarbons existing in the condensed phase in the interstellar medium. An interstellar dust grain mimic based on amorphous SiO_2, to represent the interstellar silicate grain population, has been developed for use as a substrate in these experiments. Temperature programmed desorption experiments reveal a broad distribution of binding sites on this surface, with C_6H_6 desorbing thermally over a wide temperature range. The desorption from compact amorphous solid water displays simpler desorption kinetics with evidence for the formation of C_6H_6 islands on the water surface, demonstrating the importance of using realistic interstellar grain mimics in experiments probing surface sensitive interstellar processes. Kinetic parameters have been obtained for these systems, along with those for thicker multilayer films of ice.

Photon irradiation of C_6H_6 / H_2O layered ice systems at 250 nm results in the desorption of both species as observed using time-of-flight mass spectrometry. The molecules desorb with high translational energies which would represent a significant energy injection into the cold interstellar gas phase. Three desorption processes, desorption *via* direct adsorbate-, indirect adsorbate- and substrate-mediated desorption, are proposed for the observed desorption profiles. The desorption of H_2O relies on energy transfer following photon absorption by a C_6H_6 molecule bound to a surface $(H_2O)_n$ cluster, which results in the unimolecular decomposition of the complex. Kinetic simulations indicate that such processes may lead to an enhancement of photon-induced desorption at the edges of dense interstellar clouds.

Experiments have also been performed to study the electron-stimulated desorption of molecules from C_6H_6 adsorbed on top of a water ice film. A highly efficient desorption channel with a cross-section in excess of 10^{-15} cm^2 is in operation for low coverages of C_6H_6 and is attributed to the migration of excitons formed within the bulk of the H_2O ice to the vacuum interface. A slower desorption component was also observed, which is attributed to a diffusion limited desorption step. These observations imply that electron stimulated desorption is likely to be an important non-thermal desorption process within dense clouds. No evidence for any chemical reaction products was observed through IR spectroscopy.

ACKNOWLEDGMENTS

The work presented in this thesis would not have been possible without the support and assistance of many people. It would not be possible to list everyone individually by name, but my thanks go to anyone who has been in any way involved.

First, and foremost, I would like to thank my primary supervisor, Prof. Martin McCoustra, for providing me with the opportunity to pursue the research presented in this thesis. His seemingly endless list of suggestions and ideas, along with his down to Earth practical approach are very much appreciated. I also acknowledge the support of my secondary supervisors, Prof. Ken McKendrick whilst at Heriot-Watt, and Dr. Frank Rutten during the first year whilst still at Nottingham.

I am also grateful for the support of the rest of the surface astrochemistry research group. Particular thanks go to Dr. Mark Collings for being a further source of ideas and suggestions, and for training me in the basics of UHV, along with Simon, Vicki and Ali.

Moving UHV equipment several hundred miles is certainly an experience, and enabled me to learn a great deal. However, without the ongoing support of workshop staff at Heriot-Watt the systems would probably still be in pieces. I would therefore like to express my gratitude to Iain, Alan and Paul, along with all those in the electronics workshop who have puzzled over a varied range of equipment. I would also like to thank Neil, Martin, John, Chris, Clive, Dave and James at Nottingham. The assistance of everyone involved at RAL is also acknowledged. Thanks also to Rosella for introducing me to PM-RAIRS, Nacho for obtaining the XPS spectra, Marion for performing the AFM and to all those who proof-read various parts of the manuscript.

A final thank you goes to my parents for their support and assistance throughout the last four years.

TABLE OF CONTENTS

GLOSSARY

AES – Auger electron spectroscopy
AFM – Atomic force microscopy
ASW – Amorphous solid water
CEM – Channel electron multiplier (channeltron)
DEA – Dissociative electron attachment
DIB – Diffuse interstellar band
DPRF – Differentially pumped rotary feedthrough
EI – Electron impact
ESD – Electron stimulated desorption
GMC – Giant molecular cloud
HOMO – Highest occupied molecular orbital
HOPG – Highly oriented pyrolytic graphite
HREELS – High resolution electron energy loss spectroscopy
HV – High vacuum
IR – Infrared
ISM – Interstellar medium
ISRF – Interstellar radiation field
ISO – Infrared space observatory
FTIR – Fourier transform infrared
LEED – Low energy electron diffraction
LoS – Line-of-sight
LUMO – Lowest unoccupied molecular orbital
MCS – Multichannel scaler
MCT – Mercury cadmium telluride
MCP – Microchannel plate
MO – Molecular orbital
OFHC – Oxygen free high conductivity
PAH – Polycyclic aromatic hydrocarbon
PEM – Photoelastic modulator
PHD – Pulse height distribution
PM – Polarization modulation
PSD – Photon stimulated desorption
PTFE – Polytetrafluroethylene
QCM – Quartz crystal microbalance
QMS – Quadrupole mass spectrometer
RAIRS – Reflection-absorption infrared spectroscopy
REMPI – Resonance enhanced multiphoton ionization
SEM – Secondary electron multiplier
SHG – Second harmonic generation
ToF-Time-of-flight
TPD – Temperature programmed desorption
TTL – Transistor transistor logic
UHV – Ultrahigh vacuum
UIR – Unidentified infrared band
UPS – Ultraviolet photoelectron spectroscopy
UV – Ultraviolet
Vis. – visible
VUV – Vacuum ultraviolet
XPS – X-ray photoelectron spectroscopy

CHAPTER 1 - Introduction

1.1 Introduction

This thesis describes experiments performed to investigate the thermal and non-thermal processing of interstellar ices containing aromatic hydrocarbons. In order to put the chemistry and physics studied into context, it is appropriate to introduce some simple aspects of astronomy and astrophysics that are relevant to this work. This chapter begins with an introduction to the interstellar medium, outlining the conditions found in that environment. Following this, a brief history of astrochemistry is provided, considering observations of molecules in astrophysical environments and the application of gas phase chemical models to explain these observations. The motivation behind the study of surface chemical and physical processes is introduced, before a more detailed discussion of polycyclic aromatic hydrocarbons (PAHs), the molecular family primarily investigated in this thesis, and a brief overview of relevant laboratory based studies. There are several good texts [1-3] that introduce the basics of astrochemistry, and an overview of the important concepts drawn from the relevant chapters in these will be provided here. Finally, the subsequent chapters are outlined.

1.2 The interstellar medium

The Interstellar Medium (ISM) is the name given to the regions of space situated between stars within our galaxy, the Milky Way. It has been estimated, that stars and planetary systems occupy no more than around 3×10^{-8}% of the volume available in the galaxy. These vast regions contain a mixture of dust and gas, comprising a surprisingly rich variety of atomic and molecular species. However, compared to the density of molecules at the bottom of the Earth's atmosphere, which is around 3×10^{25} m^{-3}, the density of the densest clouds in interstellar space is only around 10^{9} m^{-3}. Nevertheless, it is this reservoir of material that ultimately forms stars and associated planetary systems, and to where this material returns once a star reaches the end of its life.

Different regions of the ISM can be classified by their physical and chemical properties. The lowest density structures are known as diffuse clouds which are dominated by atomic hydrogen at a density of 3×10^{7} m^{-3}. Extensive observations of atomic hydrogen were made during the 1950s and 1960s with the use of radio telescopes [4,5]. H is detected through the 21 cm emission line associated with a hyperfine transition in the ground electronic state. This transition is extremely weak, and detection is only possible given the large amount of H present in the universe. Regions that contain large amounts of neutral atomic hydrogen are referred to as HI regions. Diffuse clouds typically have temperatures in the range 80-100 K and spatial dimensions of the order of 10 light years[1]. Denser clouds such as translucent and dark clouds also exist in the ISM. Some are formed by the compression of diffuse clouds by shocks resulting from supernovae, while most are held together by the increased gravitational attraction that arises as a result of their greater mass. These Giant Molecular Clouds (GMCs) are thought to be formed by collisions between diffuse clouds. The increased density leads to dark clouds being dominated by molecular hydrogen (H_2), rather than H. Increased molecular abundance arises due to the increased density, resulting in a higher probability for chemical reaction and the attenuation of radiation that would lead to the photodestruction of formed molecules. The H_2 density is typically 10^{9} m^{-3} and temperatures are lower, 10-50 K, as a result of the attenuation of radiation. The Orion nebula (see **Figure 1.1**) is a well-known example of a GMC. It is within these regions that new stars are formed. Star formation begins when clumps within a dark cloud collapse further, probably as a result of collisions between clumps or shocks from nearby supernovae. As the collapse continues, gravitational potential energy is converted to kinetic energy and the centre of the clump becomes a core with a temperature of the order of a few 100 K. Eventually, the thermal expansion becomes sufficient to balance gravitational attraction and collapse ceases, resulting in a protostar. In order for a clump to collapse further to form a protostar, and hence a small star such as the Sun, some of the thermal energy must be radiated out of the clump. It is now thought that molecules present in the collapsing clump provide a mechanism for this by emitting energy through rotational, vibrational and, as the temperature rises, electronic transitions [6].

[1] 1 light year (ly) = 9.5×10^{15} m

Figure 1.1: View of the Orion Nebula, an example of a GMC, observed with the Hubble Space Telescope. From [7].

This further collapse causes the temperature to rise to around 2000 K resulting in a hot core. This temperature is high enough for H_2 to be dissociated and as the temperature rises further the H atoms are ionized. Finally, at around 10^6 K, collisions between protons are sufficiently energetic for nuclear fusion to begin. During the later stages of star formation, some material accretes into a disk around the protostar. Some of this is lost through outflows from the poles of the forming star, but that which remains provides the material for the formation of a planetary system. An example of a forming star showing the outflows and disk is shown in **Figure 1.2** along with a schematic representation. Ultimately, the material in a star and planetary system is recycled when a star reaches the end of its life. In the case of large stars, the resulting supernova carries material back into the ISM where it may be involved in the formation of the next generation of stars. It is clear that there are a wide variety of different astrophysical environments, and molecules play an important role in many of these. The study of these molecules, how they are formed and evolve, along with their involvement in processes such as star formation, forms the basis of the relatively new field of astrochemistry.

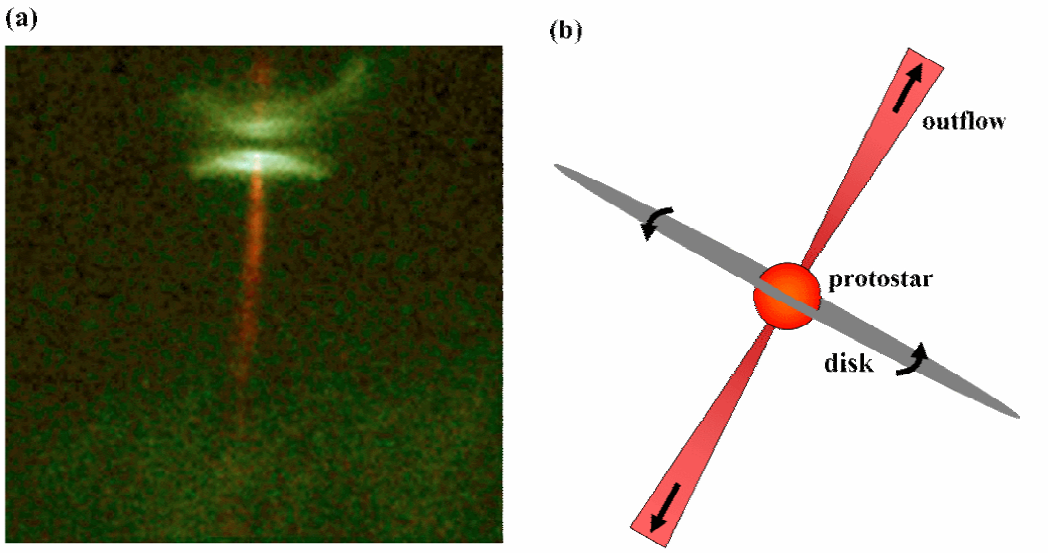

Figure 1.2: (a) Disk and outflow associated with the forming star HH-30 [8]. (b) A schematic of a forming star showing the disk and outflow.

1.3 Astrochemistry

Astrochemistry has its roots in the early 20th century with the detection of simple chemical species in the ISM of the Milky Way. The first detection that suggested the presence of interstellar gas was that of Ca^+ in the visible by Hartmann in 1904 [9]. In the 1930s, the first detection of the molecular species CH, CH^+ and CN was confirmed [10-12]. Following the detection of H in 1951, the development of millimetre wavelength astronomy led to the observation of important species such as OH, NH_3, H_2O and H_2CO. However, it was the detection in 1970 of ^{12}CO in the Orion Nebula through its R(0) transition at 115 GHz [13] that led the way to large scale mapping of molecules in the ISM. The detection of H_2 has proved particularly difficult. It possesses no permanent dipole moment, so there are no allowed rotations or vibrations limiting IR detection to the weak emission that results from forbidden quadrupolar transitions [14], though this requires gas temperatures in excess of 500 K for the required excited states to be occupied. H_2 can however be detected through its electronic transitions, though the UV wavelengths required are absorbed by the Earth's atmosphere and such observations [15,16] must be made from above the atmosphere. CO is much more readily detected, having both allowed vibrations and rotations. Indeed, CO has frequently been used as tracer for H_2, assuming a constant value for the CO/H_2 ratio.

To date, over 120 molecules have been detected in interstellar and circumstellar space [17] (see **Table 1.1)**. These molecules have been detected through observations at wavelengths across the electromagnetic spectrum. This list represents a lower limit on the range of molecules present, with the presence of many others being inferred from those that have been observed. It is also necessary to consider also ionic species, present in exposed regions as a result of photon and cosmic ray induced ionization. Furthermore, radicals and short-lived reaction intermediates are difficult to detect as a result of low abundances.

2 atoms	**3 atoms**	**4 atoms**	**5 atoms**	**6 atoms**	**7 atoms**	**≥ 8 atoms**
H_2	C_3	c-C_3H	C_5	C_5H	C_6H	CH_3C_3N
AlF	C_2H	l-C_3H	C_4H	l-H_2C_4	CH_2CHCN	$HCOOCH_3$
AlCl	C_2O	C_3N	C_4Si	C_2H_4	CH_3C_2H	CH_3COOH?
C_2	C_2S	C_3O	l-C_3H_2	CH_3CN	HC_5N	C_7H
CH	CH_2	C_3S	c-C_3H_2	CH_3NC	$HCOCH_3$	H_2C_6
CH^+	HCN	C_2H_2	CH_2CN	CH_3OH	NH_2CH_3	CH_2OHCHO
CN	HCO	CH_2D^+?	CH_4	CH_3SH	c-C_2H_4O	CH_2CHCHO
CO	HCO^+	HCCN	HC_3N	HC_3NH^+	CH_2CHOH	CH_3C_4H
CO^+	HCS^+	$HCNH^+$	HC_2NC	HC_2CHO		CH_3CH_2CN
CP	HOC^+	HNCO	HCOOH	NH_2CHO		$(CH_3)_2O$
CSi	H_2O	HNCS	H_2CHN	C_5N		CH_3CH_2OH
HCl	H_2S	$HOCO^+$	H_2C_2O	HC_4N		HC_7N
KCl	HNC	H_2CO	H_2NCN			C_8H
NH	HNO	H_2CN	HNC_3			CH_3C_5N?
NO	MgCN	H_2CS	SiH_4			$(CH_3)_2CO$
NS	MgNC	H_3O^+	H_2COH^+			CH_3CH_2CHO
NaCl	N_2H^+	NH_3				HC_9N
OH	N_2O	SiC_3				$CH_3OC_2H_5$
PN	NaCN	C_4				$HC_{11}N$
SO	OCS					
SO^+	SO_2					
SiN	c-SiC_2					
SiO	CO_2					
SiS	NH_2					
CS	H_3^+					
HF						
SH						

Table 1.1: Detected IS and circumstellar molecules as of 2005. Adapted from **http://www.cv.nrao.edu/~awootten/allmols.html**. ? indicates a tentative detection. c- and l- indicate cyclic and linear species respectively.

This list also makes no reference to the many polycyclic aromatic hydrocarbons (PAHs) that are thought to account for up to 20% of galactic carbon, with up to 70% of these being present in carbonaceous grains [18,19]. Given the wide range of species detected, it is clear that there is a rich chemistry in the ISM. The majority of this must occur within molecular clouds where number densities are sufficiently high. However, the number densities are still extremely low compared to the terrestrial environment which, when combined with low temperatures, puts severe constraints on the range of chemical reactions that are likely to occur. The common types of reactions will now be outlined.

1.3.1 Gas phase chemistry

The early universe contained only H and H^+ and thus H_2 formation was important at this time. However, two neutral H atoms colliding must lose energy in order to form H_2 in a bound state. Energy could be removed from the system by a third collision partner, but with number densities so low, three-body collisions would be extremely rare events. Radiative association reactions provide a means to remove excess energy from the collision partners during reaction:

$$A + B \rightarrow AB + h\nu \qquad \textbf{Equation 1.1}$$

However, as H_2 has no permanent dipole moment, relaxation to the ground state is extremely inefficient. H_2 was therefore formed by a combination of electron and proton attachment to neutral H, followed by reaction with another H to yield H_2.

$$H(g) + e^- \rightarrow H^-(g) \qquad \textbf{Equation 1.2}$$

$$H^-(g) + H(g) \rightarrow H_2(g) + e^- \qquad \textbf{Equation 1.3}$$

$$H(g) + H^+(g) \rightarrow H_2^+(g) \qquad \textbf{Equation 1.4}$$

$$H_2^+(g) + H(g) \rightarrow H_2(g) + H^+(g) \qquad \textbf{Equation 1.5}$$

H and H_2 were important coolants during the formation of the first generation of stars. Highly energetic collisions were sufficient to ionize some of the H atoms, with radiation being emitted upon recombination. Collisions between H_2

molecules and H atoms can excite H_2 to an excited vibrational state. In returning to the ground state *via* a quadrupolar transition, radiation is emitted. In both cases, the result is that the overall kinetic energy, and hence temperature, of the gas is reduced. The first generation of stars were large and short-lived as they formed from only H and H_2, with no other coolant molecules being present. However, they produced heavier elements through thermonuclear fusion which naturally led to a wider range of elements, and subsequently molecules, being present during the formation of subsequent generations of stars. These provided the cooling mechanism required for the formation of small long-lived stars, such as the Sun.

The chemistry occurring in dark clouds is far more varied as a result of the presence of a wider range of chemical elements. However, the conditions are still sufficiently harsh that the range of possible reactions is limited. Three-body reactions are again highly unlikely and the low temperatures of down to 10 K preclude any reactions with all but the most modest of activation barriers. The important reactions along with typical rates are shown in **Table 1.2**. This highlights the inefficiency of three body collision association reactions. Photodissociation reactions play a more important role in diffuse clouds, where the attenuation of the interstellar UV field is much less.

Reaction type	Typical form	Typical rate
Photodissociation	$AB + h\nu \rightarrow A + B$	10^{-9} s^{-1}
Neutral-neutral	$A + B \rightarrow C + D$	10^{-11} cm^3 s^{-1}
Ion-molecules	$A^+ + B \rightarrow C^+ + D$	10^{-9} cm^3 s^{-1}
Charge transfer	$A^+ + B \rightarrow A + B^+$	10^{-9} cm^3 s^{-1}
Radiative association	$A + B \rightarrow AB + h\nu$	Reaction dependent
Dissociative recombination	$A^+ + e \rightarrow C + D$	10^{-7} cm^3 s^{-1}
Collisional association	$A + B + M \rightarrow AB + M$	10^{-32} cm^6 s^{-1}
Associative detachment	$A^- + B \rightarrow AB + e^-$	10^{-9} cm^3 s^{-1}

Table 1.2: General forms of some important gas phase chemical reactions occurring in the ISM

Whilst UV photons may cause photodissociation close to the edge of a dark cloud, primary electrons from cosmic rays provide the only dissociation mechanism deep within such a cloud. However, protons account for around 90% of cosmic rays, and these are extremely important in providing a route for the formation of hydrogenated species. Reaction of H_2 with O, C, and N are forbidden, and reaction relies on the H_3^+ ion. H_3^+ is formed by collisions between cosmic ray H^+ and H_2 and readily donates a proton to other species, reforming H_2 in the process. The importance of this ion and its detection have been discussed elsewhere [20]. In summary, it provides gas phase routes to species such as OH, H_2O, CH_3^+, and importantly CO through the following reaction sequence:

$$CH_3^+(g) + O(g) \rightarrow HCO^+(g) + H_2(g) \qquad \textbf{Equation 1.6}$$

$$HCO^+(g) + e^- \rightarrow CO(g) + H(g) \qquad \textbf{Equation 1.7}$$

The abundance of any particular species will depend on a range of reactions including formation, destruction and interconversion. It is therefore necessary to consider a large number of species and reactions together when comparing calculated abundances with observations. This is achieved through the use of chemical reaction networks which contain large numbers of species and chemical reactions. Examples include the model developed at the Ohio State University [21] and the UMIST astrochemistry database [22-24] developed at the University of Manchester. The most recent version of the latter includes 420 species and 4572 gas phase reactions. These reaction networks are able to describe well the observed abundances in many astrophysical environments. The calculated abundances of typically up to 80% of species are in agreement with observations. It is clear that gas phase reactions are important for the formation of many observed molecules, and further refinements in rate constants and appropriate conditions will lead to better agreement. However, there are some species for which formation in the gas phase cannot be sufficiently efficient to account for the observed abundances. Examples of these include the three highly abundant molecules H_2, H_2O and CH_3OH. The inefficiency of H_2 formation in the gas phase, resulting from it possessing no allowed vibrations and rotations to radiate

collision energy, has already been highlighted. Thus it has been found necessary to invoke surface chemistry in order to properly account for the formation of these and other species on the surfaces of interstellar dust grains. Before considering some typical surface process, it is appropriate to consider the evidence for and nature of interstellar grains.

1.3.2 The evidence for interstellar grains

There are several good reviews on the presence and nature of interstellar dust [25,26], though the key points will be highlighted here. Interstellar dust accounts for only around 1% by mass of the material in the ISM. However, light can interact with grains in a number of ways, revealing their presence. Trumpler [27] is credited with the first definitive identification of dust within the ISM with his suggestion that obscuration of star light might occur as a result of absorption and scattering. This leads to an apparent reddening of stars situated behind a region containing dust, an effect known as interstellar extinction. As such, the apparent magnitude of a star, $m(\lambda)$, is dependent on both the distance of the star from the observer, *d*, and the extinction due to dust, $A(\lambda)$:

$$m(\lambda) = M(\lambda) + 5\log[d] + A(\lambda) \qquad \textbf{Equation 1.8}$$

where $M(\lambda)$ is the absolute magnitude of the star. It is usual to express the extinction at a particular wavelength relative to some reference wavelength, *V*, usually in the visible, *i.e.* $A(\lambda)/A(V)$[28]. The observed extinction curve shows a general trend of decreasing extinction towards the red end of the spectrum, which is what gives rise to the reddening of stars situated behind a region containing dust. Scattering of light is most efficient for light having wavelengths comparable to the dimensions of the scattering particles. This means that typical grain sizes can be estimated from the curve. In general the curve is fairly featureless, with the exception of a sharp "bump" around 217 nm as shown in **Figure 1.3**. It is possible to obtain estimates for grain sizes by using dust models and fitting to the observed extinction curves, with such models suggesting three contributions [30].

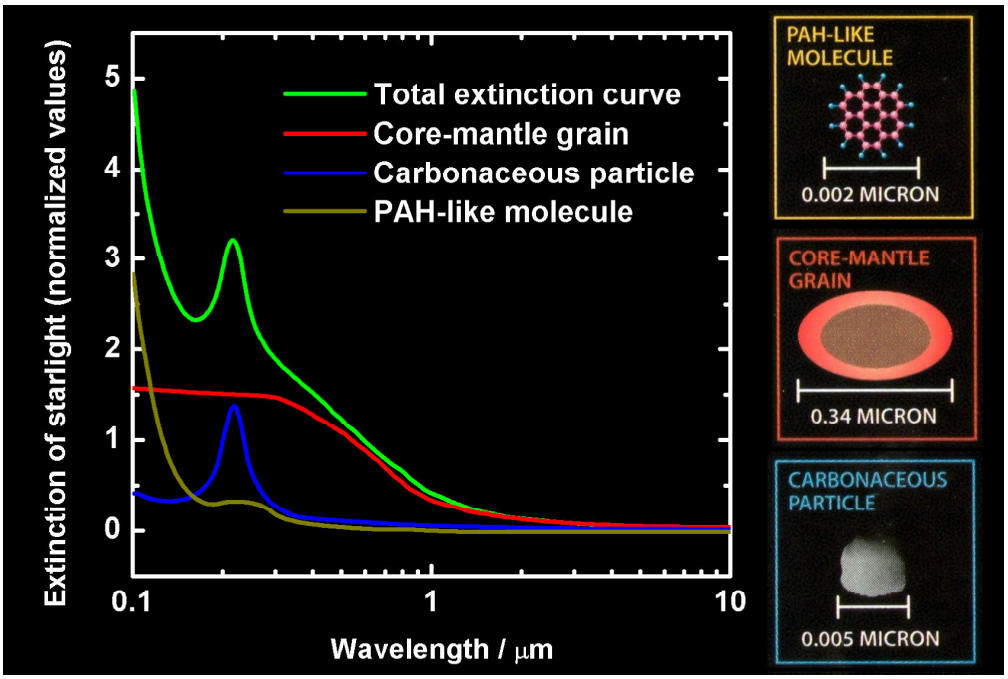

Figure 1.3: The interstellar extinction curve showing contributions from different grain populations. Adapted from [29].

Grains with dimensions of the order of 0.1 μm account for the extinction at longer wavelengths and into the visible, though this contribution levels off for shorter wavelengths. The "bump" feature is therefore thought to be a result of the presence of much smaller particles having a mean radius of around 0.003 μm. Large molecules, in particular large polycyclic aromatic hydrocarbons (PAHs), have the required size to account for the rise in extinction at shorter wavelengths. The origin of the "bump" feature has been the subject of much debate. It is thought to arise from small carbonaceous particles, though the morphology of these is unclear with a range of structures including graphite, amorphous carbon and carbon "onion" structures being suggested. For all of these, absorption around 220 nm can be accounted for by $\pi \rightarrow \pi^*$ transitions, which occur in materials where carbon forms delocalized sp^2 hybrid bonds [31].

As well as absorbing starlight, dust grains can also scatter light. This scattering can be observed in reflection nebulae through the scattering cross-section, or albedo. For small particles of diameter r, where $r<\lambda$, the process can be described by Rayleigh scattering where the scattering efficiency varies inversely with the fourth power of the wavelength. As a result, scattering is most efficient at shorter

wavelengths, which gives rise to reflection nebulae having a characteristic blue colour. Typically, a strong decrease in albedo is observed around 217 nm, confirming that this feature in the extinction curve arises as a result of absorption. Further evidence for dust comes from the polarization of starlight. This indicates that grains are non-spherical and aligned by the interstellar magnetic field. This results in selective extinction of one plane of polarization leading to linear polarization.

1.3.3 The composition of grains

Though they reveal the presence and physical nature of interstellar grains, none of the effects described so far provide much insight into the chemical nature and composition of these grains. Some evidence for grain composition comes from observations of gas phase species within clouds, which reveal significant depletion of some elements, which results from them being locked up in the solid phase [32]. Importantly, the depletion of C and Si is thought to indicate the presence of the two main populations of grains, those composed of carbonaceous particles, and those derived from silicates. The carbonaceous grain population is thought to account for the 217 nm feature in the interstellar extinction curve, with graphitic materials generally taken as being representative of these grains. Much information regarding the composition of grains has been obtained by utilizing infrared observations carried out from above the Earth's atmosphere. In particular, the Infrared Space Observatory (ISO) mission has provided valuable evidence for the presence of both amorphous and crystalline silicates along with a range of molecular ices [33]. The presence of silicates is revealed by a strong absorption band at *ca.* 9.7 μm, characteristic of the Si-O stretch typically found around 10 μm in silicates, see **Figure 1.4**. A broad absorption feature centred around 18 μm is thought to be associated with the O-Si-O bending mode [34], providing further support for a silicate grain population. These features tend to be found in the outflows from cool oxygen-rich stars where silicate dust is thought to condense, and are absent in the outflows from carbon rich stars, where the oxygen tends to be locked up in CO [31]. The interstellar 9.7 μm feature tends to be rather broad and featureless when compared with laboratory absorption spectra of crystalline silicates, suggesting that grains are dominated by amorphous silicates. The

observed depletions of Mg and Fe suggest that these are likely to be the primary metallic components of interstellar silicates. Magnesium silicates such as olivine, which has the general formula $Mg_{2x}Fe_{2-2x}SiO_4$, are frequently thought to be representative of interstellar silicates, and laboratory spectra [35] of both the olivine forsterite, Mg_2SiO_4, and enstatite, $MgSiO_2$, provide a good match to the interstellar 9.7 μm feature. There is some evidence for crystalline silicates, though estimates for the fraction of silicates that are crystalline vary widely. A recent study [36] has suggested that no more than 5% of interstellar silicates are crystalline when adsorbed ice mantles are taken into consideration.

1.3.4 Grain mantles

The depletion of other elements suggests the presence of a range of molecular ices frozen onto the grain surfaces. Typical grain temperatures in dense clouds are 10 K, sufficient for the majority of atomic and molecular species to reside on the grain surface for significant periods of time. Even in warmer, more diffuse regions, mantles of less volatile species such as H_2O can form. The first detection of H_2O ice was made in 1973 [37] through IR absorption at 3.1 μm. This absorption band is characteristic of the OH stretch of adsorbed bulk ice [38,39]. More recently, the ISO mission has been extremely valuable in elucidating the nature of these adsorbed ices, revealing the presence of around 40 species [40]. The ices have predominantly been observed through absorption in the cold outer envelopes surrounding high mass protostars, though there have also been some observations of ices around low mass objects. An example of the former is the embedded massive protostar, W33A, observations of which demonstrate the wide range of ice features typically observed [41]. An example ISO spectrum for a line of sight towards this source is shown in **Figure 1.4**.

H_2O is by far the most abundant ice, its absorptions dominating the spectra with the optical depth often exceeding that of the silicate feature at 10 μm. Apart from H_2O, the ices appear to contain significant amounts of CO, CO_2 and CH_3OH, with other species being present in much smaller concentrations.

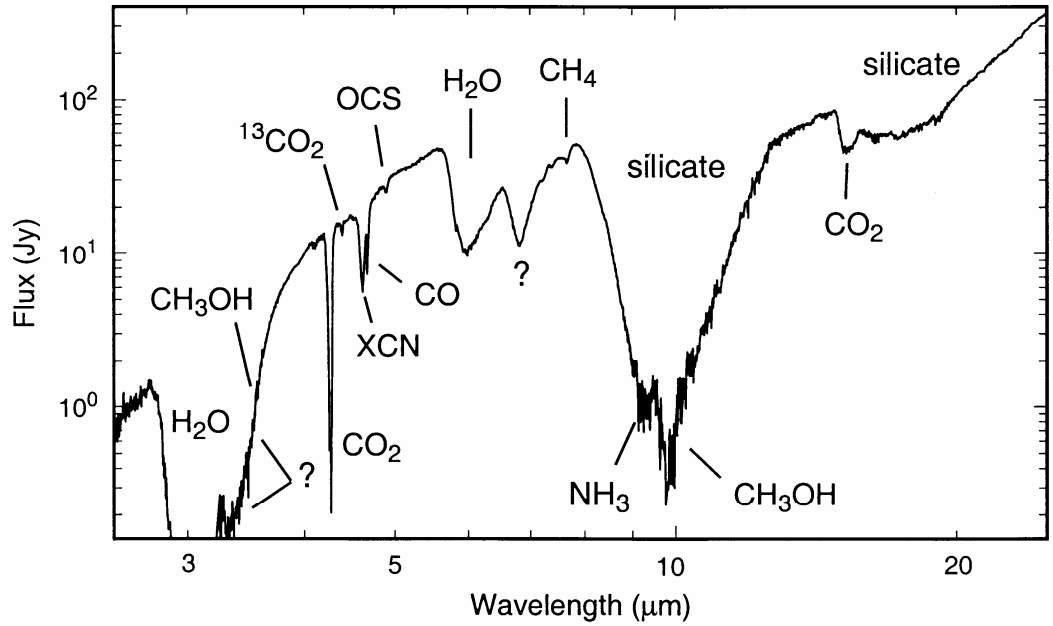

Figure 1.4: ISO spectrum showing absorptions by ices around the massive embedded protostar, W 33A [41].

The abundance of H_2O is typically around 10^{-5}-10^{-4} relative to that of H_2, with CO and CO_2 together accounting for 10-30% of the ices, though this may be significantly higher depending on the environment [40]. Other carbon containing species such as CH_3OH, HCOOH, CH_4 and H_2CO may also contribute 20-30 %, giving a typical ratio of 50% H_2O ice to 50% other species. It is important to note that whilst N_2 and O_2 detection is difficult as a result of these molecules possessing no permanent dipole moment, they can be detected when the transitions become weakly allowed due to the presence of other molecules. However, a strong CO_2 stretching mode overlaps with this transition in N_2. It is however generally accepted that O_2 and N_2 molecules exist as ices, though probably in relatively low concentrations. The obtained ISO spectra for 23 sources have been analyzed in detail [42] providing a valuable summary of the data obtained during the mission.

The shifts and lineshape variations imposed on the spectral features of ice molecules by the presence of other ices have indicated that ices are frequently non-homogenous, with layering of ices occurring [43]. Layers of ice dominated by H_2O, sometimes referred to as polar layers, are thought to form when the rate of H accretion is high. As well as forming H_2O, any accreted CO will react forming HCO, resulting in a layer that is poor in CO. So called non-polar layers,

rich in CO and CO_2, form when H accretion is much lower and hydrogenation reactions are much less important. This highlights the importance of cloud conditions on the formation of ice mantles.

Some species, including atomic H and O along with CO, within the ices are accreted from the gas phase. However, the gas phase abundances of some species cannot be sufficient to account for the observed amounts of ice. H_2O can be formed in the gas phase by a number of routes. In warm regions, neutral-neutral reactions between H_2 and O can form H_2O *via* OH [44]. However, these reactions have non-negligible activation barriers and are not viable at temperatures below 300 K. At lower temperatures, H_2O can be formed through the following ion-molecule scheme with H_3O^+ subsequently forming OH or H_2O *via* recombination with an electron [1].

$$O^+(g) \xrightarrow{H_2(g)} OH^+(g) \xrightarrow{H_2(g)} H_2O^+(g) \xrightarrow{H_2(g)} H_3O^+(g) \qquad \textbf{Equation 1.9}$$

However, the freeze-out of atomic O onto grain surfaces is likely to limit H_2O in the gas phase by this route. Models have shown that the low gas phase abundance of H_2O in dark clouds can be reproduced by incorporating grain surface mechanisms [45]. Grain surface reactions also provide a route to forming H_2 which, as has been discussed earlier, cannot be formed efficiently in the gas phase.

The formation of species on grain surfaces was first postulated by van de Hulst in the 1940s [46]. This was further developed in relation to the problem of H_2 formation during the 1960s [47]. At this time it was suggested that grain surface reactions could produce H_2 at a rate $>10^5$ times that possible in the gas phase. A model was constructed based on the assumption that every H atom striking a grain sticks to it. The migration of H atoms across the surface, recombination with a second H atom and evaporation of H_2 were considered. Recombination was considered to occur if two hydrogen atoms approached each other closer than two lattice spacings on a given surface. It was also demonstrated that at low grain temperatures of around 10 K quantum mechanical tunnelling through barriers between surface sites is required, as thermal diffusion is relatively inefficient.

Initial calculations suggested a maximum in recombination efficiency at surface temperatures of between 5 and 15 K. This approach, though considering an ideal surface, was useful in indicating the important parameters in grain surface reactions. It highlighted the need for experimental studies of the formation processes themselves, and in obtaining detailed values for quantities such as adsorption energies. Some examples of laboratory experiments will be provided in subsequent sections. However, from an astrophysical viewpoint, it is useful to consider the ways in which the ices, once formed, can be processed through both thermal and non-thermal mechanisms in the interstellar environment.

1.3.5 Processing of ices

Ices can be processed in a number of ways in the interstellar environment as a result of energy being deposited within the mantle. Physical processes include desorption of molecules from icy mantles, and structural changes such as mixing, segregation and phase changes. Chemical processing is also possible, which can lead to the formation of more complex molecules. The mechanisms that drive these processes can be classified as being thermal or non-thermal. The most obvious cause of thermal processing is the warm-up of a molecular cloud during star formation. It has been suggested that the time for a cloud to warm-up to above the temperature required for H_2O desorption is determined by the time taken for a forming star to reach the main sequence, which is of the order of 10^4-10^6 years [48]. This results in typical heating rates of 0.1-1 K century^{-1}. Non-thermal processing can arise as a result of the irradiation of ices with photons and charged particles. Photons are generally present in the ISM in the form of the interstellar radiation field (ISRF) which typically contains contributions from nearby stars and emission both from dust and molecules such as PAHs [2]. The ISRF has been calculated, taking different galactocentric distances, D_G and stellar contributions into account [49]. The intensity within a cloud is reduced as a result of attenuation by scattering and absorption by grains as shown in **Figure 1.5**. Astrochemical models have shown photoprocessing to be particularly important in protoplanetary disks [50], where the UV flux consists of both stellar and interstellar components.

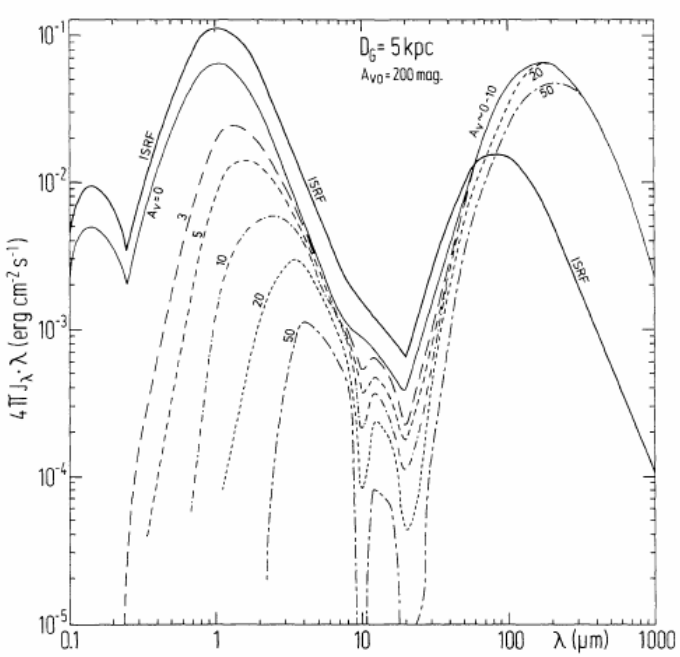

Figure 1.5: Interstellar radiation field at a D_G value of 5 kpc and within a GMC having a visible extinction of 200 magnitudes at its centre[2]. Individual curves show the intensity at a particular visual extinction corresponding to a particular distance from the centre of the cloud. From [49].

However, processing by interstellar photons is likely to be important close to the surface of a wide range of objects. Indeed, photodesorption and photodissociation of H_2O by UV photons from the ISRF have been shown to be efficient in the outer layers of both protoplanetary disks [51] and molecular clouds [52]. In all cases, photodesorption was used to explain the observed relatively high gas-phase abundances of species normally expected to be strongly depleted through adsorption on grain surfaces.

The major primary sources of charged particles are cosmic rays. Some particles may have energies exceeding 100 MeV which provides a significant contribution to the energy density of the ISM. The highest energy cosmic rays lead to the emission of gamma rays upon collision with gas molecules. Lower energy cosmic rays can lead to the generation of secondary electrons through cosmic ray ionization of species, which will be most pronounced in the outer regions of dense clouds. Low energy electrons with energies up to a few thousand eV are

[2] 1 erg = 10^{-7} J

particularly important for the chemistry within dense clouds as these energies correspond to those required to excite valance and core electrons in molecules. It is clear that given the typical lifetimes of molecular clouds, the effect of photon and low energy electron irradiation on interstellar ices must be considered.

1.4 Polycyclic aromatic hydrocarbons

Polycyclic aromatic hydrocarbons (PAHs) are a class of planar carbon bearing molecules that are made up of fused benzene rings. They possess many properties that arise as a result of their aromaticity. In all cases this results from the delocalization of electrons in planes that are parallel to the plane of the molecule. As the molecules are planar, the carbon atoms can be considered to bond through sp^2 hybrid orbitals, with the remaining p_z orbitals overlapping to form a delocalized system. For benzene, molecular orbital theory indicates that the six p_z orbitals give rise to six molecular orbitals (MOs), three of which are bonding (π) and three of which are anti-bonding (π^*). The six electrons from the p_z orbitals fill the π orbitals, leading to a closed-shell configuration that is particularly stable. The same concepts also apply to PAHs, which become increasingly stable as a result of the increase in the size of the delocalized electron system. The structures of some simple PAHs, along with benzene, are shown in **Figure 1.6**.

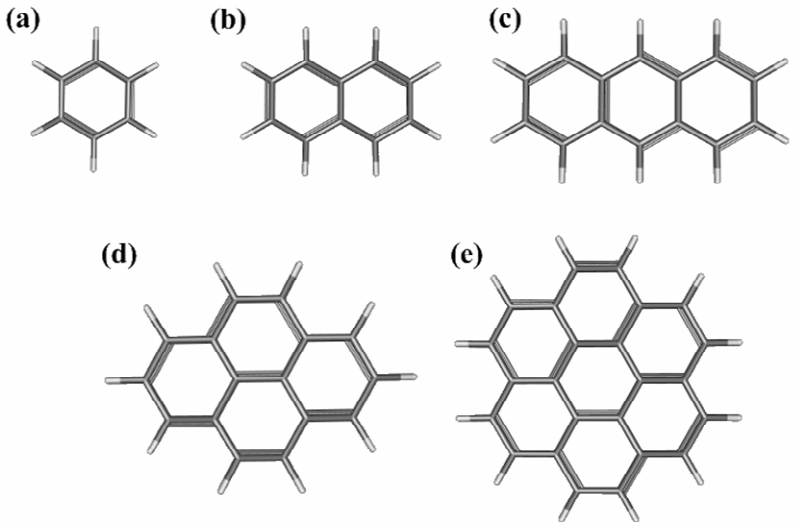

Figure 1.6: Structures of (a)benzene (C_6H_6), (b) naphthalene ($C_{10}H_8$), (c) anthracene ($C_{14}H_{10}$), (d) pyrene ($C_{16}H_{10}$) and (e) coronene ($C_{24}H_{12}$).

1.4.1 PAHs in the ISM

PAH molecules are a particularly important class of molecule in many astrophysical environments. As has already been indicated, it is thought that they account for a significant proportion of the carbon in the galaxy. The photophysics of PAHs is particularly important and a good overview is provided elsewhere [2] along with an extensive review [53]. PAH molecules can be detected through both absorption and emission, with the principles described here being generally applicable to other molecules. If a neutral PAH molecule in its ground singlet state S_0 absorbs a UV photon it can be excited to an excited electronic state *e.g.* S_2, S_3 *etc*. Internal conversion to excited vibrational states in S_1 can then occur, followed by intersystem crossing which populates a range of vibrational states in T_1; the lowest lying triplet electronic state.

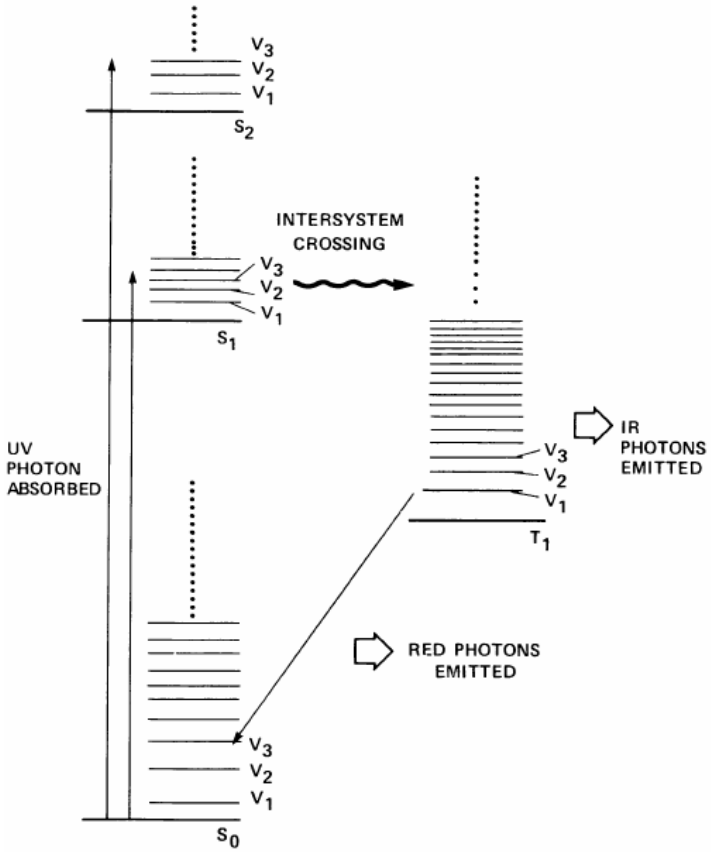

Figure 1.7: Jablonski diagram to illustrate the photophysics that drives IR and visible emission by PAH molecules. Taken from [53].

If collisions are negligible, deactivation can only occur as a result of IR emission resulting from vibrational relaxation in T_1 and visible emission as a result of an electronic transition to S_0 (phosphorescence). In the case of ionized PAHs, internal conversion to the ground state D_0, which is a doublet state, is dominant resulting in only IR emission during deactivation. A Jablonski diagram for the case of neutral PAHs is shown in **Figure 1.7**.

PAHs are commonly thought to be the carriers of a series of broad emission features in the IR known as the Unidentified IR bands (UIRs) as a result of them not being identified for around a decade after they were first observed. They were first observed in the 1970s [54] and have since been found towards a large number of objects including stars, nebulae and even extragalactic sources. These features are observed at 3.3, 6.2, 7.7, 8.6 and 11.3 μm and are sometimes now referred to as the aromatic infrared bands as it is reasonably well accepted that they are of aromatic origin. These emission features have been discussed in detail, and compared to laboratory IR spectra of PAHs [55]. PAHs were first suggested as carriers of the UIRs in the mid-1980s [56] when several of the bands were compared to the calculated emission spectrum of coronene heated to 600 K. It was concluded that PAH molecules with *ca.* 50 carbon atoms would result in the observed peak intensity ratio. Allamandola *et al.* [53] suggested that PAH molecules with between 20 and 40 carbon atoms would result in the observed sharp emission features, whilst larger PAHs with up to 500 carbon atoms could lead to the broader emission background. Larger PAHs are likely to exist as van der Waals clusters. The difficulty in obtaining an exact match between laboratory spectra and the observed emission lies not only with uncertainty of the size of the molecules, but also their nature. Ionization, hydrogenation, de-hydrogenation and excitation energy will all affect the observed spectra. The observed IR features can to some extent be correlated with the known vibrational modes of generic PAH molecules and ions. For example, bands in the 3 μm region correspond to C-H stretching modes, those in the 6 μm region to C-C stretching modes, those in the 8 μm region to C-H in plane bends whilst out of plane C-H bends can account for emission between 11 and 15 μm. The likely variety of PAH species present in the ISM presents a significant challenge to identifying any individual species

definitively. PAHs are also thought to be responsible for some of the so-called diffuse interstellar bands which were first observed in the 1930s. These UV-Vis. absorption features, which have been discussed in detail [57], are generally attributed to electronic transitions in molecules and are typically observed towards dusty regions. It is thought that carbon bearing molecules including carbon chains, PAHs and fullerenes are the most likely candidates for many of the bands [58].

The wealth of observations of spectroscopic features that can be attributed to PAHs strongly suggests that PAH molecules are ubiquitous in the ISM. It is therefore reasonable to assume that to some extent they are also present in the solid phase. It has been noted that solid state absorption features of PAHs are significantly weaker than those in the gas phase, which makes direct observation difficult [59]. In addition, in dense clouds, PAHS will be shielded from the UV irradiation required for the excitation that would lead to observable emission, resulting in an expectation that detection can only be made through absorption. In order to aid these observations, the IR spectra of a series of PAHs within a H_2O ice matrix have been obtained using laboratory experiments [60]. Examples of the IR spectra obtained are shown in **Figure 1.8**. These spectra suggest that, compared to matrix isolation experiments performed with Ar, the presence of the H_2O matrix results in peak broadening, a small degree of peak shifting and some variable changes in relative band strengths. All shifts were interpreted as being the result of PAH-PAH and PAH-H_2O interactions, as were the modest variations in relative band strengths. The broadening was attributed to PAH-H_2O interactions and the presence of a range of PAH adsorption geometries within the amorphous ice matrix. The spectra were observed to be relatively insensitive to both the PAH concentration and ice temperature up to the amorphous to crystalline phase transition. Given the relatively minor effects of the presence of the H_2O matrix on the IR spectra, it was suggested that IR spectra obtained through matrix isolation experiments using inert species, such as Ar or N_2, are likely to be useful in initial interpretations of interstellar PAH spectra. It was however stressed that the band strength variations mean that experiments conducted in an H_2O matrix would be crucial for the determination of column densities.

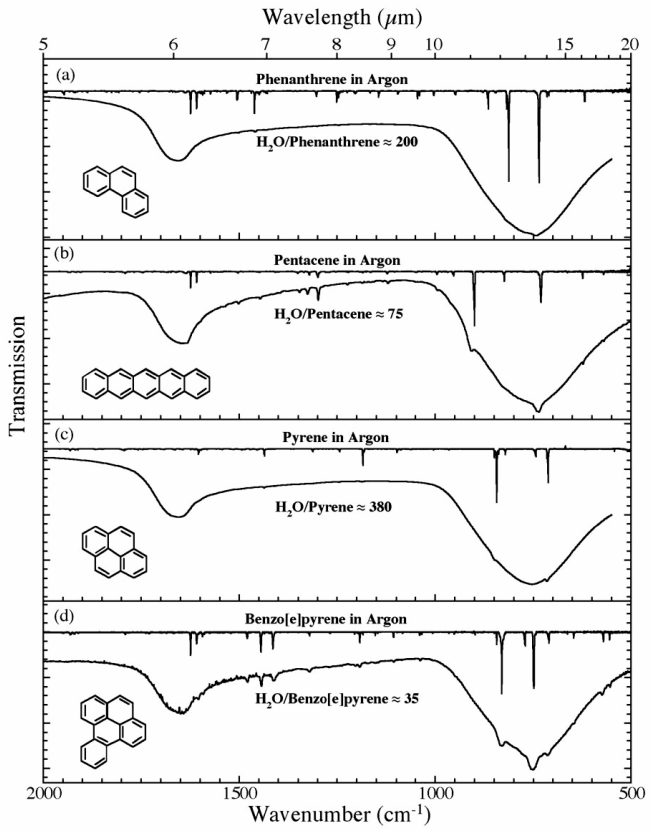

Figure 1.8: Comparison between IR spectra for several PAHS obtained in Ar and H_2O matrices [60].

In the experiments described in this thesis, benzene, C_6H_6, was used to study the thermal and non-thermal processing of PAHs. This was primarily for experimental convenience. However, C_6H_6 is also important in its own right as it has been detected around the protoplanetary nebula CRL 618 [61]. However, the reduction in size of the aromatic network compared to larger PAHs results in a much shorter lifetime in more exposed regions of the diffuse ISM [62] where photon irradiation rapidly destroys C_6H_6 molecules. There is evidence that the lifetime in dense clouds may be significant, but there have been to date no definitive identifications. Nevertheless, C_6H_6 is thought to be an important molecule in the interstellar carbon cycle in being a key intermediate in the formation of PAHs from acetylene [63-66].

In summary, it is clear that PAHs are an extremely important class of carbon bearing molecule in a wide range of astrophysical environments. Further work is needed, both in terms of observing PAH molecules through comparison with

laboratory spectra and in understanding how they interact with their local environment.

1.5 Overview of relevant laboratory astrophysics

Laboratory experiments can provide a range of data that are of use in better understanding the chemistry and physics of the interstellar medium. Studies of gas phase reactions have been used to provide experimental rate constants for many of the reactions in the reaction networks that have previously been discussed. As the focus of this thesis is on surface chemistry, these will be discussed no further here, though it is important to stress their importance. A wide range of research, both experimental and theoretical, has been conducted into relevant surface processes. Examples include the formation of simple molecules on grain surfaces, the properties of adsorbed ices, thermal desorption of ices, chemical reactions within ices to form more complex species and non-thermal processing of ices. A brief overview of some of the work conducted in these areas will be presented here.

1.5.1 Formation of simple molecules on grain surfaces

As has already been discussed, the formation of H_2 on grain surfaces is of particular interest. Laboratory experiments provide the opportunity to probe the reaction mechanisms involved, and the efficiency of formation under a range of conditions, and on different surfaces. An understanding of how the energy released during H_2 formation is partitioned is extremely important when considering the low temperature environment of the ISM. H_2 formation will be used here as an example of the types of laboratory experiments that can be conducted, and it should be noted that work has also been conducted into the formation of other simple molecules such as H_2O.

Three mechanisms are possible for the formation of H_2 and other molecules on surfaces, (1) the Langmuir-Hinshelwood mechanism, (2) the Eley-Rideal mechanism and (3) the hot atom mechanism. In (1) atoms are adsorbed and are thermally accommodated. Reaction then occurs as a result of encounters between atoms that are diffusing across the surface. In (2) an atom hits the surface close to a previously adsorbed atom and reaction occurs without thermal accommodation.

Finally, in (3) an atom hits the surface and travels across the surface without being accommodated with reaction occurring when it encounters an adsorbed atom. The observed efficiencies of these mechanisms are therefore expected to be sensitive functions of surface morphology, surface temperature, H atom flux and gas phase H temperature.

The first dedicated experimental study into interstellar H_2 looked at the formation of HD on an olivine substrate from atomic beams of H and D atoms formed by radio frequency dissociation of the precursor molecular species [67,68]. HD that was formed was detected by a quadrupole mass spectrometer, both during the irradiation and afterwards in a TPD experiment. The key findings were that HD formation efficiency decreases as substrate temperature is increased as a result of decreased residence time and that the HD detected during the TPD was formed during the warm-up, as evidenced by second order desorption kinetics. Subsequently, recombination on amorphous carbon and water ice surfaces were also considered [69]. It was concluded that recombination is activated, occurring predominantly during warm-up. A study by Hornekaer *et al.* [70] however demonstrated efficient formation of HD at temperatures as low as 10 K, with TPD yields of HD with sequential H and D dosing much reduced compared to those obtained with simultaneous dosing. This indicates rapid diffusion of H and D atoms across the surface even at 8 K. The importance of the morphology of the ice was also demonstrated in terms of the partitioning of the 4.5 eV released. HD formed on porous water ice is accommodated within the pores and subsequently thermally desorbed. On non-porous ice, the HD cannot be thermalized in this way, and the HD desorbs during irradiation. It was concluded that the HD is formed at low temperatures *via* the Langmuir-Hinshelwood or hot atom mechanisms.

Experiments have also been conducted to explore the quantum state of formed H_2 molecules [71,72]. Some of the 4.5 eV released during the H-H bond formation will be transferred to the substrate. However, it is likely that the H_2 molecules will be formed in excited rovibrational states. Resonance Enhanced Multiphoton Ionisation (REMPI) experiments have been conducted in which H_2 molecules formed under astrophysically relevant conditions are state-selectively ionized by a pulsed laser. The resulting H_2^+ ions were then detected by time-of-flight mass

spectrometry. The results indicated that excited state formation may contribute to the population of excited H_2 molecules in the ISM, previously attributed to direct UV pumping of ground state H_2 molecules.

At higher grain temperatures, H atoms must be chemisorbed in order to remain on the surface long enough for reaction to occur. Under such conditions, H_2 formation following chemisorption of H atoms on carbonaceous surfaces has been proposed. This has been studied experimentally and theoretically on a graphite surface [73,74], and theoretically on a series of PAH surfaces [75]. The results indicate that a range of pathways are available for H_2 formation with the energetics being determined by the chemisorption sites in which H atoms are adsorbed.

1.5.2 The morphology of water ice

A significant amount of attention had been focused on the properties and thermal desorption of H_2O. The phase of H_2O is known to be very sensitive to deposition conditions and the thermal history of ices. There is some uncertainty regarding the morphology of H_2O ice as formed *in situ* on grain surfaces, though analogous experiments to those performed for studying H_2 formation should provide useful information. It is generally accepted that vapour deposition of H_2O onto a cold substrate under high or ultrahigh vacuum conditions produces a film that is a reasonable approximation to that existing on cold dust grains [76]. This is based on the good agreement between the IR spectra of H_2O films prepared in this manner and those of ice in interstellar clouds. Electron diffraction studies [77] have been used to probe the changes in ice morphology as ice deposited at 15 K is warmed up. H_2O deposited below 130-140 K forms an amorphous ice film, commonly referred to as amorphous solid water (ASW). When deposited at temperatures lower than 38 K the ice is extremely porous with a high *local* density of around 1.1 g cm^{-3} and is referred to as porous ASW (p-ASW) or high density ASW (I_{hda}). It should be stressed that the density refers to the *local* density rather than the *bulk* density which is low as a result of the porosity. Annealing I_{hda} to temperatures above 38 K results in a gradual conversion to low density (*ca.* 0.94 g cm^{-3}), compact ASW (I_{lda} or c-ASW) which is complete by around 68 K. When

heated above 140 K the ice crystallizes into a cubic crystalline morphology (I_c) and eventually a hexagonal crystalline phase (I_h) above 170-180 K. The latter is not of particular relevance under astrophysical conditions where the relatively thin layers of ice will be lost through thermal desorption before significant I_h is formed. The porosity of low temperature deposited ASW has been demonstrated by its ability to trap volatile species such as N_2 [78], CO [79] and CCl_4 [80] to temperatures far in excess of their expected desorption temperatures. This has been interpreted in terms of migration of adsorbed species into the pore network as the film is heated up. As the film is heated above 35 K the pores begin to seal off, trapping the volatiles within. A sharp desorption feature is observed above 140 K, coincident with the change in H_2O desorption rate associated with the formation of I_c. This restructuring of the ice film opens pathways for the trapped volatiles to escape from the pore network resulting in the so-called "molecular volcano". Any remaining volatiles not desorbed during the crystallization co-desorb with the H_2O film at higher temperature. This trapping has been used to demonstrate how the porosity of ASW varies with deposition conditions [78]. For background vapour deposition, the porosity decreases rapidly with increasing temperature, with films deposited above 90 K being considered non-porous or compact (c-ASW). There is also a strong dependence on incidence angle which has been revealed using molecular beam deposition. When the beam is incident at high angles to the surface normal, shadowing effects result in a high degree of porosity, which decreases as the incidence angle is reduced. If the beam is at close to normal incidence compact ASW is formed, even at the lowest substrate temperatures. Another important finding is that both the initial phase of deposited H_2O and the subsequent crystallization kinetics during warm-up are independent of the kinetic energy of the incoming H_2O molecules during adsorption [81]. Therefore, deposition of H_2O from a reservoir at ambient temperature is likely to have a negligible effect on the ice morphology compared to the substrate temperature and angle of incidence. The thermal desorption of H_2O ice under astrophysical conditions has been studied and revealed zero-order [82] or close to zero-order desorption kinetics [83] which is characteristic of the desorption from bulk ice. In the former study, conducted on a polycrystalline Au surface, no distinct monolayer feature was observed, which was attributed to the H_2O-H_2O

interaction being dominant. For deposition on a highly oriented pyrolitic graphite (HOPG) surface [83] it was concluded that H_2O forms two- and three-dimensional islands. In both cases the change in the rate of desorption at temperatures of 145-150 K as a result of ice crystallization were observed.

1.5.3 Thermal desorption studies

Thermal desorption has been studied using temperature programmed desorption (TPD) experiments under UHV conditions for many years. However, only recently have such experiments been performed using interstellar ice mimics. Probably most important is the desorption of H_2O ice, the dominant species in the icy mantles found in dense interstellar clouds. TPD experiments demonstrated that the desorption of H_2O from grain mantles obeys close to zero order desorption kinetics [82-84], in contrast to first order desorption as previously assumed by the astronomy community. As well as the desorption order, the pre-exponential factor and desorption energy can be obtained through TPD experiments. Knowledge of these parameters can then be used within physical models of dense clouds to include the effect of grain mantle desorption. In the laboratory TPD profiles, for H_2O deposited under conditions where it forms an amorphous ice, a characteristic bump in the leading edge is present. This is attributed to the amorphous to cubic-crystalline phase transition and arises as a result of competition between desorption and crystallization of amorphous ice, along with small differences in desorption energies between the two phases.

H_2O ice formed under low temperature conditions where p-ASW is formed, thought to be characteristic of the ice formed on grain surfaces, has been shown to be able to trap volatile molecules such as CO to temperatures far above their normal sublimation temperatures [85]. Experiments where CO was adsorbed on top of a p-ASW film showed three desorption regimes; the first of these was at around 30-40 K and can be attributed to the desorption in CO from the surface of the p-ASW film. This desorption temperature is only slightly higher than that observed for the desorption of multilayers of CO. A further CO desorption occurred at the same temperature as the H_2O amorphous to crystalline phase transition, with a small amount of CO desorbing simultaneously with the H_2O

film. This was interpreted as being due to the diffusion of CO into the pores of the p-ASW at around 30 K, in competition with desorption. During the conversion from I_{hda} to I_{lda} the pores are effectively sealed off, trapping the CO within. Only when the film restructures during crystallization are sufficient passages to the vacuum re-opened, allowing the sharp desorption observed at higher temperatures, referred to as a molecular volcano. The highest temperature desorption is then attributed to that of residual CO that does not desorb during the molecular volcano. This has important consequences for astrochemical models where, previously, the desorption of CO was assumed to be complete by 30 K.

Subsequently, the thermal desorption of a wide range of species adsorbed on and in p-ASW was studied [86]. The molecules studied were N_2, O_2, CO, H_2S, OCS, CO_2, C_2H_2, SO_2, CS_2, CH_3OH, CH_3CN and HCOOH, all of which have been identified as being important in the chemistry of hot cores. The molecules were classified according to their thermal desorption behaviour. N_2, O_2 and CO all displayed the trapping behaviour described for CO, whilst a second class of molecules including NH_3, CH_3OH and HCOOH were shown to desorb in a very similar manner to that observed when they were deposited on a weakly interacting polycrystalline Au substrate. No molecular volcano was observed indicating that these molecules are unable to diffuse into the pore of the p-ASW. Significant co-desorption with H_2O was observed, indicating the presence of hydrogen-bonding interactions between these molecules and H_2O. The remaining molecules were classified as being intermediate between these two extremes. However, in contrast, Wolff *et al.* [87] saw evidence for a molecular volcano when a thicker layer of CH_3OH was adsorbed on top of an ASW film. These experiments were conducted with a base temperature of 97 K, and therefore the ASW deposited would have been relatively compact. It was therefore suggested that the observed trapping was the result of thermally induced mixing of the two components of the ice.

It is clear from these experiments that a full understanding of the desorption process requires a systematic study of the desorption of initially pure ices before considering from more complex ice mixtures that are more realistic analogues of interstellar ice mantles. The study of mixtures requires experiments performed

over a wide range of layer thicknesses and relative concentrations in order to ascertain how a particular species might desorb under a given set of conditions. In summary, although thermal desorption might at first sight seem to be a relatively simple process, the complex interactions that occur between different species in realistic ice mixtures have a significant impact on the desorption process. Further experimental studies are therefore crucial for future development of astrochemical models that include the thermal desorption of species from grain surfaces.

1.5.4 Photon irradiation of ices

Photochemistry, and photon driven physical processing such as desorption, induced on metal surfaces have been studied since the early years of surface science. However, much of the chemistry relies on the formation of hot electrons within the metal substrate, which is clearly not relevant in an astrophysical context. Rather it is the direct interaction of photons with the electronic structure of adsorbate molecules that is important. The discussion here will therefore be limited to those experiments performed using bulk ices. The case of relevant photodesorption studies will be considered first. The photon induced desorption of H_2O in an interstellar context has been studied by several groups. Westley *et al*. [88,89] have demonstrated efficient H_2O desorption during irradiation with Lyman-α photons (121.6 nm). This photon energy is above the 7 eV threshold for absorption by H_2O molecules, which was sufficient to cause dissociation forming H, and OH, H_2 and O, which subsequently reacted to form H_2O, HO_2, O_2 and H_2O_2. An overall H_2O desorption cross-section of 8×10^{-18} cm^2 was determined, though with significant uncertainties. Nishi *et al*. [90] studied the two-photon desorption mechanism using photons at 248 nm, though multi-photon processes are unlikely to be significant in the ISM where photon fluxes are extremely low compared with those obtainable in the laboratory. Further multi-photon channels were observed by Bargeld *et al*. [91] at a range of wavelengths between 270 and 670 nm for H_2O adsorbed on graphite. This work also revealed an enhanced desorption yield for amorphous ice, indicating the preferential desorption of more weakly bound H_2O molecules from defect sites. It was therefore suggested that excitons (bound electron-hole pairs), which are formed more efficiently at defects, were responsible for desorption. In this mechanism the excitons propagate

through the ice, dissipating their energy to weakly bound "edge" H_2O molecules, which are also more numerous in amorphous ice. More recently, the Leiden Astrophysics Laboratory have used RAIRS to study the desorption of H_2O during photon irradiation with broadband VUV centred around 121 nm [92]. Desorbing species were detected with a QMS. They were able to separate the processing into photodissociation of bulk H_2O molecules, and desorption of surface bound H_2O molecules. OH, H_2 and O_2 photoproducts were also detected with the QMS. The photodesorption yield was found to increase to 8 ML, with no increase for thicker H_2O films, confirming that photodesorption occurs only in the surface region. It was suggested that photodissociation products would desorb directly, result in H_2O desorption through recombination or kick-out, freeze-out (*i.e.* become thermalized) within the ice or recombine and freeze-out. These mechanisms have also been observed in molecular dynamics simulations [93] where the majority H_2O desorption was shown to result from recombination. Irradiation at 157 nm has, however, indicated that the kick-out mechanism might be dominant [94]. These experiments also probed the dynamics of desorbing molecules, indicating a translational temperature of around 1800 K and a rotational temperature of around 300 K. Only H_2O (v=0) was monitored, but it was indicated that vibrational excitation cannot be ruled out. Related experiments [95] have shown that photoproduced H_2 can be desorbed translationally and internally hot when it is formed by reaction of two H atom photoproducts. The endothermic abstraction of H from H_2O by H atoms was shown to result in the desorption of internally cold H_2 molecules.

Apart from water, the photodesorption of the more volatile species, CO, N_2 and CO_2 has been investigated [96,97]. The desorption of CO during irradiation using broadband VUV centred around 121 nm was shown to result from the surface layer, and was as efficient as H_2O desorption. The efficiency of N_2 desorption was around an order of magnitude lower, and it is thought that this is related to the presence of adsorbed contaminant H_2O and there is no direct desorption channel for N_2. Experiments with layered and mixed ices of CO and N_2 resulted in an increased N_2 yield further suggesting that absorption by one molecule can lead to desorption of a neighbouring molecule. Whilst no CO or N_2 dissociation was

possible at the energy used, CO_2 dissociation into CO and O was observed to occur, which also resulted in the formation of CO_3. Recombination of photoproducts leading to CO_2 desorption, analogous to the mechanism for H_2O desorption, was suggested as being responsible for the observed CO_2 desorption, which occurred with an efficiency of the same order of magnitude as that observed for H_2O.

There have been many studies of UV irradiation of bulk ices that have considered the formation of more complex organic species. For example, irradiation of H_2O ice containing CH_3OH, CO and NH_3 resulted in the formation of a whole series of compounds including CO, CO_2, CH_4, HCO, H_2CO, CH_3CH_2OH, $HC(=O)NH_2$ and other more complex species still [98]. Similar studies have also been performed with PAH molecules where the formation of aromatic alcohols, quinones and ethers has been observed [99]. It was noted that chemical reactions induced in PAHs might play a significant role in the formation of more complex species given that up to 20% of the galactic carbon is thought to be locked up in these molecules. Mixed H_2O ices with H_2O/PAH ratios of between 800 and 3200 were irradiated with broadband UV light centred around 160 nm. The loss of PAHs was observed through infrared spectroscopy whilst the detection of newly formed species also confirmed using microprobe laser desorption laser ionization mass spectrometry. The mass spectral data obtained indicated the addition of O and/or H atoms to the PAH molecules. The IR data confirmed the presence of C=O stretching modes, indicating the formation of ketones. Addition of H resulted in the formation of aliphatic regions, and both aliphatic and aromatic alcohols were detected through OH stretching and bending modes. The use of perdeuterated coronene demonstrated that hydrogen exchange between PAH and H_2O molecules is also efficient.

While these experiments clearly suggested that functional groups can be added, no evidence of breaking of the aromatic skeleton of the PAH molecules was observed. This is consistent with the known stability of these aromatic systems. It was noted that the molecules that were formed, some of which are important biologically, were similar to those that have been detected in meteorites such as the Merchison meteorite.

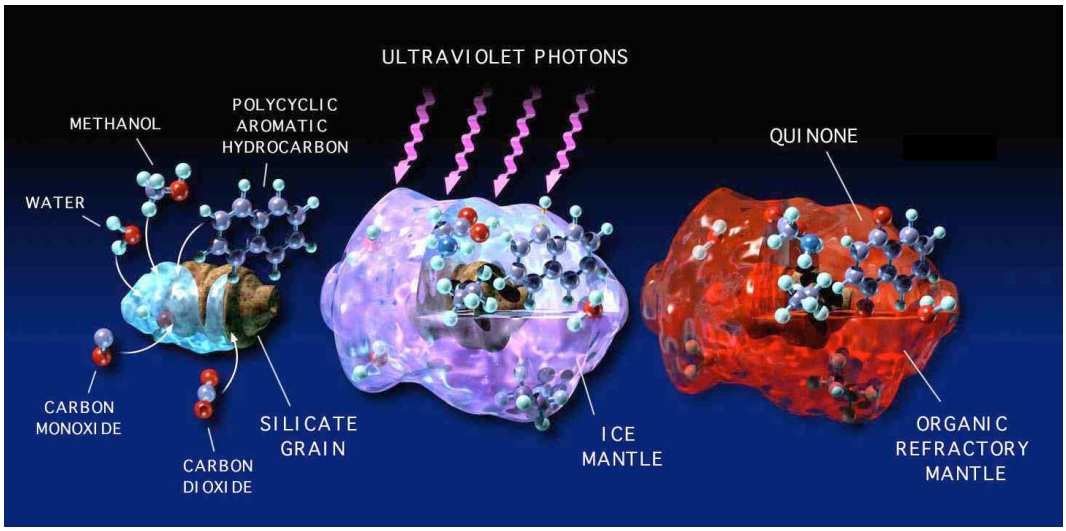

Figure 1.9 UV irradiation of ices involving both simple and more complex molecules including PAHs has been shown to result in a rich chemistry. From [100]**.**

However, it should be noted that this experiment was performed using a relatively small wavelength range and other processes occurring at other energies such as photodesorption cannot be ruled out. The presence of other species within the ice may also impact on the possible reactions. Two studies have indicated the possible formation of amino acids in UV irradiated interstellar ice mimics [101,102]. These indicated that the molecules formed are extremely sensitive to the initial ice composition. However, the importance of interstellar formation of biologically important molecules has been questioned. Ehrenfreund *et al.* [103] pointed out that the UV field within clouds is likely to be insufficient to result in the chemistry observed when using much higher experimental photon fluxes, and that if they were to form they tend to be rapidly degraded by UV photons. It was suggested that the organic species typically found within meteorites might more reasonably have been formed during the formation of the solar system. Indeed, the irradiation of molecules as complex as amino acids has been explored, with results indicating that such molecules are extremely susceptible to destruction by UV photons [104].

The value of performing bulk ice experiments such as these, with assumed ice mixtures has been questioned [105]. It was indicated that it would be more useful to adopt a more systematic and fundamental approach. Such experiments would consider simple systems such as pure ices, and binary mixtures and layered

systems. Quantitative data such as reaction rates and an understanding of reaction mechanisms would enable astrophysically relevant routes to be determined. These experiments have only considered reaction products formed within the ice, and have made no attempt to study any products, or indeed unprocessed molecules, that desorb *during* the irradiation. For a full understanding, different loss channels such as reaction, and desorption need to be studied independently. Furthermore, the majority of these experiments used thick ices deposited in high vacuum chambers pumped with un-trapped diffusion pumps. The associated high background H_2O concentration, which will affect the ice composition, and the ever present risk of contamination by pump oils, make experiments performed within clean, ultrahigh vacuum systems highly desirable. It is also worth noting that whilst many of these experiments suggest that UV irradiation is a viable route to forming complex organics, the UV field deep within molecular clouds is extremely weak. Here the UV field is dominated by photons emitted during radiative association reactions, rather than the ISRF which is strongly attenuated. In such regions, chemistry is more likely to be initiated by the passage of energetic cosmic ray particles as well as low energy secondary electrons produced as a result of cosmic ray ionization within clouds. Experiments considering the ion irradiation of interstellar ice mimics will now be considered.

1.5.5 Ion irradiation of ices

Cosmic ray irradiation of interstellar ices can be studied in the laboratory by bombarding ice mimics with energetic protons and other charged species. Palumbo [106] performed experiments where ice mixtures consisting of H_2O, CH_3OH, CH_4, CO_2, CO, O_2 and N_2 were bombarded with 3 keV He^+, 1.5 keV H^+ and 15 keV O^+ ions. The formation of CO and CO_2 was observed in all mixtures (the species under investigation was not present in the initial ice mixtures), independent of the ion used. The product yields depended only on the energy released into the sample. This demonstrates the ability of energetic ions to break chemical bonds, with products forming from the recombination of the resulting fragments. 3 keV He^+ ion irradiation of C_6H_6 [106] has been shown to initiate a complex chemistry in which C_2H_2 was formed, along with an organic residue, although no detailed analysis of this was made at the time. Similar results were

obtained by irradiating CH_4, CH_3OH and C_6H_6 with 200 eV H^+ and Ar^+ ions, and 400 keV Ar^{2+} ions [107]. In a more detailed study, the 3 keV He^+ ion irradiation of pure CH_3OH ice [108] resulted in the formation of CO, CO_2, H_2CO, $(CH_3)_2CO$, H_2O and CH_4. As well as chemical changes, physical processing was also apparent as evidenced by variations, other than a simple decrease in integrated absorbance, in the CH_3OH IR absorption bands following irradiation. This indicated that integrated absorbances of unirradiated ices may not be appropriate for the determination of column densities in astrophysical environments. 0.8 MeV H^+ irradiation of solid C_6H_6, C_6H_6 isolated in an Ar matrix and C_6H_6 within a H_2O film has also been studied [62]. The observed products were dehydrogenated benzene, methylacetylene and acetylene. Comparison with experiments performed with UV photons showed a significantly higher C_6H_6 destruction cross-section for the ion irradiation experiments. Some evidence of CO and CO_2 formation when H_2O presence indicated the oxidation of C_6H_6 fragments, although these species were also formed in pure ices where their presence was attributed to contaminants within the vacuum chamber. It was concluded that C_6H_6 would be destroyed on a relatively short timescale, and that subsequent chemistry involving intact C_6H_6 molecules can only occur in dense regions of the ISM where the UV field is strongly attenuated.

Further evidence for physical changes induced in interstellar ices by the passage of ions has been provided by studies of the ion irradiation of pure H_2O ice [109,110]. These experiments have demonstrated that irradiation with H^+ or Ar^+ of p-ASW can cause compaction and loss of porosity. This was implied by both a decrease in the ability of the ices to trap CO, used as a probe of porosity, and by a decrease in the dangling OH stretch vibration at around 3700 cm^{-1} associated with H_2O molecules on internal pore surfaces that are not fully coordinated. It was suggested that the lack of detection of this dangling bond feature might result from this compaction, bringing into question the porosity of interstellar ices. However, experiments on ice mixtures containing CO, CO_2 and CH_4 demonstrated a much slower rate of compaction, and it was suggested that full compaction may not occur even during the lifetime of an interstellar cloud. A lack of porosity is a possible explanation for the 2152 cm^{-1} CO band associated with

CO adsorbed on dangling OH sites. However, the lack of this feature has also been interpreted as being due to the adsorption of other species on the dangling bonds, effectively blocking the adsorption of CO [111].

1.5.6 Electron irradiation of ices

Electron stimulated desorption experiments using single crystal metal substrates have been conducted for a considerable period of time. The focus of this discussion will be on experiments conducted with the aim of stimulating physical and/or chemical processing within ice films of astrophysical relevance. The low energy electron irradiation of H_2O ice has been shown to result in the desorption of a wide range of species. The desorption of H^- and D^- from adsorbed H_2O and D_2O films has been observed [112] and shown to result from dissociative electron attachment (DEA). The threshold for anion desorption was 5.5 eV, with a maximum anion yield for an electron energy of 7.4 eV which indicated the formation of the $^2B_1$ and $^2A_1$ anion states. The parent triplet states are formed by the excitation to the $4a_1$ orbital of an electron from the non-bonding $1b_1$ orbital (HOMO) and the H-O bonding $3a_1$ (HOMO-1) orbital respectively. The relevant molecular orbitals are shown schematically in **Figure 1.10**. These representations were obtained from *ab initio* calculations using the 6-31G(2p,2d) basis set performed using the 2008 version of the GAMESS-US software suite [113]. Molecular orbitals were viewed using the GABEDIT software package [114]. Subsequent studies have indicated the desorption of a wide range of species including H and O(^{3}P, ^{1}D)[115] and ionic species. The formation of H_2[116] and O_2[117] have also been observed, where trapping within porous amorphous ice has been shown to significantly enhance the yield of both species [118]. Protonated water clusters, $H^+(H_2O)_n$ have also been detected [119,120]. In general, product yields increase with energy as a wider range of excited states become accessible. H_2O desorption has been shown to result from both direct electron stimulated desorption of neutral molecules and recombination of electron stimulated reaction products [121].

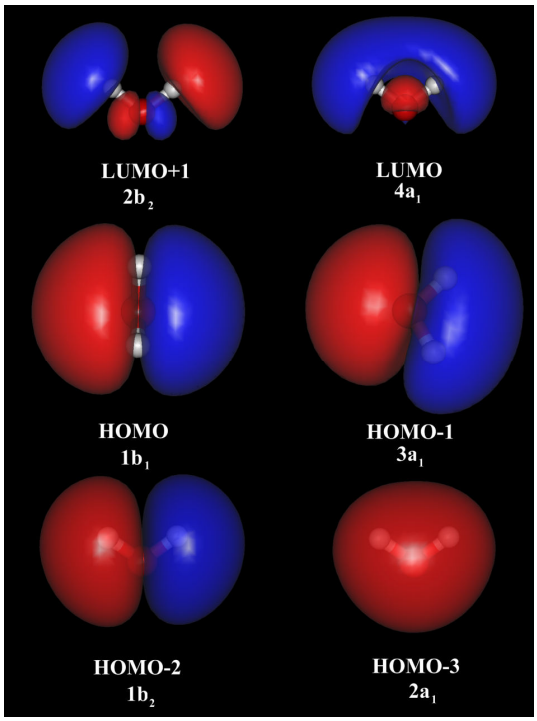

Figure 1.10: Some of the molecular orbitals of H_2O.

Finally, H_2O_2, which is thought to be an important intermediate in O_2 formation, and HO_2 have also been observed [122]. Where trapping occurs, the products of the low energy electron irradiation of H_2O ice are likely to be important in the processing of other species that are mixed within the H_2O matrix.

Examples of other reactions include the low energy electron irradiation of CO and H_2O ice in a layered $H_2O/CO/H_2O$ film, which has been studied for electron energies up to 50 eV [123]. The reaction products CO_2, CHO, H_2CO and CH_3OH were detected using post-irradiation infrared spectroscopic measurements. A mechanism involving first the dissociation of H_2O leading to reactive OH, H and O species followed by subsequent reaction was invoked. At 25 K only CO_2 and CHO were formed, representing the simple oxidation and reduction of CO. Heating the ice up to 60 K during irradiation resulted in the formation of H_2CO and CH_3OH. This was attributed to increased thermally induced migration of reactants. The formation of CO_2 was also enhanced at higher temperature.

CH_3OH formation has also been observed during the irradiation of H_2O/CH_4 ice with 100 eV electrons at low temperature [124]. The reaction products CH_3OH, H_2CO, C_2H_6 and C_2H_2 were observed using *in situ* IR studies. The product yield was observed to increase with increasing H_2O/CH_4 film thickness, levelling off above 20 monolayers, in agreement with the expected electron penetration depth. CO_2 formation was observed, although this was also the case following the irradiation of pure H_2O ice, suggesting that the electron induced oxidation of hydrocarbon contaminants may be in part responsible. The same products were also observed in post irradiation TPD studies. There was also some evidence for CH_4 and H_2O desorption during irradiation. The CH_3OH yield was observed to increase monotonically with electron energy in the range 10-300 eV. The reaction was largely independent of temperature up to 30 K. Recombination of CH_3 and OH and the insertion reaction between CH_2 and H_2O were found to be equally important.

Similar experimental studies have confirmed the electron induced formation of other species. Bennett *et al*. [125] observed the formation of CH_3CHO, c-C_2H_4O, CH_2CHOH resulting from the 5 keV electron irradiation of a CO_2/C_2H_4 (2:1) ice mixture at 10 K . Irradiation of CH_4 at these higher energies has been shown to result in the formation of C_2H_6, C_2H_5 and C_2H_4 with subsequent irradiation leading to C_2H_3 and C_2H_2 [126]. Work by the same group has also demonstrated the formation of O_3 [127] along with H_2, O_2 and H_2O_2 from the irradiation of H_2O ice with 5 keV electrons. Similar experiments have revealed the formation of CH_3COOH from CH_4/CO_2 [128] and $HCOCH_2OH$ and $HCOOCH_3$ from CH_3OH/CO [129]. These higher energy experiments are useful in revealing a wide range of possible chemical reaction mechanisms. However, these higher energy electrons are likely to result in a cascade of low energy electrons as a result of ionization of H_2O molecules as will be discussed in **Chapter 5**. Therefore, experiments probing lower electron energies are crucial to obtain a full understanding of the possible mechanisms for electron stimulated chemical and physical processing. It is also worth noting that the presence of the H_2O ice, which frequently dominates grain mantles in the dense ISM, is likely to have a

significant impact on the reaction mechanisms through the necessary formation of reactive species such as OH.

To conclude this section, it is worth considering an overview of the general mechanisms by which low energy electrons can initiate reactions in ices. At high energies the dominant channel is ionization of adsorbed species. This leads to the desorption of ions, and the possibility of reaction between ionic species. Electronic excitations are also important in this regime, becoming dominant for electron energies of a few tens of eV. In general, there is a gradual increase in the cross-section for electron induced processes for increasing energy above around 20 eV, simply as a result of increased energy input to the system. Resonance features related to the electronic excitations may also be superimposed on the monotonically increasing background. Below 20 eV there is frequently a significant increase in cross-sections as a result of electron attachment processes. The nature of these excitations have been discussed in detail by Bass and Sanche [130], and have already been discussed briefly in relation to the anion yields obtained during low energy electron irradiation of H_2O ice. The low energy electron attachment to a molecule, often referred to as a resonance, leads to the formation of a transient negative ion. A *single particle resonance* results when the electron occupies a previously unfilled molecular orbital of the molecule, whilst a *core-excited resonance* is when electronic excitation occurs simultaneously with electron attachment. This leads to the occupation of two, previously unoccupied, molecular orbitals and is the mechanism by which the anion formation in H_2O described previously occurs. Once the transient negative ion has formed, it may dissociate with the process then being referred to as dissociative electron attachment (DEA). DEA requires the anion state to be dissociative, the electron to be localized for at least the dissociation time scale and one of the resulting fragments to have a positive electron affinity. The cross-section for DEA is proportional to the electron capture-cross section and the probability of the anion surviving without autodetachment of the electron occurring. DEA can result in the formation of both ionic and neutral species that are reactive and therefore provide an efficient route to complex chemical reactions for very low energy electrons. This means that even the very lowest energy electrons resulting from ion

irradiation of interstellar ices have the potential to initiate significant chemical change within the ices.

1.6 Outline of this thesis

This thesis considers the thermal and non-thermal processing of interstellar ice mimics, with a particular emphasis on C_6H_6, both adsorbed alone and on top of a pre-adsorbed H_2O ice film. C_6H_6 has been used as an experimentally convenient model system for more complex PAHs, which by virtue of their lower vapour pressure are more difficult to handle under UHV conditions. **Chapter 2** discusses the experimental systems used in the experiments described in this thesis along with discussions of the techniques employed.

Chapter 3 considers the thermal desorption of C_6H_6 beginning with the desorption of C_6H_6 from a flat stainless steel substrate. The results of this experiment were used as a reference for subsequent TPD experiments. The development of an interstellar grain mimic based on amorphous SiO_2 is then discussed with details of characterization by both atomic force microscopy (AFM) and IR spectroscopy. Results of the thermal desorption of C_6H_6 from the amorphous SiO_2 are then presented and compared with those obtained using the stainless steel reference substrate. A model based on a distribution of binding sites is then developed to describe the observed desorption behaviour. RAIR spectra are also used to gain further insight into the adsorption of C_6H_6 and to provide a set of reference spectra for subsequent non-thermal processing experiments. The thermal desorption of C_6H_6 from c-ASW is also discussed in this chapter. The chapter concludes with a discussion of the astrophysical implications of the different thermal desorption behaviour observed from the two substrates.

Chapter 4 considers the non-thermal desorption of C_6H_6 and H_2O from layered systems of the two species as a result of photon irradiation using photons that are on resonance with an electronic transition in the C_6H_6 molecule. The dynamics of the desorption process is explored using time-of-flight (ToF) mass spectrometry to obtain the translational temperatures of the desorbing molecules. Possible mechanisms for the desorption process are then discussed in detail. The discussion

then turns to the non-thermal desorption kinetics in which the desorption cross-sections for both C_6H_6 and H_2O are obtained.

Chapter 5 continues the discussion of non-thermal processing by considering the irradiation of C_6H_6 adsorbed on both SiO_2 and c-ASW with low energy electrons in the range 100-350 eV. The lack of any observable desorption from the SiO_2 is first discussed along with a determination of the cross-section for C_6H_6 loss. Possible destruction routes C_6H_6 are considered. The remainder of the chapter considers the electron irradiation of C_6H_6 adsorbed on a thick c-ASW film. Significant desorption is observed and the electron stimulated desorption (ESD) traces are used to obtain desorption cross-sections that can be attributed to two distinct desorption mechanisms, both of which depend on the presence of H_2O molecules. RAIR spectra are used to obtain the cross-section for total C_6H_6 loss which confirms that the observed ESD results from a limited population of C_6H_6 molecules that are in close proximity to the H_2O film. This chapter concludes with a discussion of the astrophysical implications of these observations.

An overview of all of the results along with a discussion of the overall astrophysical implications is presented in **Chapter 6**. This chapter concludes with possible future work.

1.7 References

[1] T. W. Hartquist and D. A. Williams, *The Chemically Controlled Cosmos*, 1st ed., Cambridge University Press, Cambridge, 1995.

[2] A. G. G. M. Tielens, *The Physics and Chemistry of the Interstellar Medium*, 1st ed., Cambridge University Press, Cambridge, 2001.

[3] A. M. Shaw, *Astrochemistry: From Astronomy to Astrobiology*, 1st ed., Wiley, Chichester, 2005.

[4] H. I. Ewen and E. M. Purcell, *Nature*, 1951, **168**, 356.

[5] C. A. Muller and J. H. Oort, *Nature*, 1951, **168**, 357.

[6] H. J. Fraser, M. R. S. McCoustra, and D. A. Williams, *Astron. Geophys.*, 2002, **43**, 10.

[7] Image retrieved from "Hubblesite", http://hubblesite.org/newscenter/archive/releases/2006/01/image/a on 04 May 2009

[8] Image retrieved from "Hubblesite", http://hubblesite.org/gallery/album/entire/pr1995024e/ on 27 July 2009

[9] J. Hartmann, *Astrophys. J.*, 1904, **19**, 268.

[10] P. Swings and L. Rosenfeld, *Astrophys. J.*, 1937, **86**, 483.

[11] A. McKellar, *Pub. Astron. Soc. Pacific*, 1940, **52**, 187.

[12] A. E. Douglas and G. Herzberg, *Astrophys. J.*, 1941, **94**, 381.

[13] R. W. Wilson, K. B. Jefferts, and A. A. Penzias, *Astrophys. J.*, 1970, **161**, L43.

[14] T. P. Snow, in *Astrochemistry: Recent Successes and Current Challenges. Proceedings of the 231st symposium of the International Astronomical Union*, edited by D. C. Lis, G. A. Blake, and E. Herbst (Cambridge University Press, Cambridge, 2005), Vol. 231, pp. 175.

[15] G. R. Carruthers, *Astrophys. J.*, 1970, **161**, L81.

[16] L. Spitzer, J. F. Drake, E. B. Jenkins, D. C. Morton, J. B. Rogerson, and D. G. York, *Astrophys. J.*, 1973, **181**, L116.

[17] P. Ehrenfreund and S. B. Charnley, *Ann. Rev. Astron. Astrophys.*, 2000, **38**, 427.

[18] E. Dwek, R. G. Arendt, D. J. Fixsen, T. J. Sodroski, N. Odegard, J. L. Weiland, W. T. Reach, M. G. Hauser, T. Kelsall, S. H. Moseley, R. F. Silverberg, R. A. Shafer, J. Ballester, D. Bazell, and R. Isaacman, *Astrophys. J.*, 1997, **475**, 565.

[19] J. M. Greenberg and A. Li, *Adv. Space Res.*, 1999, **24**, 497.

[20] B. J. McCall, K. H. Hinkle, T. R. Geballe, and T. Oka, *Faraday Discuss.*, 1998, **109**, 267.

[21] R. Terzieva and E. Herbst, *Astrophys. J.*, 1998, **501**, 207.

[22] T. J. Millar, P. R. A. Farquhar, and K. Willacy, *Astron. Astrophys. Suppl. Ser.*, 1997, **121**, 139.

[23] Y. H. Le Teuff, T. J. Millar, and A. J. Markwick, *Astron. Astrophys. Suppl. Ser.*, 2000, **146**, 157.

[24] J. Woodall, M. Agúndez, A. J. Markwick-Kemper, and T. J. Millar, *Astron. Astrophys.*, 2007, **466**, 1197.

[25] J. M. Greenberg, *Surf. Sci.*, 2002, **500**, 793.

[26] D. A. Williams and E. Herbst, *Surf. Sci.*, 2002, **500**, 823.

[27] R. J. Trumpler, *Publ. Astron. Soc. Pacific*, 1930, **42**, 214.

[28] J. S. Mathis, *Ann. Rev. Astron. Astrophys.*, 1990, **28**, 37.

[29] J. M. Greenberg, *Sci. Am.*, 2000, **283**, 46.

[30] A. Li and J. M. Greenberg, *Astron. Astrophys.*, 1997, **323**, 566.

[31] B. T. Draine, *Ann. Rev. Astron. Astrophys.*, 2003, **41**, 241.

[32] T. P. Snow and A. N. Witt, *Astrophys. J.*, 1996, **468**, L65.

[33] D. C. B. Whittet, W. A. Schutte, A. G. G. M. Tielens, A. C. A. Boogert, T. de Graauw, P. Ehrenfreund, P. A. Gerakines, F. P. Helmich, T. Prusti, and E. F. van Dishoeck, *Astron. Astrophys.*, 1996, **315**, L357.

[34] J. F. McCarthy, W. J. Forrest, D. A. Briotta, Jr., and J. R. Houck, *Astrophys. J.*, 1980, **242**, 965.

[35] A. Scott and W. W. Duley, *Astrophys. J.*, 1996, **105**, 401.

[36] M. P. Li, G. Zhao, and A. Li, *Mon. Not. Roy. Astron. Soc.*, 2007, **382**, L26.

[37] F. C. Gillett and W. J. Forrest, *Astrophys. J.*, 1973, **179**, 483.

[38] P. A. Thiel and T. E. Madey, *Surf. Sci. Rep.*, 1987, **7**, 211.

[39] M. A. Henderson, *Surf. Sci. Rep.*, 2002, **46**, 1.

[40] E. F. van Dishoeck, *Ann. Rev. Astron. Astrophys.*, 2004, **42**, 119.

[41] E. L. Gibb, D. C. B. Whittet, W. A. Schutte, A. C. A. Boogert, J. E. Chiar, P. Ehrenfreund, P. A. Gerakines, J. V. Keane, A. G. G. M. Tielens, E. F. van Dishoeck, and O. Kerkhof, *Astrophys. J.*, 2000, **536**, 347.

[42] E. L. Gibb, D. C. B. Whittet, A. C. A. Boogert, and A. G. G. M. Tielens, *Astrophys. J. Sup.*, 2004, **151**, 35.

[43] A. G. G. M. Tielens, A. T. Tokunaga, T. R. Geballe, and F. Baas, *Astrophys. J.*, 1991, **381**, 181.

[44] M. Elitzur and T. de Jong, *Astron. Astrophys.*, 1978, **67**, 323.

[45] E. A. Bergin, G. J. Melnick, J. R. Stauffer, M. L. N. Ashby, G. Chin, N. R. Erickson, P. F. Goldsmith, M. Harwit, J. E. Howe, S. C. Kleiner, D. G. Koch, D. A. Neufeld, B. M. Patten, R. Plume, R. Schieder, R. L. Snell, V. Tolls, Z. Wang, G. Winnewisser, and Y. F. Zhang, *Astrophys. J.*, 2000, **539**, L129.

[46] H. C. van de Hulst., *Rech. Astr. Obs. Utrecht.*, 1949, **vol. 11**, part 2.

[47] R. J. Gould and E. E. Salpeter, *Astrophys. J.*, 1963, **138**, 393.

[48] S. Viti, M. P. Collings, J. W. Dever, M. R. S. McCoustra, and D. A. Williams, *Mon. Not. Roy. Astron. Soc.*, 2004, **354**, 1141.

[49] J. S. Mathis, P. G. Mezger, and N. Panagia, *Astron. Astrophys.*, 1983, **128**, 212.

[50] K. Willacy and W. D. Langer, *Astrophys. J.*, 2000, **544**, 903.

[51] C. Dominik, C. Ceccarelli, D. Hollenbach, and M. Kaufman, *Astrophys. J.*, 2005, **635**, L85.

[52] D. Hollenbach, M. J. Kaufman, E. A. Bergin, and G. J. Melnick, *Astrophys. J.*, 2009, **690**, 1497.

[53] L. J. Allamandola, A. G. G. M. Tielens, and J. R. Barker, *Astrophys. J. Sup.*, 1989, **71**, 733.

[54] F. C. Gillett, W. J. Forrest, and K. M. Merrill, *Astrophys. J.*, 1973, **183**, 87.

[55] E. Peeters, S. Hony, C. Van Kerckhoven, A. G. G. M. Tielens, L. J. Allamandola, D. M. Hudgins, and C. W. Bauschlicher, *Astron. Astrophys.*, 2002, **390**, 1089.

[56] A. Leger and J. L. Puget, *Astron. Astrophys.*, 1984, **137**, L5.

[57] G. H. Herbig, *Ann. Rev. Astron. Astrophys.*, 1995, **33**, 19.

[58] P. Ehrenfreund, J. Cami, E. Dartois, and B. H. Foing, *Astron. Astrophys.*, 1997, **318**, L28.

[59] J. D. Bregman and P. Temi, *Astrophys. J.*, 2001, **554**, 126.

[60] M. P. Bernstein, S. A. Sandford, and L. J. Allamandola, *Astrophys. J. Sup.*, 2005, **161**, 53.

[61] J. Cernicharo, A. M. Heras, A. Tielens, J. R. Pardo, F. Herpin, M. Guelin, and L. Waters, *Astrophys. J.*, 2001, **546**, L123.

[62] R. Ruiterkamp, Z. Peeters, M. H. Moore, R. L. Hudson, and P. Ehrenfreund, *Astron. Astrophys.*, 2005, **440**, 391.

[63] I. Cherchneff, J. R. Barker, and A. G. G. M. Tielens, *Astrophys. J.*, 1992, **401**, 269.

[64] P. M. Woods, T. J. Millar, A. A. Zijlstra, and E. Herbst, *Astrophys. J.*, 2002, **574**, L167.

[65] P. M. Woods and K. Willacy, *Astrophys. J.*, 2007, **655**, L49.

[66] M. Frenklach and E. D. Feigelson, *Astrophys. J.*, 1989, **341**, 372.

[67] V. Pirronello, C. Liu, L. Shen, and G. Vidali, *Astrophys. J.*, 1997, **475**, L69.

[68] V. Pirronello, O. Biham, C. Liu, L. Shen, and G. Vidali, *Astrophys. J.*, 1997, **483**, L131.

[69] G. Vidali, J. E. Roser, G. Manicó, and V. Pirronello, in *Astrochemistry: Recent Successes and Current Challenges. Proceedings of the 231st symposium of the International Astronomical Union*, edited by D. C. Lis, G. A. Blake, and E. Herbst (Cambridge University Press, Cambridge, 2005), Vol. 231, pp. 355.

[70] L. Hornekær, A. Baurichter, V. V. Petrunin, D. Field, and A. C. Luntz, *Science*, 2003, **302**, 1943.

[71] F. Islam, E. R. Latimer, and S. D. Price, *J. Chem. Phys.*, 2007, **127**, 064701.

[72] E. R. Latimer, F. Islam, and S. D. Price, *Chem. Phys. Lett.*, 2008, **455**, 174.

[73] S. Baouche, G. Gamborg, V. V. Petrunin, A. C. Luntz, A. Baurichter, and L. Hornekaer, *J. Chem. Phys.*, 2006, **125**, 084712.

[74] L. Hornekaer, Z. Sljivancanin, W. Xu, R. Otero, E. Rauls, I. Stensgaard, E. Laegsgaard, B. Hammer, and F. Besenbacher, *Phys. Rev. Lett.*, 2006, **96**, 156104.

[75] E. Rauls and L. Hornekaer, *Astrophys. J.*, 2008, **679**, 531.

[76] W. Hagen, A. G. G. M. Tielens, and J. M. Greenberg, *Chem. Phys.*, 1981, **56**, 367.

[77] P. Jenniskens and D. F. Blake, *Science*, 1994, **265**, 753.

[78] K. P. Stevenson, G. A. Kimmel, Z. Dohnálek, R. S. Smith, and B. D. Kay, *Science*, 1999, **283**, 1505.

[79] M. P. Collings, J. W. Dever, H. J. Fraser, and M. R. S. McCoustra, *Astrophys. Space Sci.*, 2003, **285**, 633.

[80] R. S. Smith, C. Huang, E. K. L. Wong, and B. D. Kay, *Phys. Rev. Lett.*, 1997, **79**, 909.

[81] R. S. Smith, T. Zubkov, and B. D. Kay, *J. Chem. Phys.*, 2006, **124**, 114710.

[82] H. J. Fraser, M. P. Collings, M. R. S. McCoustra, and D. A. Williams, *Mon. Not. Roy. Astron. Soc.*, 2001, **327**, 1165.

[83] A. S. Bolina, A. J. Wolff, and W. A. Brown, *J. Phys. Chem. B*, 2005, **109**, 16836.

[84] W. A. Brown and A. S. Bolina, *Mon. Not. Roy. Astron. Soc.*, 2007, **374**, 1006.

[85] M. P. Collings, J. W. Dever, H. J. Fraser, M. R. S. McCoustra, and D. A. Williams, *Astrophys. J.*, 2003, **583**, 1058.

[86] M. P. Collings, M. A. Anderson, R. Chen, J. W. Dever, S. Viti, D. A. Williams, and M. R. S. McCoustra, *Mon. Not. Roy. Astron. Soc.*, 2004, **354**, 1133.

[87] A. J. Wolff, C. Carlstedt, and W. A. Brown, *J. Phys. Chem. C.*, 2007, **111**, 5990.

[88] M. S. Westley, R. A. Baragiola, R. E. Johnson, and G. A. Baratta, *Nature*, 1995, **373**, 405.

[89] M. S. Westley, R. A. Baragiola, R. E. Johnson, and G. A. Baratta, *Planet. Space. Sci.*, 1995, **43**, 1311.

[90] N. Nishi, H. Shinohara, and T. Okuyama, *J. Chem. Phys.*, 1984, **80**, 3898.

[91] J. Bergeld and D. Chakarov, *J. Chem. Phys.*, 2006, **125**, 141103.

[92] K. I. Öberg, H. Linnartz, R. Visser, and E. F. van Dishoeck, *Astrophys. J.*, 2009, **693**, 1209.

[93] S. Andersson, A. Al-Halabi, G.-J. Kroes, and E. F. van Dishoeck, *J. Chem. Phys.*, 2006, **124**, 064715.

[94] A. Yabushita, T. Hama, M. Yokoyama, M. Kawasaki, S. Andersson, R. N. Dixon, M. N. R. Ashfold, and N. Watanabe, *Astrophys. J.*, 2009, L80.

[95] A. Yabushita, T. Hama, D. Iida, N. Kawanaka, M. Kawasaki, N. Watanabe, M. N. R. Ashfold, and H.-P. Loock, *J. Chem. Phys.*, 2008, **129**, 044501.

[96] K. I. Öberg, G. W. Fuchs, Z. Awad, H. J. Fraser, S. Schlemmer, E. F. van Dishoeck, and H. Linnartz, *Astrophys. J.*, 2007, **662**, L23.

[97] K. I. Öberg, E. F. v. Dishoeck, and H. Linnartz, *Astron. Astrophys.*, 2009, **496**, 281.

[98] M. P. Bernstein, S. A. Sandford, L. J. Allamandola, S. Chang, and M. A. Scharberg, *Astrophys. J.*, 1995, **454**, 327.

[99] M. P. Bernstein, S. A. Sandford, L. J. Allamandola, J. S. Gillette, S. J. Clemett, and R. N. Zare, *Science*, 1999, **283**, 1135.

[100] M. P. Bernstein, S. A. Sandford, and L. J. Allamandola, in *Sci.Am.* (July 1999), 26.

[101] G. M. Muñoz Caro, U. J. Meierhenrich, W. A. Schutte, B. Barbier, A. Arcones Segovia, H. Rosenbauer, W. H. P. Thiemann, A. Brack, and J. M. Greenberg, *Nature*, 2002, **416**, 403.

[102] M. P. Bernstein, J. P. Dworkin, S. A. Sandford, G. W. Cooper, and L. J. Allamandola, *Nature*, 2002, **416**, 401.

[103] P. Ehrenfreund and M. A. Sephton, *Faraday Discuss.*, 2006, **133**, 277.

[104] P. Ehrenfreund, M. P. Bernstein, J. P. Dworkin, S. A. Sandford, and L. J. Allamandola, *Astrophys. J.*, 2001, **550**, L95.

[105] E. L. Shock, *Nature*, 2002, **416**, 380.

[106] M. E. Palumbo, *Adv. Space. Res.*, 1997, **20**, 1637.

[107] R. Brunetto, M. A. Barucci, E. Dotto, and G. Strazzulla, *Astrophys. J.*, 2006, **644**, 646.

[108] M. E. Palumbo, A. C. Castorina, and G. Strazzulla, *Astron. Astrophys.*, 1999, **342**, 551.

[109] M. E. Palumbo, *Astron. Astrophys.*, 2006, **453**, 903.

[110] U. Raut, B. D. Teolis, M. J. Loeffler, R. A. Vidal, M. Fama, and R. A. Baragiola, *J. Chem. Phys.*, 2007, **126**, 244511.

[111] H. J. Fraser, M. P. Collings, J. W. Dever, and M. R. S. McCoustra, *Mon. Not. Roy. Astron. Soc.*, 2004, **353**, 59.

[112] P. Rowntree, L. Parenteau, and L. Sanche, *J. Phys. Chem.*, 1991, **94**, 8570.

[113] M. W. Schmidt, K. K. Baldridge, J. A. Boatz, S. T. Elbert, M. S. Gordon, J. H. Jensen, S. Koseki, N. Matsunaga, K. A. Nguyen, S. Su, T. L. Windus, M. Dupuis, and J. J. A. Montgomery, *J. Comp. Chem.*, 1993, **14**, 1347.

[114] A. R. Allouche, Gabedit is a free Graphical User Interface for computational chemistry packages. It is available from http://gabedit.sourceforge.net/.

[115] G. A. Kimmel and T. M. Orlando, *Phys. Rev. Lett.*, 1995, **75**, 2606.

[116] G. A. Kimmel, T. M. Orlando, C. Vezina, and L. Sanche, *J. Chem. Phys.*, 1994, **101**, 3282.

[117] T. M. Orlando and M. T. Sieger, *Surf. Sci.*, 2003, **528**, 1.

[118] G. A. Grieves and T. M. Orlando, *Surf. Sci.*, 2005, **593**, 180.

[119] R. H. Prince and G. R. Floyd, *Chem. Phys. Lett.*, 1976, **43**, 326.

[120] J. Herring-Captain, G. A. Grieves, A. Alexandrov, M. T. Sieger, H. Chen, and T. M. Orlando, *Phys. Rev. B.*, 2005, **72**, 035431.

[121] N. G. Petrik and G. A. Kimmel, *J. Chem. Phys.*, 2005, **123**, 054702.

[122] X. Pan, A. D. Bass, J.-P. Jay-Gerin, and L. Sanche, *Icarus*, 2004, **172**, 521.

[123] S. Yamamoto, A. Beniya, K. Mukai, Y. Yamashita, and J. Yoshinobu, *Chem. Phys. Lett.*, 2004, **388**, 384.

[124] A. Wada, N. Mochizuki, and K. Hiraoka, *Astrophys. J.*, 2006, **644**, 300.

[125] C. J. Bennett, Y. Osamura, M. D. Lebar, and R. I. Kaiser, *Astrophys. J.*, 2005, **634**, 698.

[126] C. J. Bennett, C. S. Jamieson, Y. Osamura, and R. I. Kaiser, *Astrophys. J.*, 2006, **653**, 792.

[127] C. J. Bennett and R. I. Kaiser, *Astrophys. J.*, 2005, **635**, 1362.

[128] C. J. Bennett and R. I. Kaiser, *Astrophys. J.*, 2007, **660**, 1289.

[129] C. J. Bennett and R. I. Kaiser, *Astrophys. J.*, 2007, **661**, 899.

[130] A. D. Bass and L. Sanche, *Low Temp. Phys.*, 2003, **29**, 202.

CHAPTER 2 - Experimental

2.1 Introduction

In this chapter, the experimental techniques used in this work will be described. The use of ultrahigh vacuum (UHV) in surface science will be explained, followed by a discussion of the UHV systems employed in the work presented in this thesis. The background behind the techniques will be presented, along with a discussion of how these were implemented with the apparatus described here.

2.2 Surface science and ultrahigh vacuum

The study of physical and chemical processes occurring at solid surfaces was originally motivated by the need for an understanding of heterogeneous catalysis [1], where two or more phases are present. A large number of processes, such as the Haber-Bosch process through to the conversion of exhaust gases from the internal combustion engine rely on the presence of a catalytic solid surface. Whilst these processes usually employ a catalyst in a finely divided form such as nanoparticles dispersed on an oxide support, to understand the details of the catalytic activity, it was soon realized that a simpler approximation to the catalytic surface was required. This resulted in attention being focused on single crystal metal surfaces; those in which a particular crystal face has been exposed. The development of the semiconductor industry also required a detailed understanding of solid surfaces, and many of the techniques and practices developed in surface science, including the use of ultrahigh vacuum, have been essential to its growth. One of the great difficulties in studying processes occurring at such a surface is to maintain surface cleanness for a sufficiently long period of time for an experiment to be conducted. This can be demonstrated by considering the rate, Z_w, at which molecules, having temperature T and molecular mass m, collide with a surface exposed to a pressure P:

$$Z_w = \frac{P}{\sqrt{2\pi m k_B T}} \text{ m}^{-2}\text{ s}^{-1}. \qquad \textbf{Equation 2.1}$$

It is clear that the surface must be mounted within a vacuum chamber in order to reduce the collision frequency. If it is assumed that every molecule that collides with the surface sticks to it, *i.e.* the sticking probability is unity, then Z_w can be equated to the rate at which molecules are adsorbed onto the surface per unit area. In order to ascertain how long a surface will remain clean, one can consider the time taken for a complete monolayer of adsorbed molecules to form. This value will depend on the number of adsorption sites available on the surface, which is typically of the order of 10^{15} cm^{-2}. High vacuum (HV) is used widely throughout the physical sciences, with pressures of 10^{-7} mbar being typical in many experimental chambers. However, by use of **Equation 2.1** such a pressure yields a monolayer formation time of *ca.* 10 s, insufficient for most experiments. In order to conduct an experiment on a clean surface, a monolayer formation time of the order of a few hours is required. Such a timescale is obtained when the pressure, P, is less that 10^{-9} mbar, which is defined as UHV. Obtaining UHV is not straight forward and requires a combination of pumping technologies and a consideration of the nature of the residual gas in the HV chamber. Use of a simple residual gas analyser (RGA) reveals that the residual gas background in such a HV chamber is dominated by H_2O vapour. This H_2O results from the gradual desorption of H_2O that adsorbs onto internal surfaces within the chamber whilst at atmospheric pressure. The rate of desorption of this H_2O is high enough to yield the observed background, but sufficiently slow that it would require many months of pumping to reduce the partial pressure of H_2O to an acceptable level. In order to obtain UHV, it is necessary to increase the desorption rate of H_2O for a period of time in order to reduce the surface concentration significantly. This is achieved by heating the chamber to an elevated temperature (120-250 °C depending on attached apparatus) for up to 60 hours. Once cooled, the desorption rate of H_2O will be significantly lower than before heating, hence resulting in a reduction in chamber pressure. The process of heating the chamber whilst the vacuum pumps are operating is known as bake-out. **Figure 2.1** shows typical pre- and post-bake RGA traces.

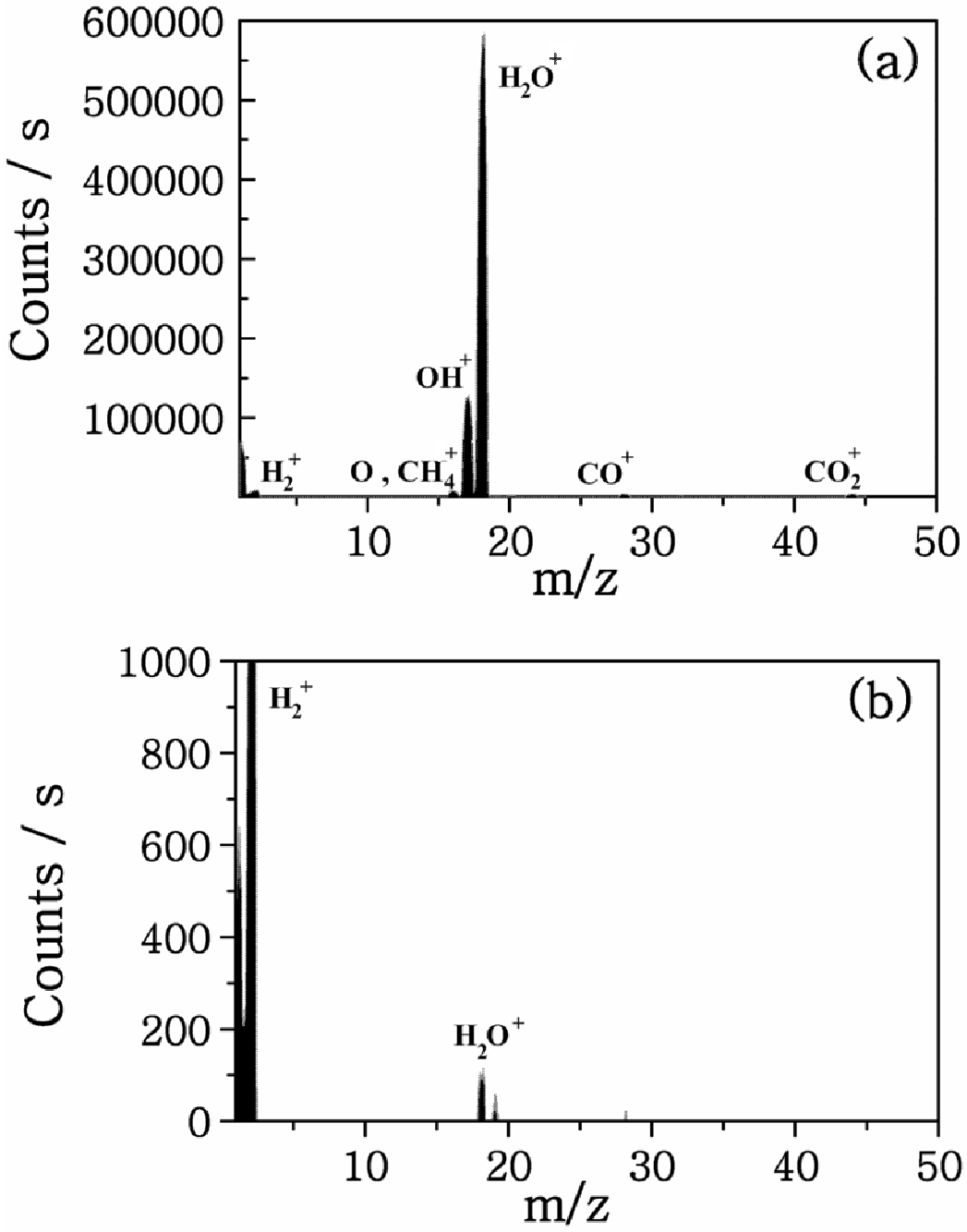

Figure 2.1: Residual gas analyses of a typical UHV chamber (a) before and (b) following bakeout at 120 °C for 48 hours. Note that the m/z=2 signal has been cropped from 2500 counts/s in (b) to improve clarity. The features labelled in (a) are at m/z=2,16,17,18,28 and 44.

Another important consideration is the mean free path of molecules and other particles such as electrons in the UHV chamber. For example, some experiments require the use of low energy electrons or ions which need to reach the surface without significant gas-phase scattering. For example, the mean free path, λ, for a neutral molecule is given by:

$$\lambda = \frac{k_B T}{\sqrt{2} P \sigma} \qquad \textbf{Equation 2.2}$$

where T is the gas temperature, P the gas pressure and σ the collision cross section. Under UHV conditions, and assuming a typical molecular collision cross section of *ca.* 10^{-15} cm^2 this yields a mean free path of the order of tens of km. Thus, UHV conditions allow both surface cleanness over sufficiently long periods of time and also maintain suitably low collision rate conditions necessary for many experiments.

2.3 Experimental Systems Used

2.3.1 UHV chamber 1

This UHV system was originally designed for work utilizing single crystal surfaces, particularly focusing on the interaction between supersonic molecular beams and the surface of interest. Details of the original experimental arrangement for this system can be found elsewhere [2]. Several modifications have been made to this system in order to perform these experiments, and these will be outlined during the subsequent discussion.

Vacuum system and pumping

This system comprised a 40 cm diameter stainless steel chamber (Leisk Engineering) pumped by a liquid nitrogen trapped 9" oil diffusion pump (Edwards High Vacuum E09) charged with polyphenyl ether fluid (Santovac 5) and backed by an oil sealed mechanical rotary vane pump (Edwards High Vacuum E2M40). Additional pumping was provided by a titanium sublimation pump (Leisk Engineering) mounted between the chamber and main diffusion pump.

Figure 2.2: Photograph of UHV chamber 1.

The pressure in the main chamber was measured by an uncalibrated, hot cathode ion gauge (Caburn MDC Ltd.). Backing pressures were measured using pirani gauges (Vacuum Generators) controlled by the same controller (Vacuum Generators IGP3) as the ion gauge.

The second differential pumping stage of the molecular beam system was integral to the main chamber, separated by internal walls, and with a line-of-sight to the substrate *via* an orifice with variable diameter. This chamber was pumped by a liquid nitrogen trapped 6" oil diffusion pump (Edwards High Vacuum E06) charged with polyphenyl ether fluid (Santovac 5) and backed by an oil sealed mechanical rotary vane pump (Edwards High Vacuum E2M18). No pressure gauge was fitted to this chamber; however, without a gas load from the molecular beam system, is was reasonable to assume a base pressure of $< 1\times10^{-9}$ torr. In order to obtain UHV, it was necessary to bake the system at a temperature of 120 °C for 48-60 hours to increase the desorption rate of H_2O adsorbed on internal surfaces. After the system had cooled and any filaments and the substrate had been sufficiently degassed the liquid nitrogen traps were filled. Following this procedure, a base pressure of $<2\times10^{-10}$ torr was routinely obtainable. A schematic of the pumping on this system is shown in **Figure 2.3**.

The molecular beam source was housed in a separate high vacuum (HV) chamber attached to the main UHV system *via* a DN38CF flange to the integral second differential chamber. The source could be isolated from the UHV chamber by means of a gate valve (Edwards High Vacuum) and remained outside the bakeout region. The source consisted of two chambers; the source chamber and the first differential chamber. These were separated by a 5 mm diameter orifice onto which a skimmer could be mounted. For the experiments described here, no skimmer was used as the other orifices present provided sufficient collimation. This orifice could be moved using two linear drives in order to align the beam with the substrate in the main chamber.

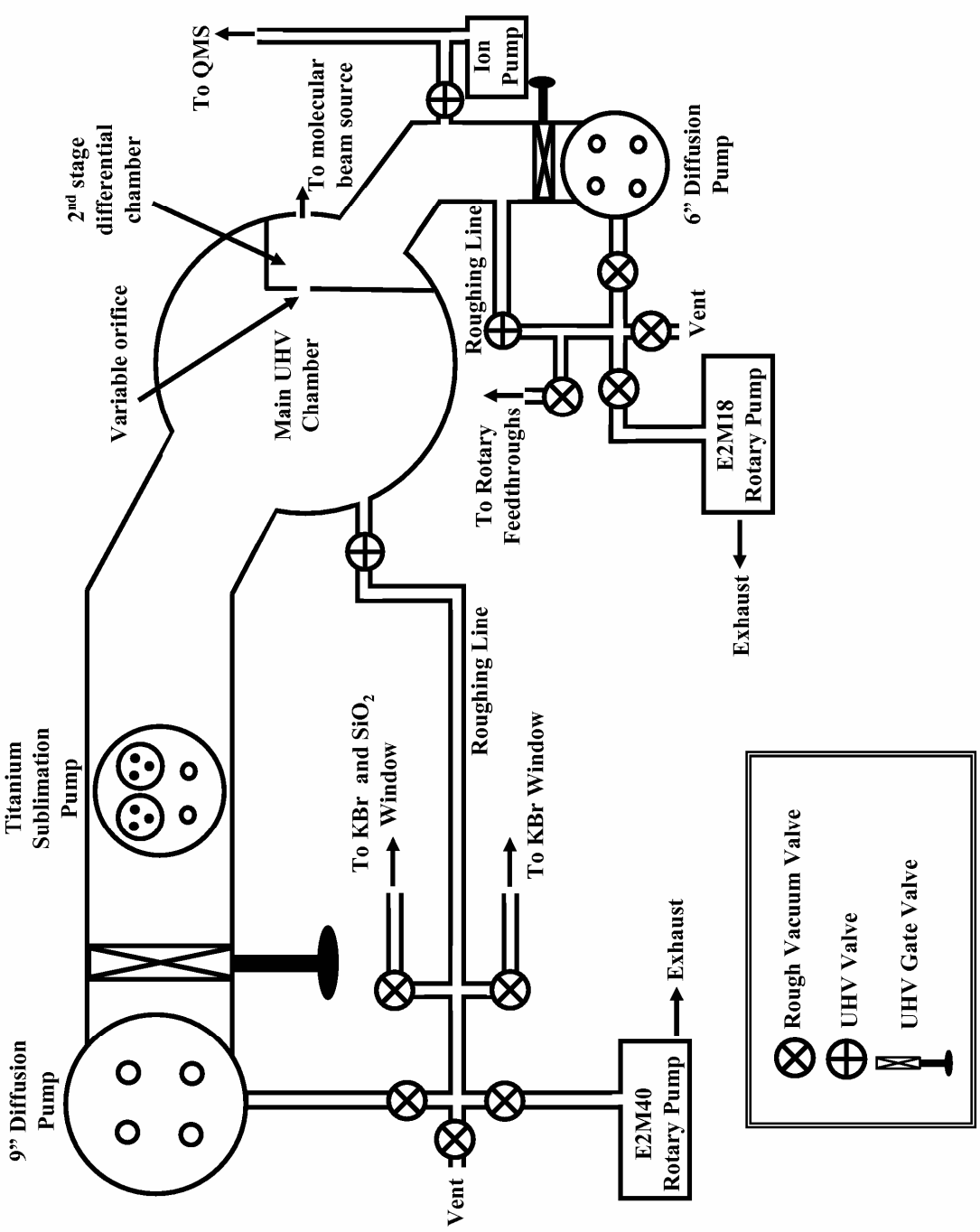

Figure 2.3: Schematic of the pumping arrangement for chamber 1.

Pumping was provided by a 9” oil diffusion pump (Edwards High Vacuum E09) and a 6” oil diffusion pump (Edwards High Vacuum E06) in the source and differential chambers respectively. The diffusion pumps were charged with silicone fluid (Dow Corning DC-704). The 9” diffusion pump was backed by an oil sealed rotary vane pump (Edwards High Vacuum E2M40) which was aided by a mechanical booster (Edwards High Vacuum EH250) to provide a sufficient pumping speed when the source was in operation. The 6” diffusion pump was backed by an Edwards High Vacuum E2M18 rotary vane pump. Chamber pressures were measured with Penning gauges (Edwards High Vacuum CP25-K) and backing pressures with Pirani gauges (Edwards High Vacuum PRL10). Pressure gauges were controlled by two Edwards High Vacuum Pirani Penning 1005 controllers. Base pressures in the low 10^{-7} mbar region were routinely obtained in both chambers, rising to the low 10^{-4} mbar range and low 10^{-6} mbar range in the source and differential chambers respectively during beam operation. During continuous H_2O beam operation with the substrate out of line-of-sight with the beam the pressure in the main chamber rose to around 8×10^{-10} torr. The species of interest entered the source chamber through a 6 mm diameter glass nozzle having a hole approximately 0.5 mm in diameter. The nozzle was attached to a stainless steel tube using compression fittings and a graphite ferrule. The nozzle assembly was mounted on an *x*-*y* translation stage to allow the beam to be aligned with the other orifices in the system. This in turn was mounted through edge-welded flexible bellows such that the end of the nozzle could be positioned near to the orifice to the differential chamber. The system was also equipped with a mechanical chopper to provide a pulsed molecular beam in order to obtain the time-of-flight (ToF) of molecules in the molecular beam. This was not used in these experiments where an effusive beam was produced. A schematic of the pumping arrangement for the molecular beam source is shown in **Figure 2.4**.

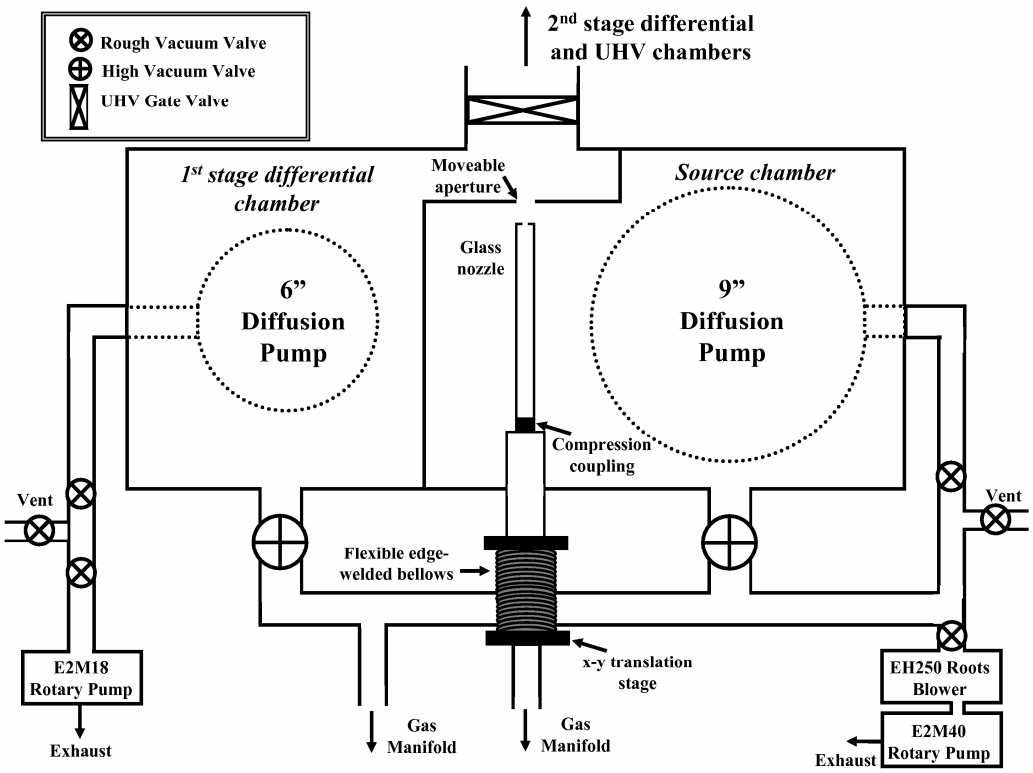

Figure 2.4: Schematic of the pumping arrangement for the molecular beam source.

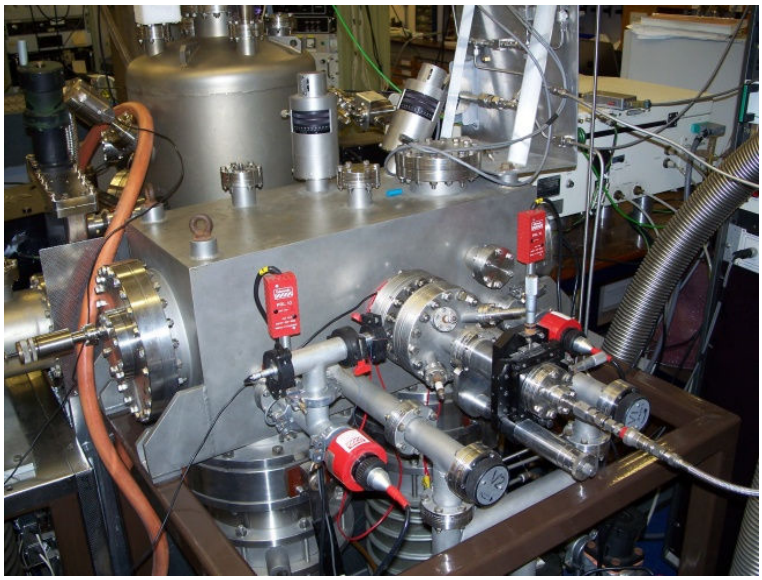

Figure 2.5: Photograph of the molecular beam source.

Instrumentation

Much of the instrumentation on the system was for use with single crystal substrates and was not used in this work and so will be discussed briefly. The system was equipped with an ion sputter gun for cleaning. An electron gun and hemispherical electron energy analyzer (VG Microtech CLAM 100) were provided for Auger electron spectroscopy (AES) to ascertain substrate cleanliness. In order to examine surface order, rear view low energy electron diffraction (LEED) optics (VG Microtech RVL 640) with integral electron gun were fitted to the chamber. In previous experiments a twin microchannel plate (MCP) detector (Photek VPM 218) was used to collect ions produced during resonance enhanced multiphoton ionization (REMPI) experiments. During the experiments described here, both the LEED optics and MCP were removed from the system. A low energy electron gun (Kimball Physics ELG-2) was mounted in place of the MCP for the electron irradiation experiments described here. This was capable of producing 2-2000 eV electrons with an energy spread of 0.5 eV. A cross-beam source quadrupole mass spectrometer (QMS; VG Microtech PC300D) for TPD and electron stimulated desorption experiments was mounted on a table in the base of the chamber. The QMS had been modified from the original design (European Spectrometry Systems) to allow operation in pulse counting mode. This could be rotated about the sample using a gear system mounted through a differentially pumped rotary feedthrough. The QMS was contained within a differentially pumped chamber that was pumped *via* a connection to the 6" diffusion pump and an 8 l s^{-1} diode ion pump (Varian VacIon). A 5 mm tube protruding from the wall of this chamber provided a direct line-of-sight between the sample and the ion source of the QMS. This reduced the detection of molecules desorbing from any surfaces other than the substrate itself, such as the sample mount. The instrumentation was mounted in two distinct levels within the main chamber, with the upper preparation level for cleaning and AES. Two fine leak valves were also situated within the upper level, through which gases could be introduced into the chamber in a controlled manner. The lower experimental level contained the low energy electron gun and two differentially pumped KBr windows through which the IR beam for conducting RAIRS experiments entered and exited the chamber. The ion source of the QMS and line-of-sight tube were

also situated in this level. A second QMS (VG Quadrupoles Q7) was fitted to the chamber directly opposite to the orifice through which the molecular beam entered the chamber. This could be used to assess the purity and stability of the molecular beam, as well as compare relative fluxes between experiments. RAIR spectra were obtained with a Fourier Transform Infrared (FTIR) spectrometer (BioRad FTS-60A). The external IR beam from the spectrometer was first directed into a box clamped onto one of the KBr window ports on the UHV chamber. The beam was directed into the chamber and focused onto the sample at an angle of 6° to the plane of the surface using a combination of a plane mirror and a parabolic mirror. The reflected beam was directed and focussed onto the detection element of a mercury cadmium telluride (MCT) detector using a second plane mirror and an ellipsoidal mirror. These optics were housed in a second box clamped to the exit KBr window port. Both optics housings were purged with dry CO_2 free air to reduce absorption due to atmospheric H_2O and CO_2. The experimental level of the chamber is shown schematically in **Figure 2.6**.

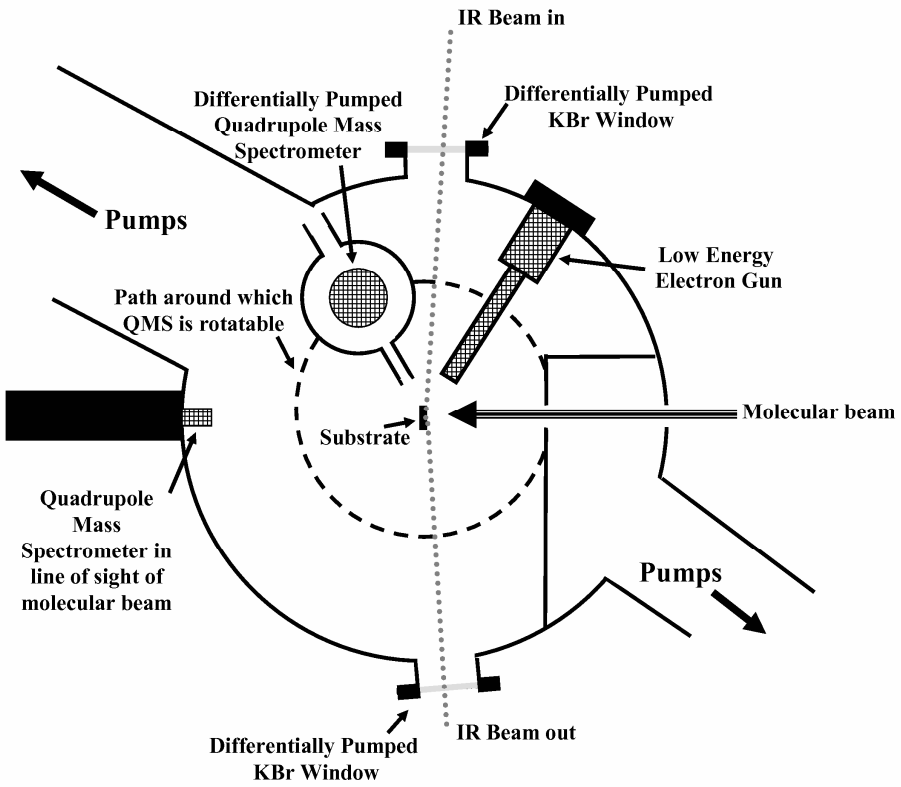

Figure 2.6: Schematic showing the experimental level of UHV Chamber 1.

Sample mounting

The sample mounting arrangement is shown in **Figure 2.7**. The substrate used was a 10 mm diameter, 2 mm thick stainless steel disc with 1 mm holes drilled through at the top and bottom such that it could be suspended on several 0.25 mm diameter tantalum wires. These were spot-welded to 0.075 mm thick nickel foil that had been wrapped around and spot-welded to 2 mm diameter molybdenum heating rods. Each of the rods was attached to an oxygen free high conductivity (OFHC) copper semi-circular block. The two semi-circles were bolted to a circular OFHC copper block with a sapphire insulator inserted between. This, along with a small gap between the two semi-circular pieces meant that it was possible to pass a current through the tantalum wires in order to heat the substrate. The electrical isolation provided by the sapphire insulator also made it possible to float the substrate relative to the chamber. This meant that it was possible to apply a bias to the substrate in order to attract electrons or ions or to reduce their energy, depending on the polarity of the bias. It is important to note that in order to properly float the substrate, it was necessary to remove all external wiring connected to the heating wires and thermocouple, which would otherwise provide a route to ground. The upper OFHC copper block had a tapped hole in the centre, such that it could be screwed onto a threaded stud on the end of a liquid nitrogen dewar. A K-type thermocouple was spot-welded to the edge of the substrate for temperature monitoring. This type of thermocouple consists of chromel (90% Ni, 10% Cr) and alumel (95% Ni, 2% Mn, 2% Al, 1% Si) wires. Both heating and thermocouple wires were wrapped around the dewar and connected to appropriate feedthroughs at the top of the manipulator. It was important to check at all times that there were no shorts between the heating wires, thermocouple wires and chamber. All wires were insulated using glass fibre sleeving that had been thoroughly cleaned in isopropyl alcohol prior to use to remove any residual organic contaminants.

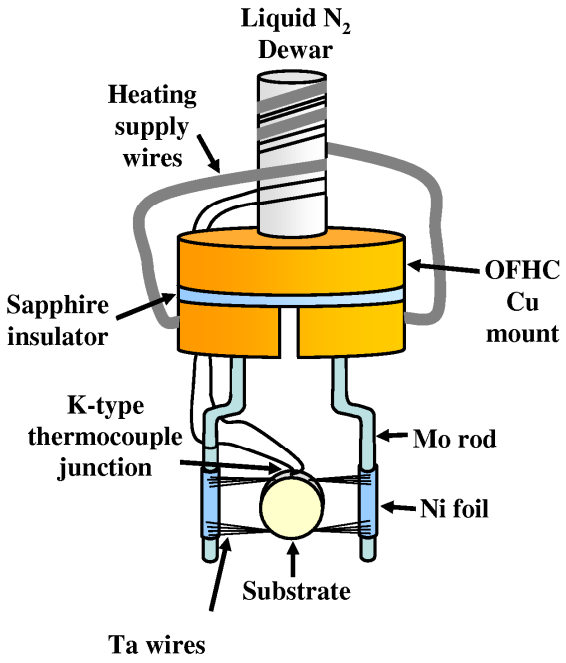

Figure 2.7: The sample mounting arrangement used in UHV chamber 1.

The substrate could be moved by means of a precision *xyz* manipulator (Leisk Engineering) mounted on the top flange of the main chamber. The entire substrate mounting and control assembly was mounted through the manipulator. The position of the sample in the *x,y* plane could be adjusted by means of a platform moved by using a micrometer scale. The assembly could be raised and lowered using both a coarse control hand wheel, and a fine micrometer control, moving the upper platform of the manipulator which was connected to the lower platform *via* flexible edge welded bellows. In order to facilitate rotation of the sample, a precision differentially pumped rotary feedthrough (DPRF; Vacuum Generators DPRF25) was mounted on the top of the manipulator. This was sealed using two PTFE ring seals, with a cavity between that was pumped *via* a suitable connection to one of the rotary pumps. The resulting pressure gradient reduces the leak rate during rotation. The manipulator assembly is shown schematically in **Figure 2.8**.

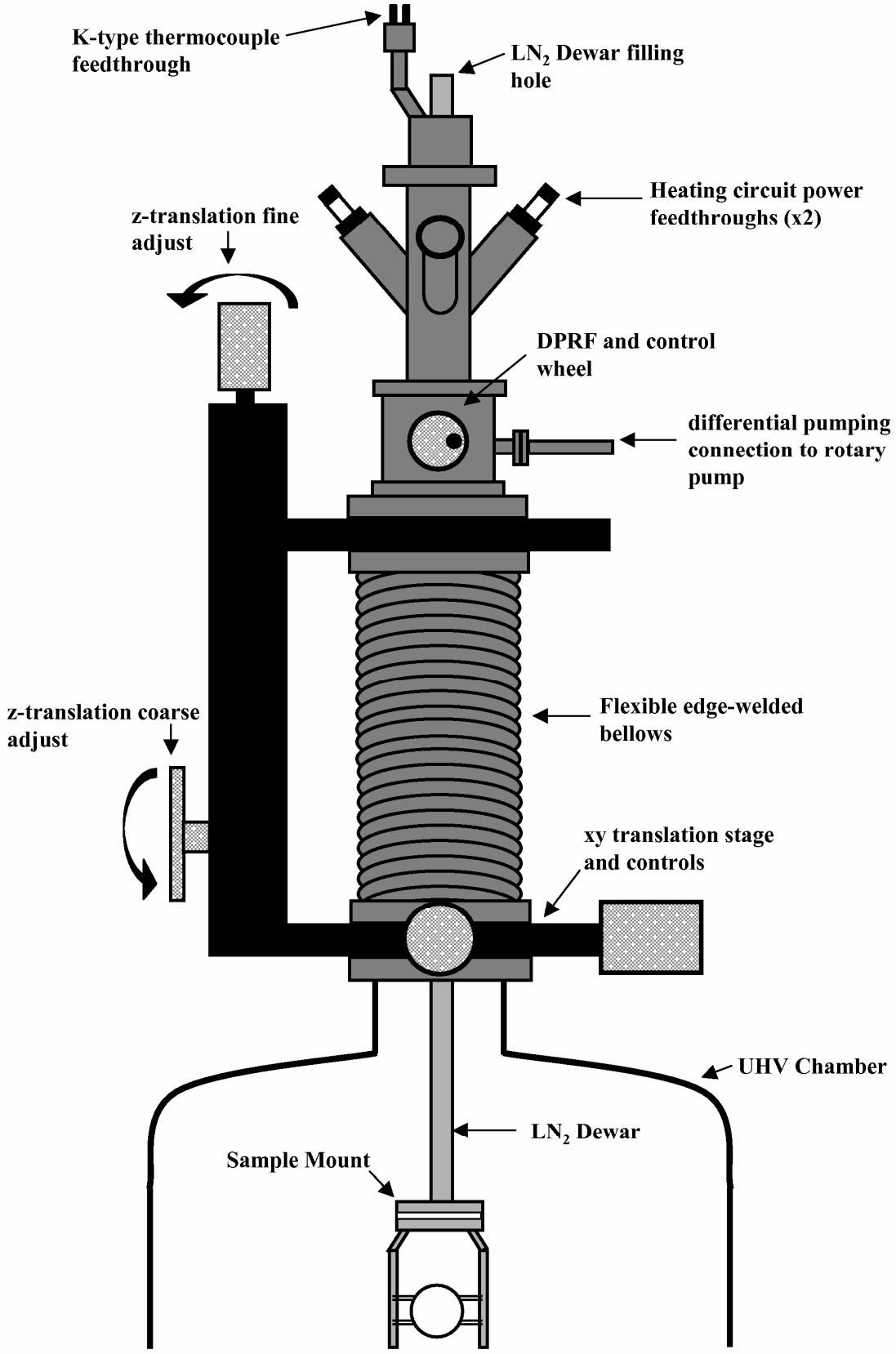

Figure 2.8: Schematic of the manipulator assembly on UHV chamber 1.

Temperature control system

The substrate could be heated by passing a current through the tantalum support wires. As the thin tantalum wires have a significantly higher resistance than the copper wires used in the rest of the heating circuit, they heat up when a current is passed through them. The current was provided by a power supply capable of providing up to 50 A (Farnell Type H60/50). As well as manual temperature control using the current adjustment on this supply, automatic control was provided by a controller (Eurotherm 815S) capable of maintaining set-points down to -150°C. This was interfaced to both the power supply and the K-type thermocouple spot-welded to the edge of the substrate. With this arrangement it was also possible to achieve heating ramps of 0.1 K s^{-1} with good linearity for TPD experiments. When conducting TPD experiments it is necessary to record the thermocouple voltage along with the ion signals for the fragments being monitored with the QMS. The QMS could record this voltage using one of the 0-10 V auxiliary input channels provided. A K-type thermocouple generates an emf of a few millivolts, with 0 V centered at around 0 °C, thus it was necessary to amplify the raw thermocouple voltage and offset it sufficiently that the region of interest was within the 0-10 V limits. Amplification was achieved using a commercially available integrated circuit (Analog Devices AD595) and offset by +2.5 V using a voltage reference integrated circuit (Analog Devices AD680JTZ). The voltage was then calibrated by making a measurement of raw thermocouple voltage at base temperature (*ca.* 115 K) with the substrate cooled with liquid nitrogen. This was corrected for the room temperature junction at the vacuum feedthrough using values from a standard K-type thermocouple calibration chart. The substrate was then heated at a rate of 0.1 K s^{-1} to 273 K and the raw voltage again recorded and corrected. During the heating the voltage channel in the QMS was recorded, along with a series of readings from the Eurotherm controller, which were adjusted to agree with the corrected raw voltage values. The recorded amplified voltage was then plotted against the recorded temperatures and fitted with a 6^{th} order polynomial. A typical calibration curve is shown in **Figure 2.9** and the associated polynomial coefficients in **Table 2.1**.

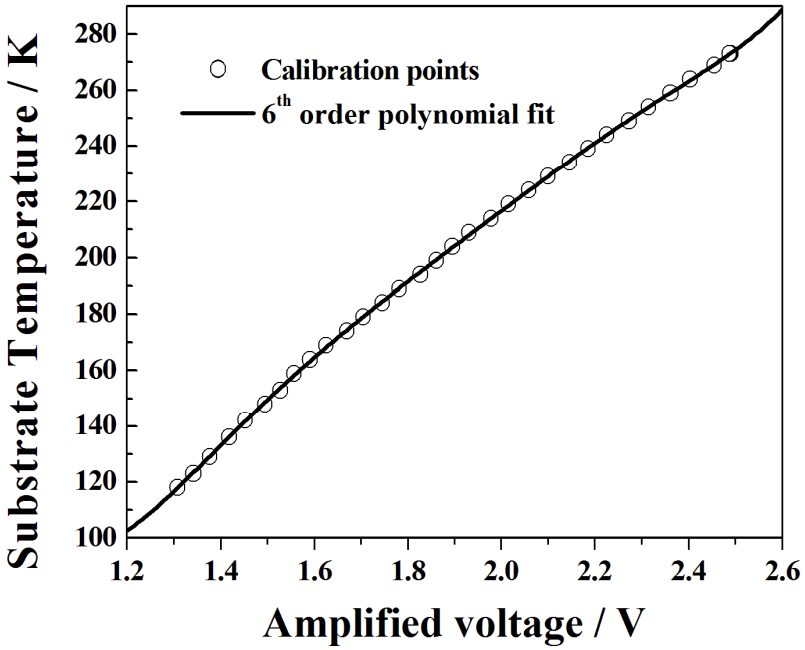

Figure 2.9: Calibration curve for the K-type thermocouple of chamber 1.

Coefficient for polynomial $AV^6+ BV^5+ CV^4+ DV^3+ EV^3+ FV+ G$	Coefficient value
A	208.6 K V^{-6}
B	-2391.3 K V^{-5}
C	11298.3 K V^{-4}
D	-28126.4 K V^{-3}
E	38848.5 K V^{-2}
F	-28032.2 K V^{-1}
G	8301.4 K

Table 2.1: Coefficients for 6th order polynomial calibration curve for K-type thermocouple.

Gas dosing

In addition to using the molecular beam, dosing could also be performed by back filling the chamber to a pressure as measured using the ion gauge on the main chamber. Gases could be introduced into the chamber *via* two fine control leak valves (Vacuum Generators MD95) situated in the experimental level. These were connected to two independent gas handling manifolds. Each of these consisted of four DN16CF ports to which vessels containing the species to be dosed could be attached. Typically this was achieved using glass ball and cup joints attached to

the port using a glass to metal transition. Liquids and gases were contained within test tubes and bulbs respectively which were connected to the transition *via* a valve. Further isolation from the manifold was provided by a DN16CF bellows valve on each port. One manifold was used for dosing species of experimental interest whilst the other was set aside for CO, H_2 and O_2 for use in single crystal cleaning cycles. Both manifolds were pumped by an oil diffusion pump (Edwards High Vacuum E02) backed by a mechanical rotary pump (Edwards High Vacuum E2M5). The manifolds could be isolated from the pumping system using a pair of right angle valves (Caburn MDC). Pressure measurement within the dosing system was limited to a pirani gauge, though preliminary tests with an ion gauge demonstrated that base pressures in the 10^{-8} torr range or better could be achieved.

2.3.2 Calibration of molecular beam

Before using the molecular beam to deposit H_2O films it was necessary to conduct some simple calibration experiments in order to obtain the optimum beam, in terms of both flux and profile. For this the beam was operated without being incident on the sample. H_2O molecules were detected using the QMS in line-of-sight with the beam. The source chamber pressure was adjusted by carefully opening the valve to the bulb containing H_2O that had previously been purified by several freeze-pump-thaw cycles. The source pressure was then stabilized at a value that resulted in the maximum flux as observed by the maximum signal at m/z=18. The source pressure varies as a function of nozzle pressure which will be somewhat higher. A Baratron gauge is present for monitoring the nozzle pressure, but with a 0.5 mm diameter hole the optimum pressure is reached at a pressure below the lower limit that this gauge can read. If the nozzle pressure is too low, a beam will be formed, but will have a low flux. As the pressure is increased the flux will also increase until collisions between molecules within the nozzle begin to cause the beam to break down. The maximum flux was obtained with a source pressure of $(2.0\pm0.2)\times10^{-4}$ mbar which likely corresponds to a nozzle pressure somewhere in the low 10^{-2} mbar range. After optimizing the flux the nozzle was moved using the x,y translation stage on which it was mounted to maximize the signal at the QMS. This was to ensure that the beam passed through the centre point of the chamber. The nozzle was also moved forwards, close to the orifice to

the first differential pumping stage, to ensure maximum flux through the collimating orifice between the two chambers.

It was also necessary to align the sample properly such that the beam was centered upon it. As the beam had been aligned to pass through the centre of the chamber, this ensured that the beam position is also suitable for performing RAIRS experiments without having to move the sample. The line-of-sight QMS was again used and the sample moved in both the Y and Z planes, which are perpendicular to the beam. The area under the m/z=17 and 18 peaks was calculated using the oscilloscope (Lecroy 9420) used to observe the QMS signal. The integrated signal then was recorded for each Y and Z position, with minimum signals being obtained with the sample in optimum position, blocking the beam. By comparing the recorded signal to that obtained with the sample well out of the beam, the fraction of the beam intercepted could be calculated. The variation of beam interception with Y and Z position is shown in **Figure 2.10**. The sample was then positioned at the centre of the relatively flat region in the uptake plot. The features at Y and Z values far from the centre can be attributed to varying amounts of beam blocking by support and thermocouple wires.

In order to obtain an estimate of the beam flux for an H_2O beam, H_2O films were deposited by using both background dosing and beam dosing. The surface concentration was calculated for background doses using simple collision theory, where the sticking probability was assumed to be unity. This procedure will be described in subsequent chapters. By comparing the areas under TPD profiles (TPD yield) for films deposited using the two dosing methods it was possible to calculate surface concentrations for the beam deposited films. These were then converted into fluxes using the known beam dosing times. This approach gave $(3\pm1)\times10^{13}$ molecules cm^{-2} s^{-1} with the error being derived from variations in the value obtained for different beam dose times. **Figure 2.11** shows the comparison between a 10 L background dosed H_2O film and a 100 s beam dosed film which was found to correspond to an effective dose of 7 L.

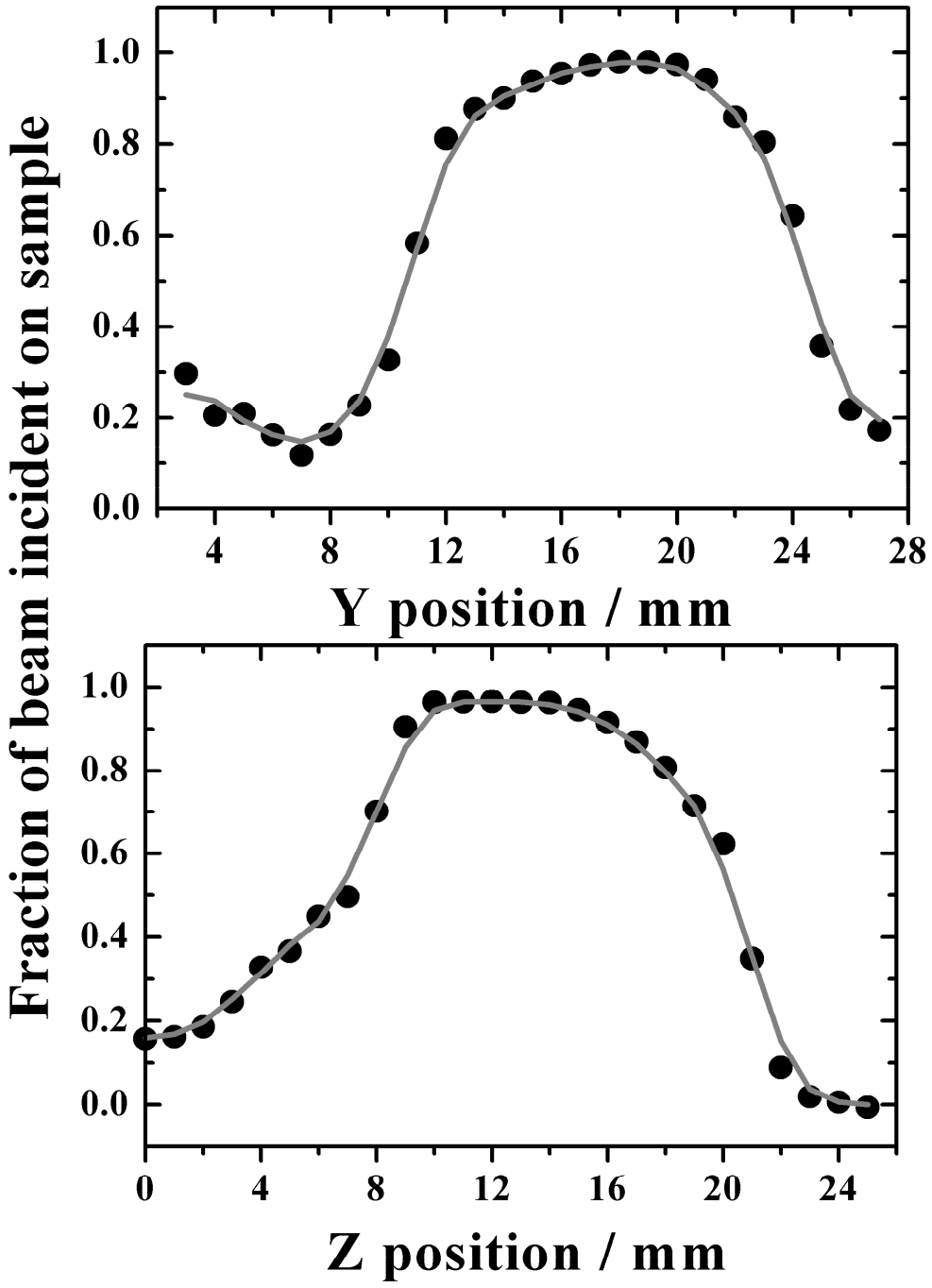

Figure 2.10: Fraction of the molecular beam that is incident on the sample for different positions in both the Y and Z directions.

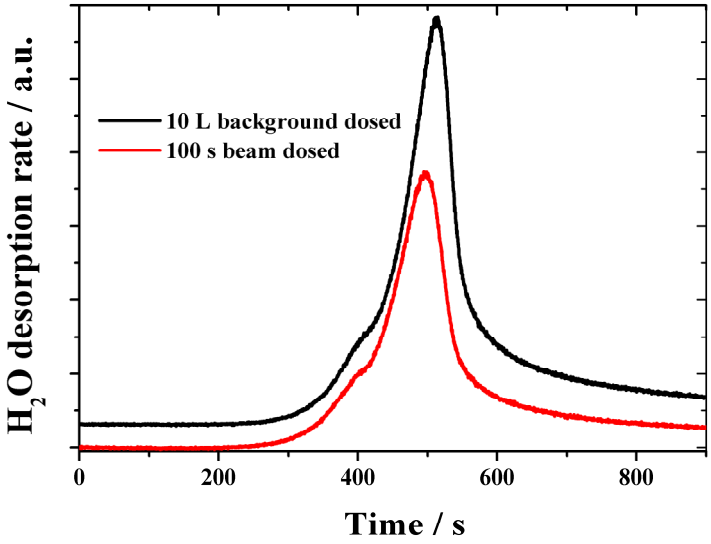

Figure 2.11: Comparison between H_2O TPD profiles used for calculation of the molecular beam flux. A heating rate of 0.1 K s^{-1} was used. The traces have been offset for clarity.

2.3.3 UHV chamber 2

Vacuum system and pumping

This UHV chamber was used for those experiments involving the irradiation of ices with photons. It was designed for use in both traditional single crystal surface science and astrochemistry experiments. The 30 cm diameter stainless steel chamber (Instrument Technology Ltd.) was pumped by a liquid nitrogen trapped 6" oil diffusion pump (Edwards High Vacuum E06), with additional pumping provided by a liquid nitrogen cooled titanium sublimation pump (Instrument Technology Ltd.) with associated controller (AML TSP2). A liquid nitrogen trapped 4" oil diffusion pump (Edwards High Vacuum E04) provided differential pumping for a pulsed dosing valve (Parker Instrumentation Iota One), which was mounted on a precision *x*, *y*, *z* manipulator (Vacuum Generators Miniax), and the quadrupole mass spectrometer. The pulsed dosing valve was not used in these experiments and will not be discussed further. The UHV chamber pressure was measured with a nude hot cathode ionization gauge (Instrument Technology Ltd.), whilst the pressure in the differential chamber of the pulsed dosing valve was measured with a cold cathode inverted magnetron ionization gauge (Edwards High Vacuum AIM).

Figure 2.12: Photograph of UHV chamber 2.

All backing pressures were monitored with Pirani gauges (Edwards High Vacuum APG-L). All gauges were interfaced to two gauge controllers (Edwards High Vacuum Active Gauge Controller). A base pressure of $<2\times10^{-10}$ mbar was routinely obtained following bakeout at 100°C for 60 hours. A schematic diagram of the UHV chamber pumping arrangement is shown in **Figure 2.13**.

Instrumentation

As this system was designed for both single crystal surface science and astrochemistry experiments, a wide range of instrumentation was available on this UHV chamber. For determination of surface order and cleanliness, rear view combined LEED/AES optics (SPeCS ErLEED 150) with integral electron gun were fitted to the chamber, though not used in the experiments described here. Single crystal cleaning through sputtering was possible using an Ar^+ sputter gun (Vacuum Science Instruments IS2000) through which Ar gas was introduced *via* a fine control leak valve (Vacuum Generators). Gases could be introduced into the background *via* a second fine control leak valve (Vacuum Generators). The system was equipped with two quadrupole mass spectrometers. For assessing the purity of species dosed into the chamber a residual gas analyzer (Stanford Research System RGA-200) quadrupole mass spectrometer with a *m*/*z* range of 1-200 was used. TPD and photon irradiation experiments were performed using a pulse counting quadrupole mass spectrometer with a *m*/*z* range of 1-300 (Hiden Analytical HAL IV RC PIC-RGA 301). This device was equipped with a channel electron multiplier and provided detection of species down to partial pressures in the 10^{-13} mbar range. Auxilliary input channels on the control unit allowed the simultaneous recording of ion counts and, for example, thermocouple voltages. A transistor transistor logic (TTL) output was also available for use with additional pulse counting electronics such as a multichannel scaler. The TTL pulse output was fed into a multichannel scaler (Stanford Research Systems SR430) for the acquisition of Time-of-Flight profiles. The experimental level also contained two fused SiO_2 viewports through which the UV laser beam could be directed during irradiation experiments.

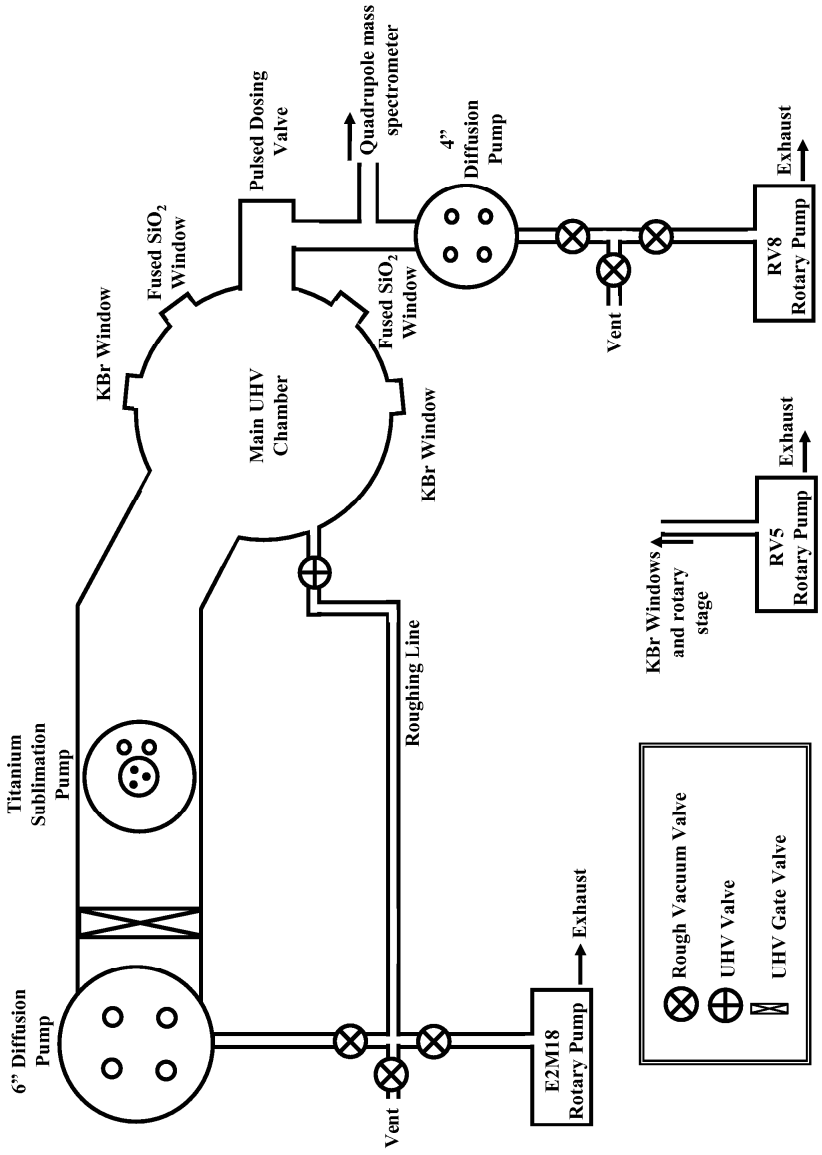

Figure 2.13: Schematic of the UHV chamber used for photon irradiation experiments.

These were positioned such that the beam was incident at an angle of 45° to the surface normal when the sample was rotated to face the mass spectrometer line-of-sight tube. Differentially pumped mountings were also fitted for KBr windows for performing IR experiments. The design of the flange for this mounting arrangement allowed two configurations to be adopted by rotating the flange through 180°. This allowed experiments with the beam either incident at a grazing angle to the sample for RAIRS experiments, or along the surface normal for transmission experiments. Spectra were obtained using a FTIR spectrometer (Thermo Nicolet Nexus 470) equipped with a KBr beamsplitter and an external liquid cooled mercury-cadmium-telluride (MCT) detector. The beam was steered by a plane mirror (50 × 50 mm) towards a 90^{o} off-axis parabolic mirror (∞:330 mm, Aero Research Associates Inc.) to focus the IR beam onto the sample. Upon leaving the chamber, the beam was steered and focussed onto detector with a 90^{o} off-axis ellipsoidal mirror (330:33 mm, Aero Research Associates Inc.). All steering optics and the detector were housed in custom built boxes mounted on either side of the UHV chamber. These were purged with dry nitrogen, along with the FTIR spectrometer to reduce absorption by atmospheric H_2O and CO_2 along the beam path. The two arrangements for IR experiments are shown in **Figure 2.14**. A schematic of the experimental level of the chamber used for photon irradiation experiments is shown in **Figure 2.15**.

As this system was specifically designed for studying the interaction of species with extremely cold dust grains in the interstellar medium, it was equipped with a closed cycle helium cryostat (SHI-APD DE-202B) in order to cool the sample. This, in principle, allows the sample to be cooled to around 10 K, enabling more volatile species such as CO, N_2, and NH_3 to be adsorbed. However, during these experiments technical problems limited the base temperature to around 80 K. This type of cryostat utilizes the expansion of a compressed gas to cool an OFHC Cu cold finger. A compressor compresses CP grade Helium (BOC) to 320 psi which passes into the cryostat head mounted on the top of the sample manipulator. This contains a displacer, moved up and down within a closely fitted housing. Initially the helium enters with the displacer in the down position.

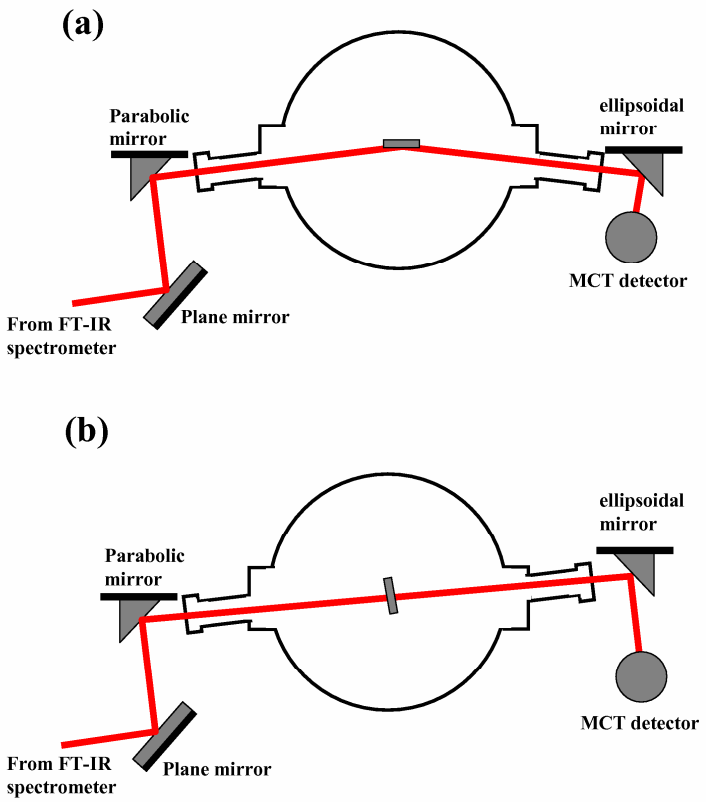

Figure 2.14: Arrangement for (a) RAIRS and (b) transmission IR experiments.

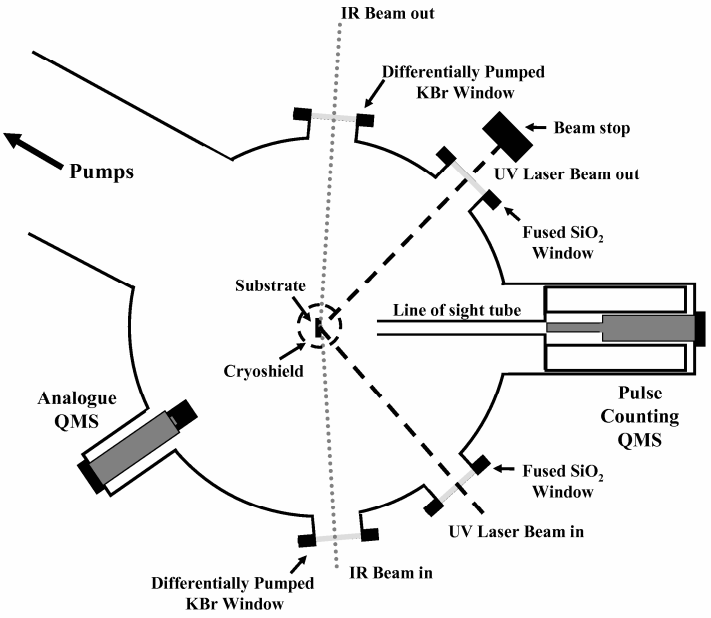

Figure 2.15: Schematic of the experimental level of the UHV chamber used for photon irradiation experiments.

The displacer then moves up, increasing the volume occupied by the helium. Heat is then transferred from the housing to the helium in order that it can expand to fill the volume. As this process is repeated, the housing and the OFHC copper cold finger which is attached to it gradually cools down. The cold finger and lower section of the cryostat assembly were surrounded by a gold plated OFHC copper cryoshield to reflect incident radiation that may present an additional heat load. All thermocouple and heating wires were tightly wound around the cold finger in order to reduce any heat load that they might otherwise provide.

Sample mounting

The sample mount used for these experiments was designed for mounting either a single crystal or interstellar grain mimic, depending on the experiments being conducted. This requirement poses the challenge of being able to rapidly heat a single crystal to *ca.* 1000 K for annealing during single crystal cleaning cycles, and then cool to 10 K for experiments. Unfortunately, the full capability of the mount was not realized due to difficulties with the closed-cycle helium cryostat. The mounting arrangement is shown in **Figure 2.16**. The mount assembly was constructed from OFHC copper and was attached to the end of the cryostat cold finger using an M6 bolt with electrical isolation provided by a cylindrical ceramic insulator. The mount was electrically isolated from the cold finger by a sapphire spacer (25 mm diameter × 1 mm thickness). In order to maximize thermal contact, polished silver gaskets (thickness 0.1 mm) were inserted between all components. The substrate could be heated by means of a customized "button" style resistive heating cartridge (HeatWave Labs Inc.) contained within a Mo thermal shield. The heater assembly was held in place by clamping it within a hole at the lower end of the mount. Electrical isolation of all components was achieved using appropriate ceramic pieces. The substrate itself was clamped onto the front face of the heater by small pieces of Ta which were bolted onto the mount. Temperature measurements were made using three thermocouples. The first was a K-type (NiCr/NiAl) thermocouple inserted into the rear of the heater such that the junction was positioned on the rear of the heater's front face, on which the substrate was mounted. A further K-type thermocouple and a KP-type (0.7% Fe in Au/Cr) thermocouple were attached to the sample mount itself.

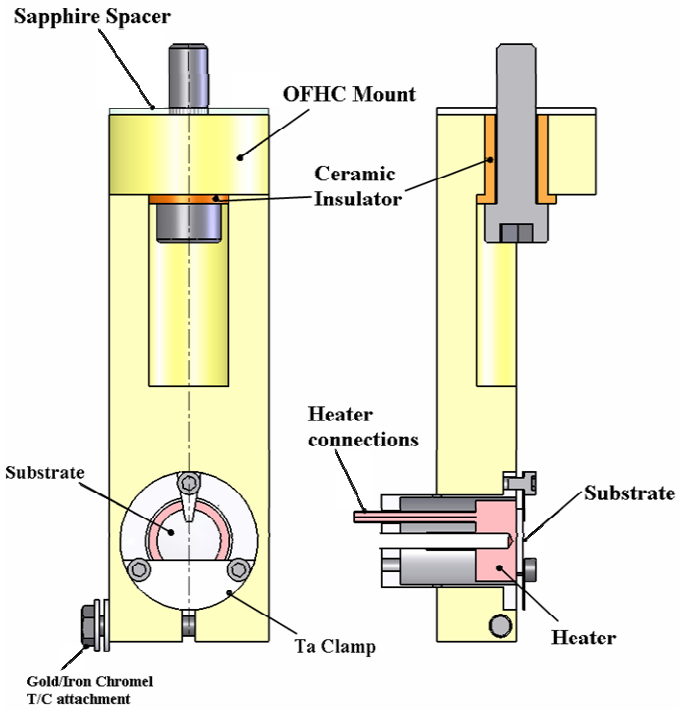

Figure 2.16: Sample mounting arrangement for photon irradiation experiments.

The junctions of these thermocouples were spot-welded onto small washers that were pressed against the side of the mount by the bolt used to clamp the heater in place. A maximum substrate temperature of 1500 K was possible, which is more than adequate for routine single crystal cleaning.

The entire cryostat assembly was mounted on a precision *xyzθ* manipulator assembly to allow full control of sample positioning within the chamber for a range of experiments. The *xyz* manipulator (Vacuum Generators Centiax) had *x* and *y* motions of ±25 mm with 5 μm precision. Translation in the *z*-direction of 150 mm was adjusted using a hexagonal drive nut, giving 4 mm motion per revolution. Unlimited rotation with 0.05° resolution was possible using a two stage differentially pumped rotation stage (Vacuum Generators RP100). Appropriate thermocouple feedthroughs and connections for the substrate heater were mounted on flanges close to the top of the cryostat assembly.

Line-of-sight QMS

The design of the sample mount meant that during TPD experiments with large temperature ranges, significant desorption would occur from other parts of the sample mount. In order to constrain the detection of desorbing molecules to those

originating from the sample surface, a Line-of-Sight (LoS) design based on that of Jones and Turton [3,4] was used. In this design the QMS was mounted within a liquid nitrogen cooled shroud. This was connected by flexible bellows to the main chamber diffusion pump to provide differential pumping. An OFHC copper tube (inner diameter, 10 mm) was attached to the end of the shroud such that the entire tube would reach *ca*. 80 K when the shroud was filled with liquid nitrogen. This provided a line-of-sight between the sample surface and the ion source of the QMS. Consequently any molecules desorbing from surfaces other than that defined by the line-of-sight would collide with and freeze out onto the surface of the tube before reaching the ion source. This would only be the case for species that will adsorb at 80 K, and the constraint for more volatile species is reliant on the geometrical constraints alone. A schematic of the LoS arrangement is shown in **Figure 2.17**.

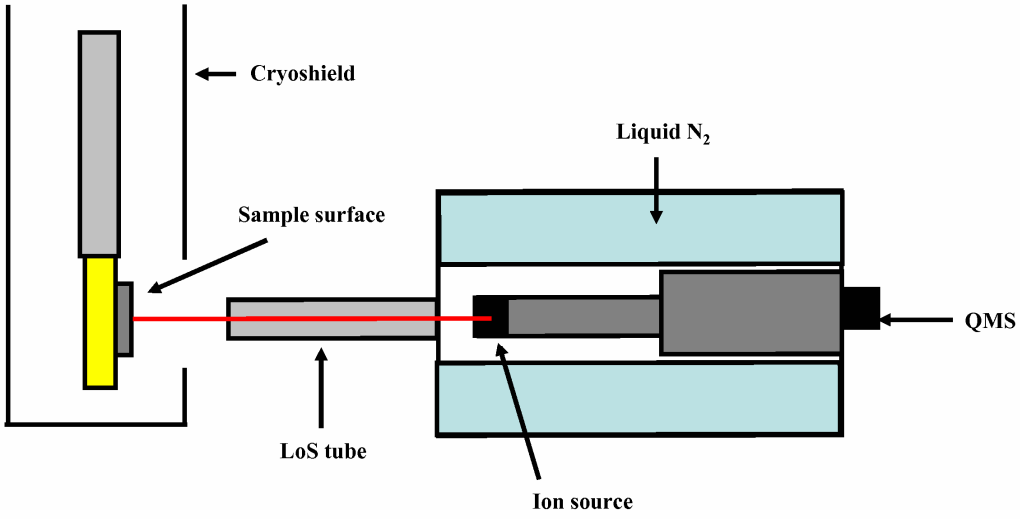

Figure 2.17: Arrangement for LoS TPD measurements.

Temperature control system

The substrate heater was controlled by a programmable controller (Scientific Instruments Model 9700) connected to the low voltage DC heater power supply (Glassman Europe LP40-30). The power supply was capable of providing a maximum current of 10 A at 30 V. The programmable controller had two independent thermocouple inputs, and was able to store calibration curves in order to convert the thermocouple voltage to temperature. This combination of power

supply control and thermocouple feedback allowed the controller to be programmed to hold the temperature at a specific set point, and produce heating ramps based on a user specified function. Modification of parameters was possible directly through the front panel of the controller unit, and also remotely using National Instruments LabView software supplied with the unit (LabView driver M9700) through a RS232 interface to a desktop PC. The controller also provided raw thermocouple voltage outputs. By reading one of these into the auxiliary input channel of the pulse counting QMS it was possible to record thermocouple voltage simultaneously with ion counts using the QMS software, as required in TPD experiments.

Laser system

The laser system described here was used for UV irradiation experiments performed with wavelengths of 248.8 nm, 250.0 nm and 275.0 nm. The UV irradiation beam was generated using a Nd^{3+}:YAG pumped dye laser. The pump laser (Continuum Powerlite 8000) was operated in the third harmonic (355 nm). This output was used to pump the dye laser (Sirah CobraStretch) that was operated with Coumarin 307 dye. This dye gives a peak output centred around 500 nm when pumped at 355 nm. A frequency doubled output was obtained through second harmonic generation (SHG), thus allowing the target wavelengths to be obtained. The beam was steered to the UHV chamber using UV dichroic mirrors (MaxiBrite). The steering system incorporated a periscope to bring the beam up to the experimental level of the UHV chamber. Pulse energy was measured using a power meter positioned just before the beam entered the chamber through the fused SiO_2 window. The pump laser was operated at a repetition rate of 10 Hz, controlled by a standard pulse generator (Stanford Research Systems DG535). Initially, the shutter to let the beam into the chamber was controlled manually, though this was replaced in later experiments by control from a second pulse generator (Stanford Research Systems DG535).

2.3.4 PM-RAIRS system

The system for performing Polarization Modulation RAIRS (PM-RAIRS) experiments was housed in a dry box that was purged with dry, CO_2 free, air to reduce absorption by atmospheric contaminants such as H_2O and CO_2. Spectra were acquired with an FTIR spectrometer (Nicolet Nexus 870) and an external two channel MCT detector (Nicolet MCT-A). The polarization of the IR beam was modulated using the PEM-90 photoelastic modulator (Hinds Instruments Model II/ZS50) which incorporates a ZnSe crystal. The obtained signal was demodulated with a synchronous demodulator (GWC Technology SSD-200). The IR beam was steered using a plane mirror and subsequently focused into the PEM with a parabolic mirror. The sample was mounted on a rotatable holder for easy beam alignment with a reflection angle >75° to the surface normal being used. The reflected beam was focused into the window of the MCT detector by use of a lens. The experimental arrangement is shown in **Figure 2.18**.

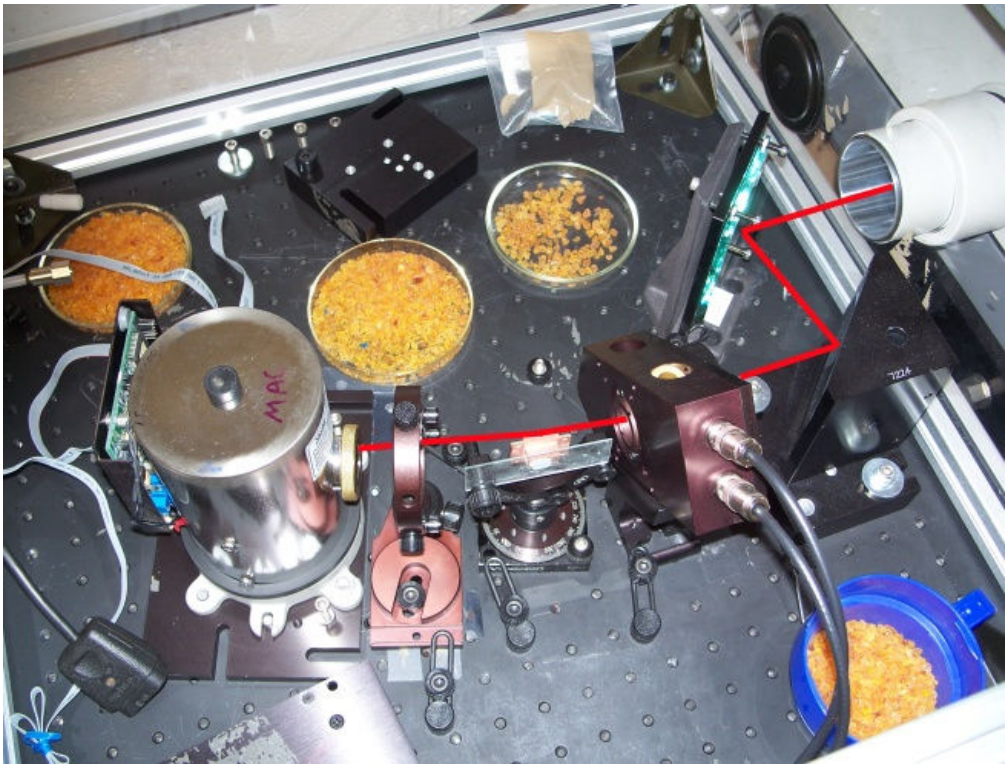

Figure 2.18: Photograph of the PM-RAIRS system. The path of the IR beam is shown in red.

2.4 Experimental techniques and procedures

2.4.1 Neutral detection using quadrupole mass spectrometry (QMS)

Mass Spectrometry has found applications in a great many areas of science and is performed using a wide range of different techniques. The general principle behind mass spectrometry is to separate molecules according to their molecular mass and provide a measure of the abundance of one or more species in the medium of interest. In QMS, molecules are first ionized and then mass filtered by their mass to charge ratio, *m/z*. This is due to the inherent difficulty in detecting neutral species. The quadrupole mass spectrometers used in this work were equipped with electron impact (EI) ion sources. In such a source electrons are generated through thermionic emission by passing a current through a filament, usually made of tungsten, W, or thoriated iridium. These electrons are then accelerated towards the source electrode acquiring an energy of typically 70 eV. These electrons will then ionize molecules that enter the source. Ions that are produced are then accelerated into the mass filter by the ion focus electrode. The quadrupole mass filter lies at the heart of the QMS and consists of four parallel rods arranged such that their cross-section forms a square arrangement to which a combined RF and DC field is applied. Ions entering the filter from the source will tend to spiral down through the filter. Each mass to charge ratio has a specific RF/DC amplitude that will allow it to pass stably through the filter. Ions with different mass to charge ratios will spiral out of the filter. By increasing the RF/DC amplitude gradually, a range of *m*/*z* values can be scanned. Once mass selected, ions are detected using an appropriate detection system. A Faraday cup detector may be used, in which the ion current of a particular mass ion is measured directly. This ion current is typically very small (< 1 pA) and so the signal must be pre-amplified. This limits the application of this type of detector to higher pressure ranges, and is generally not sufficient for use in UHV studies. More frequently, a secondary electron multiplier (SEM) is used which can achieve much higher sensitivities. The commonly used channel electron multiplier (CEM) consists of a curved glass channel constructed out of a special lead silicate glass.

This material releases a large number of electrons per incident electron or ion. Mass selected ions are deflected into the wide entrance to the CEM held at a large negative potential (*ca*. -2 to -3 kV) by a deflection plate. Upon striking the surface of the CEM a large number of electrons are released which move down the channel, eventually striking the surface. In this way a cascade of electrons is generated giving an overall signal gain of the order of 10^7. This allows for sensitivities down to around 10^{-13} torr. In some systems, the CEM can be operated in two modes. In analogue mode the output current from the CEM is amplified and recorded in much the same was as with a Faraday cup detector. For analogue operation the CEM is operated at a potential of between -1500 and -2000 V, calibrated to give the same total pressure reading as, for example, the chamber ion gauge. However, in some circumstances it is more desirable to obtain the current pulses associated with an ion detection event. In pulse counting mode, the output from the CEM displays a characteristic dependence on the applied potential whereby it increases rapidly to some potential, then forms a plateau to higher voltages. Pulse counting using a CEM has been described previously [5]. The potential is chosen to be as low as possible whilst still being in the plateau region. Operating at lower potentials reduces the sensitivity, and may result in poor stability, given the strong dependence on applied potential. Operating at higher potentials will not result in a significant gain in sensitivity, but may increase noise, and will ultimately reduce the lifetime of the detector. The output current pulses are usually converted to TTL voltage pulses for further processing. A discriminator is used to select the largest pulses in the pulse height distribution (PHD), such that pulses can be separated from any noise. A typical PHD is shown in **Figure 2.19** with the dotted line showing where the discriminator voltage should be set such that noise is discarded without losing a significant number of signal pulses. The resulting detection method gives a highly sensitive, rapid response that can be used in time-resolved studies down to intervals of the order of 1 μs.

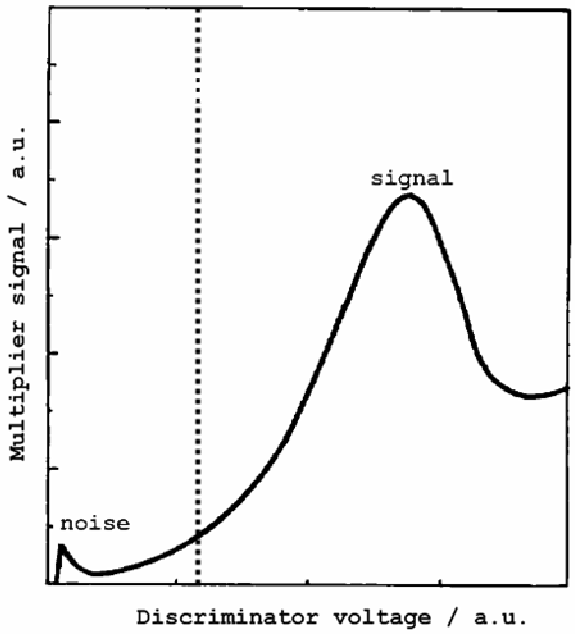

Figure 2.19: Pulse height distribution for a CEM operated at 3100 V. The dotted line shows where the discriminator voltage that should be used to separate the signal from the noise. Adapted from [5].

2.4.2 Temperature programmed desorption (TPD)

Temperature programmed desorption is a simple experimental technique in which the desorption rate of molecules from a surface is monitored whilst the surface is heated, typically with a linear temperature ramp. Desorbing molecules are usually detected using a QMS situated close to the surface of interest. TPD can be used to determine the activation energy for desorption of a particular molecular species from a surface, yielding an approximate value for the adsorption energy. For multilayer systems, the adsorbate-adsorbate interaction energy can be obtained. Information on different binding sites and orientation can be also be obtained, and the technique is typically combined with RAIRS experiments to obtain complementary results. Despite the experimental simplicity, analysis of TPD data is frequently complicated, and a good understanding of the kinetics of the desorption process is required to fully exploit the potential of the technique. Nevertheless, a TPD experiment is a good place to start when studying the adsorption of molecular species on solid surfaces.

The TPD technique has been described previously, along with detailed discussions on the analysis of TPD data [6,7]. Here a general overview of the

technique and general analysis used in this work will be provided. There are several important experimental considerations when performing TPD experiments. The first concerns the pumping speed of the vacuum chamber. If the pumping speed is lower than the rate of desorption, then the desorbed species with accumulate in the chamber and the measured ion signal in the QMS will not be proportional to the desorption rate. For this reason, TPD experiments are usually performed at UHV where the pumping speed is usually sufficiently high that the QMS signal is proportional to desorption rate. It is also important to ensure that the substrate is, as far as possible, heated uniformly across the surface. Non-uniform heating can lead to broadening of TPD peaks, which can make analysis difficult and less reliable. The resulting TPD traces are also prone to the detection of species desorbing from surfaces other than that of interest, leading to additional peaks. This is not a problem if the peaks are well separated from the peaks of interest, but this is frequently not the case, and TPD experiments may incorporate line-of-sight techniques where molecules desorbing from other surfaces are prevented from reaching the QMS by a combination of geometric constraints and liquid nitrogen trapping. Desorption from heating wires can be reduced by briefly flash heating them before conducting the TPD experiment.

Analysis of TPD data requires a consideration of the kinetics of the desorption process, for example the desorption of species A from a surface can be represented by:

$$\mathrm{A(ads)} \rightarrow \mathrm{A(g)} \qquad \textbf{Equation 2.3}$$

where A(ads) represents the adsorbed species and A(g) represents the gas phase species following desorption. The rate of desorption, r_{des} can be written in terms of an Arrhenius equation known as the Polanyi-Wigner Equation:

$$r_{\mathrm{des}}(\theta) = -\frac{\mathrm{d}\theta}{\mathrm{d}t} = \nu\theta^{n} \exp\left[-\frac{E_{\mathrm{des}}(\theta)}{RT}\right] \qquad \textbf{Equation 2.4}$$

where θ is the coverage, t is time in s, T is the substrate temperature in K, $\nu(\theta)$ is the pre-exponential factor in units appropriate for the desorption order, also

known as the frequency factor, n is the order of the desorption process, E_{des} is the desorption energy in J mol^{-1} and R is the gas constant in J K mol^{-1}. This expression may also be written in terms of a surface concentration N in molecules cm^{-2}.

In order to be able to use **Equation 2.4** to obtain kinetic parameters from TPD data, it must be transformed into a form where the rate is expressed in terms of temperature, as it is in an experimental TPD trace. This can be done by recognising that the desorption rate can be written in terms of the heating rate, $\beta=(dT/dt)$, yielding:

$$-\frac{d\theta}{dT} = \frac{\nu\theta^n}{\beta}\exp\left[-\frac{E_{des}(\theta)}{RT}\right]. \qquad \textbf{Equation 2.5}$$

There are several techniques used for the extraction of kinetic parameters from TPD data and these have been described in detail elsewhere [6]. One can consider the peak in a TPD trace by differentiating **Equation 2.5** with respect to temperature and setting the result equal to zero to obtain, for the case of n=1 for first order desorption:

$$E_{des} = \frac{RT_{max}^2 \nu_1}{\beta}\exp\left[-\frac{E_{des}}{RT_{max}}\right] \qquad \textbf{Equation 2.6}$$

where ν_1 is the first order pre-exponential factor and T_{max} is the temperature at which the peak in the desorption trace occurs. It can be seen that there is no dependence on coverage, θ, which indicates that a first order desorption does not shift in temperature as coverage is increased. If n=2, then the peak position will depend on θ. Most analyses of TPD traces are based on the application of an equation of the form of **Equation 2.6** appropriate for the order of the desorption kinetics. The form of this expression gives an indication of the shape of the resulting TPD peaks. For zero order desorption the peak temperature shifts to higher temperature with increasing coverage and the traces display coincident leading edges. For first order desorption, the peak temperature does not vary with coverage and the peak is slightly asymmetric. Second order desorption kinetics

display a more symmetric peak. Thus, an approximation can be made for the desorption order from inspection of experimental traces. However, it is essential to proceed with caution as in many real systems the desorption order may be fractional. Methods for obtaining more accurate desorption orders from experimental TPD data have also been described [8].

The desorption order is indicative of the nature of the desorption process. First order desorption typically occurs for the desorption of sub-monolayer coverages of adsorbate from a well defined surface. Zero order desorption is characteristic of desorption from multilayer coverages, in which the desorption energy is related to the interaction between adsorbate molecules. Second order desorption arises from recombinative desorption, or desorption where there are strong lateral interactions between adsorbate molecules. In the case of first order desorption, a simple relationship has been derived to relate the desorption energy to the peak position. This analysis was first described by Redhead in 1962 [9] and results in an easily applicable expression:

$$E_{des} = RT_{\max}\left[\ln\left(\frac{\nu_1}{\beta}\right) - 3.46\right]. \qquad \textbf{Equation 2.7}$$

This expression must be used with caution, and should only be applied in the case of first order desorption. It relies on an appropriate choice of pre-exponential factor, ν_1, though the sensitivity of this is reduced due to the logarithmic dependence. Typically a value of *ca*. 10^{13} s^{-1} is assumed for simple first order desorption.

2.4.3 Reflection-absorption infrared spectroscopy (RAIRS)

Probing the vibrations on molecules adsorbed on solid surfaces presents several challenges. A range of vibrational spectroscopies have been developed for use with surface adsorbed species [10]. Reflection-Absorption Infrared Spectroscopy (RAIRS) is the technique used in this work and will be discussed in more detail.

It is clear that traditional IR spectroscopy in transmission mode is not applicable in the case of a thin film adsorbed onto an opaque substrate. It is possible to

conduct transmission IR studies using bulk ices adsorbed on transparent, IR transmitting surfaces such as KBr. Such studies can provide information relevant to thick adsorbed multilayers, but in many cases it is desirable to be able to consider the adsorbate-substrate interaction. The development of an alternative to transmission IR has been crucial in surface science, where typically, opaque, single crystal metal surfaces are studied. It is also important to note that the study of adsorbate-substrate interactions alone requires the adsorption of up to one monolayer of adsorbate. The path length through such a film is extremely small, resulting in very small absorbance values and great difficulty in obtaining useful spectra. As will be discussed, it was found that performing IR experiments in reflection mode, where the IR beam is reflected off the surface of interest has significant advantages.

The theoretical background of RAIRS was first discussed by Greenler [11] and a brief overview will be given here. If light is incident normal to a metal surface the incident and reflected beams combine, forming a standing wave. This standing wave will have a node at the surface and, for infrared wavelengths, a very small amplitude at thicknesses corresponding to a few adsorbed layers. As it is the electric field that interacts with the oscillating dipole moments of adsorbed molecules, it follows that the absorption signal will also be small. It is clear from this that the incident beam needs to be away from the surface normal in order to achieve a reasonable absorption signal. This relies on the fact that the phase change upon reflection depends on both the angle of incidence and the polarization of the light. The relevant electric vectors are shown schematically in **Figure 2.20**.

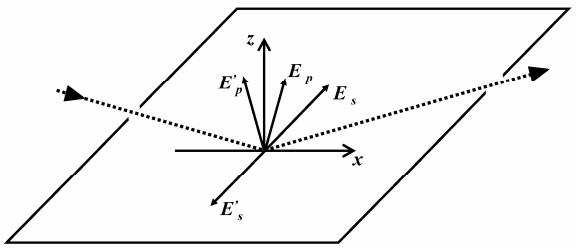

Figure 2.20: Electric field vectors for light incident on a reflective surface away from the surface normal. *p* and *s* refer to the polarization of the light and ' is used to indicate the reflected component.

The phase shift for the *s* polarized component is close to 180° for all angles of incidence. This means that the resultant vector for the *s* polarized component will be close to zero, and no significant absorption observed. However, the *p* polarized component of the incident light experiences a phase shift that is highly dependent on the angle of incidence, reaching around 90° for large angles. This means that the incident and reflected beams combine to yield a vector with a significant component perpendicular to the surface. This is enhanced by up to a factor of two compared to the magnitude of the incident vector. The enhanced absorption arising from this effect is shown in **Figure 2.21**, which shows that the maximum enhancement is achieved with an angle of incidence of *ca*. 88°. The component parallel to the surface will however be much weaker. As well as providing a significant enhancement in the absorption signal at high angles of incidence, an important condition arises; the surface selection rule. The *p* component is able to interact strongly only with vibrational modes that have a dipole orientated perpendicular to the surface. This means that any vibrations that have no perpendicular component will not be observed in the IR spectrum. Thus RAIRS can be used to obtain information of the orientation of adsorbed molecules by an analysis of which modes are present in the obtained spectrum.

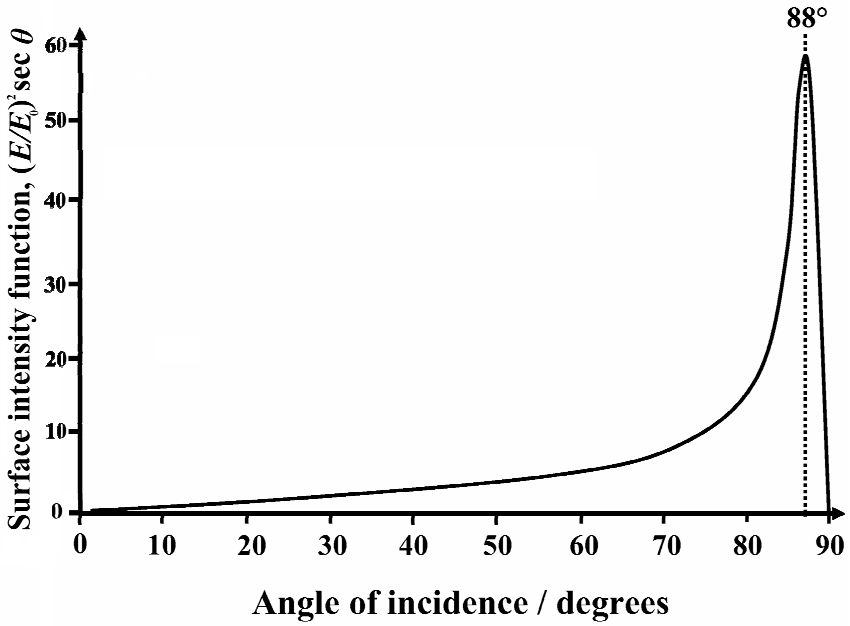

Figure 2.21: The surface intensity function as a function of angle of incidence demonstrating the enhancement achieved by using an angle close to grazing.

RAIR spectra in this work have been obtained using a Fourier transform infrared (FTIR) spectrometer. The principles behind both FTIR and dispersion spectrometers have been discussed at length elsewhere [12], nevertheless a brief overview of the principle of operation for an FTIR spectrometer will be provided here. With an FTIR spectrometer, experimental time is reduced compared the use of dispersion spectrometers as a result of all wavelengths being collected simultaneously. They can therefore achieve a higher signal-to-noise ratio in a shorter time than dispersion spectrometers. As an FTIR spectrometer requires no slits, which reduce the beam intensity in dispersion spectrometers, the optical throughput is much higher, which also increases the signal-to-noise ratio. Further signal improvements can be brought about by the co-addition of scans. This is made possible by the accuracy of the frequency scale which results from the use of a fixed frequency from the reference laser and the FT technique. Dynamic alignment of the IR beam within the FTIR spectrometer allows a high degree of stability over extended periods of time. The FTIR spectrometer is designed around the Michelson interferometer. In this arrangement IR radiation is provided by a heated ceramic source and directed into the interferometer. The interferometer is shown schematically in **Figure 2.22**. The interferometer consists of two mirrors and a beam splitter. The beam splitter reflects 50 % of the incident light, and transmits the remaining fraction. The transmitted fraction is incident on one of the mirrors, which is fixed, while the reflected fraction is directed onto the second mirror which moves back and forth over a small distance with a well defined frequency. Light from the two mirrors is then recombined at the beamsplitter, with the two components having a varying phase difference as a result of the varying path length of one of the beams. The resulting recombined beam will therefore produce an interference pattern.

The interferogram for a monochromatic beam can be expressed mathematically as the function $I_{\text{mono}}(d)$:

$$I_{\text{mono}}(d) = I(\tilde{\nu})\cos(2\pi\tilde{\nu}d) \qquad \textbf{Equation 2.8}$$

where d is the path difference, $\tilde{\nu}$ is the wavenumber of the radiation, with $\tilde{\nu} = 1/\lambda$ for the wavelength λ, and $I(\tilde{\nu})$ is the intensity of the source.

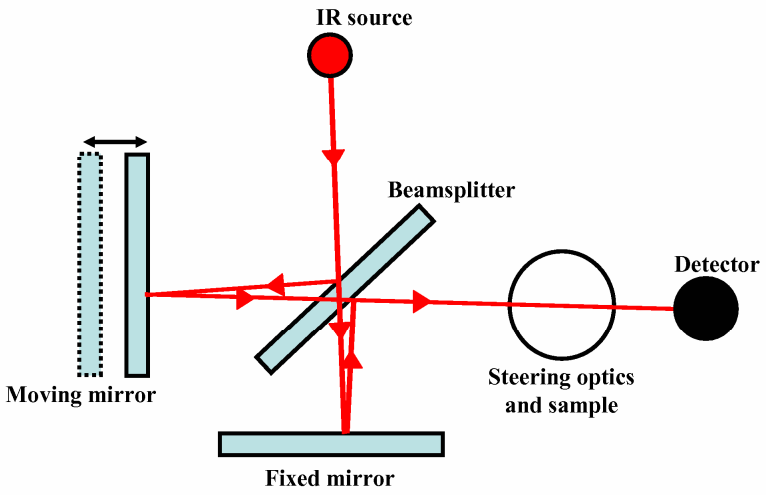

Figure 2.22: The Michelson interferometer as employed in a typical FTIR.

In an FTIR a broad band IR source emitting radiation over a range of wavelengths. The expression for the interferogram resulting from such a polychromatic source is given by an integral over all frequencies:

$$I_{\text{poly}}(d) = \int_0^\infty I(\tilde{\nu})\cos(2\pi\tilde{\nu}d)\,\mathrm{d}\nu\,. \qquad \textbf{Equation 2.9}$$

Therefore, the interferogram produced at the IR detector will contain information at all wavelengths. In order to obtain an IR spectrum, it is necessary to transform from the interferogram which is in the time domain (noting that d is a function of time, t, to the frequency domain, typically expressed in terms of wavenumbers. This is achieved mathematically be performing a Fourier transformation to obtain the single beam spectrum, $I(\tilde{\nu})$:

$$I(\tilde{\nu}) = \int_0^\infty I(d)\cos(2\pi\tilde{\nu}d)\,\mathrm{d}\nu\,. \qquad \textbf{Equation 2.10}$$

As only a single beam spectrum can be obtained, it is necessary to obtain a background spectrum before conducting experiments. This must be performed with the sample under exactly the same conditions (*i.e.* position and temperature) as for spectra obtained during the experiment. This is because the optical

properties of metal surfaces are sensitive to temperature. The final spectrum is obtained by the following relationship:

$$I_{\text{corr}} = -\log_{10}\left(\frac{I_{\text{sam}}}{I_{\text{bg}}}\right) = \log_{10}\left(\frac{\Delta R}{R}\right). \qquad \textbf{Equation 2.11}$$

where I_{corr} is the background corrected spectrum, I_{sam} is the sample spectrum and I_{bg} is the background spectrum. The resulting spectrum is on a scale of fractional absorbance, as defined by $\log_{10}(\Delta R/R)$). Following background correction is usually necessary correct the spectrum for a curved baseline. This arises as a result of small variations in the IR source and the experimental arrangement from one scan to another. **Figure 2.23** shows a 100% line obtained with the IR arrangement used in these experiments. This is essentially a spectrum obtained with no adsorption between the background and sample collection. Small contributions are present as a result of small variations in the concentrations of gas phase contaminants in the purge, and a small increase in H_2O ice in the MCT detector. The overall noise level is of the order of 1.5×10^{-4} which results in a peak being defined if it has an absorbance value of greater than 3.0×10^{-4}.

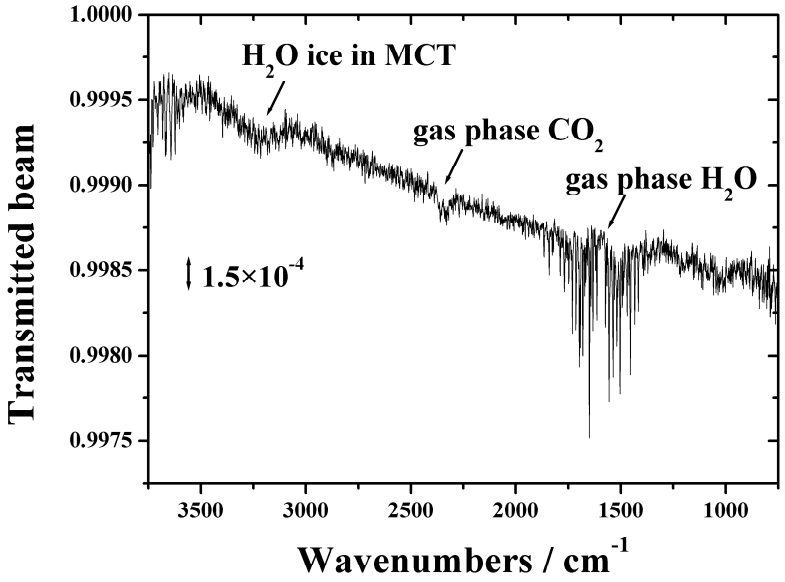

Figure 2.23: 100% line obtained with the IR arrangement used in these experiments.

2.4.4 Polarization modulation RAIRS (PM-RAIRS)

PM-RAIRS is a variation of RAIRS that can be used to effectively collect the sample and background spectrum simultaneously. This has the advantage that the IR spectrum of a thin film on a metal substrate can be obtained without obtaining a background spectrum prior to deposition of the film. It is therefore useful in characterising thin films such as deposited oxide layers or self assembled monolayers. The typical experimental arrangement employed is illustrated in **Figure 2.24**. In a PM-RAIRS experiment, the IR beam is double modulated. The intensity modulation is provided by the moving mirror within a FTIR spectrometer and contributes to the background spectrum in the same way as in conventional RAIRS. They key to the advantages of PM-RAIRS lies in the modulation of the polarization vector of the IR beam between *p* and *s*. The polarization modulation is achieved by using a photoelastic modulator (PEM) containing a transparent crystal of a birefringent material such as ZnSe [13]. The light is initially linearly polarized at 45° to the crystal. A piezoelastic transducer is used to induce an oscillating stress on the crystal which results in birefringence as illustrated in **Figure 2.25** The linear polarizations E_y and E_x travel through the crystal at different velocities, with E_y travelling faster when the crystal is stretched and E_x travelling faster when the crystal is compressed. By using the modulation condition of half-wavelength, $R=\pm\lambda/2$ the polarization can be made to oscillate between linear polarizations +45° and -45°. If the beam is directed onto the reflecting sample at close to grazing incidence, this effectively results in an oscillation between *s* and *p* polarization with respect to the surface. As in conventional RAIRS, only the *p* polarization interacts with adsorbed molecules. The *p* component therefore contains contributions from both the background and sample whilst the *s* component only contains those from the background.

After reflection from the sample surface, the beam is focussed using a lens onto a dual channel detector [14]. The first channel removes the polarization modulation and calculates an interferogram from the resulting signal. Performing a fourier transform of this yields the background spectrum $R=R_p+R_s$, where R_p and R_s are the reflectances of the *p* and *s* polarized light respectively. The second channel is locked onto the frequency of the PEM such that the signal is collected at the half-

wavelength retardation condition of $R=\pm\lambda/2$ corresponding to the two linear polarizations. The signal whilst the light is circularly or elliptically polarized is therefore discarded. The collected signal consists of the differential reflectance of light by the adsorbed sample, $\Delta R=R_p-R_s$. The PM-RAIRS differential reflectance spectrum is then calculated as the ratio $\Delta R/R$.

It is important to recognise a caveat that results from the PEM being an achromatic polarizer. As such the polarization modulation is most efficient for a particular frequency which must be chosen to be within the frequency range being investigated. The resulting efficiency curve essentially modulates the differential reflectance spectrum in a way that can be described by a second order Bessel function, J_2. The differential reflectance spectrum is therefore given by [15]:

$$\frac{\Delta R}{R}=\frac{J_2(\phi_0)(R_p-R_s)}{(R_p+R_s)}. \qquad \textbf{Equation 2.12}$$

The form of J_2 results in a sinusoidal variation in modulation efficiency that decays as $1/\sqrt{\phi_0}$ where ϕ_0 is the maximum retardance in radians induced by the PEM. The use of PM-RAIRS in characterizing adsorbed monolayers on metallic substrates has been described in detail [16] and an example of the form of raw spectra obtained is shown in **Figure 2.26**.

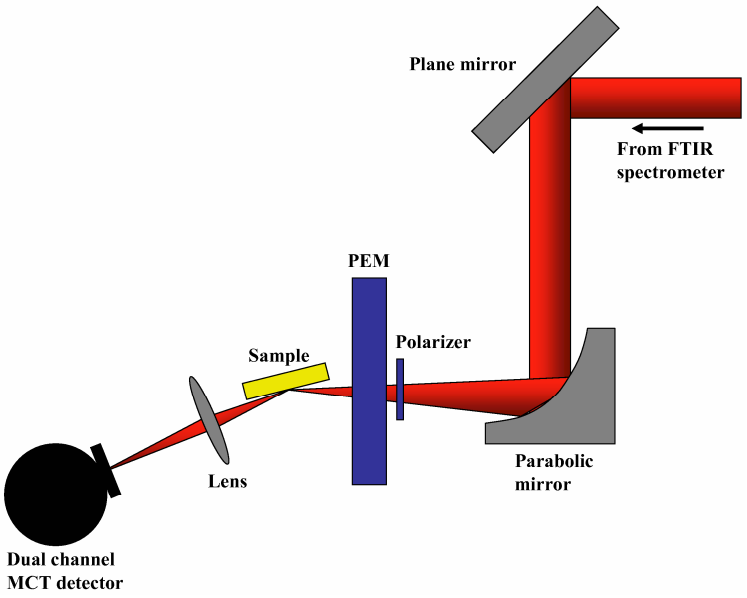

Figure 2.24: Schematic of the arrangement for PM-RAIRS experiments.

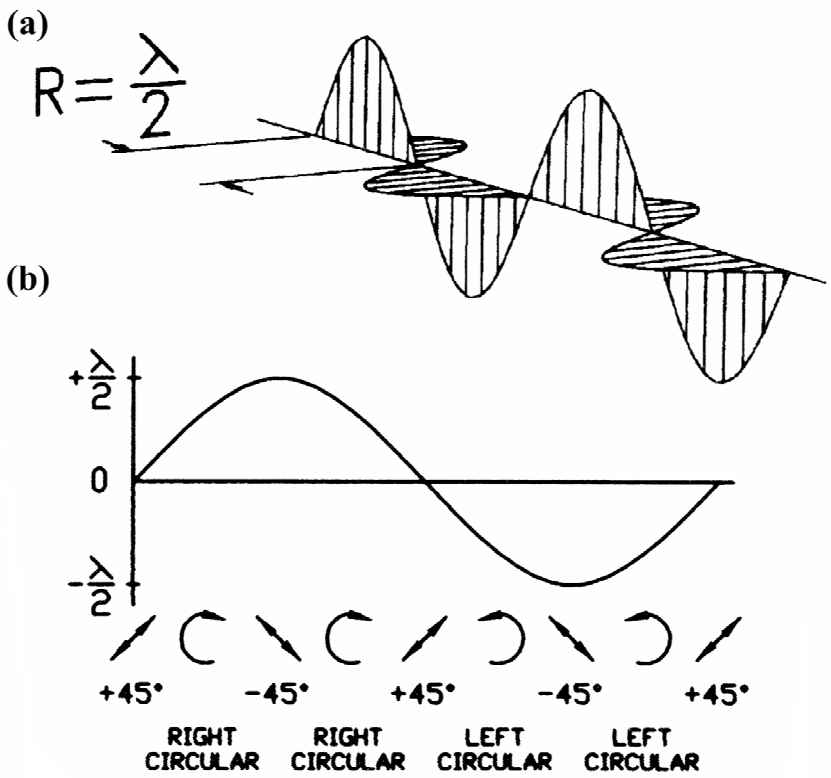

Figure 2.25: (a) half-wavelength retardation condition results in the polarization modulation shown in (b). From [13].

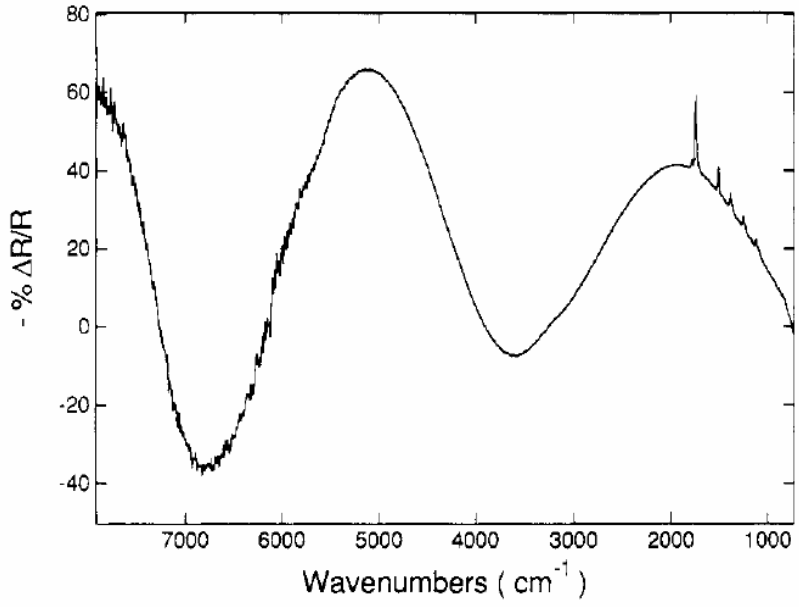

Figure 2.26: Example of a differential reflectance spectrum obtained with the PM-RAIRS technique. The effect of the modulation efficiency can be clearly seen in the oscillatory background. From [16].

2.5 References

[1] K. W. Kolasinski, *Surface Science: Foundations of Catalysis and Nanoscience*, 1st ed., Wiley, Chichester, 2002.

[2] D. J. Oakes, Ph.D. Thesis, University of East Anglia, Norwich, 1994

[3] S. Turton and R. G. Jones, *Surf. Sci.*, 1997, **377-379**, 719.

[4] R. G. Jones and C. J. Fisher, *Surf. Sci.*, 1999, **424**, 127.

[5] K. Nishizawa, K. Narisada, and N. Shinagawa, *Mass Spectr.*, 1969, **17**, 854.

[6] D. A. King, *Surf. Sci.*, 1975, **47**, 384.

[7] D. P. Woodruff and T. A. Delchar, *Modern Techniques of Surface Science*, 2nd ed., Cambridge University Press, Cambridge, 1994, p. 358.

[8] A. M. de Jong and J. W. Niemantsverdriet, *Surf. Sci.*, 1990, **233**, 355.

[9] P. A. Redhead, *Vacuum*, 1962, **12**, 203.

[10] D. P. Woodruff and T. A. Delchar, *Modern Techniques of Surface Science*, 2nd ed., Cambridge University Press, Cambridge, 1994, p. 532.

[11] R. G. Greenler, *J. Chem. Phys.*, 1966, **44**, 310.

[12] W. G. Golden, D. D. Saperstein, M. W. Severson, and J. Overend, *J. Phys. Chem.*, 1984, **88**, 574.

[13] Hinds Instruments PEM-90 Photoelastic Modulator Systems User Manual, 1998

[14] M. J. Green, B. J. Barner, and R. M. Corn, *Rev. Sci. Instrum.*, 1991, **62**, 1426.

[15] K. W. Hipps and G. A. Crosby, *J. Phys. Chem.*, 1979, **83**, 555.

[16] B. J. Barner, M. J. Green, E. I. Saez, and R. M. Corn, *Anal. Chem.*, 1991, **63**, 55.

CHAPTER 3 - Static Studies of C_6H_6 Adsorption on Amorphous SiO_2 and ASW

3.1 Introduction

This chapter describes experimental studies of the adsorption of C_6H_6 on both an amorphous SiO_2 substrate, and on a pre-adsorbed non-porous amorphous solid water (ASW) film. Temperature Programmed Desorption (TPD) experiments and Reflection-Absorption Infrared Spectroscopy (RAIRS) experiments conducted on these systems will be described.

3.2 TPD of C_6H_6 adsorbed on stainless steel

3.2.1 Introduction

In order to properly assess the impact of the use of a more realistic grain mimic on the adsorption of molecular species, a series of initial experiments were conducted on an uncoated, polished stainless steel disc. Such discs were used as the support for the amorphous SiO_2 thin films subsequently used as grain mimics in UHV chamber 1. The experimental procedures employed will be described, followed by a qualitative discussion of the results. The quantitative analysis techniques will then be described in detail, as they will be important in subsequent sections.

3.2.2 Experimental procedure

The stainless steel discs used in these experiments were first lapped to produce a flat surface. They were subsequently polished by hand using successively finer grades of diamond paste (Kemet), down to a minimum particle size of 1 μm. Such a procedure should lead to a flatness of the order of λ/2 for wavelengths in the mid-IR region. The substrate was then attached to the sample mount used in UHV chamber 1. Following bakeout the UHV chamber was brought to the usual operating base pressure of $<2\times10^{-10}$ torr. Prior to experiments being conducted the substrate was heated to 500°C and held at this temperature for 15 minutes for cleaning purposes. Cleaning cycles of ion sputtering and high temperature annealing, as employed with single crystal substrates, were not used in these

experiments. The aim was to provide a set of TPD results for a relatively flat surface, in order to allow comparison with those obtained for the SiO_2 film. Differences are likely to arise as a result of the gross morphology of the film, and thus extensive sample cleaning was deemed unnecessary. It should be noted that following the first few TPD experiments the stainless steel surface would be covered to some extent with a layer of carbon contamination resulting from the decomposition of C_6H_6 during heating. Given the cleaning procedure employed, it is therefore likely that the TPD results presented here reflect the desorption of C_6H_6 from a reasonably flat, ultra-thin mixed Cr_2O_3 / graphite film. Several experiments were conducted prior to collecting the data presented here, to ensure that the effect of increasing carbon coverage over the steel surface on an experiment to experiment basis was significantly reduced.

Following cleaning, the substrate was cooled to a base temperature of 116 K and C_6H_6 deposited using background dosing. In order to reduce the effect of minor variations in sample position from experiment to experiment, the substrate was positioned in line-of-sight position, approximately 4 mm from the opening of the tube to the QMS differential chamber. This position was maintained for both dosing and TPD acquisition for these experiments. The substrate heating rate for these experiments deviated significantly from linearity as a result of using an alternative power supply (Powerline Electronics Lab 710D). The resulting impact of this on peak shape and position were taken account of during the analysis. The initial heating rate was *ca.* 0.15 K s^{-1}, dropping to around 0.05 K s^{-1} towards the termination of heating at 160 K. The average heating rate during the C_6H_6 desorption was therefore comparable with the 0.1 K s^{-1} rate used in subsequent experiments utilizing the power supply described in **Chapter 2**.

3.2.3 Results and discussion

Figure 3.1 shows TPD traces for the lowest C_6H_6 exposures. The TPD displays a single asymmetric peak that is centred at 141 K for the lowest exposure of 0.1 L. This peak will be referred to as Peak A. As the exposure is increased Peak A grows in intensity with the peak gradually shifting to lower temperature. This peak can be assigned to the desorption of submonolayer quantities of C_6H_6 from

the underlying substrate. The shoulder visible on the high temperature side of Peak A at an exposure of 0.7 L can be attributed to desorption from a second layer of C_6H_6. At this exposure, Peak A has saturated, indicating the formation of a complete monolayer of C_6H_6 on the substrate. Therefore, an exposure of 0.6±0.05 L results in the formation of 1 ML on this surface under these experimental conditions. The desorption trace for an exposure of 0.9 L displays significantly different behaviour, as shown in **Figure 3.2**. The desorption is dominated by a peak centred at around 140 K with a shoulder at 130 K. This peak can be attributed to desorption from multilayers of C_6H_6. This peak continues to grow as the exposure is further increased, indicating the formation of layers of C_6H_6 ice. This behaviour continues for thicker layers of C_6H_6, with the traces sharing a common leading edge for exposures above 5 L as shown in **Figure 3.3** and **Figure 3.4**.

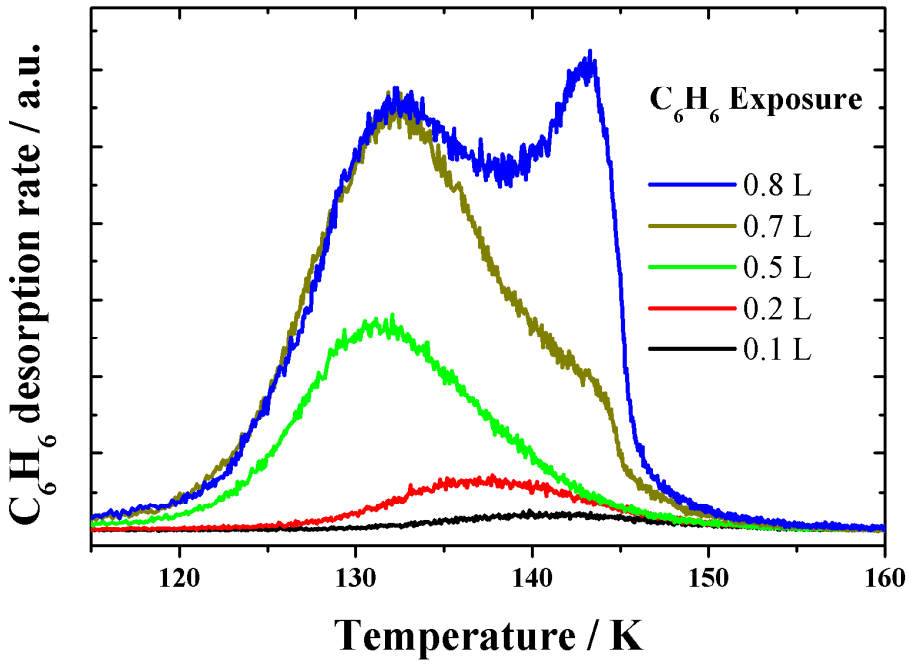

Figure 3.1: TPD traces for the desorption of submonolayer quantities of C_6H_6 from stainless steel.

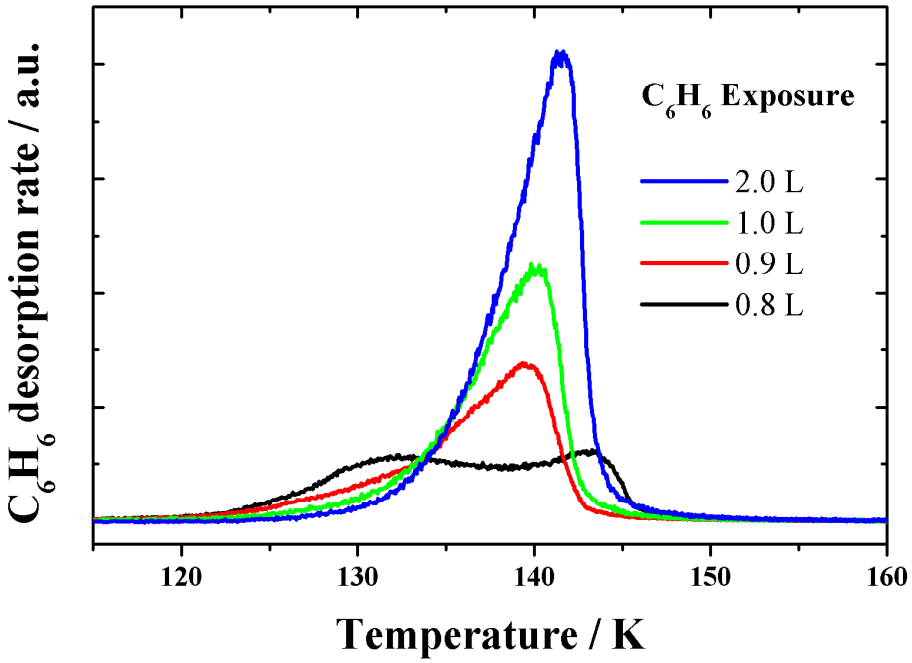

Figure 3.2: TPD traces for the desorption of C_6H_6 showing the transition from sub-monolayer to multilayer behaviour.

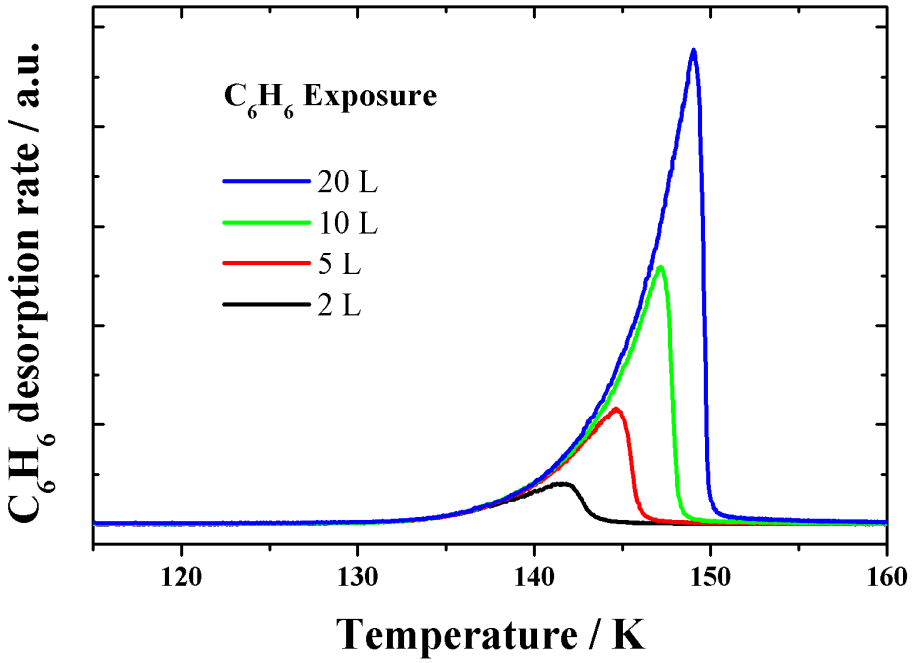

Figure 3.3: TPD traces for the desorption of thin multilayer C_6H_6 films on stainless steel.

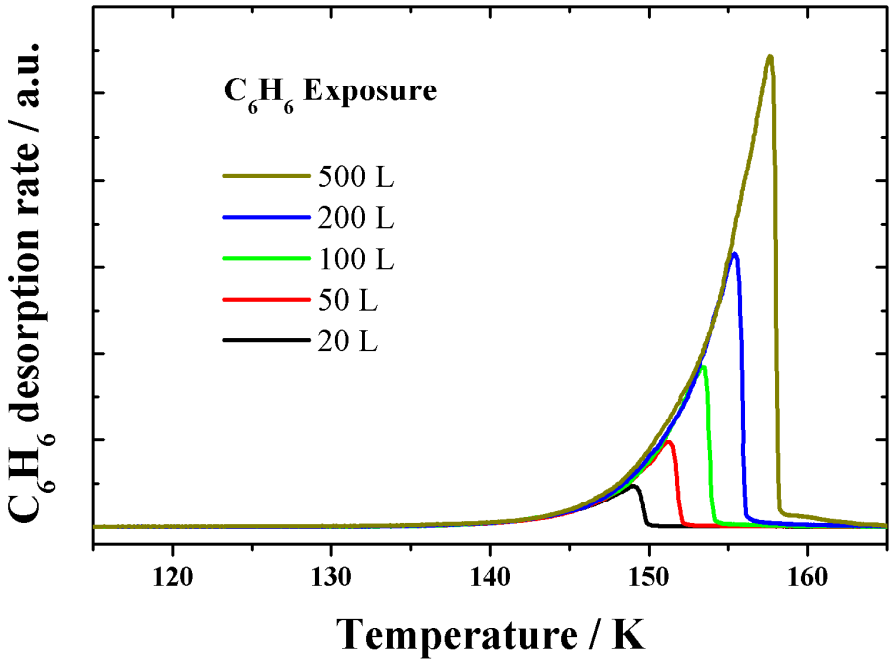

Figure 3.4: TPD traces for the desorption of thick multilayer C_6H_6 films on stainless steel.

The high temperature tail in the submonolayer desorption traces in **Figure 3.1** can be attributed to the desorption of C_6H_6 from high energy binding sites on the stainless steel surface. This is analogous to the situation on single crystal surfaces, where high temperature desorption features are frequently observed as a result of adsorption at defects such as kinks and steps. On the uncleaned surface used in these experiments defects will be more pronounced, particularly as the surface is not atomically flat which will result in an enhanced defect feature. Adsorbed carbon structures will also provide a further range of adsorption sites, leading to the observed broad tail. The shift in the desorption peak maximum to lower temperatures reflects the filling of binding sites with successively lower binding energy. It is reasonable to assume, as the adsorption temperature is close to the onset of desorption, that such sequential filling of sites occurs during adsorption. At lower temperatures adsorbing molecules will not have sufficient energy to diffuse across the surface and locate the most favourable site. Adsorption would then be essentially random. The TPD observed would then reflect the competition between diffusion and desorption. As the coverage is increased further, Peak A is observed to shift more dramatically to lower temperature, retaining the tail. This

can be attributed to an increase in intermolecular repulsion between adsorbed benzene molecules. This effect has been observed on metal surfaces such as Ag(111) [1] and Pd(111) [2]. It has been demonstrated that on graphite, for small exposures, the C_6H_6 molecules are adsorbed such that the molecular plane is parallel to the graphite basal plane [3], maximising the interaction overlap between the π-system C_6H_6 molecules and the graphite surface. As the coverage increases, intermolecular forces tend to dominate, as a result of a reduction in the average intermolecular distance, weakening the interaction with the surface. Ultimately, intermolecular repulsion causes the molecules to tend towards being orientated with the molecular plane perpendicular to the surface [4]. This results in a decrease in adsorption energy, shifting the desorption trace to lower temperature.

It is desirable to determine the desorption kinetics for the desorption traces described here. This will provide a basis for quantitative comparison when the desorption from an amorphous SiO_2 surface is considered. Initially, the kinetics for desorption from the films corresponding to the highest exposure, corresponding to films of bulk C_6H_6 ice will be considered. It is clear from the experimental traces that the desorption obeys zero order desorption kinetics. Desorption energies can be determined by transforming the Polanyi-Wigner equation to the following expression [5]:

$$\ln\left[\frac{r_{\mathrm{des}}}{\theta^n}\right] = \ln \nu_n + \frac{E_{\mathrm{des}}}{RT} \qquad \textbf{Equation 3.1}$$

where r_{des} is the desorption rate, θ is the coverage, n is the desorption order, ν_{n} is the pre-exponential factor and E_{des} is the desorption energy. It is possible to use relative coverages θ_{rel}, and recognising that the recorded trace, I, is proportional to desorption rate allows this expression to be used with the the constants of proportionality combined into the quantity A:

$$\ln\left[\frac{I}{\theta_{\mathrm{rel}}{}^n}\right] = \ln A\nu_n + \frac{E_{\mathrm{des}}}{RT}. \qquad \textbf{Equation 3.2}$$

The resulting Arrhenius plot with, in this case, n=0 for zero order desorption, will yield a straight line in the leading edge region, the gradient of which yields E_{des}. It should be noted that the use of relative coverages and desorption rates precludes the direct determination of ν from the intercept of this line. **Figure 3.5** shows the best fit lines obtained from the Arrhenius plots for exposures of 500, 200 and 100 L. Similar plots were obtained for all multilayer exposures. The resulting E_{des} values are presented in **Table 3.1**. The errors associated with the values of E_{des} obtained with this method are taken as 2 standard deviations. These values suggest a value of 50±3 kJ mol^{-1}, which is in good agreement with previous studies of the desorption of C_6H_6 multilayers [6].

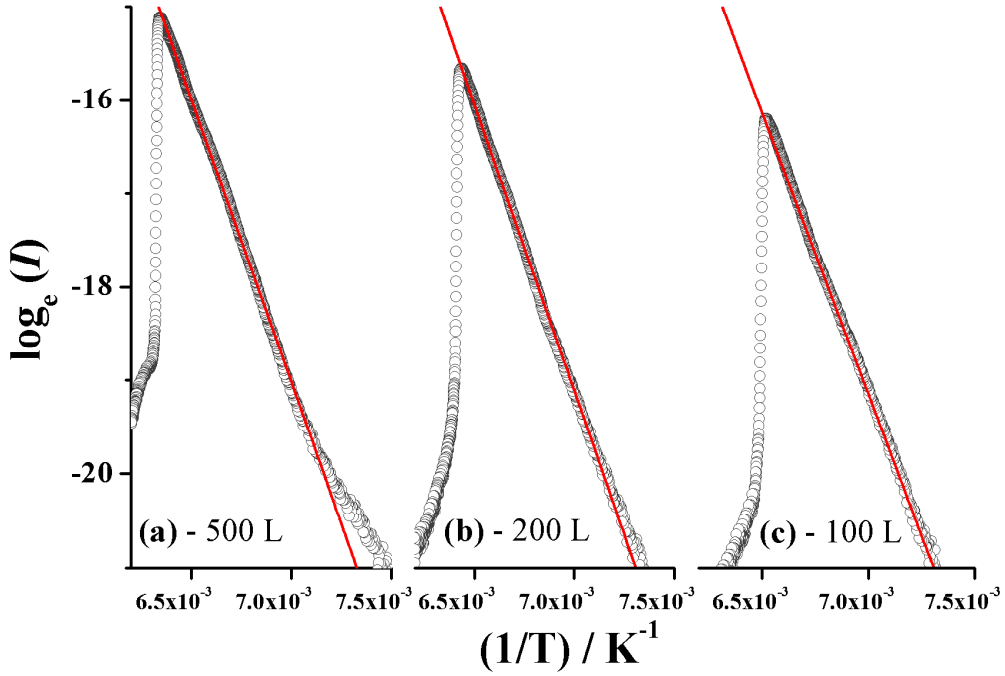

Figure 3.5: Arrhenius plots for the desorption of (a) 500, (b) 200 and (c) 100 L of C_6H_6 from stainless steel. The abscissa is reciprocal temperature in units of K^{-1}.

In order to obtain the pre-exponential factor it is possible to utilize the same approach by transforming the experimental TPD trace into a plot of absolute desorption rate in molecules cm^{-2} s^{-1}. The pre-exponential factor, ν, could then be obtained from the intercept of a best fit line to the appropriate Arrhenius plot. However, in this work a kinetic modelling approach was used. This allows direct comparison of simulated TPD traces with those obtained experimentally.

C_6H_6 Exposure / L	E_{des} / kJ mol^{-1}
2	53.0±3
5	50.1±3
10	47.9±3
20	49.0±3
50	51.0±3
100	50.0±3
200	51.0±3
500	51.0±3

Table 3.1: Desorption energies obtained from Arrhenius plots for the desorption of multilayers of C_6H_6 from stainless steel.

This allows both E_{des} and v to be varied systematically, using the value of E_{des} obtained from the Arrhenius analysis as a starting point. Such an approach can be useful in highlighting deviations from simple kinetics, providing further insight into the adsorption and desorption processes.

Kinetic modelling was performed using the *Chemical Kinetics Simulator* (*CKS*) software package developed by IBM Almaden Research Center [7]. The application of this software to the analysis of TPD analysis has been discussed in detail elsewhere [8]. The package allows the construction of a reaction mechanism based on a series of steps, each with associated Arrhenius parameters. The computational approach employs a stochastic method, rather than integrating the relevant rate equations. The method uses a fixed number of particles, representing in this case chemical species which are distributed amongst the reactants, intermediates and products defined in the reaction mechanism. A time step, Δt, is defined, and the instantaneous rate of any particular step in the mechanism taken to be proportional to the probability of that step proceeding during Δt. As the reaction proceeds, steps are selected randomly, and proceed according to their weighted probabilities. The resulting changes in populations of the different species are then carried forward to the next time step. The *CKS* package incorporates the ability to incorporate the effects of temperature variations, which makes it ideal for the study of TPD experiments.

In order to study the multilayer desorption kinetics of C_6H_6 adsorbed on stainless steel, a simple reaction mechanism containing two steps was used:

$$C_6H_6(\text{ads}) \rightarrow C_6H_6(\text{g}) \qquad \textbf{Equation 3.3}$$

$$C_6H_6(\text{g}) \rightarrow C_6H_6(\text{pumped}). \qquad \textbf{Equation 3.4}$$

In this scheme (ads) and (g) indicate adsorbed and gas phase C_6H_6 respectively, with (pumped) indicating C_6H_6 that has been removed from the UHV chamber by pumping. Each of the steps has an associated Arrhenius type reaction rate, each with a single reactant having a concentration N :

$$r = \nu_n N^n \exp\left(-\frac{E_a}{RT}\right) \qquad \textbf{Equation 3.5}$$

where v is the pre-exponential factor, n is the order of the reaction and E_a is the activation barrier. The form of this for the desorption step essentially represents the Polanyi-Wigner equation with E_a representing the desorption energy E_{des}.

In order to run the kinetic simulations, it is necessary to input the starting concentrations, which requires conversion of the experimental doses into molecular surface concentrations. As the C_6H_6 was dosed by backfilling the chamber to a certain pressure for a period of time, the resulting surface concentration was calculated using the collision theory of gases [9]. The collision frequency, Z_w, in molecules m^{-2} s^{-2} between gas phase molecules and a surface of unit area at a pressure, P, is given by:

$$Z_w = \frac{P}{\sqrt{2\pi m k_B T}} \qquad \textbf{Equation 3.6}$$

where m is the molecular mass of the colliding molecules and T is their temperature. In this case T can be assumed to be *ca.* 298 K as the molecules were dosed from thermal reservoirs. The assumption was also made that the sticking coefficient for C_6H_6 at the surface temperature during adsorption was unity at all exposures. **Figure 3.6** shows plot of TPD yield, *i.e.* integrated peak area with time as the abscissa, *versus* exposure in Langmuir. This demonstrates a near linear behaviour with a no apparent change in uptake rate as exposure is increased, indicating a uniform sticking probability. It is reasonable to assume a sticking coefficient of unity at the highest exposure, and so this was taken to be applicable to all exposures.

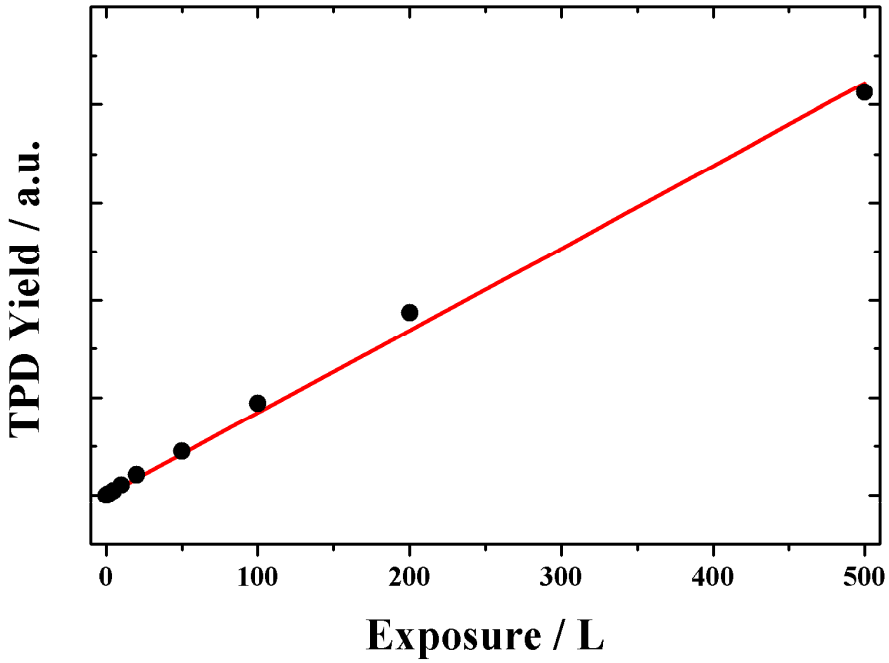

Figure 3.6: Plot of TPD yield *versus* exposure in Langmuir for the adsorption of C_6H_6 on stainless steel (black circles). Also shown is a least squares linear fit (red line).

Though the mass spectrometer was used to monitor C_6H_6 during dosing, its position within a differentially pumped chamber means that it does not sample the same background environment as the substrate. A further correction needs to be made for the sensitivity of the ion gauge to the species being dosed. This is related to the ionization cross-section of the species, with a larger cross-section leading to a greater sensitivity. Sensitivities are quoted relative to that for N_2. In the case of C_6H_6 a value of 6.0 was used in accordance with previous studies [10]. Using this procedure, a surface concentration of 1.92×10^{16} molecules cm^{-2} was obtained for an exposure of 500 L. In order to correct for smaller doses not being exactly the quoted value in L, the concentration was calculated by comparison of TPD yields with that of the 500 L TPD.

The saturation of desorption from the monolayer, and appearance of multilayer growth occurring at an exposure of 0.7 L corresponds to a surface concentration of 2.1×10^{13} molecules cm^{-2}. This is somewhat lower than that observed for the formation of a compact monolayer of C_6H_6 on Cu(111), where C_6H_6 has been shown to lie plane parallel with the surface [11]. This suggests the formation of

islands on the stainless steel surface. This is in agreement with the observed fractional order desorption for the first few multilayers as indicated by non-coincidence of leading edges. The appearance of multilayer desorption at higher temperature than monolayer desorption indicates that the C_6H_6-C_6H_6 interaction is stronger than the C_6H_6-surface interaction, suggesting that island formation would be thermodynamically favourable.

The order for the desorption step was set to zero, as indicated by the coincidence of leading edges in the original data and the order for the pumping step was taken to be one. The desorption energy, E_{des}, was initially set to 50 kJ mol^{-1} as suggested by the Arrhenius plots presented previously. It should be noted that the experimental heating curve, $T(t)$ was used, rather than defining a linear function to properly account for the non-linearity of the heating in these experiments. The pre-exponential for the desorption step was then varied in order to best reproduce the leading edge shape of the corresponding experimental trace. Small adjustments to the desorption energy were required to ensure that the peak remained at the correct temperature. The trailing edge was best fit using a pre-exponential factor for the pumping step of 0.1 s^{-1}. The resulting simulations are compared to the experimental TPD traces in **Figure 3.7**. At lower multilayer coverages the agreement between the simulations and the experimental trailing edge gradually becomes less good. This likely reflects the transition from zero order to fractional order desorption.

For smaller exposures there was a marked difference between zero order simulations and experimental traces. In order to obtain kinetic parameters it was necessary to also vary the desorption order to obtain the best agreement between the simulation and the experimental trailing edges. The fractional order simulations are shown in **Figure 3.8** and the kinetic parameters derived from this analysis are summarized in **Table 3.2**. Error estimates of two standard deviations are calculated. In all cases the desorption energies agree within experimental error, demonstrating the dominance of C_6H_6 interactions, which confirms that these exposures are in the multilayer regime. The desorption energy obtained for the multilayers is slightly lower than that obtained from the leading edge analysis, which likely represents the effect of a non-linear heating rate on the latter.

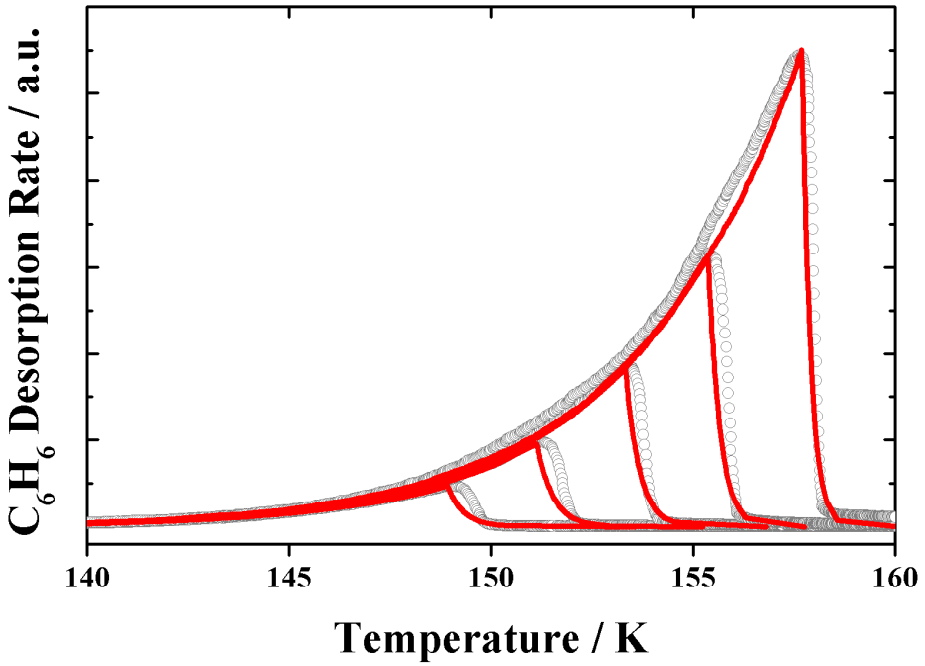

Figure 3.7: Experimental (open circles) and simulated (red lines) TPD traces for the desorption of 20, 50, 100, 200 and 500 L of C_6H_6 from stainless steel.

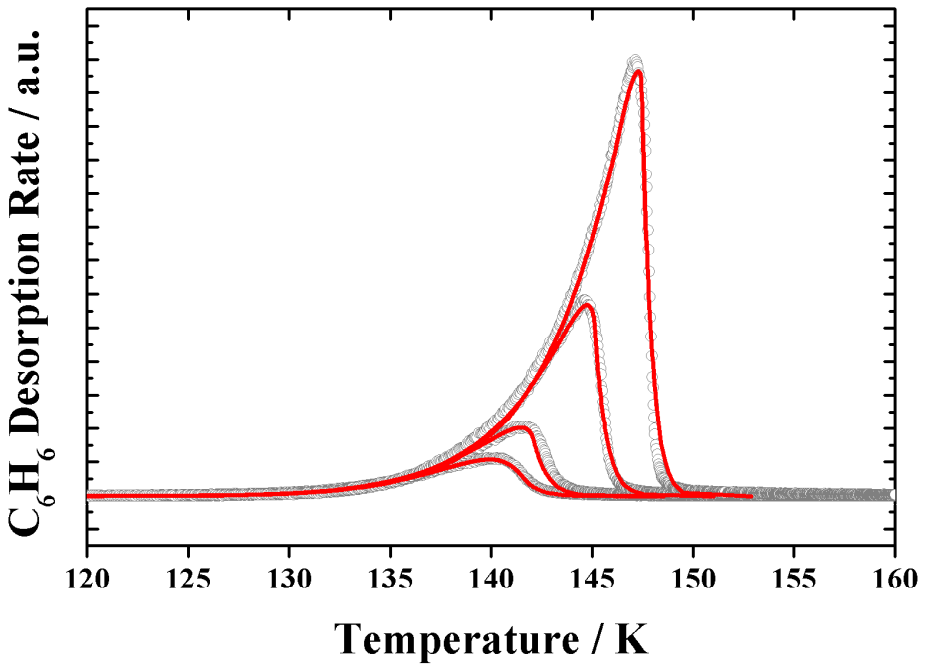

Figure 3.8: Experimental (open circles) and simulated (red lines) TPD traces for the desorption of 1, 2, 5 and 10 L of C_6H_6 from stainless steel.

As such, the values obtained using the kinetic modelling approach incorporating the experimental heating curves are more reliable.

The sub-monolayer TPD traces suggest more complicated desorption kinetics that depend both on a distribution of binding sites on the substrate, and increasing intermolecular repulsion as coverage is increased towards monolayer saturation. A detailed kinetic analysis was not conducted, though the general form of the TPD traces will be used for comparison with those obtained for the desorption of C_6H_6 from the amorphous SiO_2.

Exposure / L	**Desorption Order *n***	**Surface Concentration / molecules cm^{-2}**	***v* / molecules cm^{-2} s^{-1}**	**E_{des} / kJ mol^{-1}**
500	0	1.9×10^{16}	$10^{30.1\pm0.6}$	48.0±1
200	0	8.8×10^{15}	$10^{30.1\pm0.6}$	48.0±1
100	0	4.5×10^{15}	$10^{30.5\pm0.6}$	49.2±1
50	0	2.1×10^{15}	$10^{30.5\pm0.6}$	49.3±1
20	0	9.0×10^{14}	$10^{29.9\pm0.6}$	47.8±1
10	0.1	5.2×10^{14}	$10^{28.4\pm0.6}$ *	47.9±1
5	0.2	2.2×10^{14}	$10^{27.4\pm0.6}$ *	48.0±1
2	0.3	7.4×10^{13}	$10^{26.0\pm0.6}$ *	48.3±1
1	0.5	4.4×10^{13}	$10^{23.3\pm10.6}$ *	48.3±1

Table 3.2: Kinetic parameters derived from kinetic modelling for the desorption of C_6H_6 multilayers from stainless steel. * For fractional order desorption, the general units of molecules$^{(1-n)}$ cm$^{2(n-1)}$ s^{-1} for *v* apply.

3.3 The amorphous SiO_2 substrate

3.3.1 Introduction

In order to study chemical and physical processes of relevance to the ISM, it is necessary to consider surfaces that provide a reasonable approximation to those in interstellar environments. For studies on H_2O ice surfaces it is possible to use simple polycrystalline metal substrates such as Au or Ag, upon which a thick layer of H_2O ice can be grown. However, it is important also to consider the interaction between molecules and bare grain surfaces, *i.e.* those not coated in multilayers of H_2O-dominated ices. As has been discussed, interstellar grains can typically be split into two classes; silicates and carbonaceous grains. There is no clear understanding of the nature of interstellar grains; in particular it is still not certain if the two populations only exist separately, or can coexist in a single grain. Therefore a fundamental approach must be taken to understand gas-grain interactions with a range of materials considering general trends. In this work the substrate was chosen to represent the silicate grain population. Earlier work utilizing thin films of silicate nanoparticles derived from laser ablation of ground meteoritic material demonstrated the impact of substrate choice on thermal desorption [12]. However, it is advantageous to consider a simpler, more reproducible substrate than one containing both morphological and chemical complexity. With this in mind, a simple substrate was developed based on thin films of amorphous SiO_2. This section describes the experimental procedures involved in producing this substrate, and the characterization techniques employed to understand the nature of the surface.

3.3.2 Growth of the SiO_2 film

The amorphous SiO_2 film was grown by electron beam evaporation of bulk fused silica (quartz). This procedure was carried out within a dedicated high vacuum system in the Microsystems Engineering Centre at Heriot-Watt University (See **Figure 3.9**). The films were grown on the stainless steel discs used in the experiments described in the previous section. These were mounted on a carousel above a graphite crucible containing small fused silica pellets (Testbourne >99.99% purity). A quartz crystal microbalance (QCM) was situated in view of

the source material to obtain an estimate of film thickness. Evaporation was achieved by irradiating the silica with 7 keV electrons which were deflected towards the centre of the crucible. The electron beam position could be adjusted by varying the current through the deflection coils. Whilst the deposition rate was set to around 20-30 Å s^{-1}, which was typically obtained with an electron current of <25 mA, the carousel was rotated so that the disc was out of line-of-sight to the source material. When the deposition rate was stable and the material was properly outgassed, the carousel was rotated such that the disc was in line-of-sight to the source material. The thickness monitor on the QCM was started and the carousel was rotated back to the initial position once the desired thickness had been reached. In most cases films of 150 – 200 nm thickness were grown. As the substrate was at ambient temperature during the deposition, the film is formed by ballistic deposition, which results in an amorphous film. Crystalline films could, in principle, be formed by heating the disc to several hundred °C in order to allow the solid to relax, resulting in a more energetically favourable polycrystalline morphology. The coated disc was removed from the evaporation chamber after allowing sufficient time for the source material and electron gun components to cool to ambient temperature.

Figure 3.9: High Vacuum Chamber used for growth of amorphous SiO_2 thin films using electron beam evaporation.

3.3.3 Characterization of the amorphous SiO_2 substrate by AFM

The morphology of the deposited films was studied using atomic force microscopy. This technique utilizes a small nanoscale tip that is mounted on the end of a cantilever. The tip is scanned across the surface by moving the sample relative to the tip, and the force between surface atoms and those in the tip cause the cantilever to be deflected. This deflection can be measured using a suitably positioned laser and array of photodiodes. In these experiments, a silicon nitride tip was used, and the microscope was operated in contact, constant force mode. In this mode, a constant deflection, and hence force is maintained by moving the sample in the *z*-direction as the *x* and *y* directions are scanned. The resulting plot of *z* as a function of *x* and *y* provides a topographical image of the sample. **Figure 3.10** shows a 100 × 100 μm AFM image of amorphous SiO_2 deposited to a thickness of *ca.* 100 nm as measured by the QCM. The lack of large scale features in this image indicates a uniform coverage across the surface. It is interesting to note the presence of polishing marks in the form of dark (lower height) lines in the image. As the finest grade diamond paste used in polishing was 1 μm this confirms that the film does indeed have a sub-micrometer thickness. **Figure 3.11** shows a series of 20 × 20 μm AFM images for three amorphous SiO_2 films deposited to thicknesses of *ca.* 200, 150 and 100 nm.

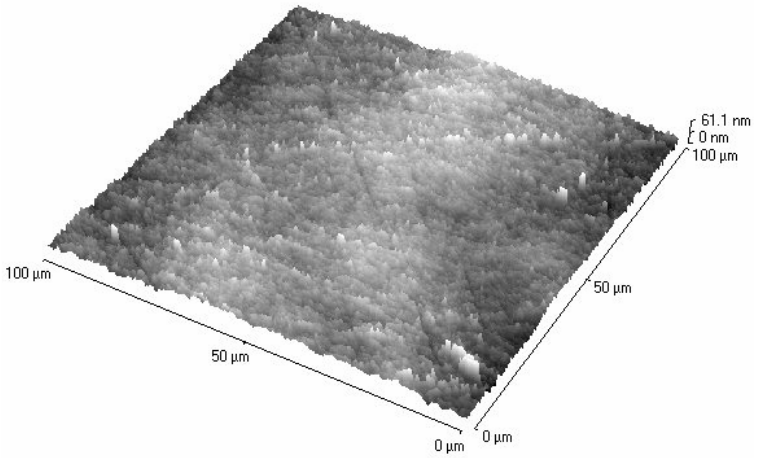

Figure 3.10: AFM image of amorphous SiO_2 deposited to a thickness of *ca.* 100 nm. The large features to the bottom right are attributed to noise. The apparent curve in the film is an experimental artefact.

The thicker samples display a higher degree of roughness which would be expected for the deposition of an amorphous film in which the molecules are immobile on the surface. The apparent increase in overall height in the thickness of the film is associated with a relatively small number of tall protrusions. This also appears to be the case with the 100 nm film. With this in mind, the average height variation increases with film thickness. In summary, thicker films appear to produce rougher films with a greater variation in height across the surface, which is likely to lead to a higher proportion of high energy binding sites in which molecules can adsorb.

The morphology of the SiO_2 film was compared to that of an interplanetary dust particle (IDP) (see **Figure 3.12**) which are thought to be have been processed relatively mildly during the formation of the solar system. As such they represent the most easily accessible source of material likely to posses a morphology similar to the interstellar grains from which the solar system formed. The structures observed in the AFM images bear some resemblance to those observed in the IDP. However, the gross morphology of the grain cannot be represented by a thin film. Nevertheless, the substrate developed for these experiments allows some understanding of the importance of the chemical nature (*i.e.* SiO_2) and amorphous structure of grain surfaces. It should also be noted that the ice films deposited on these grains are typically of the order of a few hundred monolayers thick, which corresponds to a maximum thickness of 50-100 nm.

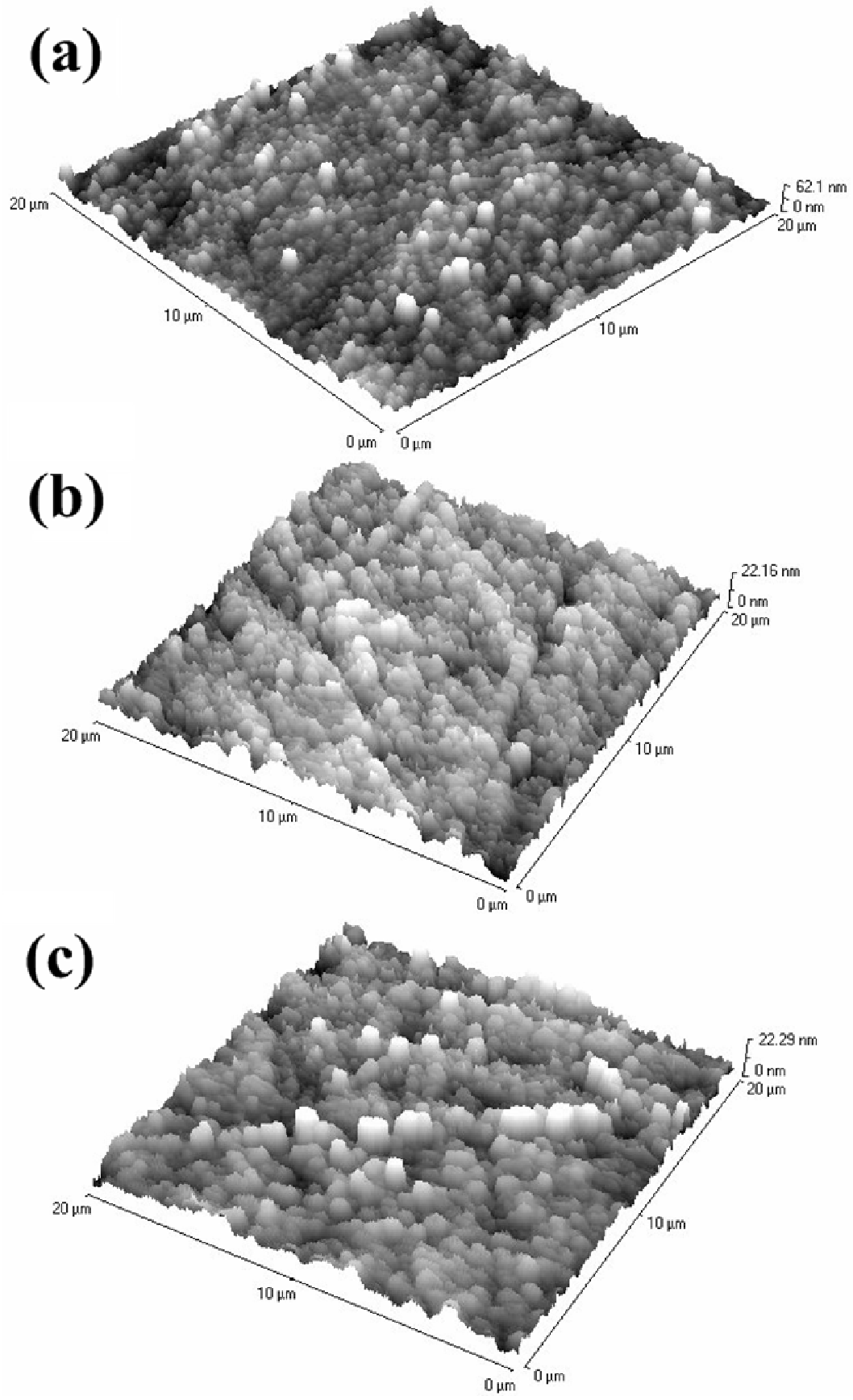

Figure 3.11: AFM images of (a) *ca.* 200 nm, (b) *ca.* 150 nm and (c) *ca.* 100 nm of amorphous SiO_2 as deposited by electron beam evaporation.

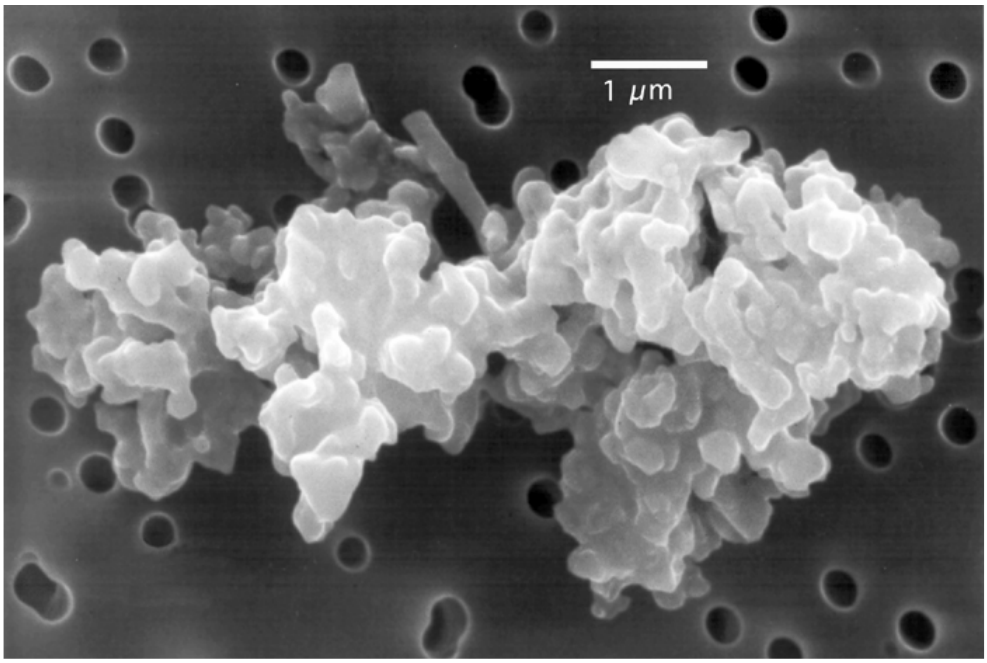

Figure 3.12: Scanning Electron Micrograph of an interplanetary dust particle [13].

3.3.4 Characterization of the amorphous SiO_2 substrate by PM-RAIRS

PM-RAIRS was used to confirm the presence of SiO_2 on the surface, and to indicate the presence of any surface bands that might show up in subsequent RAIRS experiments conducted under UHV. Whilst surface bands are normally removed when ratioing a scan to a background scan, the situation is more complex in the present case as the adsorbate/SiO_2/metal system contains three layers as opposed to the two in a simple adsorbate/metal system. The appearance of substrate bands as negative absorbance features in far-infrared RAIR spectra as a result of this has been observed in the case of $SnCl_4$ adsorbed on SnO_2, where a prominent feature was observed at 355 cm^{-1}[14]. Calculations showed that this feature is insensitive to the dielectric properties of the adsorbate, indicating that it was indeed due to the underlying SnO_2 substrate. It was also shown that depending on the dielectric properties of the substrate, the substrate bands could appear as positive or negative absorbance features. It was also apparent that such features are strongest when the IR beam is incident at a large angle to the surface normal. It is therefore anticipated that such substrate related bands might appear in the RAIR spectra of adsorbate on the amorphous SiO_2 film at the angle used in the experiments described in this thesis. **Figure 3.13** compares PM-RAIR spectra obtained for two thin films of amorphous SiO_2 deposited on a stainless steel

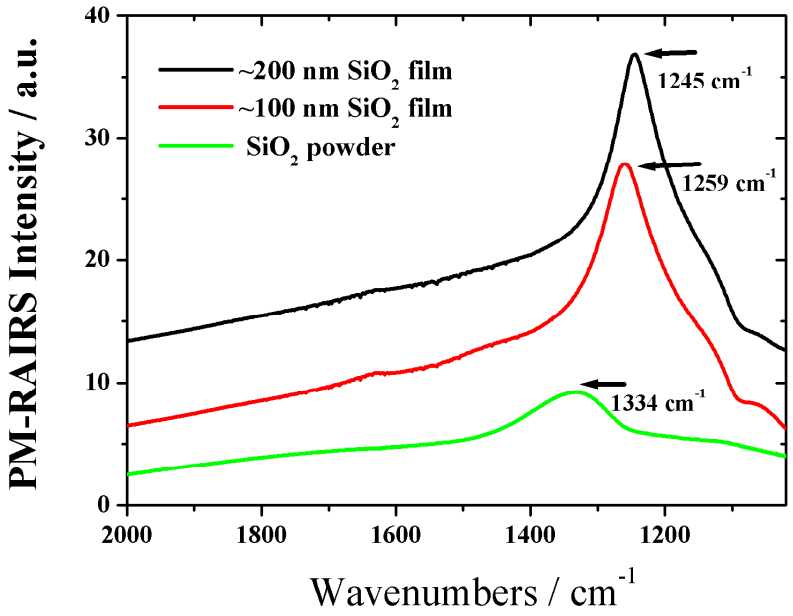

Figure 3.13: PM-RAIR spectra for two thin films of amorphous SiO_2 deposited on a stainless steel substrate compared to that obtained for a macroscopic film of finely divided SiO_2 powder electrostatically adhered to a stainless steel substrate.

substrate to thicknesses of *ca.* 200 nm and *ca.* 100 nm as estimated using the quartz crystal microbalance. These are compared to a thin film of finely divided SiO_2 powder that was allowed to adhere electrostatically to another stainless steel substrate. From these spectra it is clear that a very strong feature appears at around 1250 cm^{-1} which appears to shift to higher frequency with increasing film thickness. A weak shoulder around 1150 cm^{-1} is also visible. The powdered film also shows a similar feature, at significantly higher frequency. As the latter case represents an effective film thickness far greater than the two deposited films, this is in qualitative agreement with the observed shift to higher frequency with increasing thickness. However, it should be noted that the powder sample (a) is polycrystalline and (b) produces a granular film, both of which are likely to affect the spectrum obtained. However, for the purposes of comparison with subsequent spectra, these experiments provide a reference for assigning RAIR spectral features that might be of substrate origin.

The observed PM-RAIR features can be assigned to the longitudinal optical and transverse optical modes of SiO_2. The major vibration in SiO_2 occurs at around

1100 cm^{-1} and is attributed to the asymmetric Si-O-Si stretch. Transverse optical (TO) and longitudinal optical (LO) modes can be thought of as the onset and cutoff of an absorption band respectively. Usually the TO mode dominates the observed absorption band, though the LO band can also contribute, depending on the properties of the material, and the spectroscopic method employed. LO-TO splitting in SiO_2 was first observed by Galeener and Lucovsky [15] who suggested the presence of TO and LO bands at 1065 cm^{-1} and 1200 cm^{-1} respectively on the basis of Raman measurements. In normal incidence measurements, both TO and LO components are visible, but at close to grazing incidence the LO mode is expected to dominate. This can be interpreted in terms of the surface selection rule as TO modes are mainly associated with vibrations parallel to the surface whilst LO modes are associated with those perpendicular to the surface. Reflection IR experiments have identified two peaks at *ca.* 1130 cm^{-1} and 1260 cm^{-1} which were assigned to the TO and LO modes respectively [16].

This study demonstrated the increasing dominance of the LO mode as the angle of incidence of the incident beam is increased above 70° to the surface normal. Features attributed to the LO mode of SiO_2 have also been observed using RAIRS at 1256 cm^{-1} for a thermally grown oxide films [17,18]. An example spectrum from reference [18] for an IR beam incident at 60° is shown in **Figure 3.14**. The dominance of the LO feature in the present experiments can be attributed to the higher incidence angle used. This leads to the TO band being only visible as a weak shoulder at around 1150 cm^{-1}.

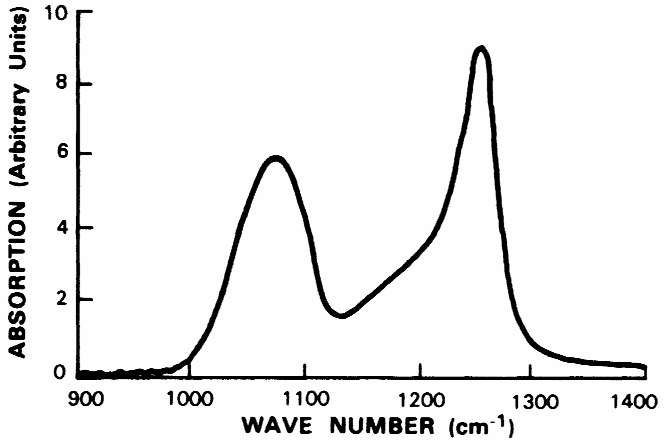

Figure 3.14: IR absorption spectrum for a thermally grown SiO_2 film on Si(111). The incident IR beam was at 60° to the surface normal. Both LO and TO components are visible at this angle. From [18].

3.4 TPD of C_6H_6 adsorbed on amorphous SiO_2

3.4.1 Introduction

This section describes a series of experiments conducted to study the thermal desorption of C_6H_6 from the amorphous SiO_2 substrate described previously. The experiments are described, along with a discussion of both multilayer desorption, which reflects the interaction between C_6H_6 molecules, and desorption from submonolayer coverages of C_6H_6 which are sensitive to the C_6H_6-SiO_2 interaction, and the morphology of the SiO_2 surface.

3.4.2 Experimental procedure

These experiments were conducted in essentially the same way as for the uncoated stainless steel substrates. The discs coated with amorphous SiO_2 were mounted in the UHV chamber and cleaned by heating to 200°C and maintaining this temperature for 15 minutes prior to conducting experiments. This lower temperature was used to avoid any thermal modifications being made to the SiO_2 that could cause variations in desorption behaviour. C_6H_6 layers were deposited by backfilling the chamber to a particular pressure and recorded in Langmuir. TPD experiments were performed using a linear heating ramp of 0.1±0.02 K s^{-1}. The substrate was again positioned close to the entrance to the QMS chamber throughout the experiments.

3.4.3 Results

Figure 3.15 and **Figure 3.16** show desorption traces for submonolayer coverages of C_6H_6 adsorbed on the amorphous SiO_2 substrate. Compared to the corresponding traces for C_6H_6 adsorbed on stainless steel, desorption extends to significantly higher temperatures. This indicates that the surface permits more efficient binding of C_6H_6. It is also clear that the submonolayer regime exists for higher exposures than observed with the stainless steel substrate. This reflects an increased surface area compared to the geometric surface area of the stainless steel disc resulting in an increase in the number of adsorbed molecules required to saturate the monolayer. The TPDs also suggest the presence of two distinct desorption regimes, with a somewhat sharper desorption component appearing as

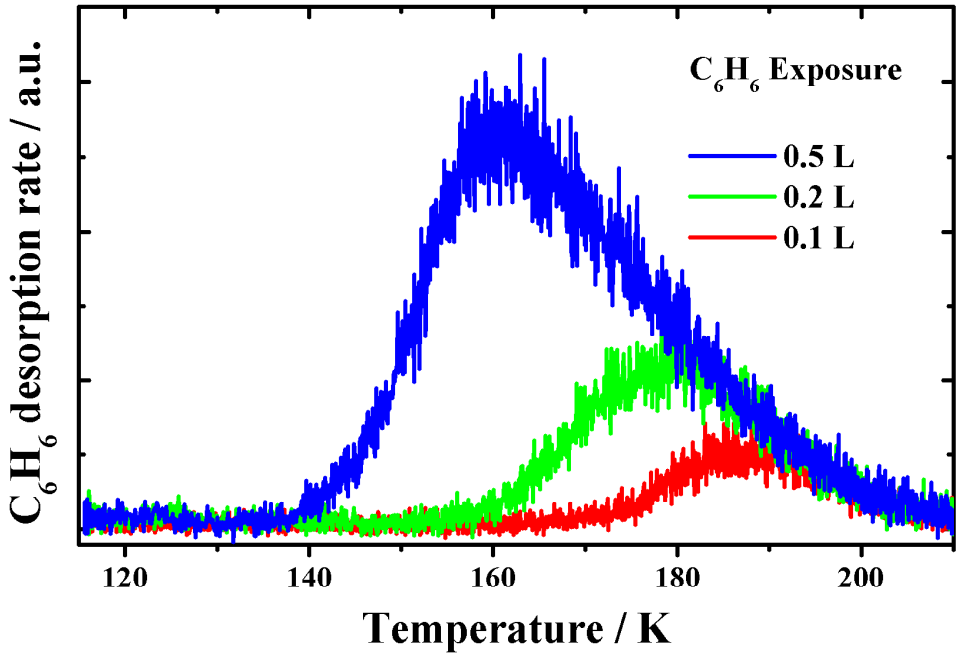

Figure 3.15: TPD traces for the desorption of the lowest submonolayer coverages of C_6H_6 from an amorphous SiO_2 substrate.

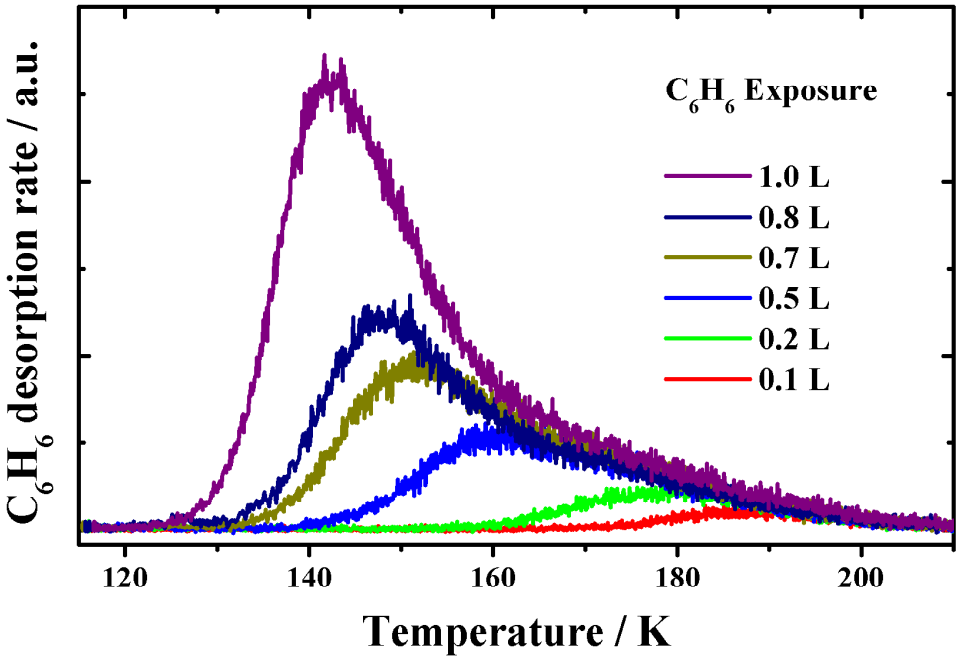

Figure 3.16: TPD traces for the desorption of all submonolayer coverages of C_6H_6 from the amorphous SiO_2 substrate showing two kinetic regimes.

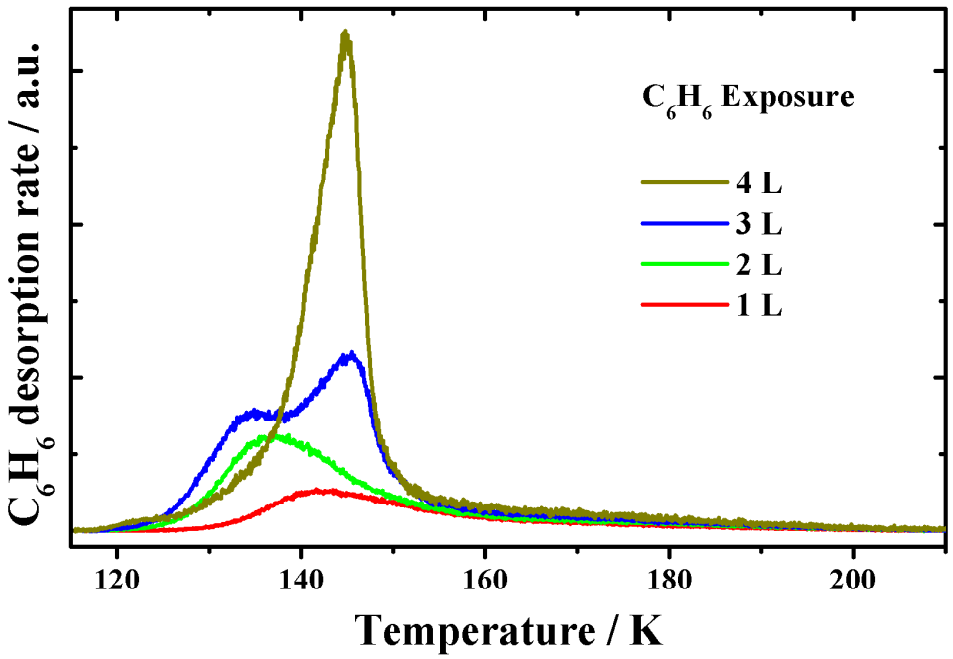

Figure 3.17: TPD traces for the showing the transition from submonolayer to multilayer desorption of C_6H_6 from the amorphous SiO_2 substrate.

the exposure is increased beyond 0.5 L. The appearance of multilayer growth occurs between 2 and 3 L as shown in **Figure 3.17**. This represents a 4-5 fold increase in the surface area available for adsorption when compared to the monolayer saturation value of *ca.* 0.65 L observed for C_6H_6 on stainless steel.

Beyond the submonolayer regime the desorption appears to be less strongly affected by the substrate morphology. Multilayer growth results initially in the appearance of a shoulder on the higher temperature side of the monolayer desorption feature. As the exposure is increased, this shifts to lower temperature, with the monolayer peak being reduced. This again suggests that monolayer desorption is rapidly blocked by the adsorption of subsequent layers. This indicates the formation of a second layer. Initially, multilayer desorption displays fractional order kinetics with non-coincident leading edges as shown in **Figure 3.18**. This behaviour is observed at higher exposures than on stainless steel. Although the formation of islands of C_6H_6 would result in fractional order kinetics, it is also reasonable that the inherent roughness of the surface results in sufficient deviation from bulk ice desorption kinetics. Ultimately substrate effects

appear to diminish completely for the desorption from thick layers shown in **Figure 3.19**, demonstrating zero order desorption kinetics with coincident leading edges. The desorption traces are very similar to those observed for the desorption of thick C_6H_6 films from stainless steel with the slight increase in desorption temperature being attributable to the increase in heating rate at high temperatures compared that for the stainless steel experiments where the heating rate dropped somewhat at these temperatures. In the next section the desorption kinetics for multilayer desorption will be obtained and compared to those for the desorption from stainless steel. The desorption of submonolayer coverages will be examined in detail in order to understand the effect of substrate morphology on the desorption kinetics.

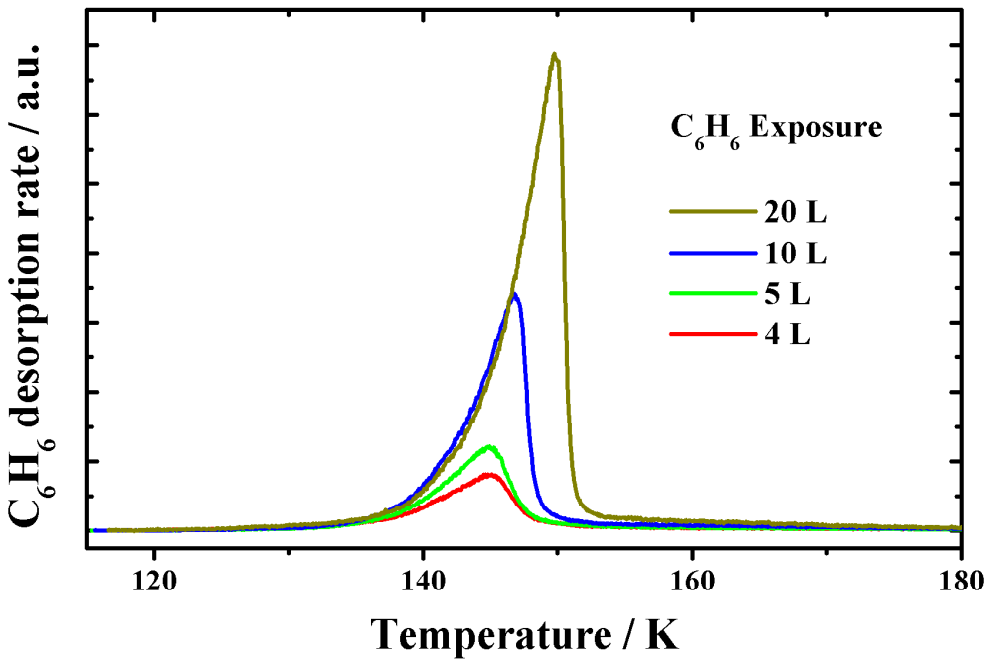

Figure 3.18: TPD traces for the desorption of thin multilayer films of C_6H_6 from the amorphous SiO_2 substrate.

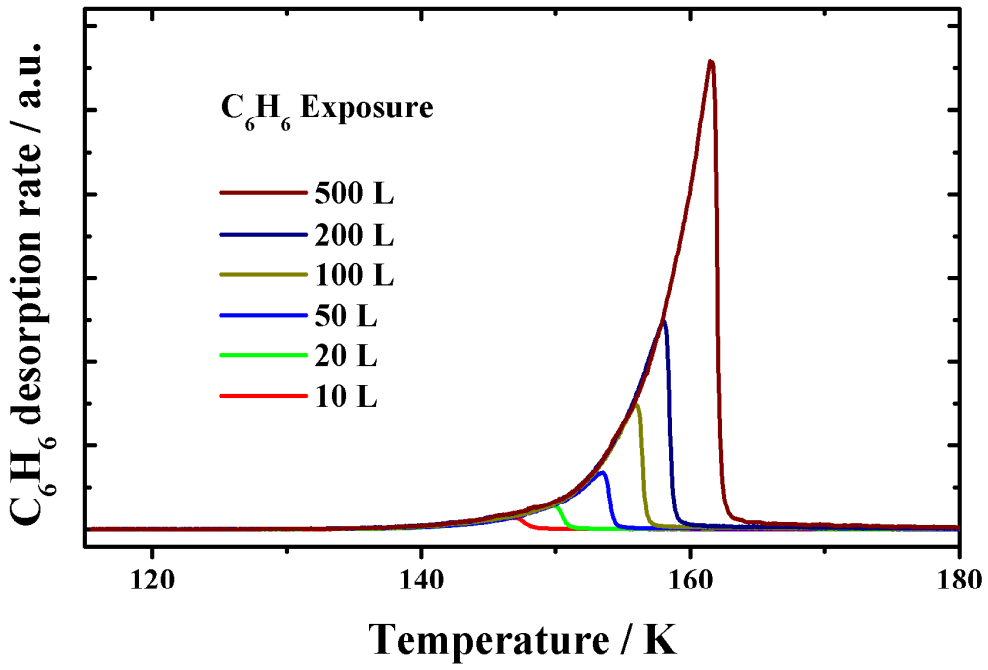

Figure 3.19: TPD traces for the desorption of thick multilayer films of C_6H_6 from the amorphous SiO_2 substrate.

3.4.4 Analysis and discussion

The TPD results for the desorption of multilayer films of C_6H_6 adsorbed on the amorphous SiO_2 substrate were analyzed using the same procedure as for the stainless steel substrate which was outlined in **Section 3.2.2.** In order to obtain an estimate for the multilayer desorption energy, leading edge analysis was again used. This procedure was carried out for all multilayer exposures down to 10 L, *i.e.* those that displayed typical zero order desorption characteristics. **Figure 3.20** shows the resulting Arrhenius plots for exposures of 500, 200 and 100 L and the desorption energy values obtained are summarized in **Table 3.3**. Errors are again calculated as two standard deviations.

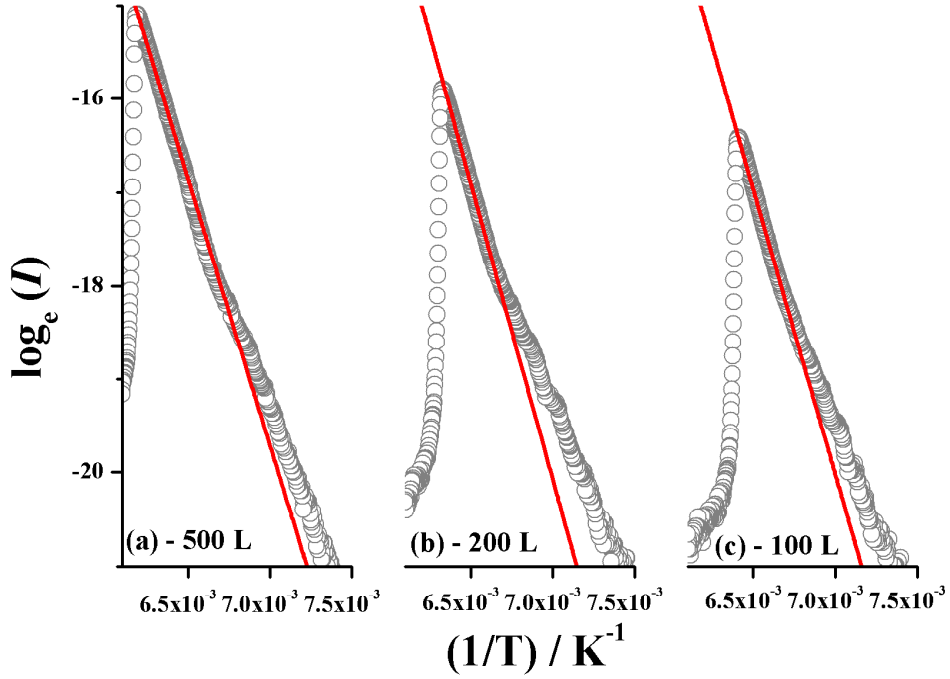

Figure 3.20: Arrhenius plots for the desorption of (a) 500, (b) 200 and (c) 100 L of C_6H_6 from amorphous SiO_2. The abscissa is reciprocal temperature in units of K^{-1}.

C_6H_6 Exposure / L	E_{des} / kJ mol^{-1}
10	47.6±4
20	46.5±4
50	47.3±4
100	50.7±4
200	52.6±4
500	47.6±4

Table 3.3: Desorption energies obtained from Arrhenius plots for the desorption of multilayers of C_6H_6 from amorphous SiO_2.

It is clear that the multilayer desorption energies agree within experimental error with those obtained using the stainless steel substrate. A value of 48.7±4 kJ mol^{-1} is therefore taken as being representative of the desorption of C_6H_6 from multilayer films where the underlying substrate is sufficiently buried that it has no appreciable effect on the desorption kinetics. The slightly higher value obtained for the 200 L exposure film most likely reflects the sensitivity of the leading edge analysis to small variations in the TPD peak shape that arise as a result of experimental issues such as heating rate variations. There is no reason to expect significant differences in the desorption energy between different exposures in the thick film regime. This highlights the importance of using alternative analysis

techniques such as kinetic modelling when determining desorption kinetic parameters.

In order to obtain the pre-exponential factor, and to confirm the obtained multilayer desorption energy values, kinetic modelling using the CKS package was performed. The same simple, two-step, reaction scheme describing zero order desorption and first order system pumping was employed, along with initial surface concentrations obtained from simple collision theory. The surface concentrations were again compared to that obtained for the 500 L exposure, which was assumed to be exactly 500 L. The uptake curve in **Figure 3.21** shows essentially the same trend as that observed for adsorption on stainless steel, with TPD yield increasing monotonically with exposure. This strongly suggests a sticking probability of close to unity over the exposure range studied. Simulated TPD traces for multilayer exposures are shown in **Figure 3.22** and the corresponding parameters in **Table 3.4**. It was not possible to obtain realistic simulations for C_6H_6 exposures of 4 and 5 L. It is clear from the peak shape that fractional order desorption kinetics dominate reflecting a combination of island formation and the presence of an underlying substrate that is rough which results in significant variations in film thickness across the surface. However, the significantly broadened submonolayer desorption likely also plays a role. It is therefore important to understand the desorption kinetics in the submonolayer regime.

Exposure / L	Desorption Order	Surface Concentration / molecules cm^{-2}	ν / molecules cm^{-2} s^{-1}	E_{des} / kJ mol^{-1}
500	0	1.92×10^{16}	$10^{30.1\pm0.4}$	48.1±0.2
200	0	8.49×10^{15}	$10^{30.1\pm0.4}$	48.1±0.2
100	0	4.90×10^{15}	$10^{30.1\pm0.4}$	48.1±0.2
50	0	1.99×10^{15}	$10^{30.0\pm0.4}$	48.0±0.2
20	0	7.5×10^{14}	$10^{29.9\pm0.4}$	47.8±0.2
10	0	3.2×10^{14}	$10^{30.0\pm0.4}$	47.8±0.2

Table 3.4: Kinetic parameters derived from kinetic modelling for the desorption of C_6H_6 multilayers from stainless steel.

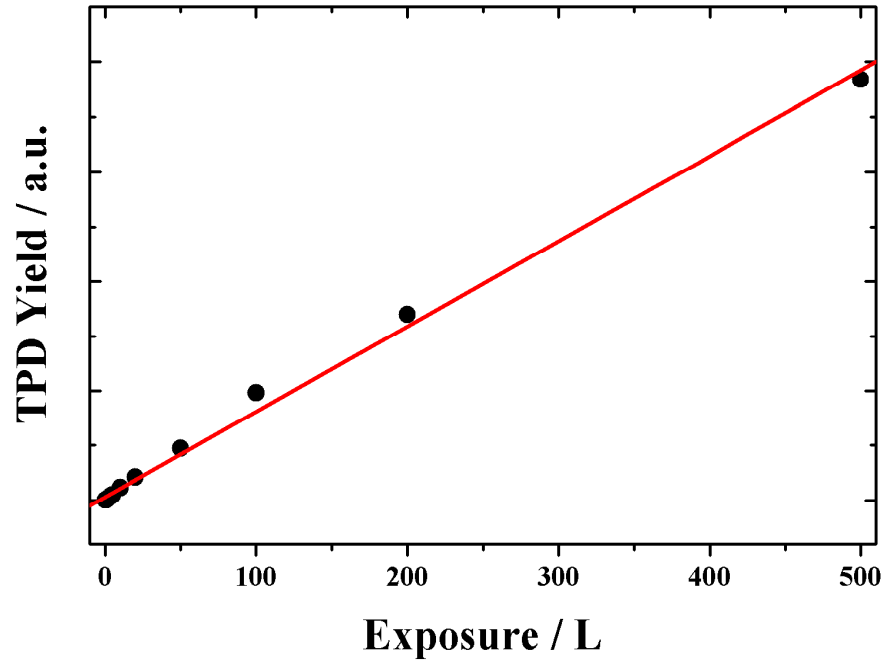

Figure 3.21: Plot of TPD yield *versus* exposure in Langmuir for the adsorption of C_6H_6 on amorhous SiO_2 (black circles). Also shown is a least squares linear fit (red line).

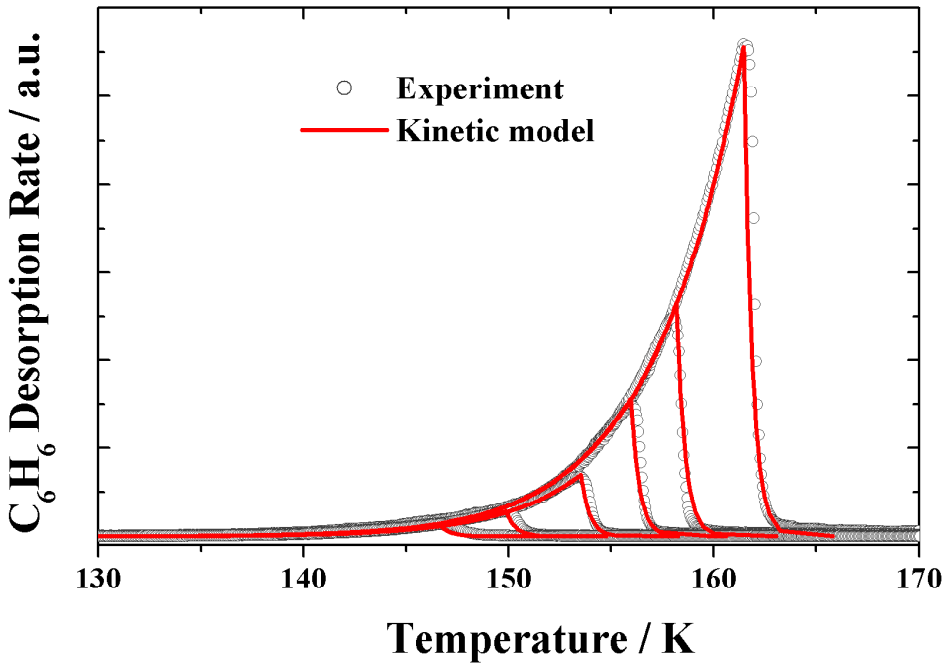

Figure 3.22: Experimental (open circles) and simulated (red lines) TPD traces for the desorption of 10, 20, 50, 100, 200 and 500 L of C_6H_6 from amorphous SiO_2.

Initially, the submonolayer desorption kinetics were considered using the same approach as for the multilayers, but with an assumed desorption order of one. **Figure 3.23** shows the leading edge analysis for submonolayer coverages of C_6H_6 on amorphous SiO_2. A reasonable linear fit to the leading edge region can be made with a desorption energy of 44.1 kJ mol^{-1}, though it is clear that there is significant deviation from this suggesting that the desorption energy is coverage dependent. The kinetic models in **Figure 3.24** were constructed using this desorption energy value. Though the leading edge regions of the desorption profiles are reasonably well reproduced, the high temperature tail is completely absent from the simulated TPD profiles. In order to obtain the leading edge agreement it was necessary to increase the pre-exponential value from 4×10^{10} s^{-1} to 7×10^{14} s^{-1} over the exposure range. Such a large range of pre-exponential values does not seem reasonable, which along with the inability of simple desorption kinetics to account for the high temperature tail suggests that models incorporating simple desorption kinetics are insufficient to describe the observed behaviour. It is clear that the underlying amorphous SiO_2 has a significant impact on the adsorption of C_6H_6 and the subsequent desorption kinetics. Comparing the submonolayer TPD traces for the two substrates reveals two major differences. On stainless steel, multilayers first appear for coverages of around 2.1×10^{13} molecules cm^{-2}, whereas on amorphous SiO_2 it requires a coverage of more than 8.8×10^{13} molecules cm^{-2}. This corresponds to an approximately four-fold increase in surface area available for adsorption. Even more striking is the extent to which the desorption extends to high temperature. On stainless steel, desorption is essentially complete by 155 K, whereas on the amorphous SiO_2 desorption continues up to temperatures in excess of 210 K. This observation could be explain either by (a) delayed desorption from pores within the SiO_2 film, (b) a broad distribution of sites and energies on the surface, or a combination of (a) and (b). The observed desorption profiles are reminiscent of those observed previously for the desorption of CO from a porous ASW film deposited at 10 K [19]. Here the CO desorption also displayed a broad tail extending to high temperature.

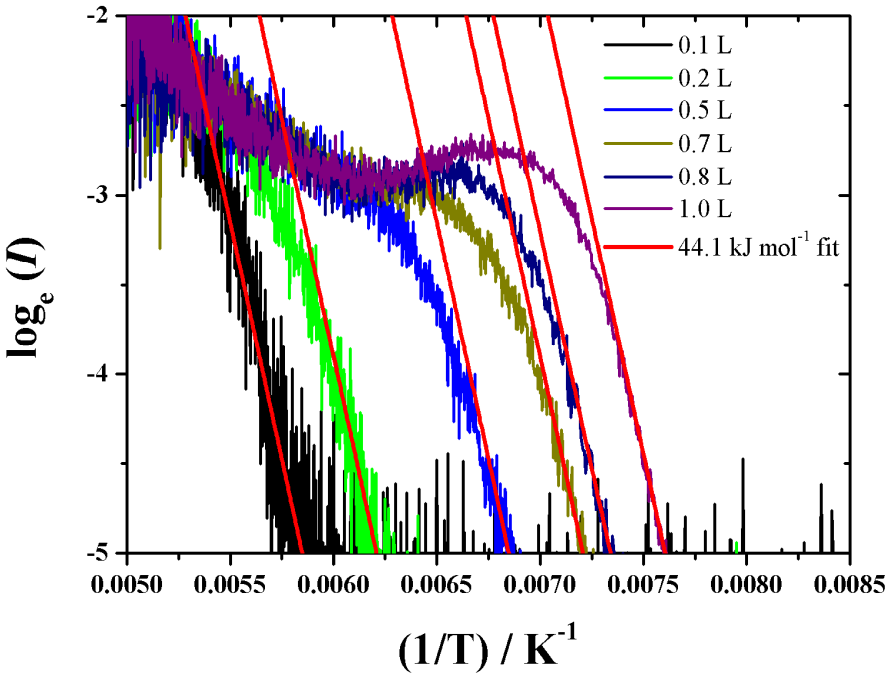

Figure 3.23: Leading edge analysis for submonolayer coverages of C_6H_6 on SiO_2 with linear fits for a desorption energy of 44.1 kJ mol^{-1}.

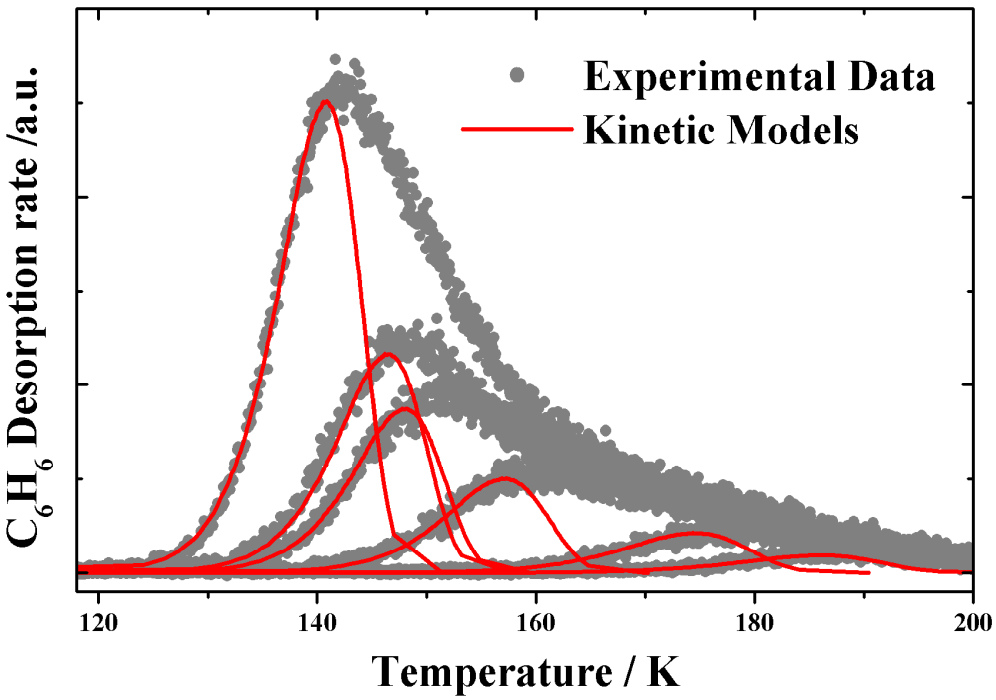

Figure 3.24: Kinetic models for the desorption of submonolayer coverages of C_6H_6 from amorphous SiO_2 using a fixed desorption energy of 44.1 kJ mol^{-1}.

The tails showed the same coincidence with increasing exposure as in the present case. In this study the observed desorption profiles were attributed to the desorption of CO molecules from within pores existing within the ASW film. A simple model was developed that considered desorption from the internal surfaces of the pores, re-adsorption onto pore surfaces and gas phase escape from the pore. Although a reasonable reproduction of the desorption tail was obtained they did not display coincidence with increasing exposure. Similar desorption profiles have been documented in the case of physisorbed CO on MgO(100) [20] and N_2 [21] and D_2 [22,23] on non-porous ASW. In all cases, the coincident tails in the desorption profiles were attributed to a desorption energy that varies as a function of coverage. This could arise both as a result of the existence of a range of binding sites on the surface that leads to a gradual decrease in binding energy as the most efficient sites are filled, and from other effects such as increasing intermolecular repulsions between adsorbate molecules.

In order to extract the desorption energy coverage dependence it is necessary to invert the Polanyi-Wigner equation to obtain an expression [20] for E_{des} in terms of N_{ads}:

$$E_{ads}(N_{ads}) = -RT \ln\left[-\frac{dN_{ads}/dt}{\nu N_{ads}} \right]. \qquad \textbf{Equation 3.7}$$

In order to evaluate this expression, the TPD profiles were converted to desorption rates in molecules cm^{-2} s^{-1}. This was achieved by scaling the plot such that the time integrated area was equal to the previously determined surface coverage. The integral up to each data point then represents the amount desorbed up to that time, which can then be inverted to yield remaining coverage, N_{ads}. It should be noted that in order to use this expression, a value for the pre-exponential factor, ν, must be assumed. Typically, simple chemisorbed and physisorbed systems can be described with pre-exponential values of 10^{13} s^{-1} and 10^{12} s^{-1} respectively. However, the interaction between C_6H_6 and SiO_2 is somewhere between the two extremes as a result of possible hydrogen-bonding interactions between the π system and OH groups on the SiO_2 surface, and between C_6H_6 H atoms and O atoms in SiO_2.

In order to represent this, a nominal value of 10^{13} s^{-1} was used in this analysis, although values of 10^{12} s^{-1}, 10^{14} s^{-1} and 10^{15} s^{-1} were also considered for comparison. The resulting plots of E_{des} *versus* N_{ads} are shown in **Figure 3.25** and demonstrate the applicability of a single desorption energy coverage dependence up to an exposure of 0.8 L. The curves for 1 L and 2 L appear to display an offset in energy of 1.5 and 3 kJ mol^{-1} respectively. This can be attributed to the growth of a more strongly bound second layer. This results in the observed shifts in desorption energy for exposures of 1 and 2 L. It was therefore necessary to obtain a universal, smooth curve that could be used in simulating the experimental data. An arbitrary choice of a third order exponential decay was used to obtain a satisfactory fit to the experimental E_{des} curves for 1, 2 and 0.8 L. The fitted curve for 2 L was then shifted down by 3.0 kJ mol^{-1} as shown in **Figure 3.26**. The good agreement between the shifted curve and that for an exposure of 0.8 L confirms the presence of a desorption energy shift as a result of the formation of a more strongly bound second layer. The final universal curve also shows good agreement with that obtained for an exposure of 1L. Of course, the excellent agreement with the 2 L curve is trivial as the curves are the same.

As *CKS* can only simulate the desorption kinetics for a fixed desorption energy, in order to generate simulated TPD profiles using a coverage dependent desorption energy it was necessary to develop a simple program to evaluate the Polanyi-Wigner equation. The program was written in Fortran 90 and will be described briefly. The program takes experimental time and temperature data as input for the calculation. For each time interval Δt between t and t+Δt as defined by the experimental data, the desorption rate is calculated by evaluating the Polyani-Wigner equation at the temperature $T(t)$ using $E_{des}(N_{ads})$, which is calculated using the function fit to describe the coverage dependence.. The change in N_{ads} in the interval Δt is then calculated based on the desorption rate. This process is then repeated for successive values of t. The resulting output data consists of the original input data along with the desorption rate and surface concentration at each time step. The source code for the program can be found in **Appendix 3A**. The resulting simulated TPDs are shown in **Figure 3.27** and **Figure 3.28**.

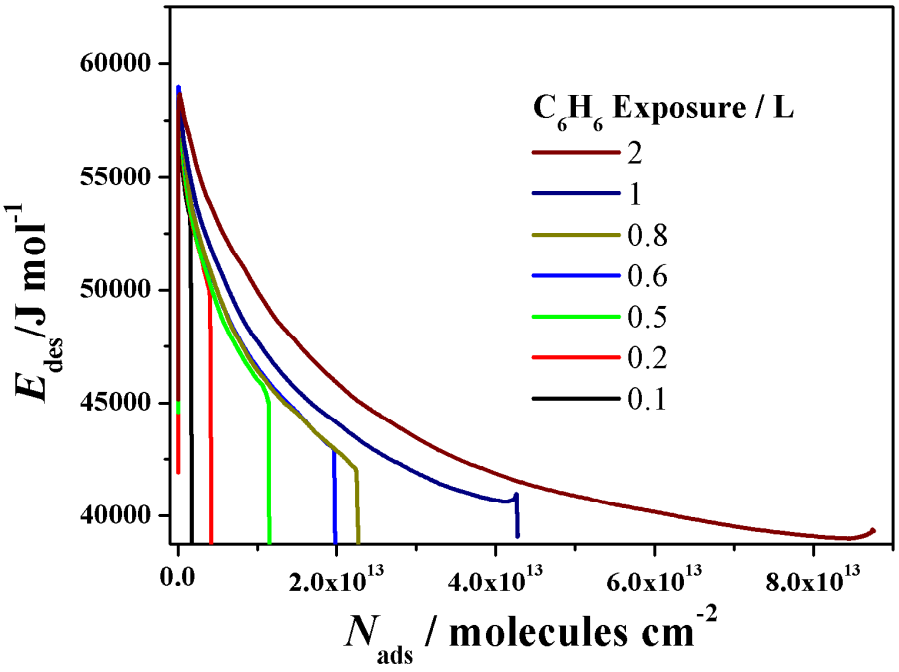

Figure 3.25: E_{des} coverage dependence for C_6H_6 adsorbed on amorphous SiO_2 obtained through inversion of the Polanyi-Wigner equation.

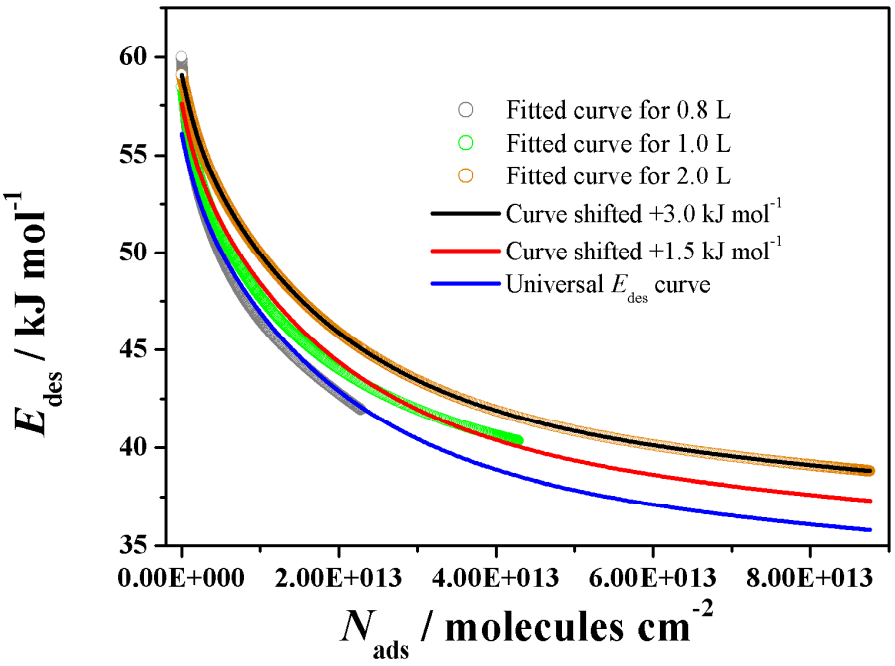

Figure 3.26: Derivation of a universal E_{des} coverage dependence curve showing agreement with all submonolayer exposures.

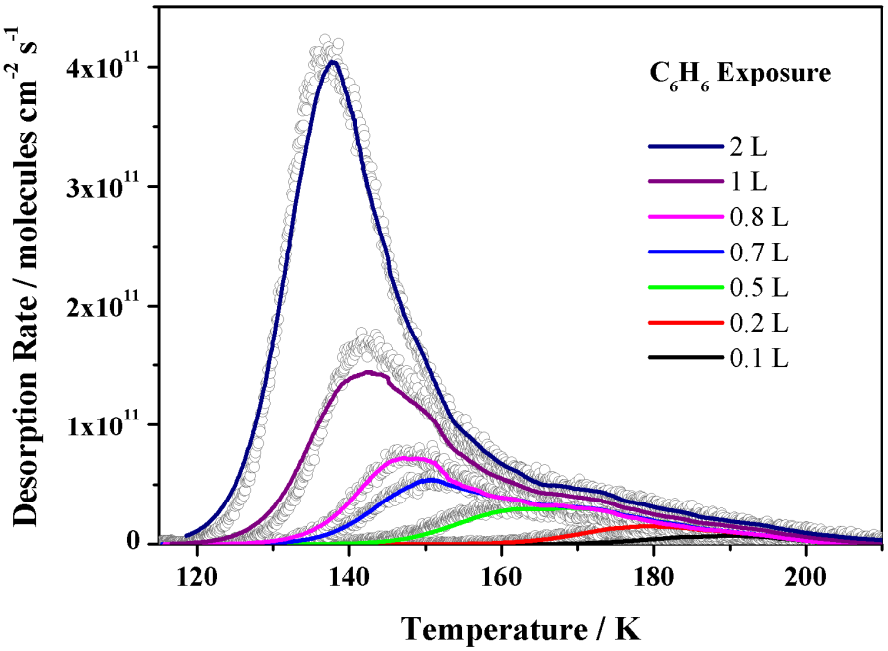

Figure 3.27: Simulated TPD profiles for all submonolayer coverages of C_6H_6 on amorphous SiO_2 assuming a distribution of desorption energies. Circles are experimental data and lines are simulations.

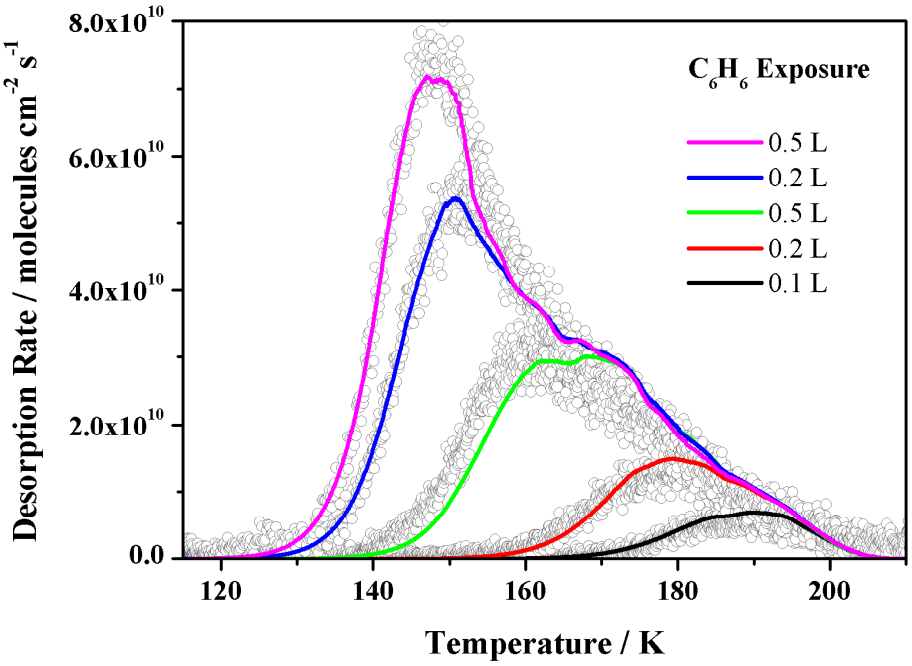

Figure 3.28: Simulated TPD profiles for the lowest submonolayer coverages of C_6H_6 on amorphous SiO_2 assuming a distribution of desorption energies. Circles are experimental data and lines are simulations.

The good agreement with experimental data at all coverages indicates the applicability of this technique. **Figure 3.29** shows the effect of not shifting the E_{des} curve by 1.5 and 3.0 kJ mol^{-1} for the 1 and 2 L TPD experiments respectively. This demonstrates the shift in desorption energy for these exposures which results in a significant translation of the TPD peak.

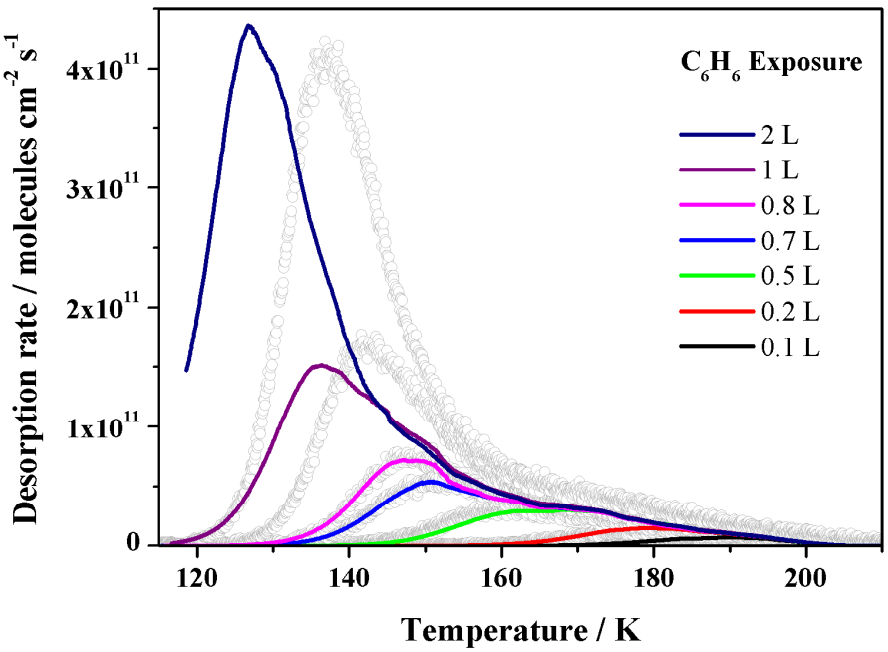

Figure 3.29: Simulated TPD profiles obtained without shifting the E_{des} curve for exposures of 1 and 2 L.

3.5 TPD of C_6H_6 adsorbed on compact ASW

3.5.1 Introduction

The aim of these experiments was to compare the thermal desorption kinetics of C_6H_6 adsorbed on the SiO_2 surface with those for C_6H_6 adsorbed on a compact ASW surface. The multilayer desorption kinetics are again considered, along with those describing the desorption of small amounts of C_6H_6 from a thick H_2O film which are sensitive to the C_6H_6 interaction. This system reflects the situation where C_6H_6 molecules are adsorbed onto a dust grain that is already coated with layers of H_2O, in contrast to the previous section which is relevant for adsorption on a bare silicate grain surface.

3.5.2 Experimental procedure

The experimental conditions were the same as for the experiments conducted with the SiO_2 substrate and the same procedure was followed prior to cooling down the substrate. Before C_6H_6 was deposited, again by backfilling the chamber, a thick film of H_2O was deposited onto the surface using the molecular beam. The beam exposure time was 2000 s, which, by a comparison between beam dosed and background dosed TPD profiles, corresponds to *ca.* 150 L.

3.5.3 Results and discussion

TPD profiles for small exposures of C_6H_6 adsorbed on compact ASW are shown in **Figure 3.30**. A single peak is visible that shifts gradually to higher temperature with increasing exposure. At an exposure of 0.5 L, a small shoulder appears on the higher temperature side of the peak that increases in intensity and shifts to higher temperature with increasing exposure as shown in **Figure 3.31**. This peak continues to grow and shift up to the maximum exposure of 200 L considered in these experiments. The high exposure profiles share coincident leading edges which strongly suggests zero order desorption kinetics. The low temperature peak is therefore attributed to small amounts of C_6H_6 that exhibit some degree of interaction with the underlying H_2O surface, with the high temperature peak being

associated with the desorption of C_6H_6 from C_6H_6 multilayers which continue to grow as shown in **Figure 3.32**.

The multilayer desorption kinetics were analyzed in the same way as for the adsorption of C_6H_6 on both the stainless steel and amorphous SiO_2 substrates. The resulting simulated TPD profiles are shown in **Figure 3.33**. The agreement with the trailing edge is not quite as good as in the previous cases which indicates de-wetting and the formation of C_6H_6 islands on the H_2O surface. A desorption energy of 45.8 kJ mol^{-1} and a pre-exponential factor of $10^{29.4}$ molecules cm^{-2} s^{-1} were found to best reproduce the experimental profiles. The pre-exponential factor is in good agreement with that obtained for the previous substrates, though the desorption energy is slightly lower which may also be the result of de-wetting altering the shape of the leading edge.

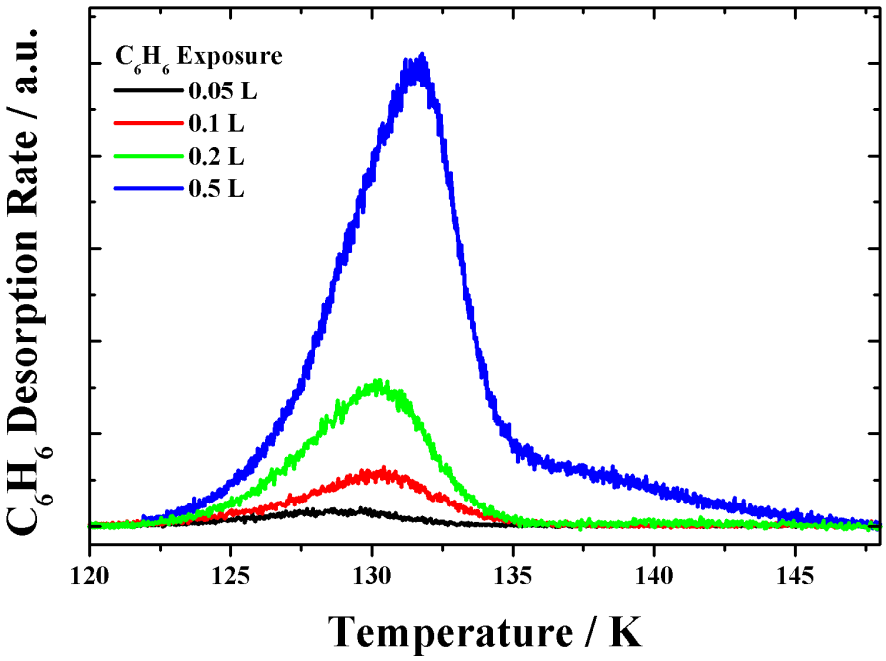

Figure 3.30: TPD profiles for the desorption of the lowest submonolayer coverages of C_6H_6 from a thick H_2O film.

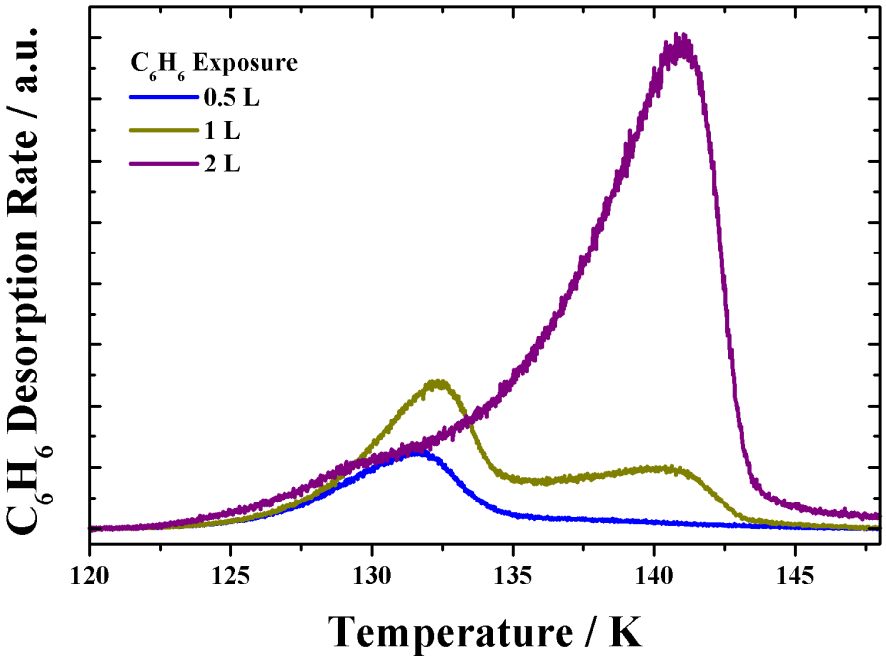

Figure 3.31: TPD profiles for the desorption of C_6H_6 from a thick H_2O film showing the transition from submonolayer to multilayer behaviour.

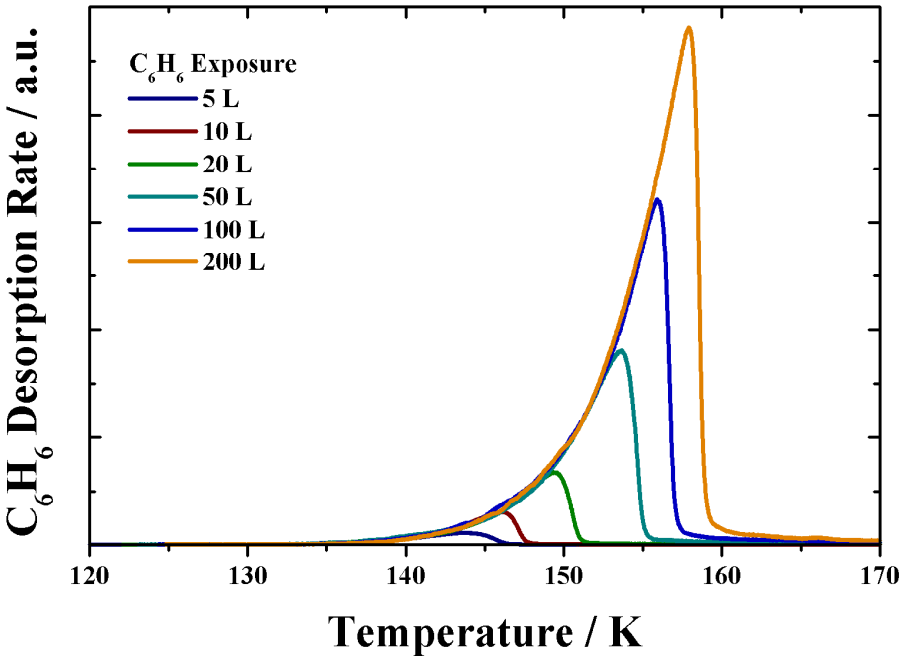

Figure 3.32: TPD profiles for the desorption of thick films of C_6H_6 from a thick H_2O film.

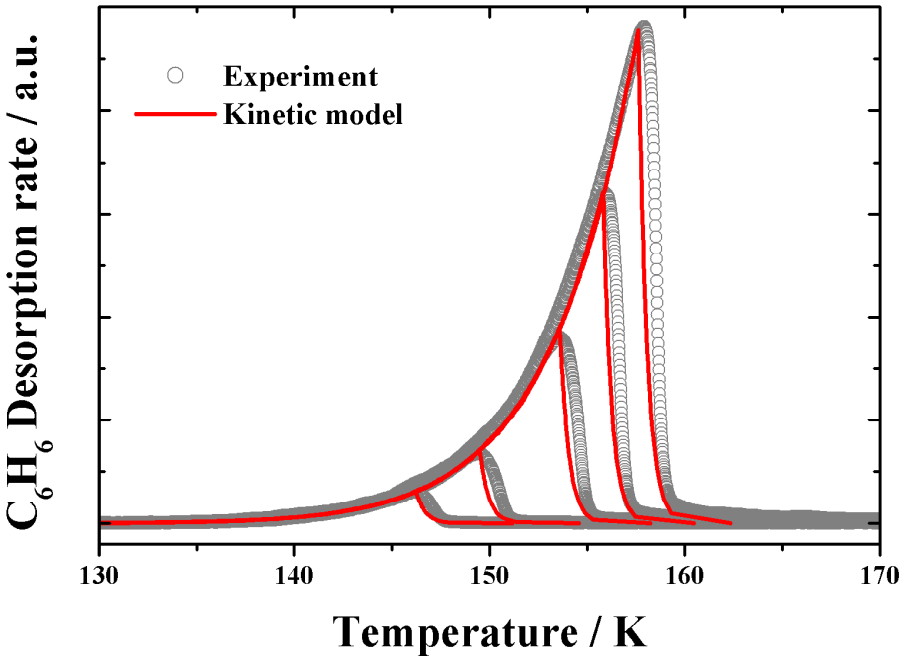

Figure 3.33: Simulated TPD profiles for the desorption of multilayer films of C_6H_6 from a thick ASW film. The simulated profiles (red lines) are compared to the experimental ones (open circles).

Further evidence for island formation comes from the observation that H_2O desorption begins before C_6H_6 desorption is complete. This is shown in **Figure 3.34**. In general, a multilayer C_6H_6 film acts as a cap which prevents H_2O desorption until C_6H_6 desorption is nearly complete. This results in a shift in the H_2O peak to higher temperatures. As well as a pronounced shift in the H_2O peak when multilayer films of C_6H_6 are adsorbed on top of the H_2O film, there is also a gradual increase in the temperature for the onset of desorption, which correlates with the completion of C_6H_6 desorption. However, this onset is typically at a temperature a few degrees lower than that for the completion of C_6H_6 desorption indicating the formation of C_6H_6 islands which reveals some of the H_2O surface. It would therefore be reasonable to expect small coverages of C_6H_6 to form islands on the H_2O surface, rather than forming a wetting layer. This means that it is possible to attribute the low temperature peak observed at low coverage to the desorption from islands of C_6H_6 on the H_2O surface, with the high temperature peak only appearing with the formation of a complete multilayer film. This is consistent with the simultaneous reduction in the intensity of the low temperature

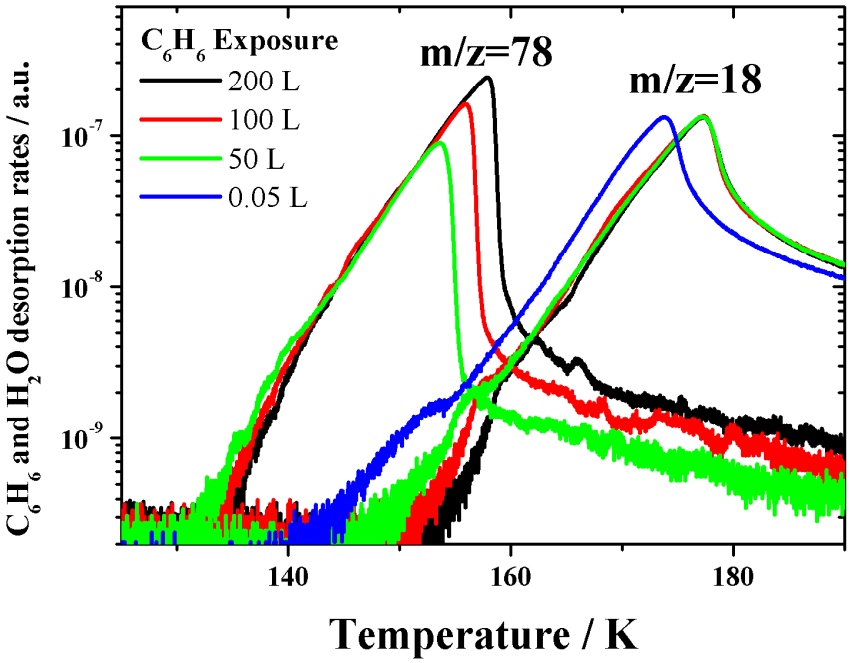

Figure 3.34: TPD profiles for the desorption of C_6H_6 and H_2O from various coverages of C_6H_6 adsorbed on a thick H_2O film. The H_2O exposure was the same in all cases.

peak indicating a reduction in the contribution of desorption from islands.

Bahr and Kempter [24] also observed two TPD peaks in the submonolayer coverage regime. They treated the low temperature desorption peak as resulting from simple first order desorption kinetics and obtained a desorption energy of 39 kJ mol^{-1}. However, as is the case with the current data, the peak shifted to higher temperature with increasing coverage, indicating that such an analysis is not valid. In order to obtain an estimate of the desorption energy, a desorption order of 0.9, reasonable for fractional order desorption that is closer to first order rather than zero order desorption, was assumed. The inversion technique used previously was employed, using a pre-exponential factor of 5×10^{14} $molecules^{0.1}$ $cm^{-0.2}$ s^{-1}. The resulting desorption energy curves are shown in **Figure 3.35**. The curve for an exposure of 0.5 L of C_6H_6 shows unusual behaviour at low coverages as a result of the appearance of the multilayer peak. The desorption energy rises as a result of the multilayer desorption energy of >45 kJ mol^{-1}.

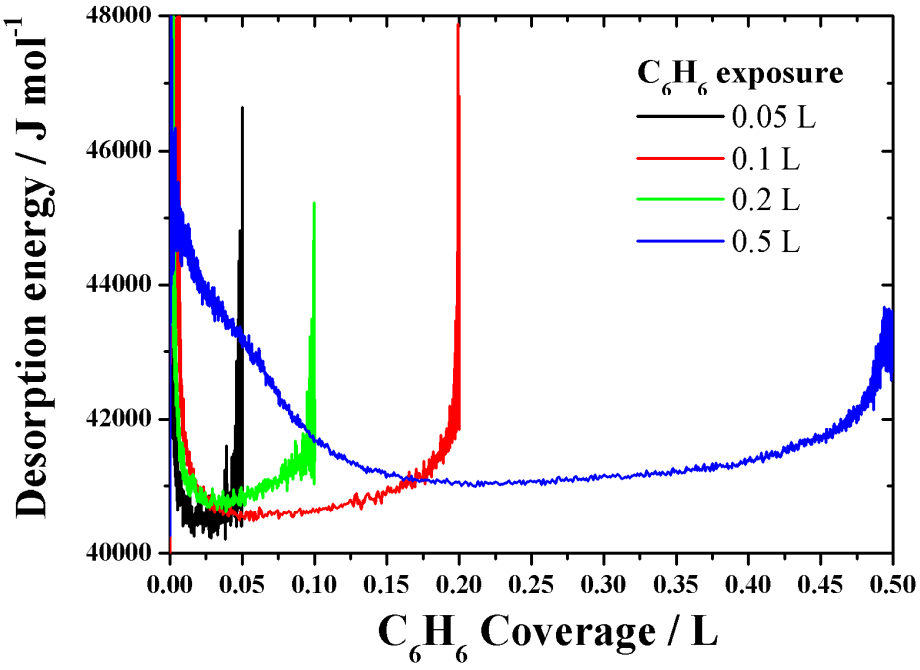

Figure 3.35: Desorption energy plots for the desorption of C_6H_6 adsorbed on a thick layer of H_2O. A desorption order of 0.9 was assumed. The near vertical regions are an artefact of the inversion procedure employed.

In general the desorption energy appears to be around 41±0.5 kJ mol^{-1}, with the curved shape of the profile likely resulting from changes in binding during island formation. The sharp spikes at the coverage extremes can be attributed to the poor signal to noise ratio for low desorption rates. Given the complicated nature of the desorption kinetics, coverage dependences of the desorption order and therefore the pre-exponential are likely to occur. The desorption energy value should therefore be taken as an estimate.

3.5.4 Comparison with C_6H_6 desorption from amorphous SiO_2

The significant differences between the submonolayer TPD profiles obtained for C_6H_6 adsorbed on amorphous SiO_2 and ASW can be attributed to differences in the adsorbate-substrate binding. In both cases, hydrogen-bonding interactions between the π-system of the C_6H_6 ring and either H_2O molecules or silanol groups on the SiO_2 surface are responsible for the binding. Any differences in binding can be related to the relative acidities of the OH groups in the two surface systems. It is known through *ab initio* calculations and experiment that the

deprotonation energy for surface bound silanol groups is around 1390 kJ mol^{-1} [25]. This shows that the silanol group is more acidic than H_2O, which has a deprotonation energy of *ca.* 1630 kJ mol^{-1} in the gas phase [26]. This is also demonstrated by the difference in solution phase pK_a values of 7 and 14 for surface silanol groups [27] and H_2O [9] respectively. This means that the H atoms in the case of silanol groups will carry a greater partial positive charge, *ca*. +0.6*e* [28], than in the case of surface H_2O molecules where the corresponding charge is +0.4*e*. As a consequence, the C_6H_6 bound to the silanol group is significantly more polarized, which in turn impacts on the interaction between the first and second C_6H_6 layers, where C_6H_6 molecules are likely to be bound edge-on to those in the first layer through hydrogen-bonding interactions. This explains the tendency to form a second layer of C_6H_6 on amorphous SiO_2 at exposures of 1 and 2 L. The increased binding in this layer will then effectively delay the desorption of the first layer, resulting in the observed shift in the TPD profiles at these exposures. This would also suggest the formation, initially, of 2-dimensional islands on top of the first layer of C_6H_6 on SiO_2. In the case of the ASW substrate, the intermolecular forces between C_6H_6 molecules dominate, resulting in the formation of 3-dimensional islands and the observed de-wetting behaviour.

3.6 RAIRS of C_6H_6 adsorbed on amorphous SiO_2 and ASW

3.6.1 Introduction

RAIRS experiments were performed for C_6H_6 adsorbed both on the amorphous SiO_2 surface and on a thick layer of compact ASW. The aims of these experiments were to obtain a reference spectrum that could be used in future irradiation experiments and to examine the nature of the binding between the C_6H_6 molecules and the two substrates.

3.6.2 Experimental procedure

The amorphous SiO_2 substrate was cleaned in the usual manner by heating to 200°C before cooling with liquid nitrogen to a base temperature of 115 K. The sample position was adjusted to optimize the interferogram and then left in that position for the duration of the RAIRS experiments. C_6H_6 films were grown using sequential background deposition where 1 L was dosed and a RAIR spectrum collected, followed by a further 1 L dose, to give a total dose of 2 L for the next spectrum. In this way, spectra for exposures of 1, 2, 5, 10, 20, 50, 100, 200 and 500 L of C_6H_6 were obtained. No peaks were observed for exposures of less than 1 L. For the C_6H_6 on ASW experiments a thick film of H_2O was deposited using the molecular beam with the sample in optimum RAIRS position. The beam exposure time was 2000 s, resulting in a surface concentration of *ca.* 7×10^{16} molecules cm^{-2} s^{-1}. C_6H_6 was deposited on top of the H_2O in the same way as for the SiO_2 substrate. In all cases, spectra were calculated by the co-addition of 1024 scans at a resolution of 2 cm^{-1}. Scans performed at a resolution of 1 cm^{-1} yielded no further information, but did lead to a reduction in signal as a result of the reduced beam intensity arising from the smaller aperture used at this resolution. Background spectra were collected before deposition, and also following deposition. In the latter case the adsorbed multilayers were first desorbed by heating and the sample subsequently cooled back down to base temperature before background acquisition. Spectra were obtained by ratioing the sample spectra to the background spectra yielding the baseline with the least curvature. Baselines were subsequently subtracted manually for (a) the entire spectrum for

the largest exposure of 500 L and (b) individual regions of interest for all exposures.

3.6.3 Results and Discussion

Figure 3.36 shows the full range RAIR spectra obtained for a 500 L exposure of C_6H_6 adsorbed on the amorphous SiO_2 substrate. Band assignments are made in accordance with a previous transmission IR study of C_6H_6 ice layers deposited on a Si(111) crystal [29] and RAIRS of C_6H_6 ice on a polished Al mirror [30]. The comparison is shown in **Table 3.5**.

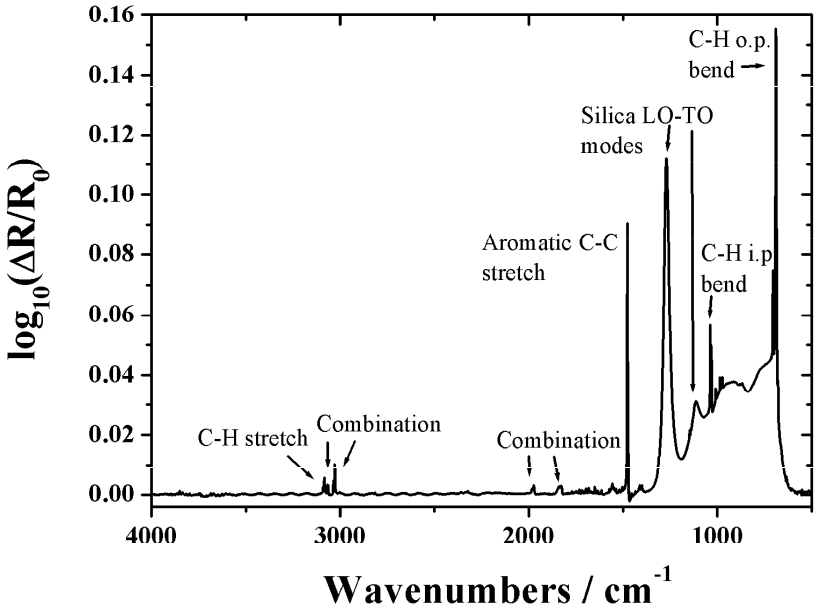

Figure 3.36: Full range RAIR spectrum of 500 L of C_6H_6 deposited on the amorphous SiO_2 film. C_6H_6 vibrations are labelled, along with the SiO_2 bands

The combination bands were assigned by comparison with the work of Tripathi *et al*. [31]. For high exposures the spectrum is dominated by a peak close to 1270 cm^{-1} which can be assigned to the longitudinal optical (LO) mode of SiO_2. The smaller peak at 1114 cm^{-1} can be attributed to the transverse optical (TO) mode which, as has been discussed, is expected to be relatively weak in reflection mode. The remaining broad features below 1000 cm^{-1} are also thought to be associated with the SiO_2 substrate. Symmetries and vibration numbers are assigned according to Herzberg [32]. The normal modes for C_6H_6 are shown in **Figure 3.37**.

Assignment	This work	Transmission IR on Si(111) (reference [29])	RAIRS on Al (reference [30])
C-H stretch (ν_{12}) e_{1u}	3082	3088	3095
Combination 1 ($\nu_2+\nu_{16}+\nu_{18}$) e_{1u}	3065	---	3075
Combination 2 ($\nu_{13}+\nu_6$) e_{1u}	3027	3036 (broad)	3043
Combination 3 ($\nu_{11}+\nu_{19}$) e_{1u}	1973	1980	1957
Combination 4 ($\nu_{18}+\nu_{19}$) e_{1u}	1832	1836	1812
C-C aromatic stretch (ν_{13}) e_{1u}	1477	1480	1481
SiO_2 LO mode	1270	---	---
SiO_2 TO mode	1114	---	---
C-H in-plane bend (ν_{14}) e_{1u}	1037	1040	1038
C-H out-of-plane bend (ν_4) a_{2u}	690	688	678

Table 3.5: Assignments for the IR features observed in the RAIR spectra of C_6H_6 on amorphous SiO_2. All frequencies are in cm^{-1}. Mode numbers and symmetries are also provided.

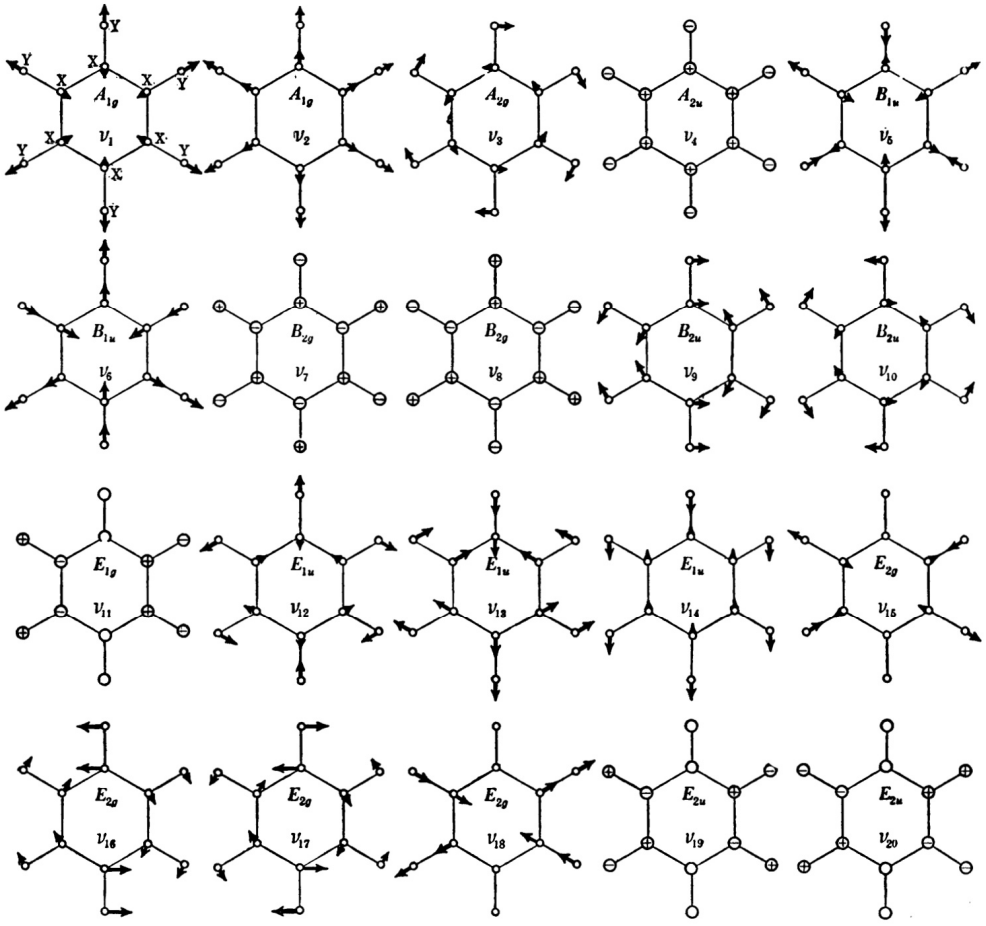

Figure 3.37: Normal modes of C_6H_6 (point group D_{6h}). Only one component for the doubly degenerate vibrations is shown. From [32].

Figure 3.38 shows the full range RAIR spectrum for an exposure of 500 L of C_6H_6 deposited on a thick layer of compact ASW. The same set of C_6H_6 peaks are again observed with no shift in frequency from those observed using the SiO_2 substrate, as expected for C_6H_6 multilayer growth. The only major difference is the addition of bands associated with the H_2O layer, namely (i) the O-H stretch at 3600-3100 cm^{-1}, (ii) O-H bend at 1800-1300 cm^{-1} and (iii) the libration at 850 cm^{-1}. The ice spectrum is in good agreement with other studies under similar conditions [33,34]. The negative feature at near 2250 cm^{-1} is due to variations in gas phase CO_2 in the purge gas. Similarly, the sharp features around 1750 cm^{-1} and 3750 cm^{-1} are due to water vapour in the purge.

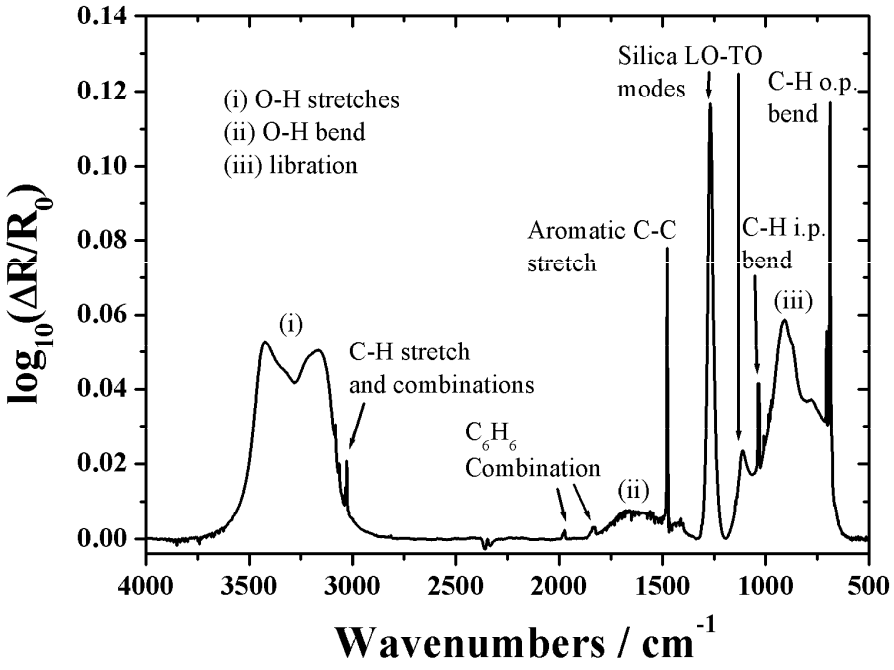

Figure 3.38: Full range RAIR spectrum of 500 L of C_6H_6 deposited on a thick H_2O film on the amorphous SiO_2 film. C_6H_6 vibrations are labelled, along with the SiO_2 bands. H_2O bands are indicated by (i), (ii) and (iii).

Figure 3.39 shows detailed RAIR spectra for all exposures of C_6H_6 on amorphous SiO_2 whilst **Figure 3.40** is limited to exposures up to 20 L. In these figures, the spectral regions corresponding to the assignments are considered separately, though. It should be noted that the C-H stretching mode and the nearby combination bands are presented together. There is no significant variation in the

appearance of the bands in the high exposure region as would be expected for the growth of a reasonably thick film of C_6H_6 multilayers. The difference in shape between the C_6H_6 bands and the SiO_2 features is quite striking, as the SiO_2 originate from bulk phonon modes. At the very lowest exposures the intensity of the peaks, when visible, appears to drop off rapidly below 5 L. Exposures below this limit correspond to adsorption on the rough surface of the SiO_2 itself, and a loss of intensity would be expected as a result of shadowing effects caused by the surface roughness. This effectively leads to a reduction in IR intensity reaching the C_6H_6. In order to properly assess the C_6H_6-SiO_2 it would be necessary to grow a flat, crystalline film of SiO_2. There is some evidence for peak shifting at the lowest exposure, which would reflect the monolayer adsorption interaction. In particular for C-H out-of-plane bend, only the high frequency shoulder is visible at low exposures, though it should be noted that the frequency at which this band occurs is very close to the low frequency limit of the MCT detector. A small shift to lower frequency of *ca.* 1 cm^{-1} is apparent for the C-C stretch. This is also visible in the combination band $\nu_{19}+\nu_8$ which has a contribution from the C-C stretch. The integrated intensities of each region of interest relative to those obtained for an exposure of 500 L are shown in **Figure 3.41**. The C-H stretching mode and the nearby combination are considered together. There is a general increase in intensity for all regions, with no strong variations in the trend between different vibrations. This is again consistent with a gradual build-up of a multilayer film. The curvature at high exposure can be attributed to deviation in the linearity of absorption intensity with respect to film thickness which occurs for thick films. As the same behaviour is observed for all peaks, this will not be discussed further. There is some unusual behaviour for the very lowest exposures, but this can be attributed to the extremely small size of these signals and small artefacts introduced during the baseline subtraction procedure.

Finally, the ratio of the integrated intensities of the in-plane and out-of-plane bending modes is shown in **Figure 3.42.** The observed trend shows that the in-plane contribution increases gradually relative to the out-of-plane contribution, for all exposures. This indicates a gradual increase in the number of tilted C_6H_6 molecules.

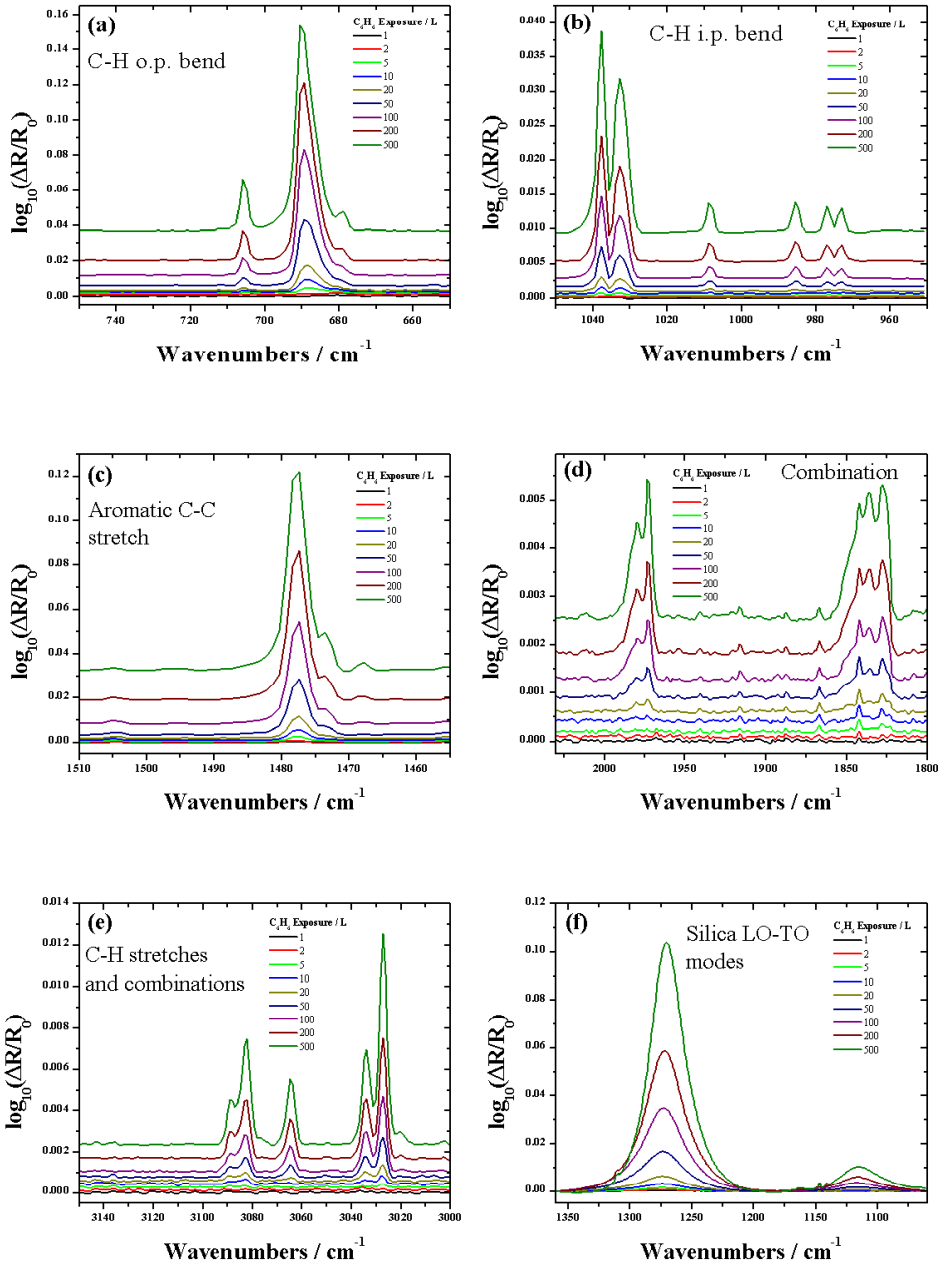

Figure 3.39: RAIR spectra obtained for 1-500 L of C_6H_6 deposited on the amorphous SiO_2 film. (a)-(e) show C_6H_6 vibrations whilst (f) shows the SiO_2 bands.

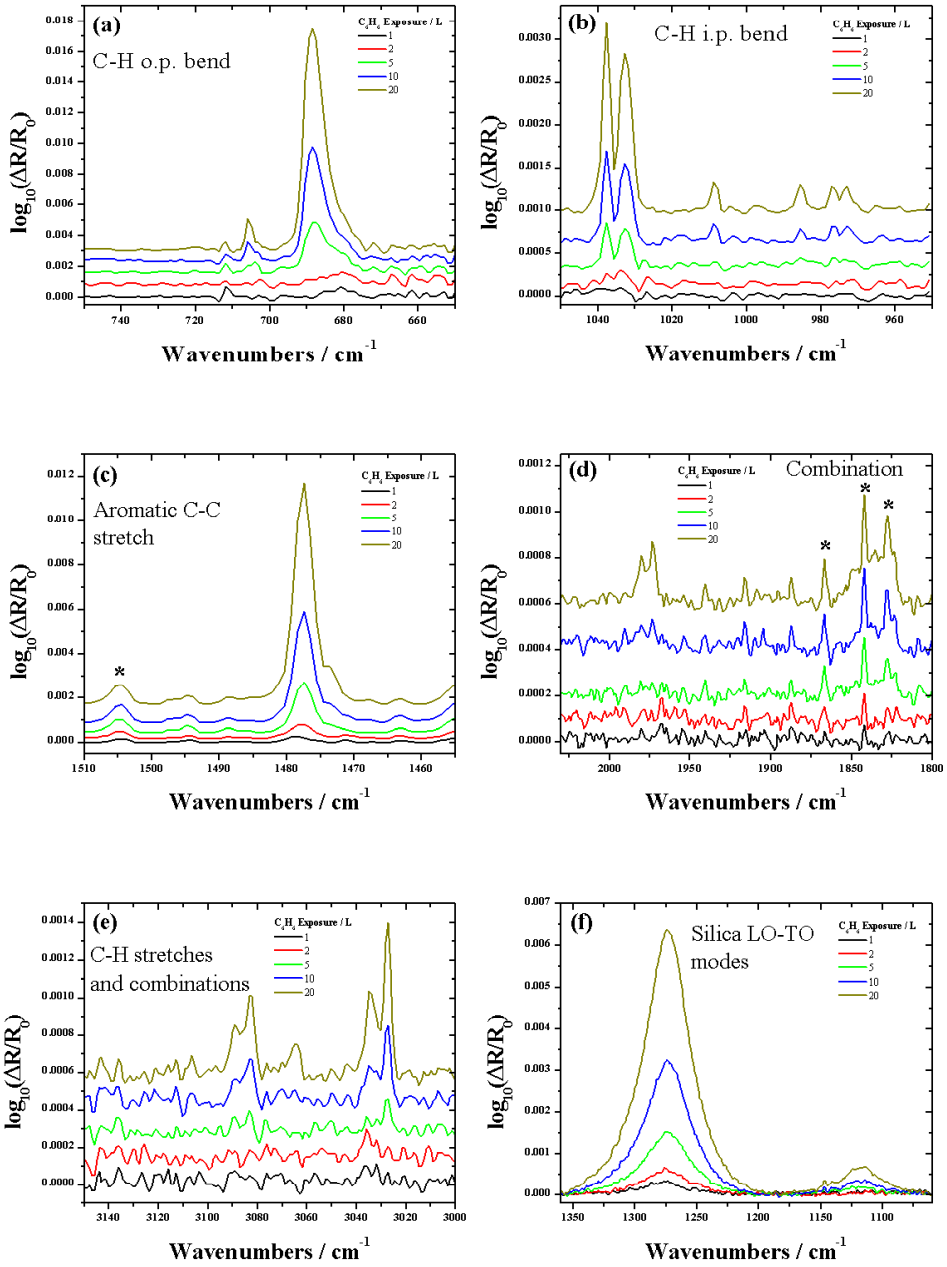

Figure 3.40: RAIR spectra obtained for 1-20 L of C_6H_6 deposited on the amorphous SiO_2 film. (a)-(e) show C_6H_6 vibrations whilst (f) shows the SiO_2 bands. The features indicated by * are attributed to gas phase H_2O vapour in the beam path outside the UHV chamber.

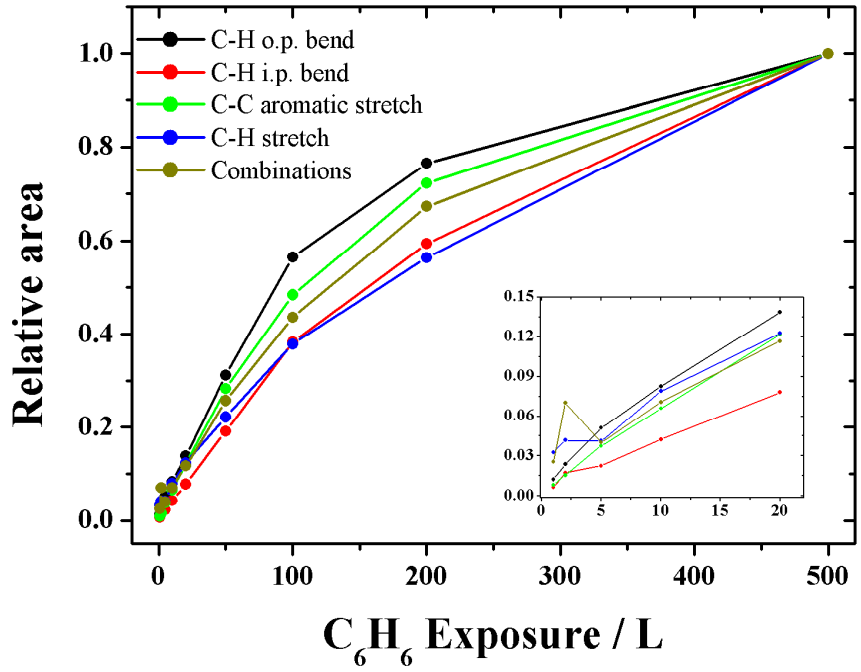

Figure 3.41: Band areas relative to 500 L for each of the main spectral regions for C_6H_6 adsorbed on amorphous SiO_2. The inset is a close-up of the low exposure region.

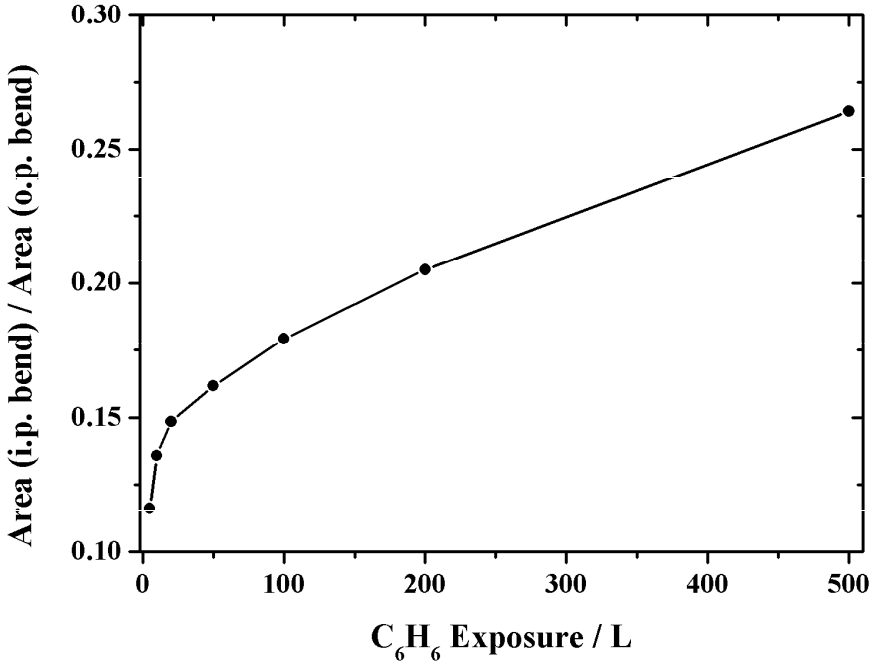

Figure 3.42: Ratio of the band area for the C-H in-plane bend and that of the C-H out-of-plane bend.

There is certainly no significant change in this behaviour which would indicate re-orientation of the C_6H_6 molecules from a plane-parallel to plane tilted orientation as has been observed in single crystals such as Ru(001) [6]. This is consistent with there being a fairly random distribution of C_6H_6 molecule orientations *relative to the metal surface* as a result of the roughness of the SiO_2 surface. Detailed RAIR spectra for C_6H_6 adsorbed on compact ASW are shown in **Figure 3.43** and **Figure 3.44** for all exposures and small exposures up to 20 L respectively. In these, the H_2O bands have been removed during the baseline subtraction. The spectra are very similar to those obtained for C_6H_6 on SiO_2 including the small shifts at the lowest exposures noted previously. This suggests that the C_6H_6-ASW and C_6H_6-SiO_2 interactions are similar as might be expected for a silica surface with many silanol groups. In order to gain more insight into the small shifts observed at submonolayer coverages, simple quantum mechanical calculations were performed on the $C_6H_6(H_2O)$ cluster. This simple model is a reasonable approach considering that for adsorption on SiO_2 and H_2O, the interaction is likely to be between C_6H_6 and OH groups. The 6-31G(2p,2d) basis set was used throughout the calculations. This basis set includes 2 p polarization functions on H atoms and 2 d polarization functions on the carbon and oxygen atoms in the calculations. All calculations were performed using the 2008 version of the GAMESS-US software suite [35]. Geometries and vibrational analyses were viewed using the GABEDIT software package [36]. The geometries of isolated C_6H_6 and H_2O molecules were first optimized. The optimized molecules were then brought close together, and the geometry re-optimized at the same level of theory. The vibrational spectra of both the optimized isolated molecules and the $C_6H_6(H_2O)$ cluster were calculated using the harmonic oscillator approximation. The total energies of the three geometries were then corrected using the harmonic zero point vibrational energy to yield a cluster binding energy of 13.7 kJ mol^{-1} which is in reasonable agreement with a value of 11 kJ mol^{-1} recently reported for calculations using density functional theory [37].

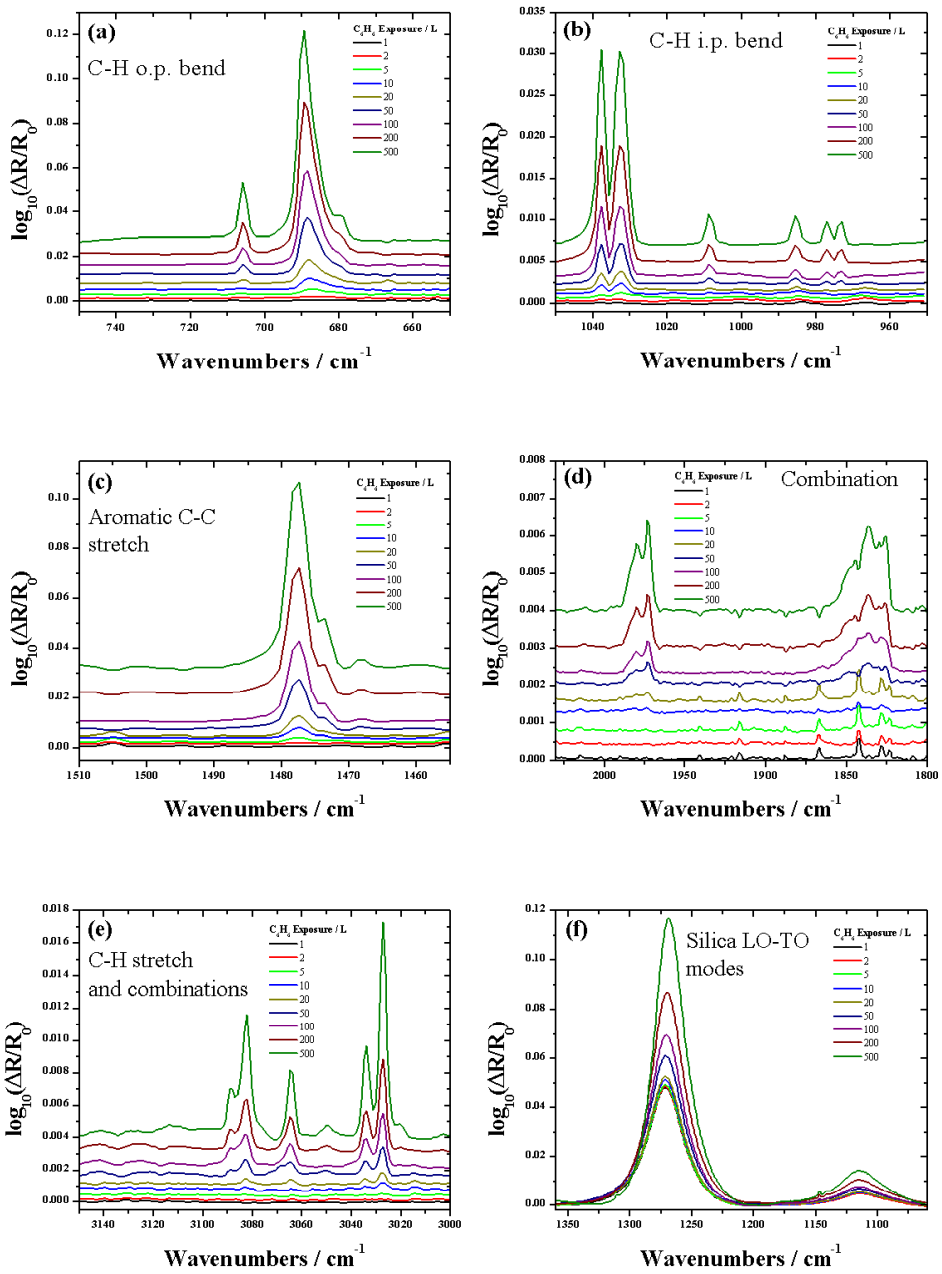

Figure 3.43: RAIR spectra obtained for 1-500 L of C_6H_6 deposited on a thick H_2O film on the amorphous SiO_2 film. (a)-(e) show C_6H_6 vibrations whilst (f) shows the SiO_2 bands. H_2O bands have been removed as part of the baseline correction. The sharp features in (d) are attributed to gas phase H_2O vapour in the beam path outside the UHV chamber.

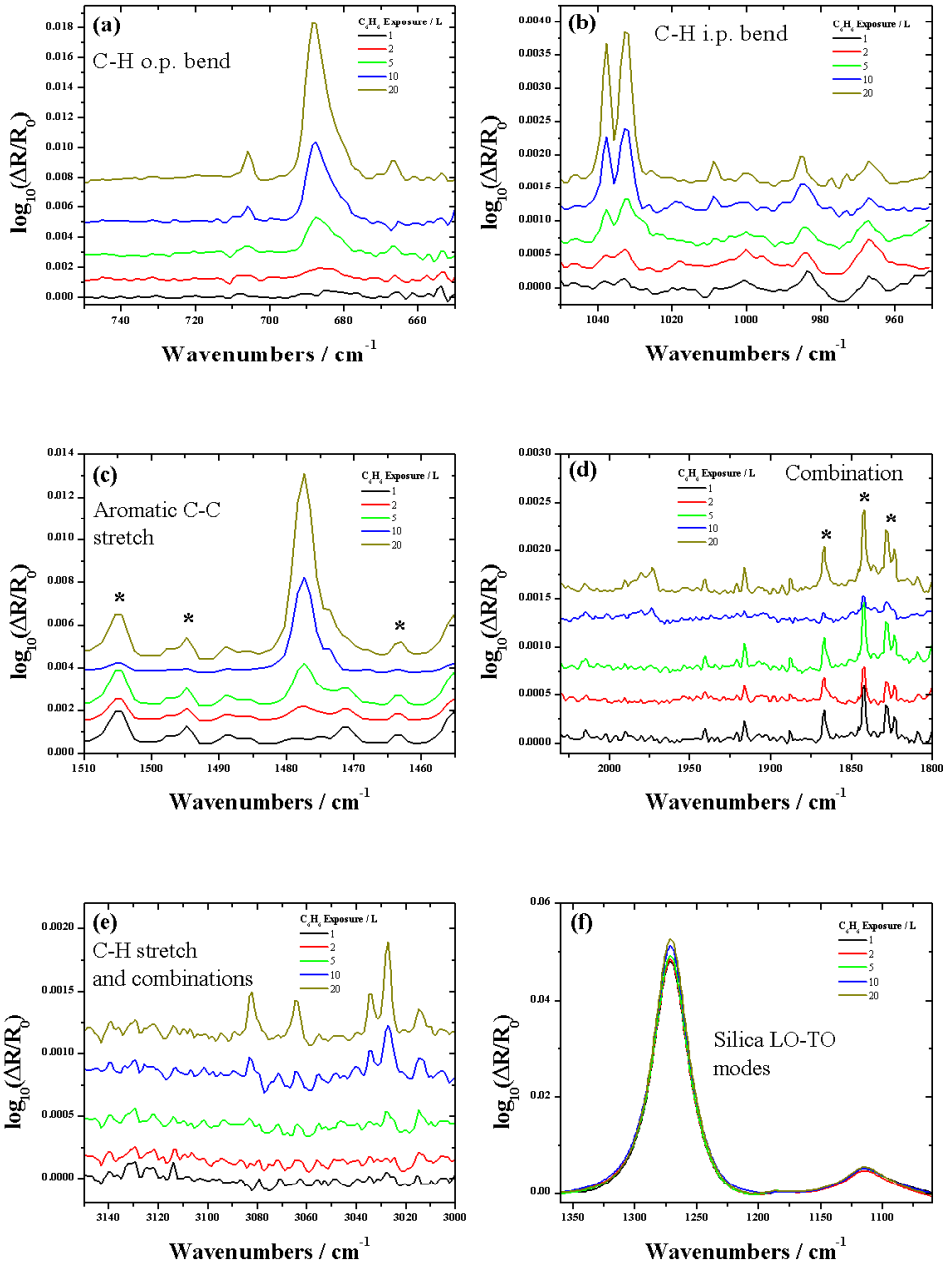

Figure 3.44: RAIR spectra obtained for 1-20 L of C_6H_6 deposited on a thick H_2O film on the amorphous SiO_2 film. (a)-(e) show C_6H_6 vibrations whilst (f) shows the SiO_2 bands. H_2O bands have been removed as part of the baseline correction. The features indicated by * are attributed to gas phase H_2O vapour in the beam path outside the UHV chamber.

This value was not corrected for the ZPVE, and applying the correction made here results in a value of *ca.* 14 kJ mol^{-1}. The geometry of the optimized cluster is shown in **Figure 3.45**.

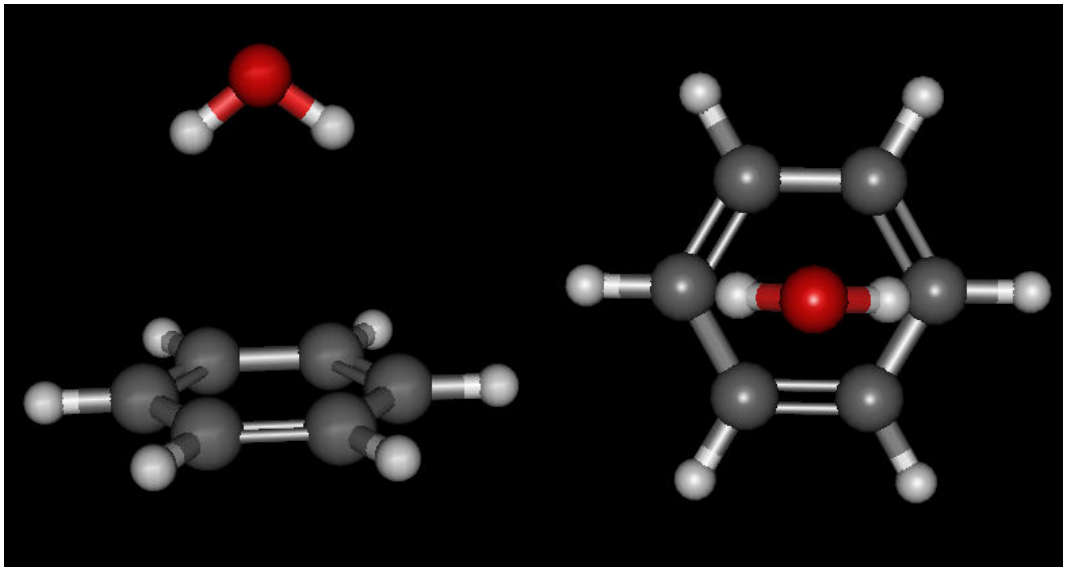

Figure 3.45: 6-31G(2p,2d) optimized geometry for the $C_6H_6(H_2O)$ cluster.

The C_6H_6 vibrations were scaled by a value of 0.90, which was obtained by comparing the 1477 cm^{-1} band position with that obtained by calculation. The frequencies for the H_2O cluster were scaled by the same factor. The calculated IR spectra in **Figure 3.46** suggest small frequency shifts of 2-3 cm^{-1} for the C-C stretching and C-H out-of-plane bending modes for the cluster relative to spectrum for the isolated C_6H_6 molecule. The C-H band also shows a small frequency increase. However, given the proximity of the experimental band to the MCT detector limit, the experimental lineshape is questionable. The C-H stretching mode also shows a small frequency increase, though the experimental signal is too weak at exposures of less than 5 L to make a comparison. Although this analysis is extremely preliminary, it suggests that the small shifts observed in the experimental data are consistent with a weak binding interaction between C_6H_6 and the underlying surface, which in both cases is likely to involve OH groups.

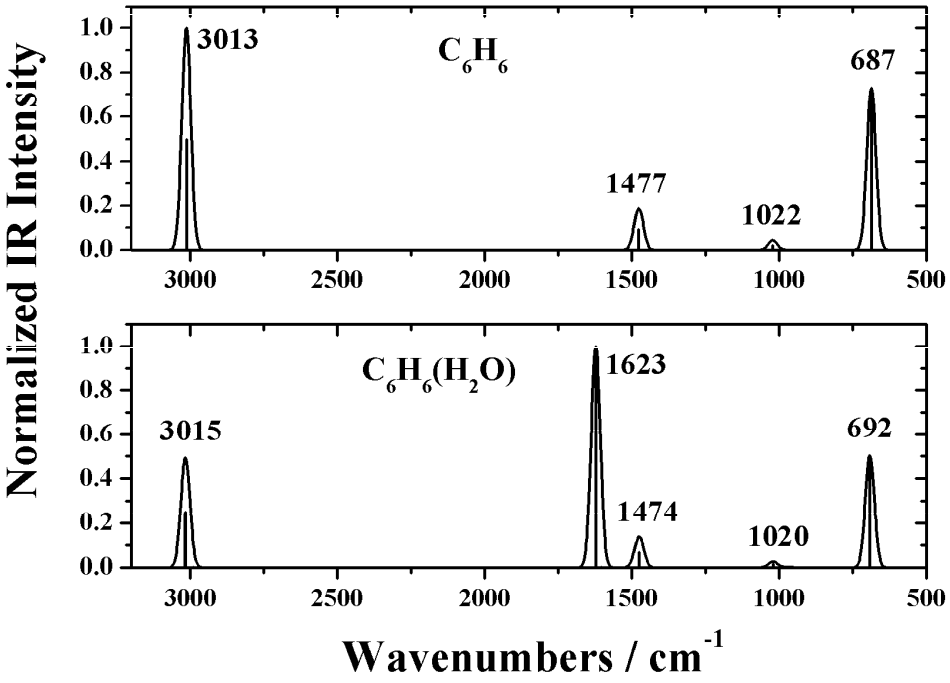

Figure 3.46: Calculated IR spectra for C_6H_6 and the $C_6H_6(H_2O)$ cluster. Each spectrum has been normalized to the largest intensity band.

3.7 Astrophysical implications and conclusions

The astrophysical impact of desorption from a substrate that presents a wide range of binding sites can be demonstrated by performing kinetic simulations with astrophysical heating rates. As was discussed in the **Chapter 1**, astrophysical heating rates are typically of the order of 0.1-1 K century^{-1}, which corresponds to 3-30×10^{-11} K s^{-1}. The amounts of C_6H_6 desorbed as a function of time at these heating rates are shown in **Figure 3.47** and **Figure 3.48** for simple first order desorption kinetics with a single desorption energy of 40 kJ mol^{-1} and first order desorption kinetics with the experimentally derived E_{des} function. These simulations were performed by removing the pumping step from simple first order desorption kinetic models constructed in *CKS* and adjusting the heating ramp accordingly. It is clear that the broad distribution of desorption energies leads to significantly delayed desorption which results in the presence of small amounts of adsorbed C_6H_6 at significantly later times than would be the case for a single desorption energy. This observation is likely to be valid for a wide range of

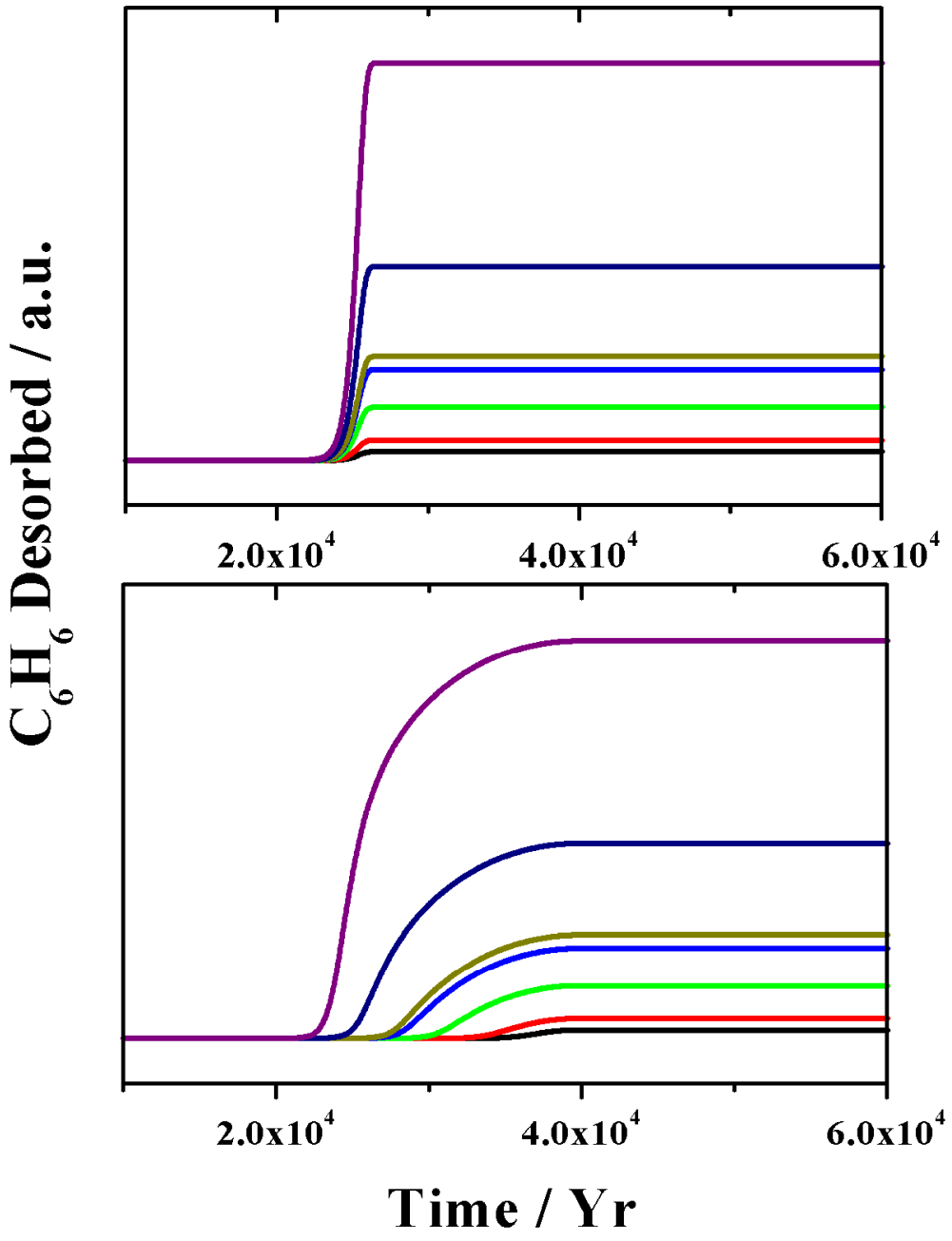

Figure 3.47: Simulated desorption profiles for (top panel) simple first order desorption and (bottom panel) first order desorption from a substrate with the experimentally determined desorption energy distribution using a heating rate of 1 K century^{-1}.

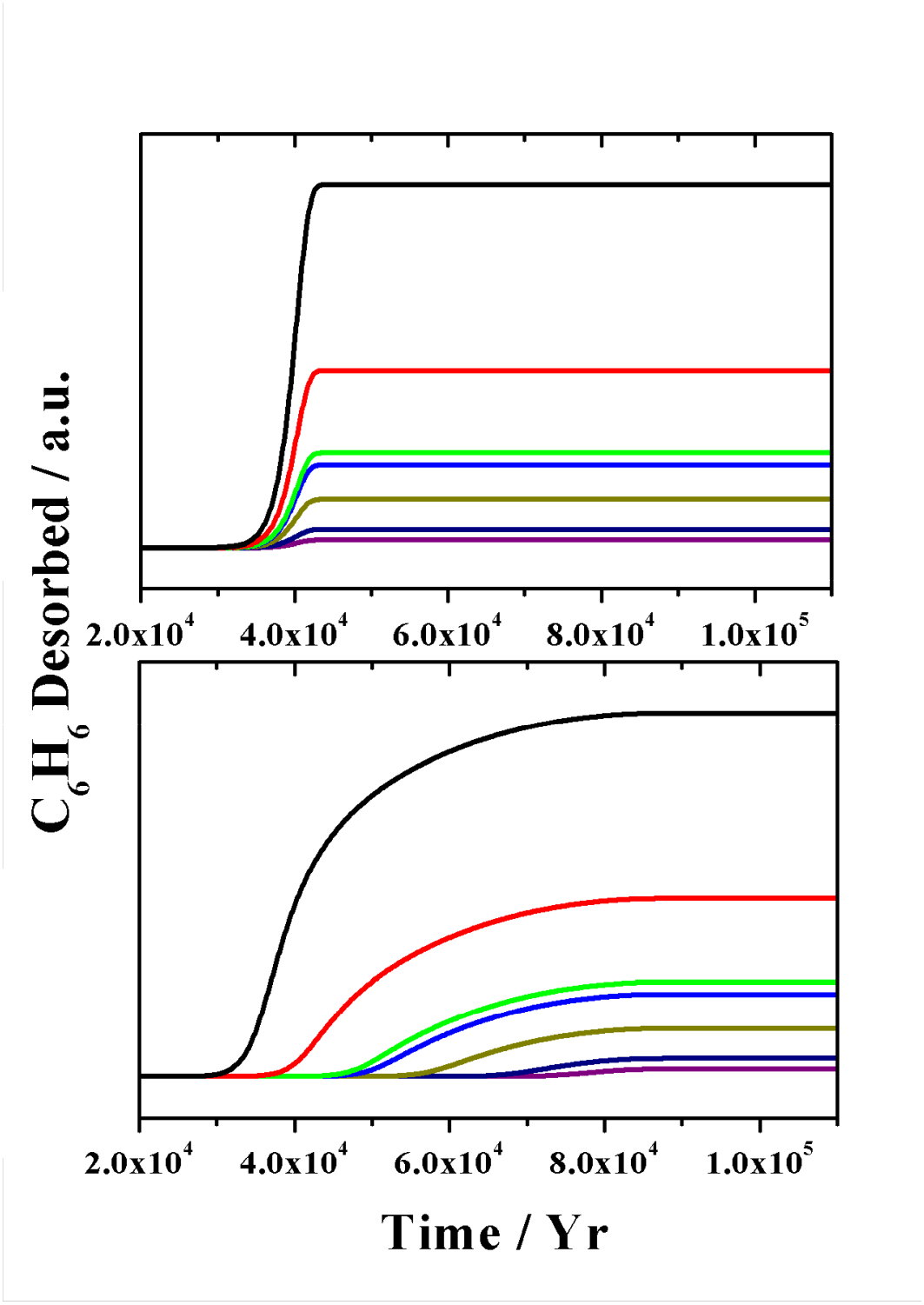

Figure 3.48: Simulated desorption profiles for (top panel) simple first order desorption and (bottom panel) first order desorption from a substrate with the experimentally determined desorption energy distribution using a heating rate of 0.1 K century^{-1}.

molecules adsorbed strongly onto bare grain surfaces. Similar behaviour has also been revealed by preliminary TPD experiments for CH_3OH, C_5H_5N and CH_3CN. The results presented also highlight the marked differences between desorption from different substrates and from multilayer films. It is clear that the desorption of small amounts of C_6H_6 from the surface of a bare grain will be very different to that from a water ice surface. It is however important to note that the experiments conducted probe the two extremes of a bare grain surface and one which is completely covered in pure water ice. Real astrophysical ices are likely to be far more complex with both mixing and layering occurring. On relatively bare grains the population of sites by different molecules will be sensitive to the relative binding energies for the different species present, and the amount of thermal energy present for site to site diffusion. Given sufficient energy, the most strongly binding sites would be expected to be populated by those molecules which bind most strongly. At very low temperature, the site population would be essentially random, though preferential binding is likely to occur during warm up. In thicker ices, the presence of other species and trapping within the ice matrix are also likely to play an important role in the observed desorption, and the TPD of C_6H_6 from within an ASW film is a necessary future experiment. Nevertheless, these experiments provide a basis for understanding the desorption from two relevant surfaces and give an insight into the complex nature of desorption from realistic grain mimics.

In summary, a mimic based on a thin film of amorphous SiO_2 for interstellar dust grains has been developed using electron beam evaporation. AFM has demonstrated the presence of a surface morphology that is reminiscent of that of interplanetary dust grains in terms of a large surface area resulting from surface roughness. PM-RAIRS experiments have confirmed the presence of the SiO_2 film as well as the presence of solid state LO-TO bands that are present in IR studies performed in reflection mode. This was useful in assigning peaks in subsequent RAIR spectra, but is not of direct astrophysical relevance as such splitting is not observed in transmission IR.

TPD experiments have demonstrated strong substrate effects in the thermal desorption of small quantities of C_6H_6 from the interstellar grain mimic. The SiO_2

surface provides a surface area several times larger than the geometric surface area. This surface presents a wide range of binding sites which results in a broad distribution of binding energies. This indicates that C_6H_6, and indeed other molecules, are likely to be retained on a bare grain to significantly higher temperatures than if a single desorption energy is considered. Desorption of C_6H_6 from a thick ASW film displays very different desorption kinetics with a much narrower range of desorption energies. The desorption of small quantities of C_6H_6 display close to first order desorption kinetics, with small deviations from this ideal behaviour arising as a result of island formation. Islanding is also evidenced by dewetting behaviour during the TPD.

RAIRS experiments have also been conducted on C_6H_6 adsorbed on both amorphous SiO_2 and ASW. Poor sensitivity to low coverages of C_6H_6 was observed and attributed to the effect of surface roughness. It is hoped that future experiments conducted on a flat crystalline SiO_2 film will enable further characterization of these small coverages through RAIRS. The spectra that were obtained indicate very little difference between the two systems. For the lowest coverage experiments there is some evidence of small shifts in peak positions compared to calculation vibrational frequencies, which are tentatively attributed to hydrogen-bonding interactions between C_6H_6 and the underlying H_2O or silanol rich SiO_2 surface.

3.8 References

[1] T. J. Rockey, M. C. Yang, and H. L. Dai, *J. Phys. Chem. B*, 2006, **110**, 19973.

[2] W. T. Tysoe, R. M. Ormerod, R. M. Lambert, G. Zgrablich, and A. Ramirez-Cuesta, *J. Phys. Chem.*, 1993, **97**, 3365.

[3] R. Zacharia, H. Ulbricht, and T. Hertel, *Phys. Rev. B*, 2004, **69**, 155406.

[4] R. Zacharia, Ph.D. Thesis, Univ. Berlin, Berlin, 2004

[5] A. M. de Jong and J. W. Niemantsverdriet, *Surf. Sci.*, 1990, **233**, 355.

[6] P. Jakob and D. Menzel, *Surf. Sci.*, 1989, **220**, 70.

[7] Chemical Kinetics Simulator (CKS), version 1.0, IBM Almaden Research Center, 650 Harry Road, Mailstop ZWX1D1, San Jose, CA, USA. Further information may be obtained from the CKS website at http://www.almaden.ibm.com/st/msim/ckspage.html

[8] F. A. Houle and W. D. Hinsberg, *Surf. Sci.*, 1995, **338**, 329.

[9] P. W. Atkins, *Physical Chemistry*, 6th ed., Oxford University Press, Oxford, 1998.

[10] G. D. Waddill and L. L. Kesmodel, *Phys. Rev. B*, 1985, **31**, 4940.

[11] M. Xi, M. X. Yang, S. K. Jo, B. E. Bent, and P. Stevens, *J. Chem. Phys.*, 1994, **101**, 9122.

[12] M. N. Mautner, V. Abdelsayed, M. S. El-Shall, J. D. Thrower, S. D. Green, M. P. Collings, and M. R. S. McCoustra, *Faraday Discuss.*, 2006, **133**, 103.

[13] IDP image obtained from Wikipedia with permission from E. K. Jessberger. Retreived from http://en.wikipedia.org/wiki/Image:Porous_chondriteIDP.jpg on 24/04/2009

[14] M. J. Pilling, S. L. Vent, P. Gardner, A. Awaluddin, P. L. Wincott, M. E. Pemble, and M. Surman, *J. Chem. Phys.*, 2002, **117**, 6780.

[15] F. L. Galeener and G. Lucovsky, *Phys. Rev. Lett.*, 1976, **37**, 1474.

[16] T. B. Wang, Z. G. Liu, and C. Z. Tan, *J. Chem. Phys.*, 2003, **119**, 505.

[17] C. T. Kirk, *Phys. Rev. B*, 1988, **38**, 1255.

[18] J. Lambers and P. Hess, *J. Appl. Phys.*, 2003, **94**, 2937.

[19] M. P. Collings, J. W. Dever, H. J. Fraser, and M. R. S. McCoustra, *Astrophys. Space Sci.*, 2003, **285**, 633.

[20] Z. Dohnálek, G. A. Kimmel, S. A. Joyce, P. Ayotte, R. S. Smith, and B. D. Kay, *J. Phys. Chem. B*, 2001, **105**, 3747.

[21] T. Zubkov, R. S. Smith, T. R. Engstrom, and B. D. Kay, *J. Chem. Phys.*, 2007, **127**, 184707.

[22] L. Hornekaer, A. Baurichter, V. V. Petrunin, A. C. Luntz, B. D. Kay, and A. Al-Halabi, *J. Chem. Phys.*, 2005, **122**, 124701.

[23] L. Amiaud, F. Dulieu, J. H. Fillion, A. Momeni, and J. L. Lemaire, *J. Chem. Phys.*, 2007, **127**, 144709.

[24] S. Bahr and V. Kempter, *J. Chem. Phys.*, 2007, **127**, 074707.

[25] J. Sauer and J.-R. Hill, *Chem. Phys. Lett.*, 1994, **218**, 333.

[26] D. Heidrich, D. Volkmann, and B. Zurawski, *Chem. Phys. Lett.*, 1981, **80**, 60.

[27] M. L. Hair and W. Hertl, *J. Phys. Chem.*, 2002, **74**, 91.

[28] A. Pedone, G. Malavasi, M. C. Menziani, U. Segre, F. Musso, M. Corno, B. Civalleri, and P. Ugliengo, *Chem. Mater.*, 2008, **20**, 2522.

[29] G. Strazzulla and G. A. Baratta, *Astron. Astrophys.*, 1991, **241**, 310.

[30] R. Ruiterkamp, Z. Peeters, M. H. Moore, R. L. Hudson, and P. Ehrenfreund, *Astron. Astrophys.*, 2005, **440**, 391.

[31] A. K. Tripathi, A. Sahasrabudhe, S. Mitra, R. Mukhopadhyay, N. M. Gupta, and V. B. Kartha, *Phys. Chem. Chem. Phys.*, 2001, **3**, 4449.

[32] G. Herzberg, *Infrared and Raman Spectra of Polyatomic Molecules*, 1st ed., Van Nostrand Reinhold Company Inc., New York, 1945.

[33] A. B. Horn, T. Koch, M. A. Chesters, M. R. S. McCoustra, and J. R. Sodeau, *J. Phys. Chem.*, 1994, **98**, 946.

[34] W. Hagen, A. G. G. M. Tielens, and J. M. Greenberg, *Chem. Phys.*, 1981, **56**, 367.

[35] M. W. Schmidt, K. K. Baldridge, J. A. Boatz, S. T. Elbert, M. S. Gordon, J. H. Jensen, S. Koseki, N. Matsunaga, K. A. Nguyen, S. Su, T. L. Windus, M. Dupuis, and J. J. A. Montgomery, *J. Comp. Chem.*, 1993, **14**, 1347.

[36] A. R. Allouche, Gabedit is a free Graphical User Interface for computational chemistry packages. It is available from http://gabedit.sourceforge.net/.

[37] S. Li, V. R. Cooper, T. Thonhauser, A. Puzder, and D. C. Langreth, *J. Phys. Chem. A*, 2008, **112**, 9031.

Appendix 3A FORTRAN 90 program to calculate TPD profiles using a distribution of desorption energies

```
PROGRAM TPDSIM

!PROGRAM TO CALCULATE TPD PROFILE USING A DESORPTION ENERGY DISTRIBUTION
    FUNCTION AND EXPERIMENTAL HEATING RAMP

!DEFINE VARIABLES
IMPLICIT NONE

DOUBLE PRECISION::ORDER, PREEXP, RATE, PUMP, R, NADS, NGAS, NPUMP, TIMESTEP, SAT
    , NORM, CONC, STEPRATE, SHIFT
CHARACTER(20)::FILENAME_OUT, FILENAME_IN, FILENAME_DIST
INTEGER::I, J, STEPS, NAMELENGTH, RESTART, IOSTATUS, DISTSTEPS
DOUBLE PRECISION,ALLOCATABLE::TABLE(:,:), TIME(:), TEMP(:), EXPRATE(:), EDES(:)

!ENSURE THAT PROGRAM PROCEEDS
RESTART=1

!DO LOOP FOR OVERALL PROGRAM OPERATION
DO
    IF(RESTART/=1)exit  !CHECKS TO SEE IF PROGRAM SHOULD PROCEED - WILL EXIT OF
        EXIT IS CHOSEN AFTER A CALCULATION

        !INITIALIZE VARIABLES

        RATE=0      !DESORPTION RATE
        PUMP=0      !PUMPING SPEED
        NADS=0      !SURFACE CONCENTRATION
        NGAS=0      !GAS PHASE CONCENTRATION
        NPUMP=0     !PUMPED CONCENTRATION
        I=1         !CALCULATION STEP
        STEPS=0     !TOTAL NUMBER OF DATA POINTS IN CALCULATION
        R=8.314472  !IDEAL GAS CONSTANT
        NORM=0      !NORMALIZATION COEFFICIENT
        ORDER=1     !DESORPTION ORDER
        PREEXP=1E13 !PRE-EXPONENTIAL FACTOR
        SHIFT=0     !DESORPTION ENERGY SHIFT IN KJ/MOL


        CALL SYSTEM('CLS') !CLEAR SCREEN

        PRINT*,"*************************************************************"
        PRINT*,"*                                                           *"
        PRINT*,"*                  TPD SIMULATOR 1.2                        *"
        PRINT*,"*       USES EXPERIMENTAL TIME AND TEMPERATURE DATA          *"
        PRINT*,"*       AND DISTRIBUTION OF BINDING SITES FOR C6H6           *"
        PRINT*,"*               WRITTEN BY J.THROWER 2009                   *"
        PRINT*,"*                                                           *"
        PRINT*,"*************************************************************"
        PRINT*,""
        PRINT*,""
        PRINT*,"KINETIC PARAMETERS INITIALIZATION"
        PRINT*,"---------------------------------"
        PRINT*,""
        PRINT*,"Ddesorption order = ", ORDER                            !DISPLAY
            DESORPTION ORDER
        PRINT*,"Pumping Rate = ", PUMP                                  !DISPLAY
            PUMPING SPEED
        PRINT*,"Pe-exponential factor: ",PREEXP, " /s"
        PRINT*,"Enter initial coverage in molecules/cm2: "; READ*, NADS !TAKE
            INITIAL SURFACE CONCENTRATION AS AN INPUT
        PRINT*,""
        PRINT*,"Monolayer saturation is 3.76E13 molecules/cm2"          !
            MONOLAYER SATURATION COVERAGE FOR C6H6
        PRINT*,""
        PRINT*,"EXPERIMENTAL DATA INITIALIZATION"
        PRINT*,"------------------------"
        PRINT*,""
        PRINT*,"Enter input file name: "                                !DATA
            FILE CONTAINING EXPERIMENTAL DATA IN COLUMNS TIME, TEMP, RATE
        PRINT*,"(Maximum 20 characters)"
        PRINT*,"Extension '.csv' will be assumed"; READ*, FILENAME_IN
        PRINT*,""
```

```
PRINT*,""
PRINT*,"OUTPUT SETTINGS"
PRINT*,"---------------"
PRINT*,"Enter output file name"                                    !DATA
    FILE CONTAINING CALCULATED TPD PROFILE
PRINT*,"(Maximum 20 characters)"
PRINT*,"Extension '.csv' will be used"; READ*, FILENAME_OUT



NAMELENGTH=LEN_TRIM(FILENAME_IN)                                   !SET UP
    INPUT FILE
FILENAME_IN=FILENAME_IN(1:NAMELENGTH)//".csv"
OPEN (UNIT=1, FILE=FILENAME_IN)

NAMELENGTH=LEN_TRIM(FILENAME_OUT)                                  !SET UP
    OUTPUT FILE
FILENAME_OUT=FILENAME_OUT(1:NAMELENGTH)//".csv"
OPEN (UNIT=2, FILE=FILENAME_OUT)


WRITE(2,*)  "Time ", "Temperature ", "Experiment ", "EDES ", "Rate ", "
    NGAS ", "NPUMP "        !WRITE COLUMN HEADINGS TO OUTPUT FILE

!COUNT LINES IN PUT FILE AND SET NUMBER OF DATA POINTS IN CALCULATION TO
    THIS VALUE

DO
IF(IOSTATUS<0) EXIT
READ(1,*,IOSTAT=IOSTATUS)
STEPS=STEPS+1
END DO
REWIND(1)           !REWIND INPUT FILE TO START
STEPS=STEPS-1

!DEFINE SIZE OF ARRAYS AS NUMBER OF DATA POINTS

ALLOCATE(TIME(STEPS))
ALLOCATE(TEMP(STEPS))
ALLOCATE(EXPRATE(STEPS))
ALLOCATE(EDES(STEPS))

!READ INPUT FILE AND WRITE TO APPROPRIATE ARRAYS

IOSTATUS=0
DO I=1,STEPS
IF(IOSTATUS<0) EXIT
READ(1,*,IOSTAT=IOSTATUS),TIME(I),TEMP(I),EXPRATE(I)
END DO

!DIPLAY CALCULATION PARAMETERS

PRINT*,""
PRINT*,"INTIALIZING CALCULATION"
PRINT*,"-----------------------"
WRITE(*,"(A,F8.2,A)")" Starting temperature is:",TEMP(1)," K"
WRITE(*,"(A,F8.2,A)")" Final temperature is: ",TEMP(STEPS)," K"
WRITE(*,"(A,F8.2,A)")" Simulation time is: ",TIME(STEPS)," s"
PRINT*,"Number of steps: ",STEPS
PRINT*,""
PRINT*,""

!DEFINE OUTPUT ARRAY

ALLOCATE(TABLE(STEPS,7))

        DO I=1,STEPS                        !DO LOOP TO CALCULATE RATE
            FOR EACH TIME STEP
        TIMESTEP=(TIME(I+1)-TIME(I))        !WORK OUT TIME INCREMENT
            FROM EXPERIMENTAL DATA
        RATE=0                              !CLEAR RATE VALUE
        EDES=27.42071+14.73463*EXP(-NADS/1.7809E13)+2.43792*EXP(-NADS/
```

```
                2.0655E12)+11.51554*EXP(-NADS/2.6598E14)    !DESORPTION
                ENERGY DISTRIBUTION FUNCTION
            EDES=EDES+SHIFT                         !ADD ANY DESORPTION ENERGY
                SHIFT TO DISTRIBUTION FUNCTION
                IF((EDES(I))<0) THEN                !CHECK THAT DESORPTION
                    ENERGY IS POSITIVE SURFACE CONCENTRATION
                EDES=0
                END IF
                    IF(NADS<=0)THEN                 !CHECK THAT SURFACE
                        CONCENTRATION IS STILL POSITIVE
                    RATE=RATE                       !RATE REMAINS ZERO IF ALL
                        MOLECULES HAVE DESORBED
                    ELSE
                    RATE=(PREEXP*NADS**ORDER)*EXP((-EDES(I)*1000)/(R*TEMP(I)
                        ))  !CALCULATE RATE FOR NON-ZEOR SURFACE
                        CONCENTRATION
                    END IF

                    IF(NADS>=((RATE*TIMESTEP))) THEN    !CHECK THAT
                        SUFFICIENT MOLECULES REMAIN FOR FULL DESORPTION
                        IMPLIED BY RATE AND NEXT TIME INCREMENT
                        NADS=NADS-(RATE*TIMESTEP)       !CALCULATE NEW
                            SURFACE CONCENTRATION
                        ELSE
                        NADS=0                          !SET SURFACE
                            CONCENTRATION TO ZERO IF INSUFFICIENT MOLECULES
                            REMAIN FOR IMPLIED DESORPTION
                        END IF

            !WRITE CALCULATION RESULTS TO OUTPUT ARRAY

            TABLE(I,1)=TIME(I)
            TABLE(I,2)=TEMP(I)
            TABLE(I,3)=EXPRATE(I)
            TABLE(I,4)=EDES(I)
            TABLE(I,5)=RATE
            TABLE(I,6)=NGAS
            TABLE(I,7)=NPUMP

            !CALCULATE GAS PHASE CONCENTRATION FOR NEXT STEP

            NGAS=NGAS+(RATE*TIMESTEP)-(PUMP*NGAS*TIMESTEP)
                IF(NGAS<0) THEN
                NGAS=0
                END IF

            !CALCULATE PUMPED CONCENTRATION FOR NEXT STEP

            NPUMP=NPUMP+(PUMP*NGAS*TIMESTEP)

        END DO  !REPEATS FOR ALL DATA POINTS IN INPUT FILE

        !WRITE OUTPUT TO FILE

        DO I=1,STEPS
        WRITE(2,*) TABLE(I,:)
        END DO

        !REPORT COMPLETION OF CALCULATION

        PRINT*,"CALCULATION COMPLETED"
        PRINT*,""
        PRINT*,"OUTPUT WRITTEN TO ", FILENAME_OUT       !REPORT OUTPUT FILE NAME
        PRINT*,""
        PRINT*,"Calculate again? (1:YES 0:NO):"         !ASK USER WHETHER NEW
            CALCULATION IS REQUIRED

        READ*,RESTART
        DEALLOCATE(TABLE,TIME,TEMP,EXPRATE,EDES)        !CLEAR ARRAY FOR NEW
            CALCULATION

END DO




         PRINT*,"EXITING TO COMMAND PROMPT"                     !EXIT PROGRAM
         PRINT*,""

         CALL SYSTEM('PAUSE')                                   !DISPLAY OPERATING
             SYSTEM PAUSE PROMPT


         END PROGRAM TPDSIM
```

CHAPTER 4 - Photon Irradiation of C_6H_6 / H_2O Ices

4.1 Introduction

This chapter describes experiments performed to study the photodesorption of C_6H_6 and H_2O molecules from pure and binary layered systems consisting of the two ices. Desorption was induced by exciting an electronic transition in the C_6H_6 molecule with laser radiation in a wavelength range at which H_2O does not absorb. This meant that any desorption detected was due to resonant absorption of photons by C_6H_6 molecules, or thermal processes resulting from absorption by the underlying substrate. The electronic spectroscopy of C_6H_6 will be discussed to highlight the chosen electronic transition, followed by a discussion of the experimental procedure employed. The absorption properties of the adsorbed films will be discussed in relation to calculated film thicknesses, followed by a consideration of both the dynamics of desorption observed through time-of-flight (ToF) experiments, and the non-thermal desorption kinetics obtained through the photon induced desorption decay. Finally the astrophysical implications of these observations will be discussed.

4.2 Electronic spectroscopy of C_6H_6

In these experiments, desorption was initiated by exciting electronic transitions within the C_6H_6. The electronic spectroscopy of the C_6H_6 molecule will therefore be considered. For this, and other polyatomic molecules, the book by Herzberg [1] is an extremely valuable resource. C_6H_6 belongs to the D_{6h} point group which contains one C_6 axis, six C_2 axes perpendicular to C_6, six σ_v planes, one σ_h plane, one each of C_2, C_3 and S_6 axes coincident with C_6 and a centre of inversion, *i*. The manner in which the C and H atomic orbitals form the molecular orbitals of C_6H_6 is shown in the correlation diagram in **Figure 4.1**.

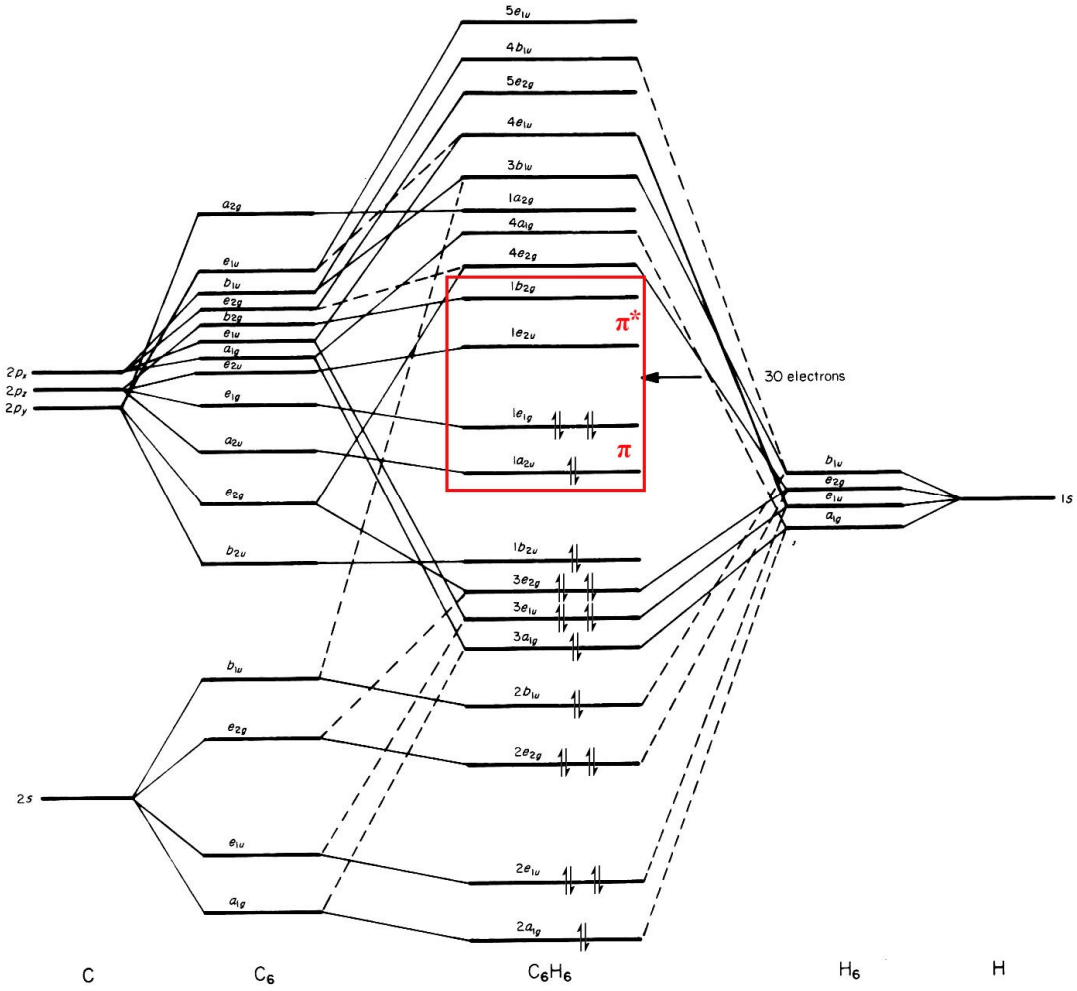

Figure 4.1: Correlation diagram for C_6H_6. The six π orbitals are highlighted in red. From [1].

In this diagram, the core C 1s atomic orbitals are not shown, which results in a series of molecular orbitals (MOs) occupied by a total of 30 valence electrons. The most important MOs are those formed by the overlap of the C p_z orbitals, which are the π bonding and π^* anti-bonding orbitals in which electron density is delocalised above and below the plane of the C_6H_6 molecule. Hückel theory shows that these are formed by the addition of the atomic orbital wavefunctions to obtain six orbitals; four of which form two degenerate pairs of orbitals. These orbitals are shown schematically in **Figure 4.2**. The correlation diagram in **Figure 4.1** shows the electron configuration for the ground electronic $^1A_{1g}$ state. This term arises as the doubly degenerate e_{1g} orbital is filled, which results in a totally symmetric A state. The singlet ground state is also referred to as S_0. The lowest energy electronic transition is the $\pi \rightarrow \pi^*$ promotion of an electron from the e_{1g} bonding orbital to the e_{2u} antibonding orbital.

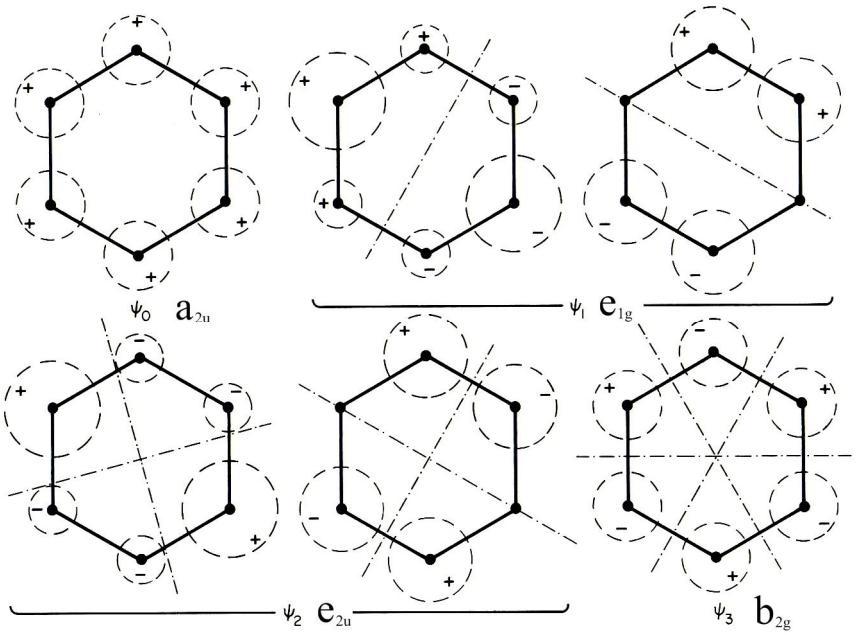

Figure 4.2: The π orbitals of C_6H_6. Only the portion of the wavefunction above the molecular plane is shown. The functions have opposite sign on the other side of the plane. The dashed lines indicate nodal planes. From [1].

This leads to two non-equivalent electrons in e_1 and e_2 orbitals, which for D_{6h} symmetry results in the direct product $E_{1g} \times E_{2u} = B_{1u} + B_{2u} + E_{1u}$. This results in six possible states, considering both singlets and triplets. The lowest energy state that can be accessed from S_0 is the $^1B_{2u}$ state, which will be referred to as S_1. Therefore the $S_1 \leftarrow S_0$ transition can be written $^1B_{2u} \leftarrow {}^1A_{1g}$. Electronic transitions are allowed when:

$$\int \psi^{ii} \hat{\mathbf{M}} \psi^{i} d\tau \neq 0 \qquad \textbf{Equation 4.1}$$

where ψ^i and ψ^{ii} are the excited and ground state wavefunctions respectively, $\hat{\mathbf{M}}$ is the dipole moment operator and $d\tau$ indicates integration over spatial coordinates. Therefore, the product of the two wavefunctions must contain the same species as one of the components of $\hat{\mathbf{M}}$. However, the direct product of an A_{1g} and a B_{2u} state is B_{2u} which is not the same as either of the components of the dipole moment operator (which are A_{2u} and E_{1u} for D_{6h}). The transition is therefore electronically forbidden. However, if the vibrational part of the wavefunction is considered, the transition is weakly allowed through vibronic transitions. A transition will then be allowed if the product of the vibrational wavefunctions of the two states contains at least one component of the electric

dipole moment. Vibrations having symmetry b_{1g} or e_{2g} will therefore result in an allowed transition. C_6H_6 has no b_{1g} vibrations and the transition is thus allowed through excitation of the ν_{18} vibration, which has e_{2g} symmetry (see **Chapter 3**). The observed progression of vibronic absorption features [1] actually indicates excitation of the ring breathing mode, ν_2, which has symmetry a_{1g} and is forbidden unless ν_{18} is also excited. The allowed transitions are shown in **Table 4.1**.

Transition	ν''_{18}	ν'_{18}	ν''_{2}	ν'_{2}
1	1	0	0	0
2	*0*	*0*	*0*	*0*
3	0	1	0	0
4	0	1	0	1
5	0	1	0	2
6	0	1	0	3
7	0	1	0	4
8	0	1	0	5

Table 4.1: Vibronic transitions for the $S_1 \leftarrow S_0$ transition of C_6H_6. Transition 2, shown in italics, is forbidden as a result of there being no excitation of the ν_{18} vibration.

The five strongest allowed transitions can be clearly seen in the gas-phase UV absorption spectrum in **Figure 4.3**.

As the experiments described here were performed using condensed C_6H_6 films deposited at temperatures below 100 K, it is necessary to consider any shifts and broadening observed in the condensed phase UV absorption spectrum. UV/HREELS has been used to obtain the UV absorption spectrum of both multilayer and monolayer films of C_6H_6 adsorbed on Pt(110) [2] revealing a broad multilayer absorption band centred around 4.71 eV (263 nm). This compares well with the absorption maximum observed in the gas phase spectrum. However, the thickest films were only a few multilayers thick which resulted in limited sensitivity to individual vibronic components.

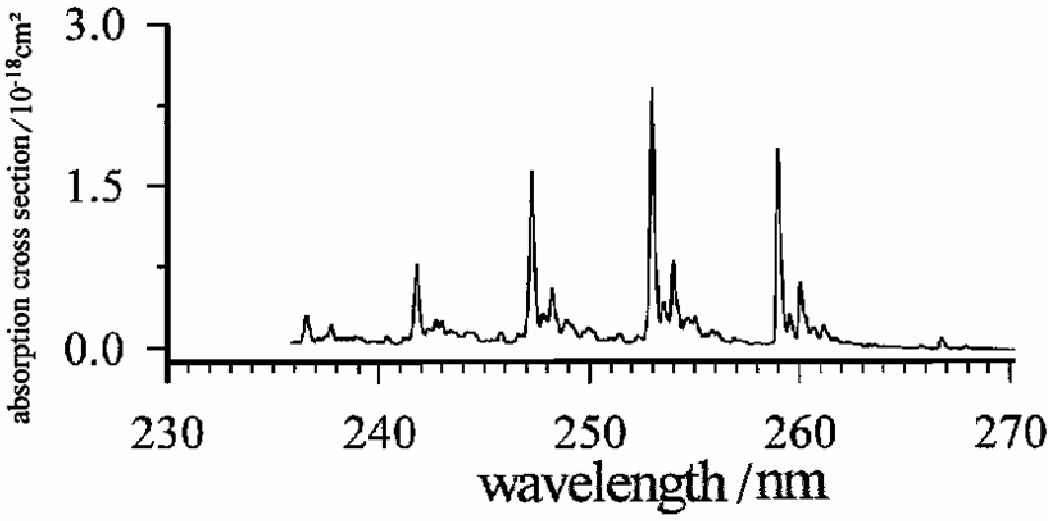

Figure 4.3: UV absorption spectrum of gas phase C_6H_6 showing the vibrational structure of the $S_1 \leftarrow S_0$ transition. Adapted from [3].

It is also possible that the underlying substrate has an effect on such thin films, resulting in different absorption properties compared to bulk ice. Therefore reference was made to recently obtained UV/VUV absorption spectra of C_6H_6 films deposited under similar conditions to those in the present study [4]. From the spectra, UV wavelengths of 250.0 nm (4.96 eV) and 248.8 nm (4.98 eV) were chosen for on-resonance and near-resonance irradiation, whilst 275.0 nm (4.5 eV) was used as an off-resonance reference wavelength. The choice of this vibronic component, rather than the larger one to longer wavelength, was made as it lies at the maximum efficiency of the Comarin 307 dye used in these experiments when pumped at 355 nm. It should be noted that H_2O ice has negligible absorption below around 7.5 eV (165 nm) [5] and can therefore be considered to be non-absorbing in the present case.

4.3 Experimental procedure

The experiments described in this chapter were performed using UHV chamber 2. The overall system set up was described in **Chapter 2**. For all experiments the sapphire substrate was maintained at its base temperature of *ca*. 80 K. Ice films were grown on the substrate by backfilling the chamber with analytical grade C_6H_6 (Sigma-Aldrich) or deionized H_2O. These were introduced *via* a fine leak valve following repeated freeze-pump-thaw cycles to remove dissolved impurities. Doses are reported in Langmuir as measured using the uncalibrated hot cathode ion gauge. Unless otherwise stated, 200 L doses were used. It should be noted that this does not lead to equal C_6H_6 and H_2O film thickness. Dose purity was monitored using the residual gas analyzer attached to the system. Four different systems were studied, (i) pure C_6H_6 ice, (ii) pure H_2O ice, (iii) C_6H_6 on H_2O ice and (iv) H_2O on C_6H_6 ice.

The deposited ice films were irradiated with UV light from the frequency-doubled Nd^{3+}:YAG pumped dye laser arrangement described previously. Three wavelengths were used, with 250 nm being used to resonantly excite the required vibronic component of the $B_{2u} \leftarrow A_{1g}$ electronic transition. A second wavelength, 248.8 nm lies in a local minimum and was used to study near-resonance behaviour. In order to clearly separate resonance effects from other processes that might occur, an off-resonance wavelength of 275 nm was used. The photon order was estimated by performing experiments at two pulse energies, 1.8±0.2 and 1.1±0.1 mJ $pulse^{-1}$ with the errors being determined from typical fluctuations in pulse energy during irradiation. The focusing of the laser beam resulted in the irradiation of a 0.5 mm^2 spot on the substrate, thus the irradiances were 360 and 220 mJ cm^{-2} $pulse^{-1}$. The bandwidth of the laser was 6.25×10^{-4} nm which is far narrower than the absorption features of interest.

Desorbing C_6H_6 and H_2O molecules were detected using the pulse counting quadrupole mass spectrometer. The CEM was operated at -2500 V, which was shown to be within the plateau region of the detector gain. Time-of-flight profiles were obtained using the multichannel scaler. TTL pulses from the auxiliary output of the QMS controller were used as the detection signal, with the discriminator set

to -85 mV. The MCS was triggered by a 1 V pulse obtained from the laser trigger circuit. Data was acquired with 16,000 bins with a bin width of 2.56 μs corresponding to an acquisition time of 41 ms, significantly shorter than the period between laser pulses ensuring that signals from separate shots did not overlap. Data was accumulated for 200 shots unless otherwise stated. In order to further increase the data quality, the data was averaged over multiple spots on the sample surface. Typically, a grid of 30 points across the surface was used.

4.4 Results and discussion

4.4.1 Introduction

In the experiments described in this chapter, two sets of results were obtained. The first of these relates to the dynamics of the process, in particular yielding the fraction of the photon energy partitioned into the translational energy of the desorbing molecules. In this case it is the ToF distributions of the desorbing molecules which contain the relevant information. The other data collected, the mass spectrometer response, contains information on the rate of desorption from which the non-thermal desorption kinetics of molecules desorbing can be determined, and hence the desorption cross-section. These two aspects will be discussed in turn.

4.4.2 Film thickness determination

Before discussing the details of the results it is important to consider the procedure employed for determining estimates of C_6H_6 and H_2O film thicknesses. A knowledge of the thickness of an absorbing film is important in determining how much of the incident energy is absorbed by a particular species. For both C_6H_6 and H_2O, raw exposures of 200 L were used for both species. Correcting for the ion gauge sensitivity factors of 1.1 and 6.0 for H_2O [6] and C_6H_6 [7] respectively. This results in corrected exposures of 182 L for H_2O and 33 L for C_6H_6. It is important to note that in this system, 1 L was defined as 1×10^{-6} mbar s rather than 1×10^{-6} torr s. This was taken into account when converting to the SI units of Pa s. By applying the expression for collision frequency in molecules m^{-2}

s^{-1}[8] the adsorbed surface concentrations, N_{ads} in molecules m^{-2}, can be obtained using the following expression:

$$N_{ads} = \frac{Pt}{\sqrt{2\pi m k_B T}} \qquad \textbf{Equation 4.2}$$

where Pt is the exposure in Pa s, m is the molecular mass of the species of interest, k_B is the Boltzmann constant and T is the gas temperature, assumed to be 298 K as the gases were dosed from a thermal source. A sticking probability of unity was assumed in both cases which is reasonable as 80 K is significantly below the onset of multilayer desorption for both H_2O and C_6H_6. The resulting surface concentrations are 6.5×10^{16} molecules cm^{-2} for H_2O and 5.8×10^{15} molecules cm^{-2} for C_6H_6. In order to determine an approximate film thickness it is necessary to know the density, ρ, of the ice film. As densities are typically sensitive to the nature of deposition, deposition temperature and thermal history of the film it is possible only to obtain estimates in this case. The structure of C_6H_6 has been studied over a wide temperature range using neutron powder diffraction [9]. The discussion was generally limited to crystalline C_6H_6, though at the deposition temperature used in these experiments this is not an unreasonable assumption. The structure consists of four C_6H_6 molecules per unit cell, with the diffraction studies giving a cell parameter, a, of 467 $Å^3$ at a temperature of 80 K. This yields a density, ρ, of 8.57×10^{21} molecules cm^{-3}. It has been shown that the porosity, and hence the density of H_2O films depends both on the substrate temperature, and the angle of incidence of adsorbing molecules [10]. H_2O deposited by background dosing onto a surface at a temperature of 80 K will lead to the formation of a fairly compact amorphous film with limited porosity. Ballistic deposition simulations have shown that [11] a density of ~0.87 g cm^{-3} results if some thermal relaxation is allowed, which significantly reduces the porosity. This corresponds to a density of 2.91×10^{22} molecules cm^{-3}. From these densities and surface concentrations, the film thickness estimates obtained are 22 nm for H_2O and 7 nm for C_6H_6.

4.4.3 Dynamics of desorption products

Results

Figure 4.4 shows a ToF profile for the desorption of C_6H_6 molecules from a 200 L film of C_6H_6 deposited on the sapphire substrate. The photon irradiation wavelength was 250 nm, and the irradiance 360 mJ cm^{-2}. A strong desorption feature is evident with a peak at around 0.6 ms. The raw data is presented, along with a smoothed curve obtained by a 54 point adjacent average routine. This is provided to increase the clarity of the presented data. Qualitatively the peak appears to resemble a Maxwellian distribution of translational energies with a single component. In order to observe the resonance behaviour of the desorption, and to isolate any mechanisms not related to absorption of the UV radiation by C_6H_6 molecules, the ToF profiles for the irradiation of this system using all three wavelengths were compared, as presented in **Figure 4.5**. It should be noted that in this figure, all ToF profiles were obtained with an irradiance of 220 mJ cm^{-2} $pulse^{-1}$ as using the higher irradiance at a wavelength of 275 nm resulted in damage to the optics used to steer the UV beam into the UHV chamber. Of course, using the same irradiance for the three wavelengths means that there will be small differences in the actual photon fluxes in photons cm^{-2} s^{-1}. These fluxes can be obtained by converting the irradiances in terms of energy to units of photons cm^{-2} $pulse^{-1}$. The flux can then be calculated by correcting for the 10 Hz pulse frequency. The resulting fluxes for the two pulse energies are shown in **Table 4.2**. It is clear that the small variations in photon flux between the three wavelengths are actually within the error limits derived from the observed pulse to pulse variation in irradiance. Therefore any differences in desorption can be attributed to wavelength dependence and not flux effects.

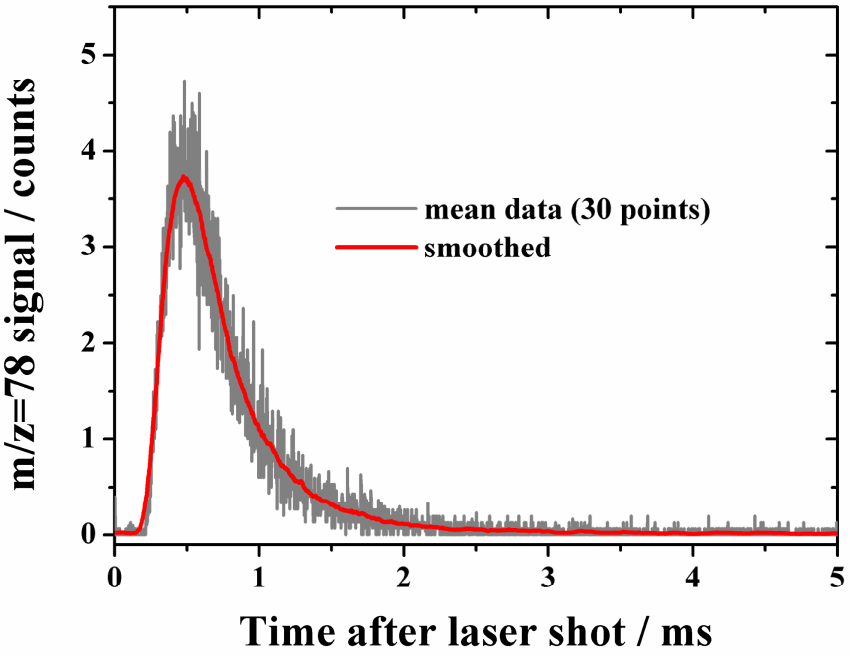

Figure 4.4: ToF profile for the desorption of C_6H_6 molecules from a 200 L film of C_6H_6 deposited on the sapphire substrate. The laser wavelength was 250 nm and the irradiance was 360 mJ cm^{-2} $pulse^{-1}$.

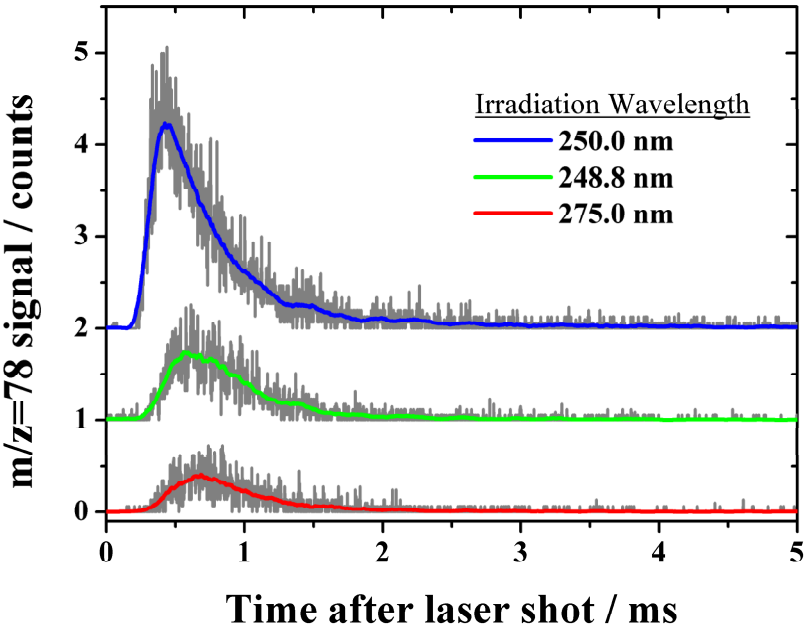

Figure 4.5: ToF profiles for the desorption of C_6H_6 molecules from a 200 L film of C_6H_6 deposited on the sapphire substrate for the three UV wavelengths used. The irradiance was 220 mJ cm^{-2} $pulse^{-1}$.

Wavelength / nm	Photon flux / photons cm^{-2} s^{-1}	
	1.8 mJ pulse^{-1}	*1.1 mJ pulse^{-1}*
250.0	$(4.53\pm0.5)\times10^{18}$	$(2.77\pm0.3)\times10^{18}$
248.8	$(4.51\pm0.5)\times10^{18}$	$(2.76\pm0.3)\times10^{18}$
275.0	$(4.98\pm0.5)\times10^{18}$	$(3.04\pm0.3)\times10^{18}$

Table 4.2: Calculated photon fluxes for the three irradiation wavelengths and the two pulse energies. Errors are derived from the observed ±10% pulse to pulse variation in irradiance.

In discussing the observed ToF profiles, it is important to note that the observed size of the ToF peak is likely to reflect the rate of desorption rather than the actual amount of C_6H_6 or H_2O desorbed. In all cases the irradiation was continued for a significant period of time after the disappearance of the QMS signal, such that it is reasonable to assumed complete desorption of molecules underneath the spot irradiated. **Figure 4.6** illustrates how for small QMS signals as observed during the ToF experiments, the size of the peak can be assumed to correlate with the *rate* of the desorption process. For slow desorption more of the desorption yield will be below the detection limit of the QMS than for faster desorption. The QMS signal is therefore biased towards the rate of desorption. Therefore, the ToF profiles in **Figure 4.5** indicate that the C_6H_6 non-thermal desorption rate is greatest for a wavelength of 250 nm, on resonance with the intended transition. The desorption at 248.8 nm shows a decreased desorption rate in accordance with the reduced absorption cross-section at this, near resonance, wavelength. The desorption can therefore be considered to arise as a result of direct photon absorption by C_6H_6 molecules. Interestingly, some desorption is also observed at the off-resonance wavelength of 275 nm where the absorption cross-section is negligible. This indicates that a second desorption channel involving the substrate must also be active. In order to appreciate this it is important to obtain estimates of the fraction of photons expected to be absorbed by both the C_6H_6 molecules and the sapphire substrate. The absorption cross-section for condensed C_6H_6 has been obtained through VUV experiments [4] and was found to be 4.5×10^{-18} cm^2 at the 250 nm peak and 1.2×10^{-18} cm^2 at the local minimum at 248.8 nm. This is in

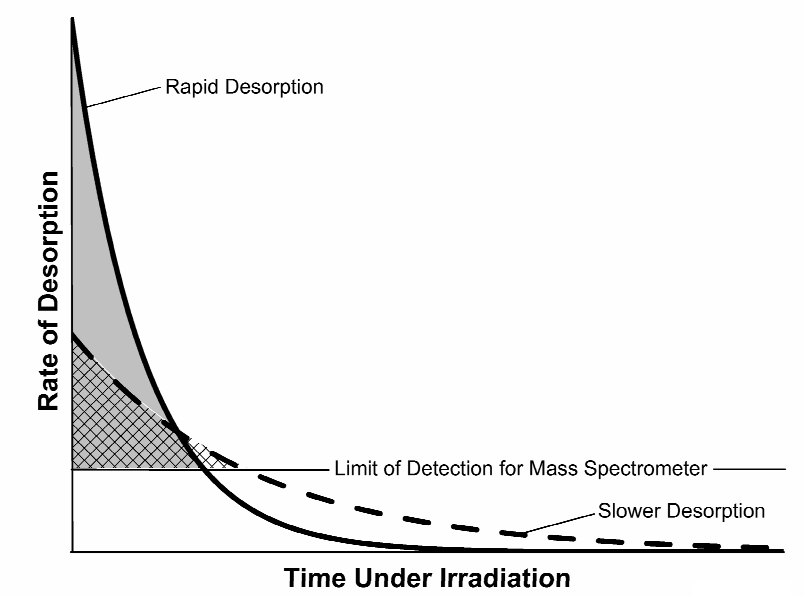

Figure 4.6: An illustration of why a fast desorption process is likely to give rise to a larger desorption yield than a slower desorption process when the detected signal is close to the QMS detection limit.

reasonable agreement with the observed desorption rates at these two wavelengths. These cross-sections correspond to absorption coefficients of 3.9×10^4 cm^{-1} and 1.0×10^4 cm^{-1} respectively assuming the previously quoted number density for C_6H_6. The UV absorption coefficient for sapphire over a wide wavelength range has been studied using a range of techniques and is fairly flat over the range used in these experiments. A typical value of 0.2 cm^{-1} is taken as being representative of absorption over the wavelength range studied [12]. The ratio of transmitted light to incident light intensity, (I/I_0), can be calculated using the Beer-Lambert Law [8]:

$$\frac{I}{I_0} = \exp[-\alpha l] \qquad \textbf{Equation 4.3}$$

where α is the absorption coefficient in cm^{-1} and l is the total path length through the absorbing film in cm. Taking a C_6H_6 film thickness of 7 nm and a sapphire disc thickness of 1 mm yields path lengths of 19 nm and 2.8 mm respectively for a beam incidence angle of 45° to the surface normal. In the case of a benzene film, this analysis suggests that 7% of the incident light is absorbed by the C_6H_6 film at 250 nm and around 5% by the underlying sapphire substrate. It is therefore reasonable to assume that some substrate heating and associated thermal

desorption will occur. This will be referred to as substrate-mediated desorption, and the C_6H_6 desorption following resonant absorption as direct adsorbate-mediated desorption.

Before considering the effect of film morphology on the non-thermal desorption process, it is important to consider the photon order of the process. In the interstellar medium, photon fluxes are much smaller than those obtained in the laboratory. Therefore, only mechanisms involving single photon absorption will contribute to the ice processing and multi-photon processes can be neglected. **Figure 4.7** shows the pulse energy dependence of the desorption signal. The ratio of the desorption yields for these two profiles is 1.64, in excellent agreement with the irradiance ratio of 1.64±0.2. This confirms that the desorption observed is the result of single photon absorption.

Figure 4.8 and **Figure 4.9** show ToF profiles for the desorption of C_6H_6 and H_2O respectively from different layered systems. In both cases the desorption from a single layer of the observed species adsorbed on the sapphire substrate is considered, along with C_6H_6 adsorbed on top of a pre-adsorbed H_2O film, and *vice versa*. For clarity, only the 54 point adjacent averaging curves are plotted for this comparison. Considering first the desorption of C_6H_6 a significant desorption rate is observed when C_6H_6 alone is adsorbed on the sapphire substrate, the direct adsorbate-mediated desorption discussed already. If a thick overlayer of H_2O is adsorbed after the C_6H_6 film, a large decrease in the desorption rate is observed. This can be attributed to the blocking of C_6H_6 by the thick overlayer. However, when C_6H_6 is adsorbed on top of a previously adsorbed thick layer of H_2O the C_6H_6 desorption rate is slightly increased compared to the case of C_6H_6 alone. This can be rationalized by considering likely morphological effects. As has already been discussed, a H_2O film deposited at 80 K is likely to be compact and relatively non-porous and has been shown to have a rough, uneven surface that presents a larger surface area than the geometric surface area [13]. A larger surface area will inevitably lead to an increase in desorption rate as it effectively results in a slight increase in irradiation spot area.

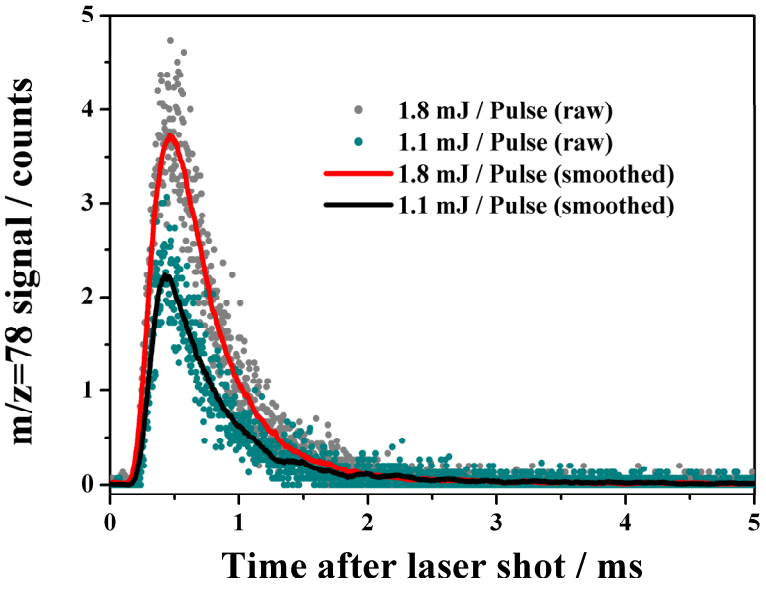

Figure 4.7: C_6H_6 ToF profiles obtained using an irradiation wavelength of 250 nm and pulse energies of 1.1 mJ and 1.8 mJ to assess the photon order of the desorption process.

For the desorption of H_2O following irradiation at 250 nm it is clear that very little desorption occurs when H_2O is deposited alone on the sapphire substrate. This is in agreement with the extremely low absorption by H_2O in this wavelength range. This has been confirmed by Kobayashi [5] who showed that photon absorption by H_2O is negligible at photon energies below around 7.5 eV, *i.e.* at wavelengths longer than 170 nm. The small H_2O desorption observed when it is deposited alone can therefore be attributed to substrate-mediated desorption, where absorption of photons by the underlying substrate leads to local substrate heating and subsequent thermal desorption. As this also seems to play a role in the desorption of C_6H_6 it is reasonable that this should also be the case with H_2O. When C_6H_6 is deposited on top of the H_2O a significantly higher rate of H_2O desorption is observed. As direct adsorbate-mediated desorption involving H_2O has already been discounted, and there is no reason to expect substrate-mediated desorption to change as a function of layer configuration, this must be attributed to a transfer of energy from C_6H_6 molecules to the H_2O film following resonant absorption. This will be referred to as indirect adsorbate-mediated desorption. A slightly enhanced H_2O desorption rate is also observed when the H_2O is deposited

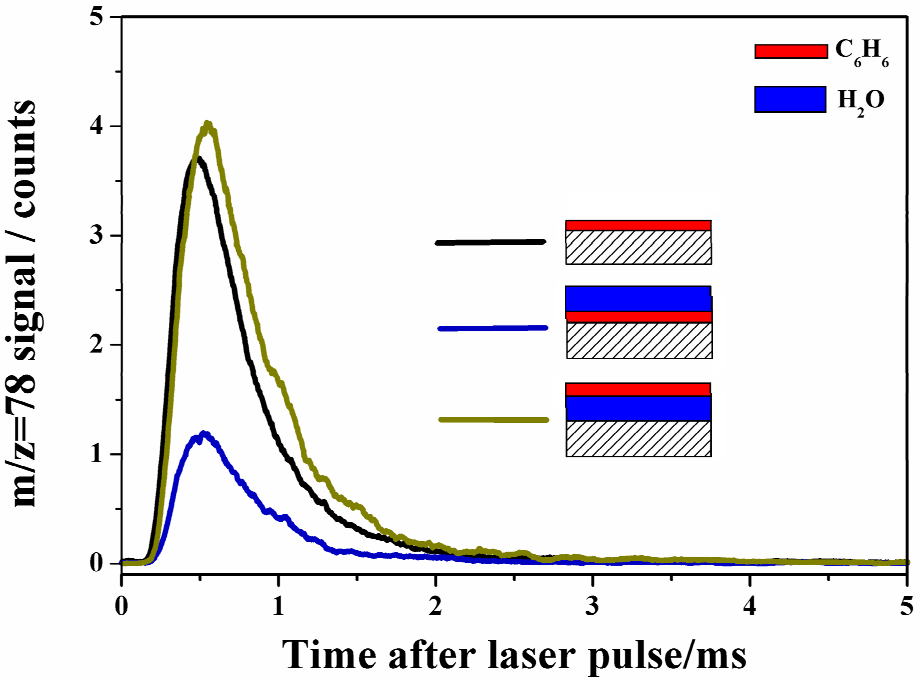

Figure 4.8: ToF profiles for C_6H_6 desorption following irradiation at 250 nm using a pulse energy of 1.8 mJ. The different profiles relate to the film layering depicted schematically.

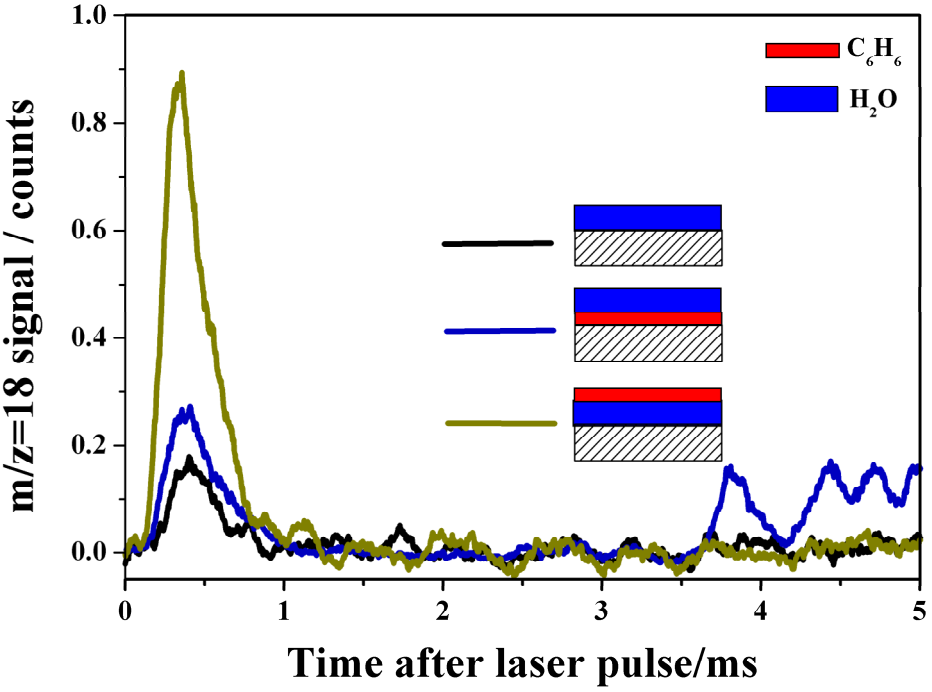

Figure 4.9: ToF profiles for H_2O desorption following irradiation at 250 nm using a pulse energy of 1.8 mJ. The different profiles relate to the film layering depicted schematically.

on top of a pre-adsorbed C_6H_6 layer, though to a far lesser extent. These observations can again be attributed to ice morphological effects. The important region in the ice is the interface between the H_2O film and the C_6H_6 film as this is where energy transfer from one species to the other will be most efficient.

Considering first the case of C_6H_6 adsorbed on top of H_2O, it has already been indicated that the C_6H_6 film is relatively thin. It is known that H_2O does not wet a graphite surface [14,15]. It has also already been shown in this thesis that C_6H_6 forms islands on a H_2O ice film. It therefore follows that (a) the C_6H_6/H_2O interface is beneath a relatively thin C_6H_6 layer which results in the desorption of H_2O being relatively unhindered by the overlayer and (b) there will be regions where the C_6H_6/H_2O interface is exposed to vacuum which would also contribute to a higher desorption rate. However, when H_2O is deposited on top of the C_6H_6 film, the thick overlayer of H_2O blocks H_2O desorption from the C_6H_6/H_2O interface, in the same way as for the desorption of C_6H_6, resulting in a reduced desorption rate. The film morphologies described here are shown schematically in **Figure 4.10**.

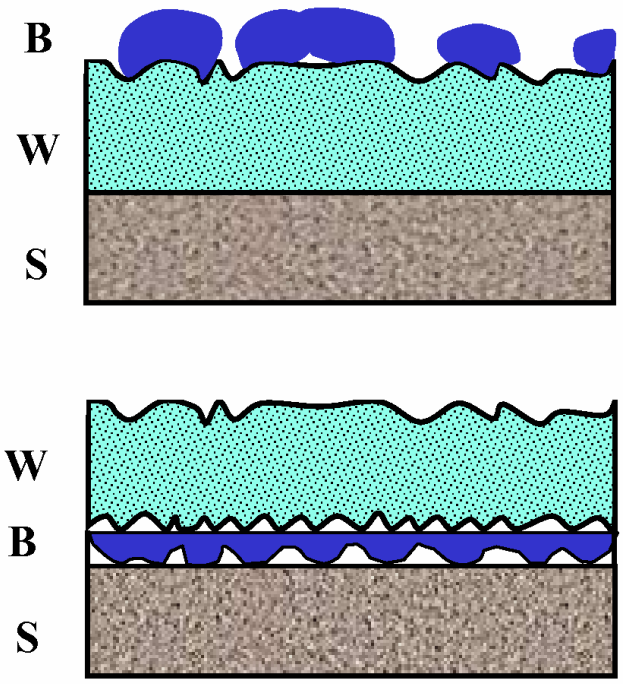

Figure 4.10: Cartoon illustrating the morphologies of the layered ice systems. The ice morphology has a significant effect on the observed desorption rate.

The ToF profile for water desorption from the H_2O on C_6H_6 system shown in **Figure 4.9** shows a series of features at around a flight time of 4 ms. This can be more clearly seen in **Figure 4.11** which shows the same ToF profiles as **Figure 4.9** but on an expanded time scale of up to 20 ms. An extremely broad desorption feature is present in the case of the H_2O on C_6H_6 system which extends from 4 ms to over 15 ms. No further desorption was observed at longer times. Interestingly, this feature is only present for this particular layer configuration, with no late desorption features being observed for the C_6H_6 on H_2O system or when H_2O was deposited alone. This feature was present for the H_2O on C_6H_6 system at both wavelengths where H_2O desorption was observed as shown in **Figure 4.12**, and also at both laser pulse energies employed. The late H_2O desorption feature is attributed to the desorption of H_2O clusters from the C_6H_6/H_2O interface region. The detection of these clusters *via* the m/z=18 channel of the QMS then results from the disintegration of these clusters within the ionization source of the QMS. It is important to note that as no m/z channels corresponding to $(H_2O)_n$ clusters for n>1 were monitored there is no direct evidence for H_2O clusters. Nevertheless, it is reasonable that H_2O clusters of a range of sizes would (a) be produced by the adsorbate-mediated desorption mechanism and (b) would be subject to a distribution of long flight times reflecting their mass distribution and the energy partitioning during fragmentation of the adsorbate-surface complex. No equivalent late C_6H_6 desorption feature was observed, which is interesting considering that the presence of C_6H_6 is required for such a feature to be observed in the H_2O desorption. Whilst there was some spot to spot variation in the intensity of the late H_2O ToF feature, it was generally fairly reproducible. For improved clarity, full timescale (up to 40 ms) ToF profiles for H_2O desorption from the H_2O on C_6H_6 system following irradiation at 250.0 and 248.8 nm with a pulse energy of 1.8 mJ are shown in **Figure 4.13**. This clearly demonstrates the reproducibility of the shape of the desorption feature and its position, being peaked at around 10 ms. Desorption is discernible up to times as late as 30 ms. The sharp features observed in this, and previous figures showing this feature, are attributed to artefacts introduced during the smoothing procedure, as no fine structure is observed in the raw profiles.

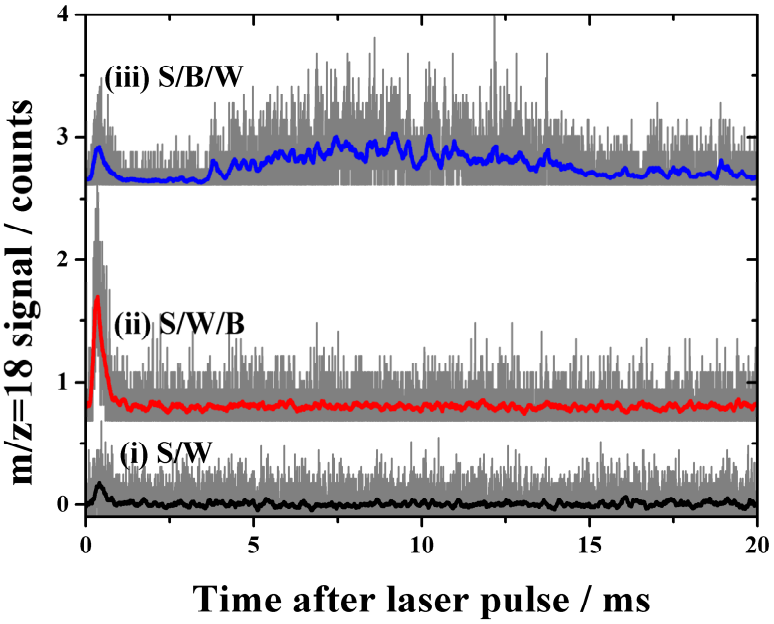

Figure 4.11: ToF profiles for the desorption of H_2O from various layer configurations where S, B and W refer to sapphire, C_6H_6 and H_2O respectively. The pulse energy was 1.8 mJ and the laser wavelength was 250.0 nm in all cases. The grey lines are the averaged raw data and the coloured thick lines are smoothed. The profiles have been offset for clarity.

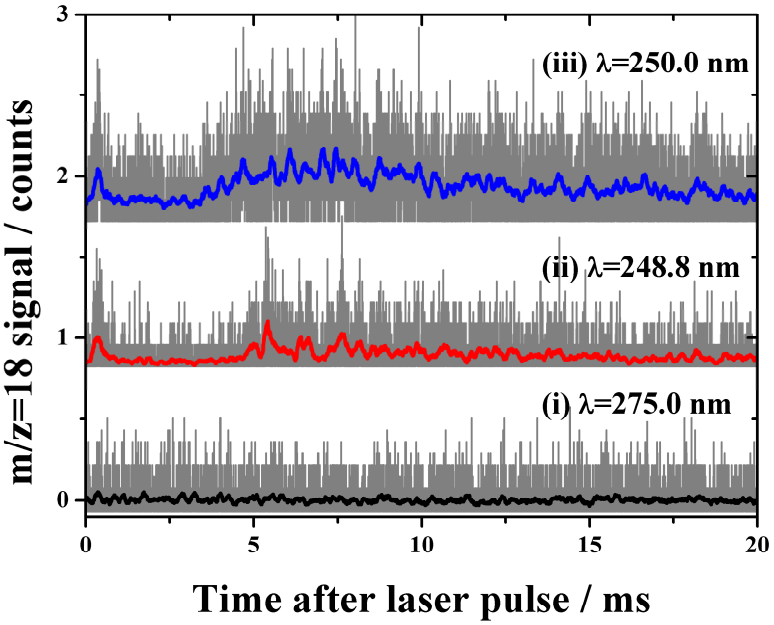

Figure 4.12: ToF profiles for the desorption of H_2O from the S/B/W system at the three laser wavelengths. The pulse energy was 1.1 mJ in all cases. The grey lines are the averaged raw data and the coloured thick lines are smoothed. The profiles have been offset for clarity.

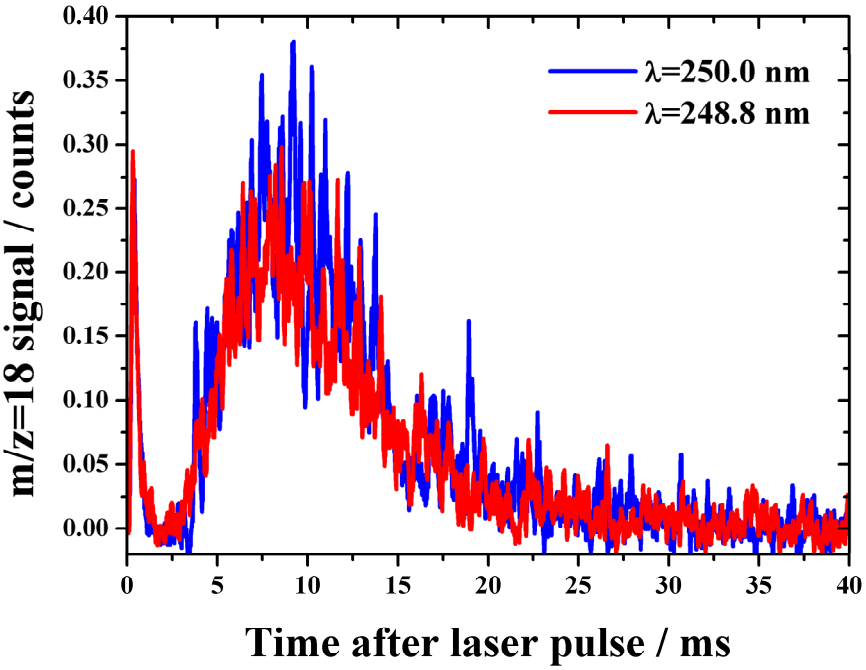

Figure 4.13: Full timescale ToF profiles for the desorption of H_2O from the C_6H_6 system following irradiation at 250.0 and 248.8 nm using a pulse energy of 1.8 mJ.

Analysis and discussion

In order to gain further insight into the mechanisms behind the desorption observed, the ToF profiles were fit with Maxwellian functions in order to obtain the translational temperatures of desorbing molecules. The fitting of ToF profiles has been discussed at length [16] along with the importance of using the correct distribution function for fitting. The expression for a density sensitive detector, such as a QMS, where the signal is proportional to the number density of molecules in the ionization source, was used:

$$S(t) \propto \frac{1}{t^4} \exp\left(-\frac{mr^2}{2k_B T} \cdot \frac{1}{t^2} \right) \qquad \textbf{Equation 4.4}$$

where t is the flight time, m is the molecular mass and T is the translational temperature of desorbing molecules. In order to apply this expression to the obtained profiles, the following functional form was used:

$$S(t) = A\frac{r^4}{t^4}\exp\left(-\frac{mr^2}{2k_B T}\cdot\frac{1}{t^2}\right) \qquad \textbf{Equation 4.5}$$

where A is a scaling parameter. In order to perform the required fitting, it was necessary to determine the flight path length for desorbing molecules, r, which is simply the distance between the surface and the ionization source of the QMS, measured as 0.307 m. In order to use this path length it is necessary to account for the time taken for the ions generated in the ionization source to reach the channeltron where they are detected. These times were calculated for both H_2O and C_6H_6 by considering acceleration into the mass filter by a focus voltage, V_F of 90 V and a mass filter entrance to channeltron distance, r', of 0.18 m. It was assumed that the ions had an initial velocity component of 0 m s^{-1} in the direction of the mass filter. For a singly charged ion, the time correction, t', is:

$$t' = r'\left(\frac{m}{2eV_F}\right)^{1/2} \qquad \textbf{Equation 4.6}$$

where e is the electronic charge, 1.60×10^{-19} C. The associated time corrections for C_6H_6 and H_2O were 1.2×10^{-5} s and 5.8×10^{-6} s respectively. These corrections are relatively minor for the detection system used in these experiments, where the long flight path leads to flight times of the order of a few ms. It is clear that in experiments where the flight path is only a few mm, which is not uncommon, such corrections are essential. Nevertheless, the experimental flight times were corrected accordingly.

Single component fits to the ToF profiles observed for the desorption of C_6H_6 from the sapphire substrate at pulse energies of 1.1 and 1.8 mJ are shown in **Figure 4.14** and **Figure 4.15** respectively. The translational temperatures obtained support the previous suggestion that two desorption channels, direct adsorbate-mediated desorption, and substrate mediated desorption play a role in this case. At the lower pulse energy of 1.1 mJ the irradiation at the on-resonance wavelength of 250.0 nm results in the desorption of C_6H_6 with a translational temperature of >1100 K, far in excess of the substrate temperature. It is clear that the direct adsorbate-mediated desorption channel is dominant in this case. At the off-resonance wavelength of 275 nm the translational temperature is significantly

lower with a value of *ca.* 530 K resulting from the fit. This can therefore be attributed to localised heating of the sapphire substrate under the laser spot, leading to thermal desorption of C_6H_6. As discussed already, it is reasonable to assume that this component is present at all three wavelengths. Therefore at 248.8 nm, the presence of two components leads to a single component fit translational temperature somewhere between the two extremes. At the higher pulse energy of 1.8 mJ the same general trend is observed, though irradiation at 275 nm was not possible, as discussed previously, which means that a translational temperature for the substrate mediated component was not obtained at this higher energy. For this reason, only the pulse energy of 1.1 mJ will be considered in the subsequent discussion. It is worthwhile noting, however, that it is reasonable to expect that the increased photon flux would lead to an increased degree of localized heating, which would result in an increase in translational temperature for the substrate-mediated desorption component. This would explain the increased translational temperature observed for the irradiation at 248.8 nm compared to that obtained at the lower pulse energy.

In order to properly assess the contributions of the two components, two component fits were performed using two strategies. In the first, the two translational temperatures, T_1 and T_2, along with the two scaling factors, A_1 and A_2, were used as fitting parameters:

$$S(t) = A_1 \frac{r^4}{t^4} \exp\left(-\frac{mr^2}{2k_B T_1} \cdot \frac{1}{t^2} \right) + A_2 \frac{r^4}{t^4} \exp\left(-\frac{mr^2}{2k_B T_2} \cdot \frac{1}{t^2} \right). \qquad \textbf{Equation 4.7}$$

In the second approach, the substrate-mediated desorption component channel was fixed at 530 K as obtained from the single component fit for the profile obtained with a wavelength of 275 nm. This relies on the reasonable assumptions that (a) only this channel is in operation at the off-resonance wavelength and (b) the translational temperature resulting from this channel is independent of wavelength as a result of the flatness of the sapphire absorption coefficient over the wavelength range studied. The contributions of each component, related to A_1 and A_2 were still used as fitting parameters.

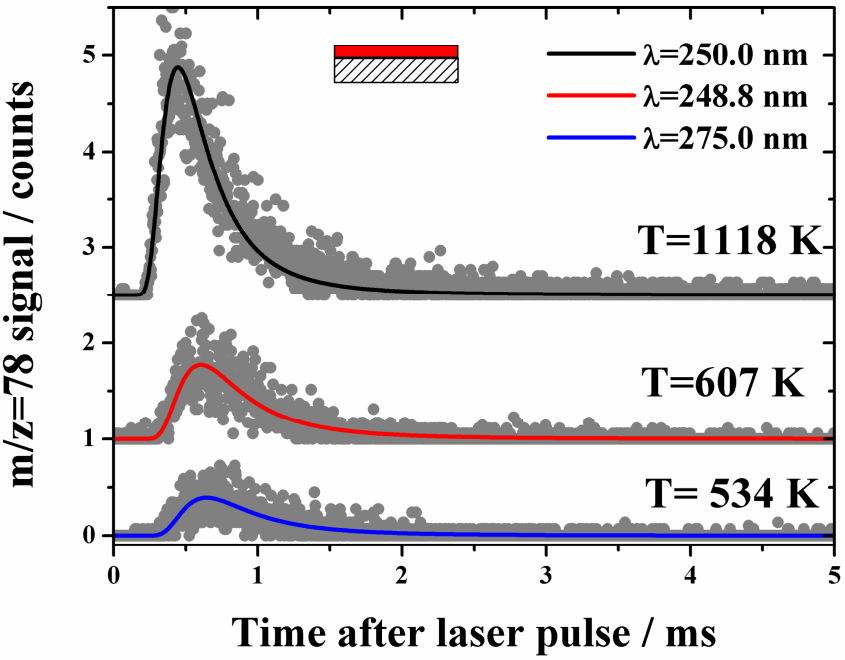

Figure 4.14: ToF profiles and single component fits for the desorption of C_6H_6 from the sapphire under irradiation at all three laser wavelengths. The pulse energy was 1.1 mJ in all cases. Traces have been offset for clarity.

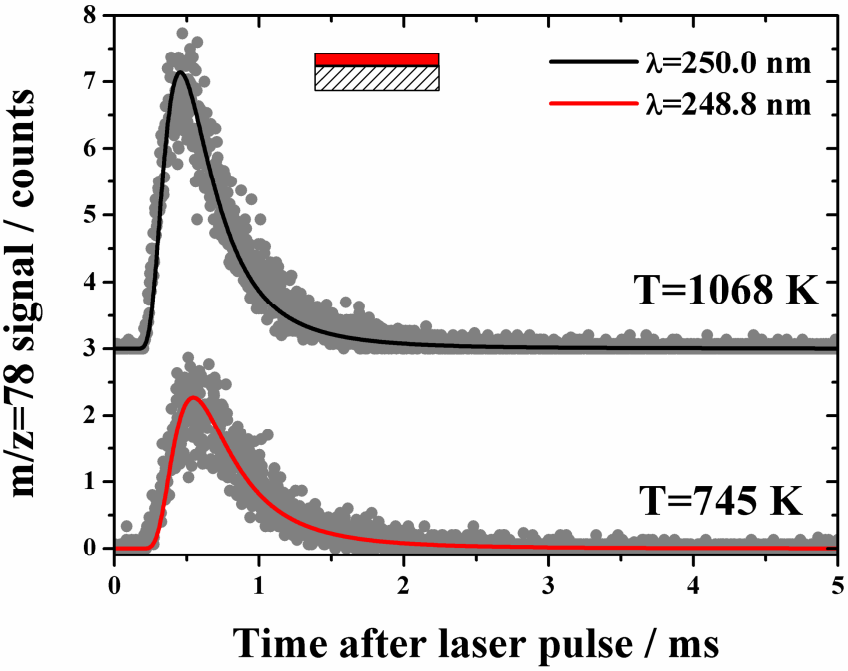

Figure 4.15: ToF profiles and single component fits for the desorption of C_6H_6 from the sapphire under irradiation at laser wavelengths of 248.8 and 250.0 nm. The pulse energy was 1.8 mJ in all cases. Traces have been offset for clarity.

The expression is modified thus:

$$S(t) = A_1 \frac{r^4}{t^4} \exp\left(-\frac{mr^2}{1060 k_B} \cdot \frac{1}{t^2} \right) + A_2 \frac{r^4}{t^4} \exp\left(-\frac{mr^2}{2 k_B T_2} \cdot \frac{1}{t^2} \right) \qquad \textbf{Equation 4.8}$$

Two component fits for the desorption of C_6H_6 from the sapphire substrate with a pulse energy of 1.1 mJ in which both translational temperatures were allowed to vary are shown in **Figure 4.16**. In **Figure 4.17** the same profiles are fitted using a two component scheme in which one component is fixed at 530 K to represent the substrate-mediated desorption component. Only this component is present for irradiation at 275 nm as it is assumed that only this desorption channel operates at this wavelength. The fits in which both translational temperatures were allowed to vary demonstrate the general trends revealed by the single component fits *i.e.* the presence of a high temperature and a low temperature component. Clearly the high temperature component is dominant when the on-resonance wavelength is used, with the low temperature component resulting from the substrate-mediated channel is relatively minor. With the off-resonance wavelength the substrate-mediated channel dominates, though a very small high temperature component is present. This may be an artefact of the fitting procedure. Given the small size of this component, its impact on the overall desorption is negligible. At 248.8 nm the two components are of approximately equal size, though the high temperature component appears to have a significantly lower temperature than that obtained at 250 nm. Given the relatively small difference in photon energy between these two wavelengths, such a large difference in translational temperature does not seem reasonable. Moreover, there is no reason to expect the observed variation in the temperature of the low temperature component given the invariance of sapphire absorption coefficient over this wavelength range. It is therefore likely that the full two component fits allow too much flexibility, given the quality of the data, to yield physically realistic values. Therefore, the approach where the low temperature component was fixed at 530 K is considered to be more reliable. Using this approach the high temperature components for the profiles observed for irradiation at 250 and 248.8 nm are 1190 and 1032 K respectively.

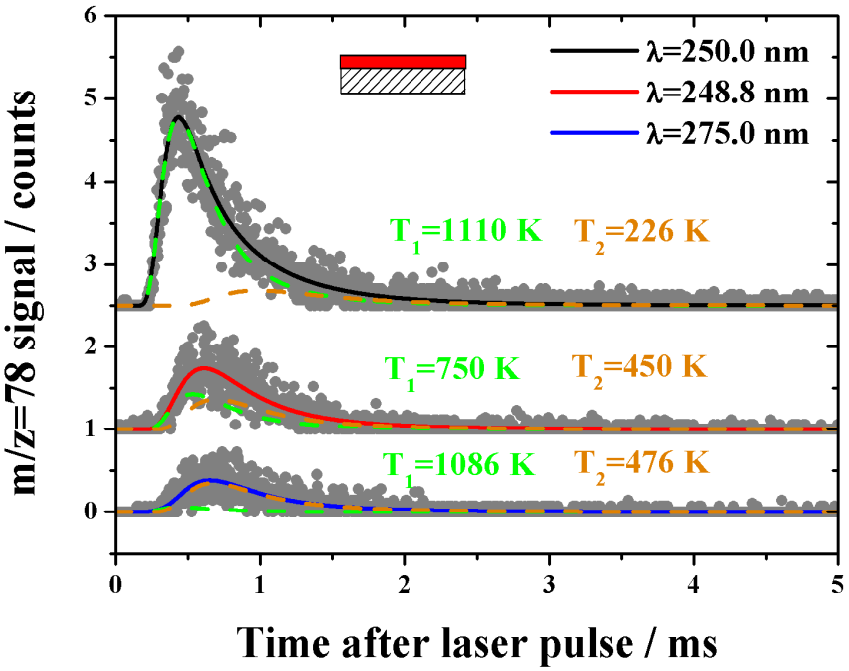

Figure 4.16: Two-component fits to C_6H_6 ToF profiles obtained using a pulse energy of 1.1 mJ. The translational temperatures of both components were used as fitting parameters. Individual components are shown in green and orange. Traces have been offset for clarity.

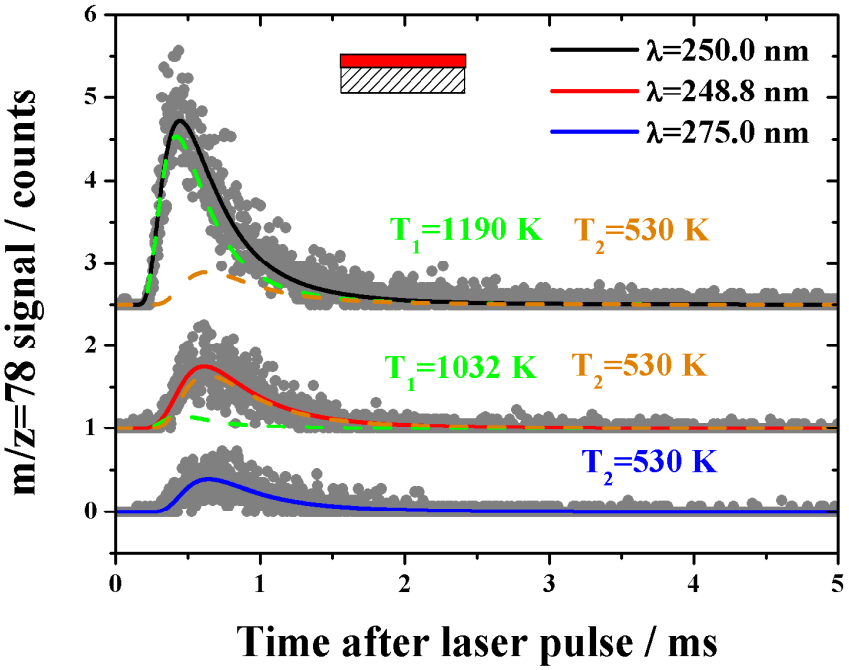

Figure 4.17: Two-component fits to C_6H_6 ToF profiles obtained using a pulse energy of 1.1 mJ. The translational temperature of one component was fixed at 530 K, and used for the single component fit to the 275.0 nm profile. Individual components are shown in green and orange. Traces have been offset for clarity.

The same fitting procedure was employed to fit the C_6H_6 from the layered systems. The obtained components for the desorption of C_6H_6 from all layer configurations for an irradiation wavelength of 250 nm are shown in **Table 4.3**. This results in a translational temperature for the direct adsorbate-mediated component of 1150±200 K. Considering the relative error to be the same in the case of the substrate mediated component yields a translation temperature of 500±100 K.

Layer configuration	Wavelength / nm	Pulse energy / mJ	T_1/K	T_2/K
S/B	250.0	1.8	1340	530
S/B/W	250.0	1.8	1200	530
S/W/B	250.0	1.8	1190	530
S/B	250.0	1.1	1190	530
S/B/W	250.0	1.1	1069	530
S/W/B	250.0	1.1	901	530

Table 4.3: Translational temperatures for C_6H_6 desorption following irradiation at 250 nm obtained using fits where a substrate mediated component with a temperature of 530 K was assumed to play a role.

The H_2O ToF profiles were also fit using the same form of function. However, the desorption at 275 nm was too small to obtain a reliable fit for the substrate-mediated component. The ToF profiles were therefore fit with a single component function to represent the indirect adsorbate-mediated desorption channel where resonant absorption by the C_6H_6 molecule results in desorption of H_2O *via* some energy transfer mechanism. The use of single component fit is likely to be valid as a result of the dominance of this channel in the desorption of H_2O. The resulting fits for the two layered systems in which C_6H_6 was also present are shown in **Figure 4.18** and **Figure 4.19** for pulse energies of 1.1 and 1.8 mJ respectively. The data for an irradiation wavelength of 250 nm is shown, though similar fits were obtained for the case of 248.8 nm. In all cases, a single component fit with a translational temperature of *ca.* 450 K reproduces the experimental profiles for H_2O desorption well. A summary of the obtained translation temperatures, T_w, for irradiation at 250 nm are shown in **Table 4.4**. This analysis yields a translational temperature for H_2O molecules desorbing *via* the indirect adsorbate-mediated desorption channel of 460±60 K.

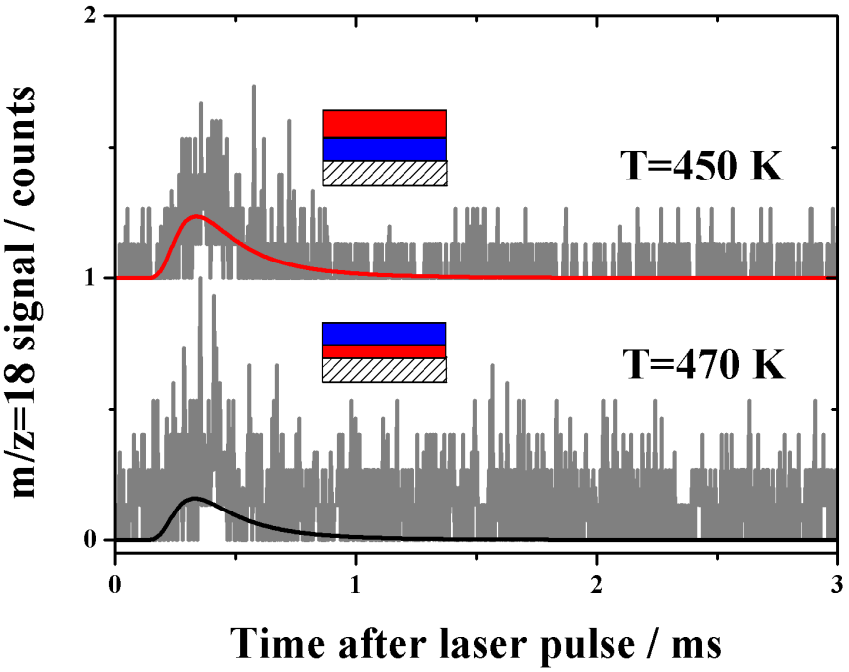

Figure 4.18: Single component fits for H_2O desorption from layered systems when irradiated at 250 nm. The pulse energy was 1.1 mJ. Traces have been offset for clarity.

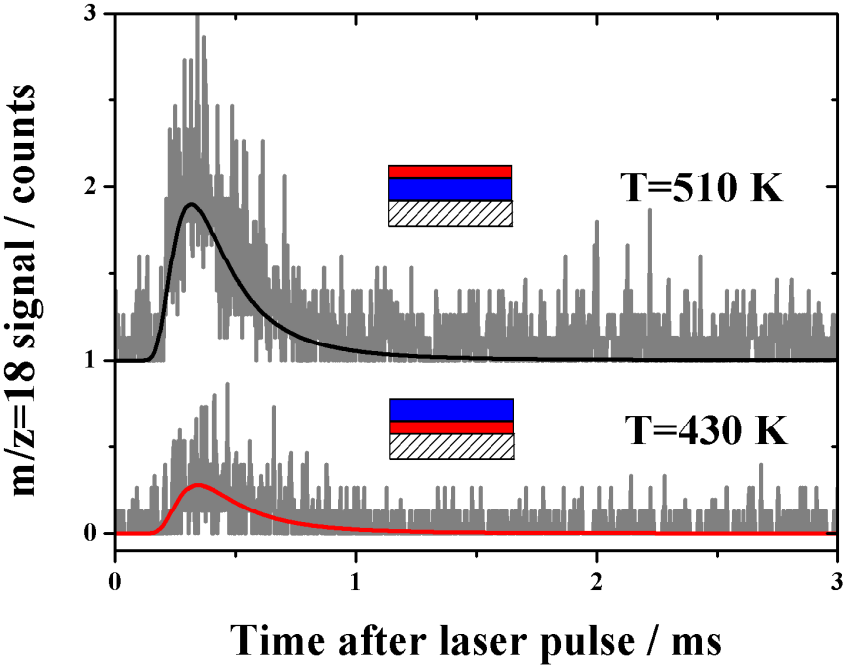

Figure 4.19: Single component fits for H_2O desorption from layered systems when irradiated at 250 nm. The pulse energy was 1.8 mJ. Traces have been offset for clarity.

Layer configuration	Wavelength / nm	Pulse energy / mJ	T_w/K
S/B/W	250.0	1.8	430
S/W/B	250.0	1.8	510
S/B/W	250.0	1.1	470
S/W/B	250.0	1.1	450

Table 4.4: Translational temperatures for H_2O desorption following irradiation at 250 nm obtained using single component M-B fits.

The desorption mechanisms will now be considered in more detail. The desorption mechanisms in operation are summarized in **Table 4.5**.

Desorbing species	Secondary species	Substrate-mediated	Direct adsorbate-mediated	Indirect adsorbate-mediated
C_6H_6	None	✓	✓	×
H_2O	None	✓	×	×
C_6H_6	H_2O	✓	✓	×
H_2O	C_6H_6	✓	×	✓

Table 4.5: Summary of desorption channels in operation.

The substrate mediated desorption channel can be interpreted as arising as a result of rapid heating of the sapphire substrate during the irradiation pulse. This heating depends on the absorption of energy by and heat flow within the substrate [17]. Here, laser heating of metals was considered, though the arguments involve only bulk properties of the solid and are therefore applicable in the present non-metallic case. In general terms, the temperature, T, at a particular position in the substrate, defined by x, y and z, as a function of time, t, obeys the heat conduction equation, which applies for all materials:

$$\rho c \frac{\partial T}{\partial t} = k_T \nabla T + AI(x, y, z, t) \qquad \textbf{Equation 4.9}$$

where ρ is the substrate material density, c is the specific heat and k_T is the heat conductivity. A is the fraction of incident energy, I, absorbed by the substrate. In the simplest approximation I is assumed to not vary with time and the one-dimensional solution is obtained where T is obtained as a function of z and t. For the top of the surface, where z=0, this solution has the form:

$$T(t) = \frac{2AI}{k_{\mathrm{T}}}\sqrt{\frac{\kappa t}{\pi}} \qquad \textbf{Equation 4.10}$$

where κ is the thermal diffusivity given by:

$$\kappa = \frac{k}{\rho c}. \qquad \textbf{Equation 4.11}$$

This expression is valid under the semi-infinite solid approximation where the sample thickness is significantly greater than the heat wave propagation length, l_{th}:

$$l_{th} = \sqrt{\kappa \tau_p} \qquad \textbf{Equation 4.12}$$

which is found to be of the order of a few μm for sapphire. T_{p} is the pulse duration. The one-dimensional approximation is valid when the laser spot radius is significantly larger than l_{th}, which is also the case.

However, the calculation is complicated by the strong temperature dependence of the thermal conductivity for sapphire. This is known to decrease from 1100 W m^{-1} K^{-1} to 155 W m^{-1} K^{-1} at 150 K [18]. Furthermore the heat capacity also shows a strong temperature dependence. At the base temperature of 80 K employed in these experiments, c is *ca.* 0.09 J $g^{-1}K^{-1}$ [19]. A was shown previously to be approximately 0.05 for sapphire and assuming a pulse length of 10 ns yields a value for I of 3.6×10^{7} J s^{-1} cm^{-2} during the pulse. Together, these values yield a temperature jump of 102 K during the 10 ns pulse. The surface temperature would therefore rise to around 180 K. This is somewhat lower than the translational temperatures of the desorbing molecules which are *ca.* 450 K for the substrate-mediated channel. This is reasonable given the decrease in thermal conductivity of the sapphire that would occur during heating. This would result in a larger temperature rise at z=0 than obtained *via* this rather simple calculation. Nevertheless, this demonstrates that (a) laser-induced thermal desorption (LITD) would be expected to result in a temperature rise of the correct order of magnitude to cause the desorption of molecules with translational temperatures of *ca.* 400 K and (b) LITD cannot explain the desorption of molecules with translational

temperatures of *ca.* 1200 K which must therefore be attributed to adsorbate-mediated processes.

A good overview of photon-induced desorption mechanisms is given elsewhere [16]. One of the most important is the Menzel-Gomer-Redhead (MGR) model [20,21]. This, however, requires a metal surface, and is only relevant for the desorption of molecules that are in direct contact with the surface. For clarity, the principle of this mechanism will be outlined. Following irradiation, the adsorbate-complex is in an excited electronic state as a result of a Franck-Condon transition. Adiabatic time evolution on the excited state potential energy surface will cause significant geometry changes in the excited state. The excited state is subsequently quenched *via* a non-radiative Franck-Condon transition to the ground state, which results in electronic excitation of the substrate. As a result of the geometry modification, the adsorbate molecule in the ground state has gained some potential energy, which if greater than the adsorption energy, leads to desorption. In the present case, the C_6H_6 film is sufficiently thick that the desorption occurs from multilayers, *i.e.* the substrate is essentially other C_6H_6 molecules. Some insight into the mechanism for C_6H_6 desorption can be obtained by considering the case of impulsive desorption in which all of the excess excitation energy goes into the translational energy of the desorbing molecule. In this case, the excited C_6H_6 molecule has a mass m_{Bz} and desorbs with a temperature T_{Bz}. It is considered to desorb from a surface of other C_6H_6 molecules which has a mass of m_S and a final velocity of v_S. The total available energy following desorption is:

$$E_{avl} = h\nu - E_{des} \qquad \textbf{Equation 4.13}$$

where ν is the frequency of the laser radiation and E_{des} is the multilayer desorption energy of C_6H_6 from a multilayer film, shown in **Chapter 3** to be 48 kJ mol^{-1}. Momentum conservation applies:

$$m_S v_S = m_{Bz} v_{Bz} \qquad \textbf{Equation 4.14}$$

which, along with energy conservation:

$$E_{avl} = \frac{1}{2} m_S v_S^2 + \frac{1}{2} m_{Bz} v_{Bz}^2 \qquad \textbf{Equation 4.15}$$

yields the following expression for the available energy:

$$E_{avl} = \frac{1}{2} m_{Bz} v_{Bz}^2 \left(\frac{m_S + m_{Bz}}{m_S} \right) \qquad \textbf{Equation 4.16}$$

For the desorption of a single C_6H_6 molecule from an effectively infinite surface of C_6H_6 molecules, the mass ratio term is close to unity, indicating that to a first approximation, all of the available energy goes into the translational energy of the desorbing molecule:

$$E_{avl} = \frac{1}{2} m_{Bz} v_{Bz}^2 \qquad \textbf{Equation 4.17}$$

From this expression, a velocity of 3300 m s^{-1} for desorbing C_6H_6 molecules can be obtained. This can be compared to the experimentally observed velocity of desorbing molecules by considering a typical C_6H_6 molecule time of flight of 0.6 ms which yields a velocity of 510 m s^{-1}. Whilst this is clearly an approximate value, it clearly indicates that not all of the available energy goes into the translation of the desorbing C_6H_6 molecules. It is therefore reasonable to consider transfer of energy to the surface *i.e.* other C_6H_6 and H_2O molecules, and to the internal degrees of freedom of the desorbing molecules. It is the former that permits the desorption of H_2O molecules following resonant absorption by C_6H_6 molecules.

Without internal state-resolved studies it is difficult to determine the detailed microscopic mechanism that leads to the direct desorption of C_6H_6. One possible mechanism is photoejection, which has been shown to result in the desorption from multilayer films of molecules with high translational energies [22]. This mechanism can be considered to be an electronic to translational, vibrational, and rotational energy transfer (E→T,V,R) process. An electronically excited molecule is quenched through collision with a ground state molecule in close proximity. The potential energy surfaces of the two molecules mix, and curve crossing

results in the formation of ground state products, with the excess energy going into the internal degrees of freedom and translation of the product molecules.

It is also possible to envisage an alternative mechanism in the present case, that would also lead to the desorption of internally hot molecules along with the desorption of H_2O as a result of energy transfer. In this mechanism, desorption can be considered to occur following the unimolecular decomposition of a surface bound cluster. In the case of the desorption of C_6H_6 from C_6H_6 multilayers, the cluster can be though of as consisting of other C_6H_6 molecules in close proximity. For C_6H_6 adsorbed on (and beneath) a H_2O film, it is reasonable to consider the cluster to consist of a C_6H_6 molecule bound to a small number, x, of H_2O molecules, *i.e.* C_6H_6-$(H_2O)_x$. C_6H_6 is known to interact with H_2O *via* its π system, effectively resulting in a hydrogen bonding interaction [23]. Calculations have indicated that the binding energy between C_6H_6 and the H_2O molecules may be as much as 17 kJ mol^{-1} [24,25], in agreement with an experimentally obtained value of 18 kJ mol^{-1} [26]. The interaction between C_6H_6 molecules and $(H_2O)_x$ clusters up to x=6 have been studied using DFT [27] and observed experimentally [28]. In the simple model considered here, absorbed energy is considered to be equally distributed amongst the internal degrees of freedom of the cluster. For the unimolecular decomposition step:

$$C_6H_6(H_2O)_x \rightarrow C_6H_6 + (H_2O)_x \qquad \textbf{Equation 4.18}$$

the activation energy, E_a is therefore considered to be 18 kJ mol^{-1}. For a large system such as a cluster, the average kinetic energy release (KER), $\langle E_k \rangle$, is given by [29]:

$$\langle E_k \rangle = 2\frac{E_{int} - E_a}{s - 1} \qquad \textbf{Equation 4.19}$$

where s is the number of vibrational degrees of freedom between which the total internal energy E_{int} is distributed. The possible routes for energy disposal following photon absorption are shown in **Figure 4.20.** Following excitation to an excited vibrational level in S_1, internal conversion (IC_1) to S_0 might occur. However, Raman lineshape analysis has demonstrated that the vibrational

relaxation time of solid C_6H_6 is of the order of 1 ps [30] and therefore rapid collision induced vibrational relaxation (CIVR) to the ground vibrational level in S_1 is likely to occur prior to internal conversion (IC_2) to S_0. The energy available, E_{int} can therefore be equated with $E_{int\,2}$ in **Figure 4.20**.

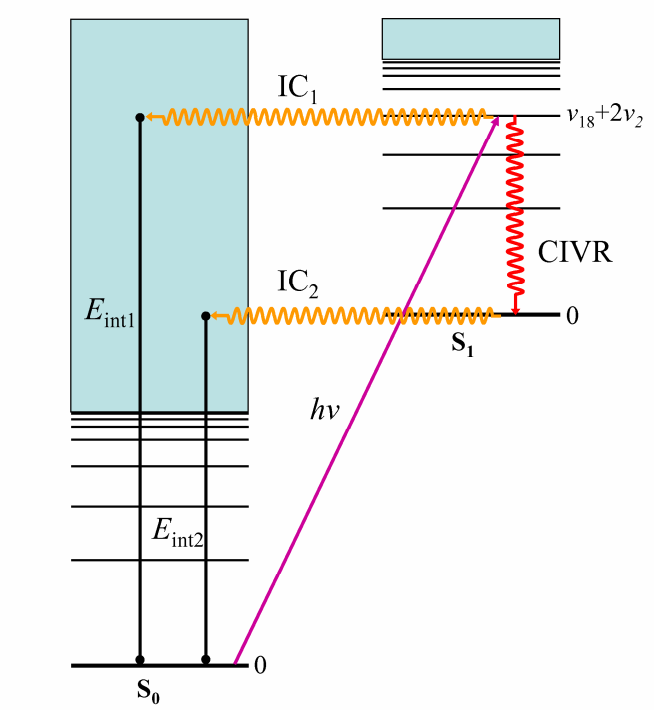

Figure 4.20: Energy disposal mechanisms following resonant excitation of solid C_6H_6. Vibrational level spacings are not representative of the true energy levels.

The excitation energy at 250 nm is 478.5 kJ mol^{-1}. The excited vibrational level in S_1 accessed by the vibronic transition can be shown to be $v_{18}+2v_2$ [1]. Using gas phase vibrational energies yields an approximate vibrational excitation of 28.2 kJ mol^{-1}. E_{int} therefore takes a value of *ca.* 450 kJ mol^{-1}. $\langle E_k \rangle$ can be estimated from the translational temperature of the desorbing C_6H_6 molecules, which for T_{trans}=1200 K yields 9.98 kJ mol^{-1} and s=88. The cluster will have a total of 30+3x intramolecular vibrational modes and 3x-3 intermolecular modes, which results in 27+6x modes in total. However, this analysis neglects the frustrated rotations of the individual molecules, which results in low frequency intermolecular vibrations. The 3x+3 molecular rotations need therefore to be included, which gives a total of 30+9x modes. This is equivalent to considering the cluster as a whole to have 3*n*-6 vibrational degrees of freedom, where the number of atoms, *n*, is 12+3x, which yields s=30+9x. The observed kinetic energy release is therefore

consistent with C_6H_6 being bound to a surface cluster of six or seven H_2O molecules.

The microscopic desorption mechanism therefore involves first the absorption of a photon by the C_6H_6 molecule, which results in a redistribution of energy between the vibrational degrees of freedom of the surface bound cluster. This results in the breaking of the weakest bond in the system, that between the C_6H_6 molecule and the H_2O cluster, leading to the translationally and internally hot C_6H_6 molecules. The H_2O molecule to which the C_6H_6 molecule was bound is likely to be less strongly bound to the cluster than the rest of the H_2O molecules, resulting in the desorption of this single H_2O molecule, also with significant translational energy. These two desorptions describe the fast ToF distributions observed for both C_6H_6 and H_2O. The long timescale H_2O desorption would then arise as a result of the desorption of H_2O clusters of a range of sizes as a result of further unimolecular decomposition of the remaining $(H_2O)_{x-1}$ cluster and destruction of the desorbing fragments in the QMS. These could in principle be observed using a ToF mass spectrometer.

4.4.4 Non-thermal desorption kinetics

The non-thermal desorption kinetics for both C_6H_6 and H_2O are contained within the QMS signal obtained simultaneously with the ToF profiles. As with the ToF profiles, the signal obtained from the irradiation of a single spot on the sample surface displayed a poor signal-to-noise ratio. However, by obtaining the average signal from spots over the surface, this was much improved. As very little desorption was observed with a laser wavelength of 275 nm, only irradiation at 250 and 248.8 nm will be considered in this discussion. As such, only those experiments performed with a pulse energy of 1.8 mJ will be considered in detail. The desorption traces obtained with the lower pulse energy of 1.1 mJ were analyzed, but the reduced signal intensity made the fitting procedures employed unreliable. The decrease in intensity was however observed to be consistent with single photon desorption processes, in agreement with the photon order derived from the ToF data.

Profiles for the C_6H_6 desorption from a 200 L film of C_6H_6 deposited on the sapphire substrate during irradiation at 250 and 248.8 nm are shown in **Figure 4.21**. The profiles are in agreement with the intensity trend observed in the ToF profiles, confirming the enhancement of desorption when the wavelength is tuned to be on resonance with the chosen C_6H_6 transition. With the exception of the intensity, the peaks obtained at the two wavelengths are qualitatively the same. As irradiation at both wavelengths leads to the same electronic transition in the C_6H_6, this is reasonable. **Figure 4.22** shows desorption profiles for the desorption of C_6H_6 from the three layer configurations during irradiation at 250 nm. Again, these are in agreement with the observed ToF profiles which indicate similar desorption for the cases where C_6H_6 was adsorbed on either sapphire or H_2O. In the case where a H_2O film was adsorbed on top of the C_6H_6 film the desorption is clearly inhibited. Finally, the desorption of H_2O from the three systems is considered in **Figure 4.23**. As with the ToF profiles, no desorption is apparent when no C_6H_6 is present. When C_6H_6 is deposited on top of the H_2O, a very small desorption peak is visible upon the commencement of irradiation. This must be related to the indirect-substrate mediated component visible in the ToF profiles. This signal is not particularly clear as a result of the H_2O background which is significantly higher than that for C_6H_6 and results in a higher level of noise than observed in the C_6H_6 traces. Only in the case where C_6H_6 is deposited first, followed by a layer of H_2O is a strong H_2O desorption signal present. This must be related to the slow broad peak in the corresponding ToF profiles which has been interpreted as resulting from the desorption of H_2O clusters which disintegrate to some extent in the ionization source of the QMS. It is clear from the intensity of this feature that this is a significant desorption channel.

In order to make more quantitative comparisons between the desorption traces, the desorption cross-sections were obtained. By assuming first order desorption kinetics, the desorption signal, S(t), for a particular mass fragment can be expressed in terms of the desorption cross-section, σ, for that fragment and the incident photon flux, F [31]:

$$S(t) = S_0 \exp[-\sigma F t] \qquad \textbf{Equation 4.20}$$

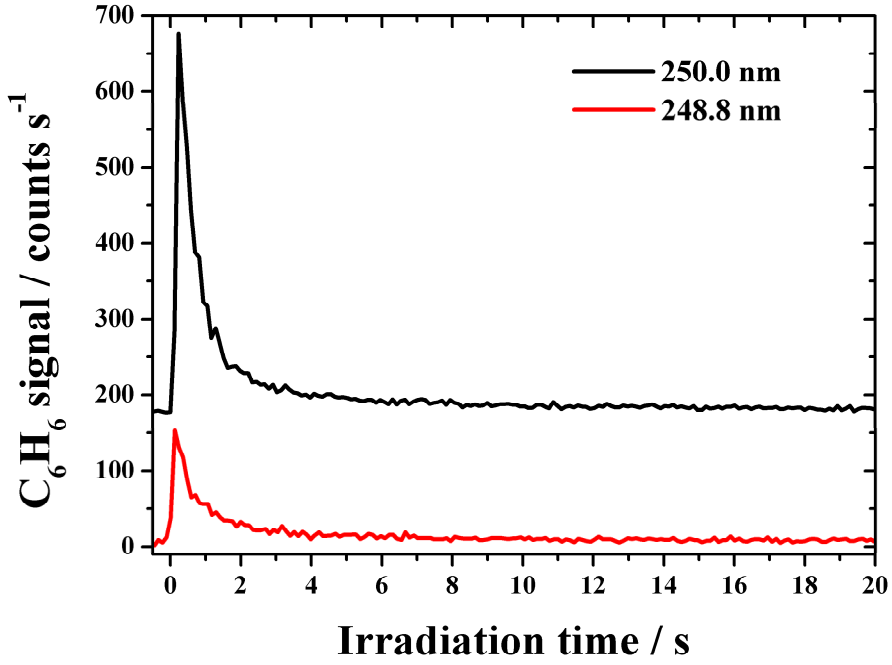

Figure 4.21: C_6H_6 desorption traces during irradiation of 200 L of C_6H_6 adsorbed on the sapphire substrate at 250.0 and 248.8 nm. The pulse energy was 1.8 mJ in both cases. Traces have been offset for clarity.

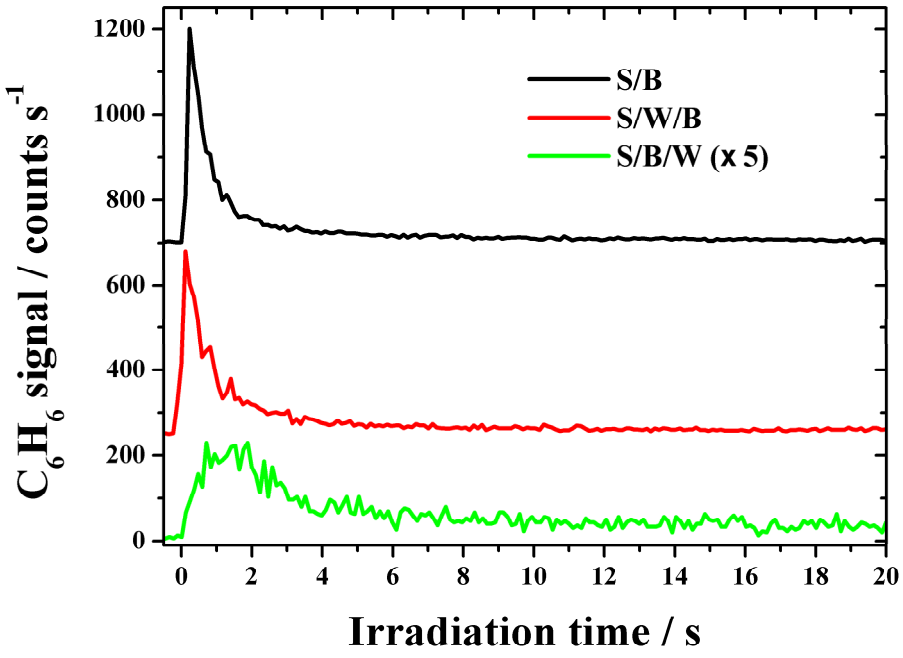

Figure 4.22: C_6H_6 desorption from the three layer configurations traces during irradiation. The wavelength and pulse energy were 250.0 nm and 1.8 mJ respectively. Traces have been offset for clarity.

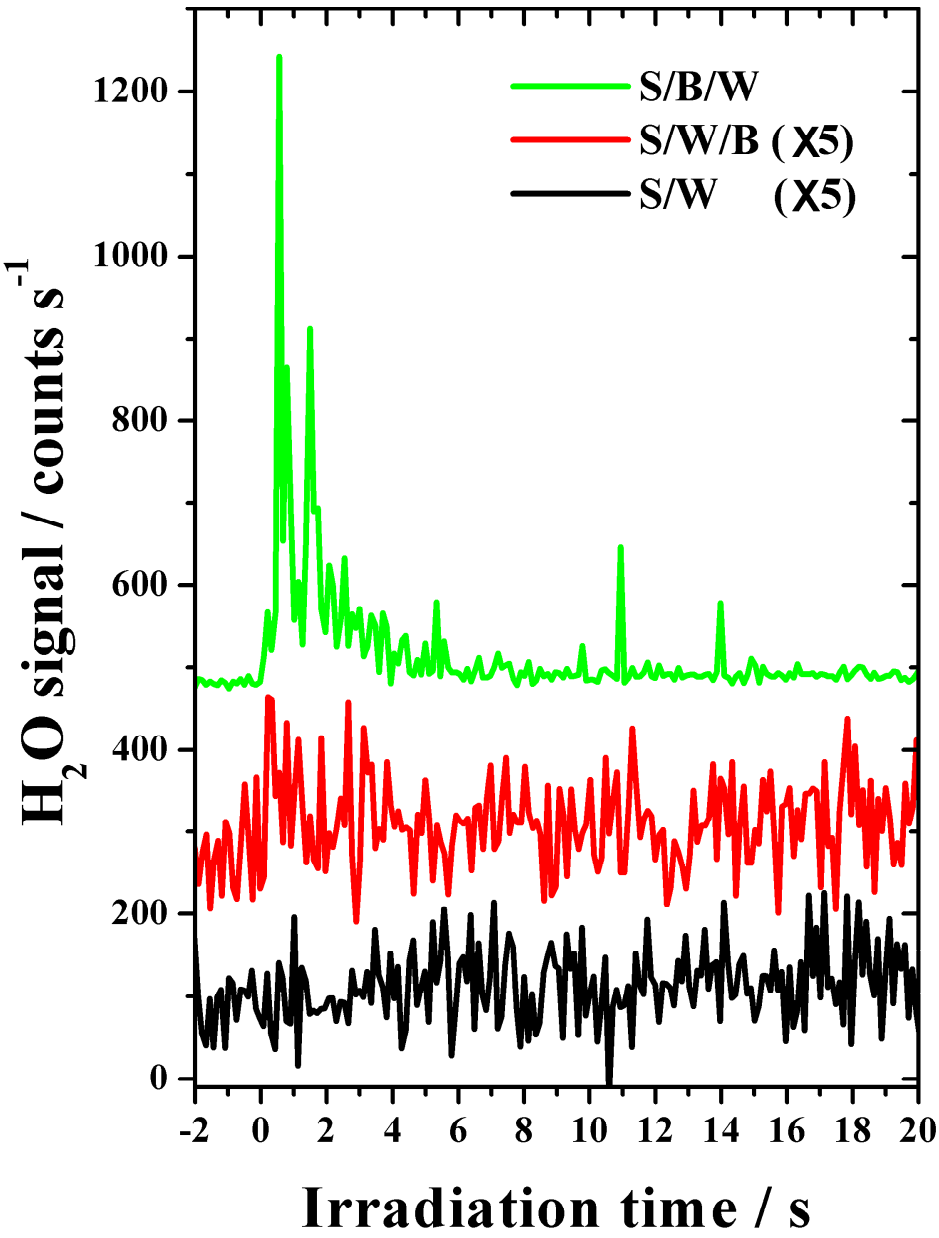

Figure 4.23: H_2O desorption traces from the three layer configurations during irradiation. The wavelength and pulse energy were 250.0 nm and 1.8 mJ respectively. Traces have been offset for clarity.

To obtain the desorption-cross sections, the experimental desorption profiles can be fitted with a simple exponential decay function with a decay constant, τ:

$$S(t) = S_0 \exp\left[-\frac{t}{\tau}\right] \qquad \textbf{Equation 4.21}$$

from which the cross-section can be obtained:

$$\sigma = \frac{1}{\tau F} \qquad \textbf{Equation 4.22}$$

For the desorption profiles presented here, a better fit was obtained by using a two component exponential decay in which the two cross-sections obtained correspond to different desorption mechanisms. The applicability of such two component fits is justified by the known presence of two mechanisms in the observed desorption. Two-component exponential decay fits to the C_6H_6 desorption profiles are presented in **Figure 4.24** and **Figure 4.25** for all three layering systems during irradiation at 250 and 248.8 nm respectively. Single component decays were sufficient to fit the H_2O desorption from the cases where the H_2O was adsorbed on top of a C_6H_6. These are shown in **Figure 4.26** for irradiation at both 250 and 248.8 nm. The smaller H_2O desorption observed when C_6H_6 was adsorbed on top of the H_2O film was too small to obtain a reliable fit. In order to obtain an order of magnitude estimate of the cross-section the desorption profiles at 250 and 248.8 nm were plotted in logarithmic form, such that the time constant for the decay could be obtained from a linear fit to the decay region. These plots are shown in **Figure 4.27**. A summary of the obtained time constants and cross-sections is provided in **Table 4.6** and **Table 4.7**. In this summary, errors are calculated by summation of the relative errors of the flux, as quoted previously, and those obtained during the desorption profile fitting procedure.

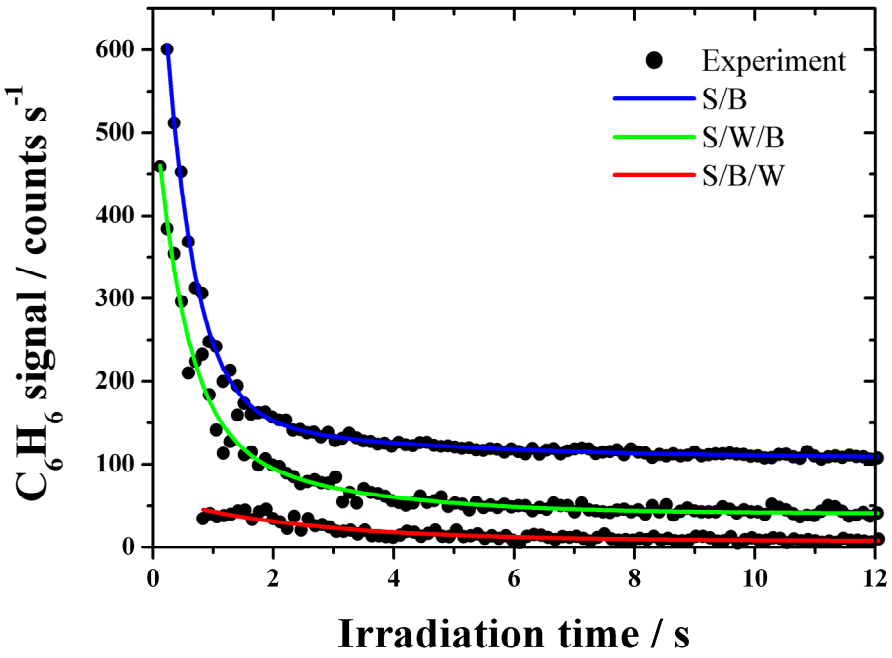

Figure 4.24: Two-component exponential decay fits to C_6H_6 desorption profiles during irradiation at 250 nm. The pulse energy was 1.8 mJ. Traces have been offset for clarity.

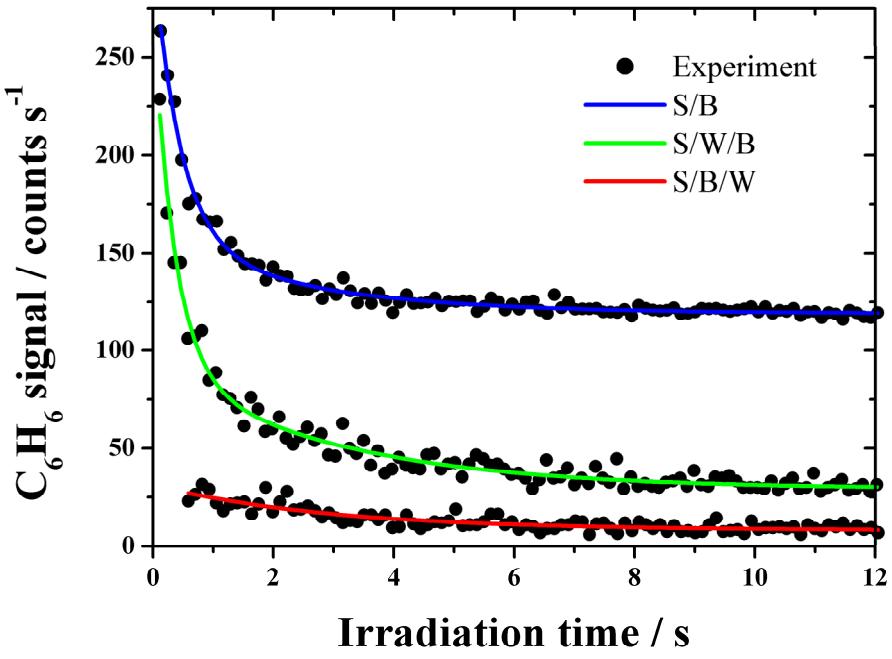

Figure 4.25: Two-component exponential decay fits to C_6H_6 desorption profiles during irradiation at 248.8 nm. The pulse energy was 1.8 mJ. Traces have been offset for clarity.

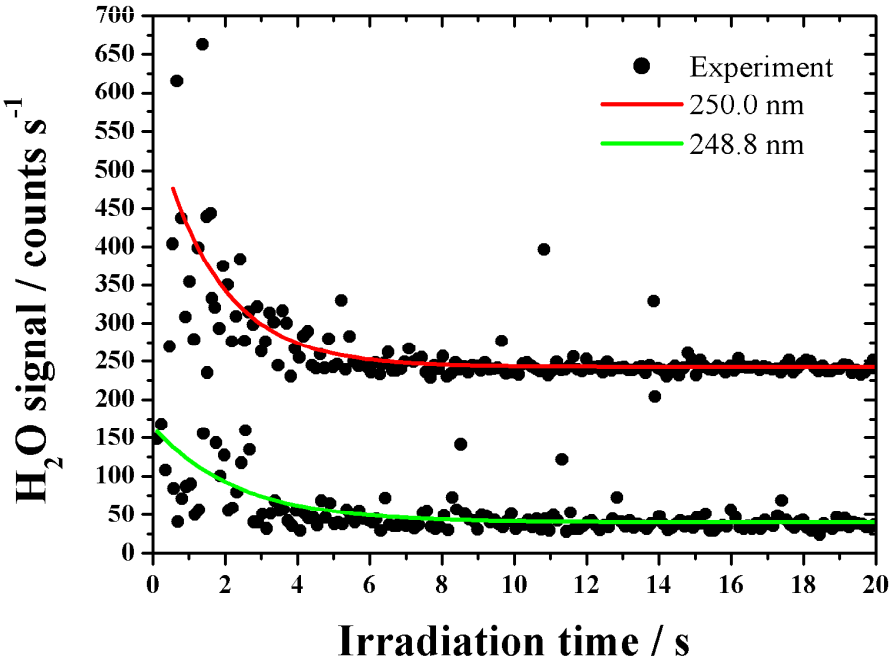

Figure 4.26: Exponential decay fits to H_2O desorption profiles during irradiation at 250 and 248.8 nm. The pulse energy was 1.8 mJ and the H_2O was absorbed on top of C_6H_6 film. Traces have been offset for clarity.

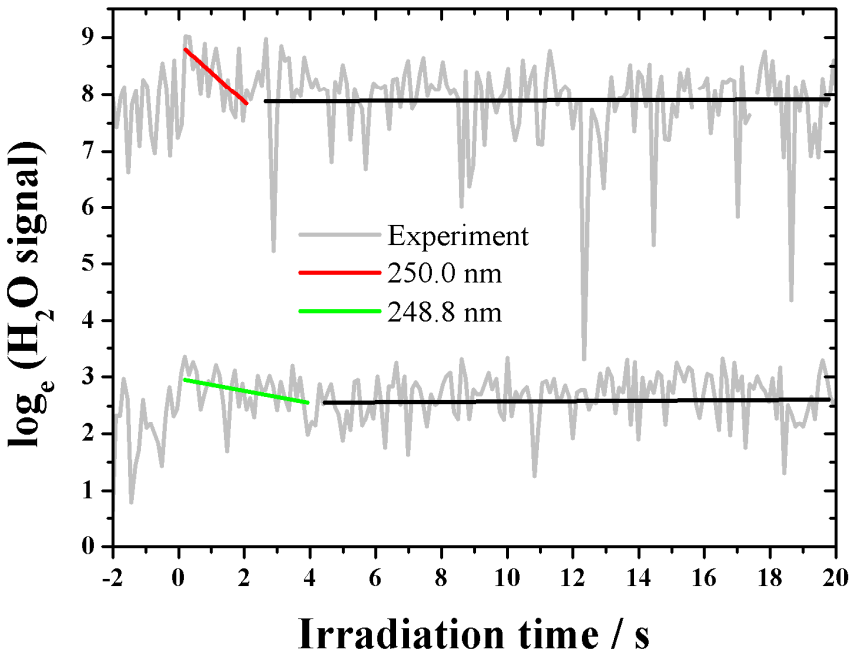

Figure 4.27: Semilog plots for H_2O desorption during irradiation at 250 and 248.8 nm. The pulse energy was 1.8 mJ and the H_2O was absorbed prior to a C_6H_6 film. The black lines are to emphasize the flat region. Traces have been offset for clarity.

Desorbing Species	Irradiation Wavelength / nm	Flux / photons cm^{-2} s^{-1}	System	τ_1 / s σ_1 / cm^2	τ_2 / s σ_2 / cm^2
C_6H_6	250.0	$(4.53\pm0.5)\times10^{18}$	S/B	0.50±0.01 $(4.5\pm0.6)\times10^{-19}$	3.57±0.3 $(6.2\pm1)\times10^{-20}$
C_6H_6	250.0	$(4.53\pm0.5)\times10^{18}$	S/W/B	0.51±0.04 $(4.4\pm0.8)\times10^{-19}$	2.36±0.3 $(9.4\pm2)\times10^{-20}$
H_2O	250.0	$(4.53\pm0.5)\times10^{18}$	S/W/B	2.00±0.3 $(1.1\pm0.3)\times10^{-19}$	---
C_6H_6	250.0	$(4.53\pm0.5)\times10^{18}$	S/B/W	2.52±0.2 $(8.8\pm2)\times10^{-20}$	---
H_2O	250.0	$(4.53\pm0.5)\times10^{18}$	S/B/W	3.30±0.4 $(6.7\pm2)\times10^{-20}$	---

Table 4.6: Summary of desorption cross-sections obtained for all systems with an irradiation wavelength of 250.0 nm.

Desorbing Species	Irradiation Wavelength / nm	Flux / photons cm^{-2} s^{-1}	System	τ_1 / s σ_1 / cm^2	τ_2 / s σ_2 / cm^2
C_6H_6	248.8	$(4.51\pm0.5)\times10^{18}$	S/B	0.45±0.03 $(5.0\pm0.9)\times10^{-19}$	2.57±0.3 $(8.6\pm2)\times10^{-20}$
C_6H_6	248.8	$(4.51\pm0.5)\times10^{18}$	S/W/B	0.36±0.03 $(6.2\pm1)\times10^{-19}$	2.99±0.2 $(7.4\pm1)\times10^{-20}$
H_2O	248.8	$(4.51\pm0.5)\times10^{18}$	S/W/B	10.0±5 $(2.2\pm1)\times10^{-20}$	---
C_6H_6	248.8	$(4.51\pm0.5)\times10^{18}$	S/B/W	2.95±0.3 $(7.5\pm2)\times10^{-20}$	---
H_2O	248.8	$(4.51\pm0.5)\times10^{18}$	S/B/W	2.30±0.5 $(9.6\pm3)\times10^{-20}$	---

Table 4.7: Summary of desorption cross-sections obtained for all systems with an irradiation wavelength of 248.8 nm.

Given the dominance of the direct adsorbate-mediated desorption channel in the desorption of C_6H_6 from sapphire and H_2O, the desorption cross-sections σ_1 and σ_2 are attributed to this mechanism, and substrate-mediated thermal desorption respectively. Given that the direct channel at 248.8 nm arises as a result of the same electronic transition, the very similar cross-section is reasonable. Likewise, the thermal desorption component is essentially the same at the two wavelengths. With this in mind, an average value for the cross-section for the desorption of C_6H_6 from sapphire and H_2O *via* the direct channel is $(5.0\pm2)\times10^{-19}$ cm^2 where the error is two standard deviations. Similarly, an average value for the thermal desorption of C_6H_6 can be calculated as $(7.9\pm2)\times10^{-20}$ cm^2. Whilst the direct channel still operates when the C_6H_6 is present under a capping layer, as indicated by the high translational temperature with which the C_6H_6 molecules desorb, the cross-section for this process is reduced, reflecting a reduction in desorption efficiency that arises as a result of the H_2O layer physically blocking the desorption. The average cross-section in this case is $(8.2\pm2)\times10^{-20}$ cm^2. This value is very similar to the C_6H_6 thermal desorption cross-section which explains why a single component fit is sufficient to fit the decay. Nevertheless, two desorption components were present in the ToF profiles, indicating that the direct channel is still in operation. The desorption cross-section for H_2O from a C_6H_6 film is, using the same considerations, $(8.2\pm4)\times10^{-20}$ cm^2. The low signal obtained for the H_2O desorption from underneath a C_6H_6 film precludes any reliable estimate beyond an order of magnitude of 10^{-20} cm^{-2}. The average values are summarized in **Table 4.8**.

Desorption Channel	**Desorption cross-section / cm^2**
Direct adsorbate-mediated (C_6H_6)	$(5.0\pm2)\times10^{-19}$
Inhibited direct adsorbate-mediated (C_6H_6)	$(8.2\pm2)\times10^{-20}$
Substrate-mediated thermal (C_6H_6)	$(7.9\pm2)\times10^{-20}$
Indirect adsorbate-mediated desorption (H_2O)	$(8.2\pm4)\times10^{-20}$

Table 4.8: Averaged desorption cross-sections for the desorption channels.

4.5 Astrophysical implications and conclusions

There are several observations reported here that are likely to be important in the ISM. It is difficult to quantify the overall impact of the results given that only a single transition was probed for absorption by C_6H_6 molecules, used as a model of the broader aromatic hydrocarbon populations. It is however possible to discuss the importance in general terms, and apply some approximations in order to further assess the likely interstellar impact.

One particularly important result is the observation of desorbing molecules having significant translation energies, corresponding to translational temperatures well in excess of the grain temperatures. This has also been observed in the case of the direct photodesorption of H_2O as a result of irradiation at 157 nm [32] where translational temperatures of up to 1800 K were observed. The desorption of molecules with such high translational energies is likely to have important consequences for gas phase chemistry. There was also evidence for vibrational and rotational excitation in the desorption, though this has not been measured in the present case. However, where viable transitions exist, internal energy will be lost through radiative processes. For example, radiative lifetimes in the IR are typically $1\text{-}10^{-3}$ s [33]. The mean free path, λ, for molecules in the gas phase is given by [8]:

$$\lambda = \frac{k_B T}{\sqrt{2}\sigma P} \qquad \textbf{Equation 4.23}$$

where T is the gas phase temperature, σ is the collision cross-section and P is the gas pressure. Considering a gas phase temperature of 50 K, a typical collision cross-section of 1 nm^2 [8] and a dense cloud pressure of 10^{-14} mbar yields a mean free path of 5×10^8 m. For a C_6H_6 molecule travelling at 500 m s^{-1} this corresponds to a collision time of the order of 10 days. Although this is clearly a very simplistic approach, it does demonstrate that it is the translational energy content that is important as internal energy will have been lost by the time collision occurs. In the case of translational energy, this energy will remain until collision. This results in the possibility of reactions otherwise excluded by the low temperature of the gas.

Another important observation is the desorption of H_2O molecules as a result of resonant absorption by C_6H_6 molecules. This indicates that the photon-induced desorption for a particular molecule may occur over wavelength ranges where that molecule itself may not absorb photons. The inclusion of such processes in chemical models that include gas-grain processes is likely to increase the overall photodesorption rates. In the present case, the observed desorption cross-section for H_2O as a result of this indirect mechanism is only a few times smaller than that for the direct desorption of C_6H_6 molecules. Although the H_2O molecules are desorbed with a translational temperature of 500 K, significantly lower than the C_6H_6 molecules and H_2O molecules desorbed *via* a direct mechanism [32], this is still far in excess of typical grain temperatures and the possibility of enhanced gas-phase reaction rates remains. The impact of H_2O desorption driven by the absorption of photons by other species will be discussed in more detail in **Chapter 6**.

The observation of desorption of C_6H_6 molecules from under a H_2O ice film of thickness comparable to interstellar ice mantles with only a slightly reduced cross-section and translational temperatures indicates that the direct channel is relatively insensitive to bulk ice composition. However, experiments on ice mixtures would be required to confirm this. Extension of these to shorter wavelengths, *e.g.* Lyman-α photons, where C_6H_6 has a larger absorption cross-section would also be a valuable extension of this work. At such energies direct H_2O desorption and dissociation is also likely. Any contribution from this channel would need to be determined in order to obtain any enhancement caused by the presence of a secondary species such as C_6H_6.

In summary, experiments probing the photon-induced desorption of C_6H_6 and H_2O molecules from pure and layered ices containing the two species have revealed the presence of several desorption mechanisms. C_6H_6 are desorbed through a direct desorption mechanism following resonant absorption of 250 nm photons. These molecules desorb with a cross-section of *ca.* 1×10^{-19} cm^2 and exhibit translational temperatures in excess of 1000 K. The cross-section and translational temperature are only slightly reduced when the C_6H_6 is present underneath a H_2O ice film of a thickness comparable to that of interstellar grain

mantles. The desorption of H_2O molecules with a similar cross-section is also observed. It is thought that this arises as a result of the unimolecular decomposition of surface bound clusters in which a C_6H_6 molecule is hydrogen bonded to a H_2O cluster. This was also evidenced by the observation of a very slow and broad ToF for desorbing H_2O molecules, suggesting the desorption of clusters of H_2O molecules of a range of sizes which then disintegrate within the QMS. Experiments involving the use of a full ToF mass spectrometer to detect the intact clusters would be advantageous in further characterising this desorption channel. The internal energy content of desorbing molecules has not been determined, and state-resolved studies would be useful in further constraining the desorption mechanisms. However, simple arguments indicate that any internal energy content will be lost when radiative relaxation channels exist before collision under dense cloud conditions.

4.6 References

[1] G. Herzberg, *Electronic Spectra and Electronic Structure of Polyatomic Molecules*, 1st ed., Van Nostrand Reinhold Company Inc., New York, 1966.

[2] F. Thomas, N. Chen, I. Lee, L. Ford, P. Blowers, and R. I. Masel, *J. Vac. Sci. Technol. A*, 1999, **17**, 2339.

[3] T. Etzkorn, B. Klotz, S. Sørensen, I. V. Patroescu, I. Barnes, K. H. Becker, and U. Platt, *Atmos. Environ.*, 1999, **33**, 525.

[4] N. J. Mason, *Private communication*.

[5] K. Kobayashi, *J. Phys. Chem.*, 1983, **87**, 4317.

[6] R. L. Summers, *NASA Technical Reports*, 1969, **NASA-TN-D-5285**.

[7] G. D. Waddill and L. L. Kesmodel, *Phys. Rev. B*, 1985, **31**, 4940.

[8] P. W. Atkins, *Physical Chemistry*, 6th ed., Oxford University Press, Oxford, 1998.

[9] C. J. Craven, P. D. Hatton, C. J. Howard, and G. S. Pawley, *J. Chem. Phys.*, 1993, **98**, 8236.

[10] G. A. Kimmel, K. P. Stevenson, Z. Dohnálek, R. S. Smith, and B. D. Kay, *J. Chem. Phys.*, 2001, **114**, 5284.

[11] G. A. Kimmel, Z. Dohnálek, K. P. Stevenson, R. S. Smith, and B. D. Kay, *J. Chem. Phys.*, 2001, **114**, 5295.

[12] B. S. Patel and Z. H. Zaidi, *Meas. Sci. Technol.*, 1999, 146.

[13] M. P. Collings, J. W. Dever, H. J. Fraser, and M. R. S. McCoustra, *Astrophys. Space Sci.*, 2003, **285**, 633.

[14] P. Lofgren, P. Ahlstrom, J. Lausma, B. Kasemo, and D. Chakarov, *Langmuir*, 2003, **19**, 265.

[15] A. S. Bolina, A. J. Wolff, and W. A. Brown, *J. Phys. Chem. B*, 2005, **109**, 16836.

[16] F. M. Zimmermann and W. Ho, *Surf. Sci. Rep.*, 1995, **22**, 127.

[17] A. M. Prokhorov , V. I. Konov, I. Ursa, and I. N. Mihailescu, *Laser Heating of Metals*, IOP Publishing, Bristol, 1990.

[18] I. S. Grigoriev and E. Z. Meilikhov, *Handbook of Physical Quantities*, CRC Press, New York, 1997.

[19] D. A. Dietmars, S. S. Ihsihara, S. S. Chang, and G. Bernstein, *J. Res. Nat. Bur. Stand.*, 1982, **87**, 159.

[20] D. Menzel and R. Gomer, *J. Chem. Phys.*, 1964, **40**, 1164.

[21] D. Menzel and R. Gomer, *J. Chem. Phys.*, 1964, **41**, 3311.

[22] I. Harrison, J. C. Polanyi, and P. A. Young, *J. Chem. Phys.*, 1988, **89**, 1498.

[23] S. Suzuki, P. G. Green, R. E. Bumgarner, S. Dasgupta, W. A. Goddard, III, and G. A. Blake, *Science*, 1992, **257**, 942.

[24] D. Feller, *J. Phys. Chem. A*, 1999, **103**, 7558.

[25] S. Li, V. R. Cooper, T. Thonhauser, A. Puzder, and D. C. Langreth, *J. Phys. Chem. A*, 2008, **112**, 9031.

[26] S. C. Silva and J. P. Devlin, *J. Phys. Chem.*, 1994, **98**, 10847.

[27] D. M. Upadhyay and P. C. Mishra, *Theochem-J. Mol. Struct.*, 2002, **584**, 113.

[28] R. N. Pribble and T. S. Zwier, *Faraday Discuss.*, 1994, **97**, 229.

[29] P. C. Engelking, *J. Chem. Phys.*, 1987, **87**, 936.

[30] H. Nomura, S. Koda, and Y. Miyaara, *Bull. Chem. Soc. Japan.*, 1979, **52**, 3249.

[31] S. W. Bellard and E. M. Williams, *Surf. Sci.*, 1979, **80**, 450.

[32] A. Yabushita, T. Hama, M. Yokoyama, M. Kawasaki, S. Andersson, R. N. Dixon, M. N. R. Ashfold, and N. Watanabe, *Astrophys. J.*, 2009, **699**, L80.

[33] R. D. Levine, *Molecular Reaction Dynamics*, 1st ed., Cambridge University Press, Cambridge, 2005.

CHAPTER 5 - Low Energy Electron Irradiation of C_6H_6 / H_2O Ices

5.1 Introduction

This chapter describes experiments performed to investigate the irradiation of C_6H_6 films with low energy electrons in the range 100-350 eV. The loss of C_6H_6 from C_6H_6 films adsorbed directly on the SiO_2 substrate as observed through TPD experiments are discussed first. No desorption of C_6H_6 was observed. This is followed by a more detailed discussion of the irradiation of C_6H_6 on ASW during which efficient desorption of C_6H_6 molecules was observed. Both ESD measurements and those of total C_6H_6 loss through TPD and RAIRS experiments are reported. Possible mechanisms for the observed desorption and other loss channels are discussed. Finally, the results are summarized along with a discussion of the astrophysical implications.

5.2 Experimental procedures

The experiments described in this chapter were performed using UHV chamber 1. Electron irradiation was performed using the Kimball Physics ELG-2 electron gun described in **Chapter 2**. Electron fluxes were determined by measuring the current through the sample using a picoammeter. For those experiments where the beam was pulsed, the average current during the pulse was determined by using a current to voltage converter and obtaining the pulse duration and current by suitable connection to an oscilloscope (LeCroy 9420). Electron-stimulated desorption (ESD) was observed during continuous irradiation experiments using the QMS in pulse counting mode with the SEM set to typically *ca*. 3000 V. Post irradiation TPDs were obtained with a heating rate of (0.1±0.02) K s^{-1}. ESD experiments were performed with the sample facing the line-of-sight tube, with the QMS positioned such that the electron beam was incident at 45° to the surface normal. During RAIRS experiments, irradiation and RAIR scans needed to be obtained without moving the sample, so the electron beam was incident at a much

larger angle to the surface normal. During ESD experiments, the electron beam was not rastered, whilst in post-irradiation TPD and RAIRS experiments, the beam was rastered across the entire surface with a *z* (vertical) period 2 s of and a *y* (horizontal) period of 50 ms resulting in a triangular scanning pattern.

5.3 Results and discussion

5.3.1 Introduction

A limited number of experiments were performed with C_6H_6 adsorbed directly on the SiO_2 surface. After several experiments, subsequent TPDs lacked the high temperature tail discussed in **Chapter 3**. This is thought to arise because of carbon build-up that occurs as result of decomposition of C_6H_6; most likely dehydrogenation. In the first section, preliminary post-irradiation TPD experiments for C_6H_6 on amorphous SiO_2 after carbon build-up will be discussed. A more in depth study of the irradiation of C_6H_6 adsorbed on ASW will then be reported. These experiments involved the use of ESD measurements, and both post-irradiation TPD and RAIRS experiments. Some of the TPD traces in this chapter are plotted *versus* time rather than temperature as the thermocouple amplifier was found to be unstable for a significant period of time following reconnection to the thermocouple after irradiation. This occurred as a result of the time taken to charge a smoothing capacitor used to remove noise from the amplified signal. As only the time integrated TPD yields were required for kinetic analysis this, has no direct impact on the results presented.

5.3.2 Electron irradiation of C_6H_6 adsorbed on SiO_2

As previously discussed, the irradiation of C_6H_6 appeared to result in a change of surface morphology which can be attributed to the build up of a carbon deposit that results from the decomposition of C_6H_6 during irradiation. Therefore, only a limited number of experiments were performed on this carbonized SiO_2 surface. The difference in the TPD profile in terms of the lack of any high temperature tail is clear in **Figure 5.1**. This figure shows the TPD traces resulting from the 250 eV

electron irradiation of 1 L of C_6H_6 adsorbed on the carbonized SiO_2 surface. This was found to result in close to monolayer saturation coverage on this surface, reflecting a loss of surface area as a result of carbon build-up. This effect was not explored further. During these experiments, the electron beam was pulsed at 100 Hz, with a pulse length of 5 μs with the aim of obtaining ToF profiles for desorbing molecules. However, no ESD signal was observed. The electron pulse current during irradiation was 6.8±0.5 μA, with the error being one standard deviation, which yields an average flux of $(4.25\pm0.3)\times10^{15}$ electrons cm^{-2} s^{-1} for continuous beam irradiation, assuming a reasonable beam spot size of 1 mm^2. Taking into account the pulsing results in a flux of $(2.2\pm0.2)\times10^{12}$ electrons cm^{-2} s^{-1}.

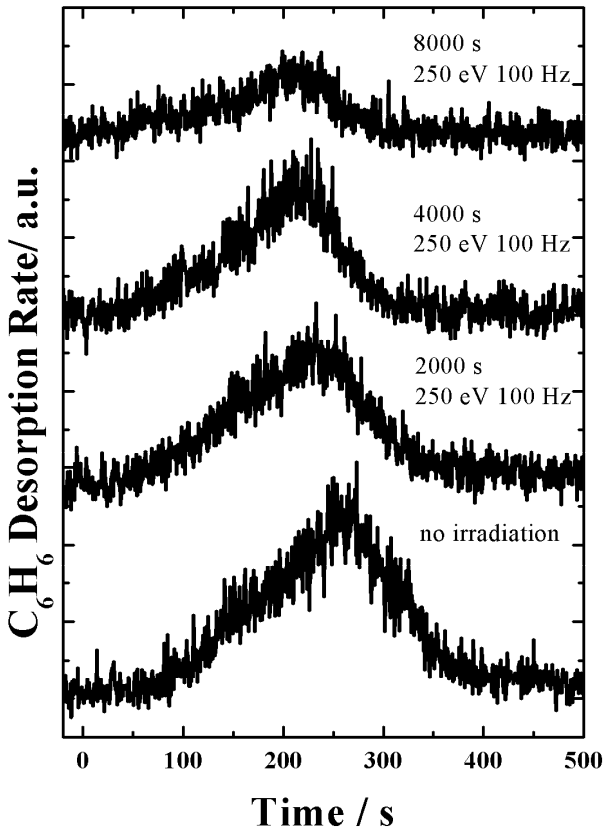

Figure 5.1: TPD traces obtained after irradiation of 1 L of C_6H_6 adsorbed on amorphous SiO_2. An electron energy of 250 eV was used. Traces have been offset for clarity.

In order to obtain the total cross-section for C_6H_6 loss, the TPD yield for each post-irradiation TPD profile was obtained. A 10% error was associated with each yield as a result of dose variability. It is possible that the beam did not entirely cover the surface during the irradiation, resulting in a non-zero baseline. The total C_6H_6 loss cross-section was therefore determined by fitting the TPD yield decay with a modified form of the single component decay introduced in **Chapter 4**:

$$S(t) = S_0 \exp\left[-\frac{t}{\tau}\right] + S_\infty \qquad \textbf{Equation 5.1}$$

where, in this case, $S(t)$ can be taken as the TPD yield with S_0 being the TPD yield when there is no irradiation. τ is the decay constant and S_∞ is the limiting value of

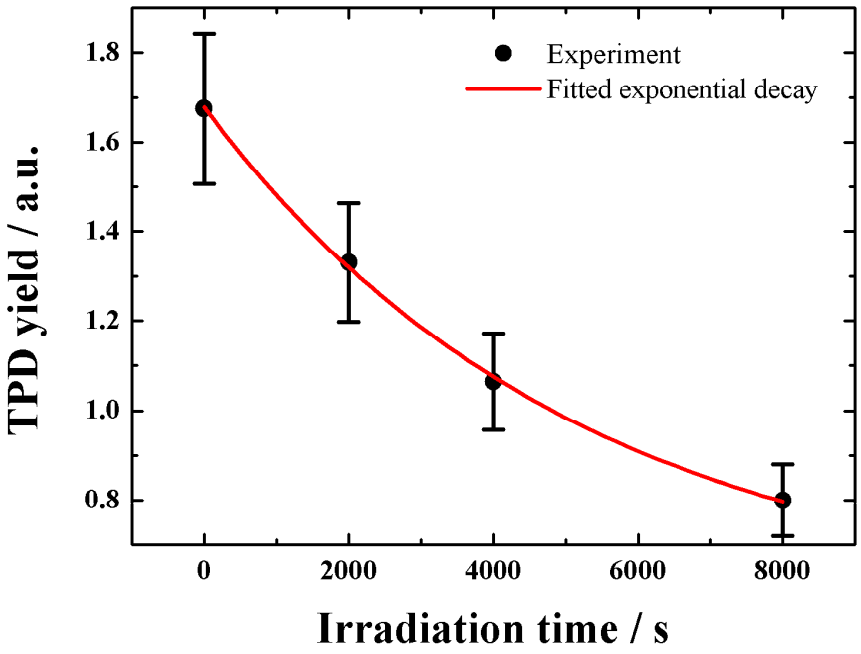

Figure 5.2: Fitted exponential decay for the 1 L C_6H_6 TPD yield decay as a function of electron irradiation time at 250 eV.

the TPD yield for infinite decay time, representing the unirradiated region. σ is then obtained from the decay constant for the fit in **Figure 5.2** as:

$$\sigma = \frac{1}{\tau F} \qquad \textbf{Equation 5.2}$$

where F is the electron flux derived previously. The errors in this plot arise as a result of the propagation of the 10% error on the measured TPD yields. This results in a cross-section for total C_6H_6 loss of $(8.8\pm2)\times10^{-17}$ cm^2. As no ESD was observed during irradiation, it is thought that the major loss channel is decomposition of C_6H_6 on the surface resulting in a deposit that was, after a significant number of experiments, visible by eye. It is not possible to completely rule out desorption, as a low cross-section for desorption might result in a desorption rate below the sensitivity of the QMS. The cross-section obtained is in reasonable agreement with that observed for the decomposition of the first few physisorbed layers on W(110) during irradiation with 150 eV electrons [1]. A value of *ca*. 3×10^{-17} cm^2 was obtained in this case. A decay in the low coverage C_6H_6 was observed, as in the present case, with XPS confirming no significant reduction in surface carbon, consistent with the current observation of no C_6H_6 desorption during irradiation. UPS confirmed the presence of C_6H_6 – like orbitals following irradiation, suggesting the formation of a carbon deposit consisting of dehydrogenated C_6H_6. Auger studies showed the appearance of a loss at around 6 eV when the substrate was annealed to temperatures in excess of 650 K after irradiation. This was attributed to a graphite plasmon, indicating the formation of a graphitic layer at higher temperatures. XPS studies of the substrates used in the experiments presented here after multiple irradiation experiments were conducted at the University of Nottingham Nanotechnology and Nanoscience Centre [2]. The presence of a peak at 285.9 eV suggests the presence of some amount of graphitic material [3]. The C 1s XPS peak for the irradiated sample, along with fitted components, is shown in **Figure 5.3**. The new peak results in a shoulder on the aliphatic C 1s peak at 284.8 eV. The peak at 284.8 eV was fixed, with shifts in other peak positions being attributable to charging effects. Peak positions and relative percentage values for unirradiated and irradiated SiO_2 films are reported in **Table 5.1**. Despite not being annealed to 650 K, it is reasonable to assume that multiple anneals to *ca*. 500 K would lead to some degree of conversion to graphitic carbon. RAIRS experiments were not conducted as the exposures used were below the detection limit as discussed in **Chapter 3**. Such studies would require the use of a flat SiO_2 surface for increased sensitivity to submonolayer films of C_6H_6.

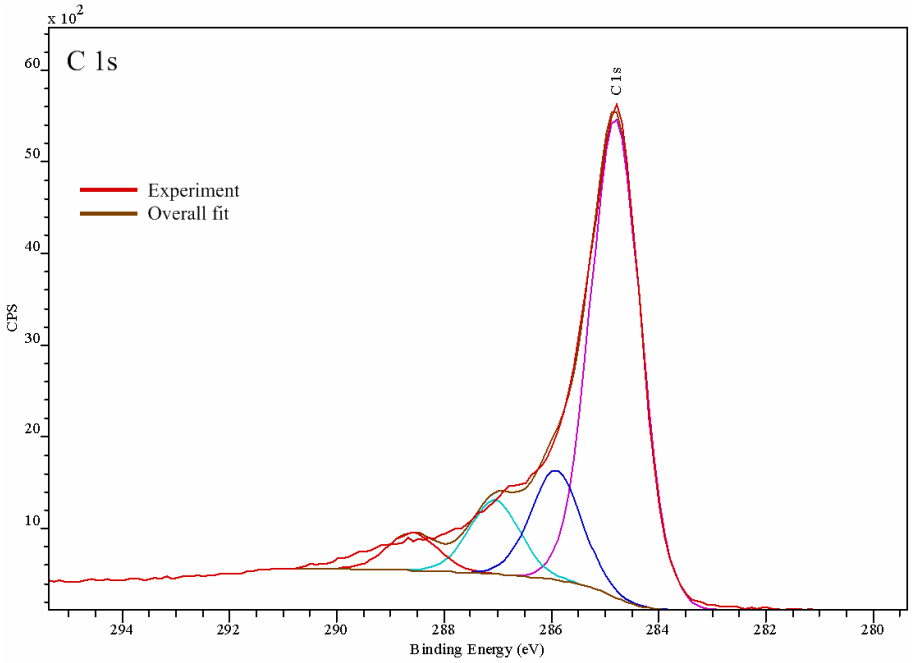

Figure 5.3: C 1s XPS spectrum for the SiO_2 substrate with significant visible staining following electron irradiation of adsorbed C_6H_6

Unirradiated peak position / eV	Unirradiated relative %	Irradiated peak position / eV	Irradiated relative %
284.8	13.7	284.8	53.6
286.4	3.4	287.1	8.3
288.4	1.7	288.6	4.3
---	---	285.9	12.0

Table 5.1: C 1s XPS peak positions and relative % values for the unused SiO_2 substrate and one which had significant visible staining following electron irradiation of adsorbed C_6H_6

Although an in-depth analysis of the obtained XPS was not performed, it is clear from the relative percentage values that the visible staining is due to the formation of carbon deposits following electron irradiation of adsorbed C_6H_6. Further detailed studies carried out in a single UHV chamber to eliminate contamination of the films whilst exposed to atmosphere would be essential in a more systematic approach. Moreover, the use of the same SiO_2 substrate for the XPS prior to, and after electron irradiation would also remove the effect of differences between the initial compositions of SiO_2 films.

To investigate the low energy electron irradiation of bulk C_6H_6, multilayer films obtained with exposures of 10 and 50 L were used. The TPD studies discussed in **Chapter 3** indicate that in both cases, these exposures result in multilayer films

that display zero-order desorption kinetics. As no ESD was observed, continuous beam irradiation was performed with an incident electron current of 15±3 nA, corresponding to $(9.4\pm2)\times10^{12}$ electrons cm^{-2} s^{-1}, within the same order of magnitude as that used for the pulsed irradiation of 1 L of C_6H_6. The TPD traces and corresponding fitted exponential decay for a C_6H_6 exposure of 10 L are shown in **Figure 5.4** and **Figure 5.5** respectively. **Figure 5.6** and **Figure 5.7** present the equivalent data obtained with a C_6H_6 exposure of 50 L. The TPD profiles are presented as obtained for qualitative analysis, whilst TPD yields were scaled by comparison with QMS traces obtained during doses to account for dose variability. The errors displayed on the decays were obtained as previously. The cross-sections for C_6H_6 loss obtained are $(1.7\pm1)\times10^{-17}$ cm^2 and $(4.1\pm2)\times10^{-17}$ cm^2 for C_6H_6 exposures of 10 and 50 L respectively. These values are somewhat lower than that obtained for the irradiation of submonolayer quantities of C_6H_6 on SiO_2 indicating that C_6H_6 loss channels may be enhanced on the SiO_2 surface. Given the larger error on the value for a C_6H_6 of 50 L, an average value for the cross-section of 3×10^{-17} cm^2 is reasonable, in agreement with the previous studies of the irradiation of C_6H_6 multilayers adsorbed on W(110) [1].

It is also apparent that a significant change in the TPD profile occurs as a result of irradiation, with the appearance of a prominent high temperature shoulder. This change in TPD profile was also observed when C_6H_6 multilayers were adsorbed on top of a thick ASW film as will be discussed later. It will be shown that no reaction products corresponding to this feature could be found with RAIRS of irradiated multilayer C_6H_6 films. It is therefore likely that the higher temperature feature arises as a result of adsorption energy changes within the multilayer film, perhaps as a result of the formation of carbon deposits. The C_6H_6 loss observed is therefore attributed to processing of the bulk C_6H_6 film. RAIR spectra and a more detailed discussion will be presented for the case of C_6H_6 adsorbed on ASW. The possibility of an enhanced total loss cross-section for C_6H_6 from thin submonolayer films adsorbed on the SiO_2 substrate was not investigated further due to the difficulties arising from the build-up of carbon deposits.

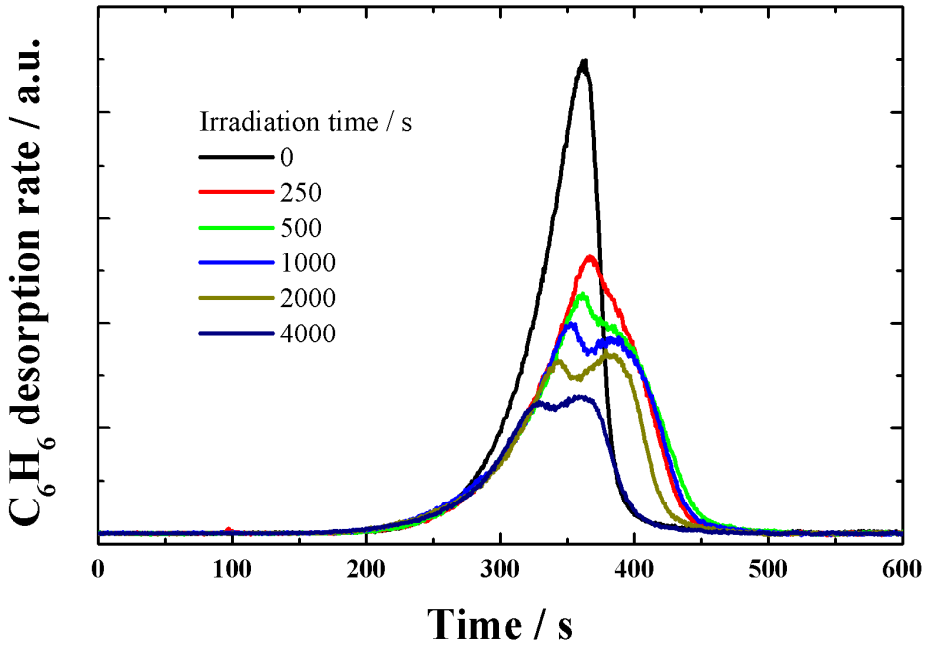

Figure 5.4: TPD traces obtained after irradiation of 10 L of C_6H_6 adsorbed on amorphous SiO_2. An electron energy of 250 eV was used.

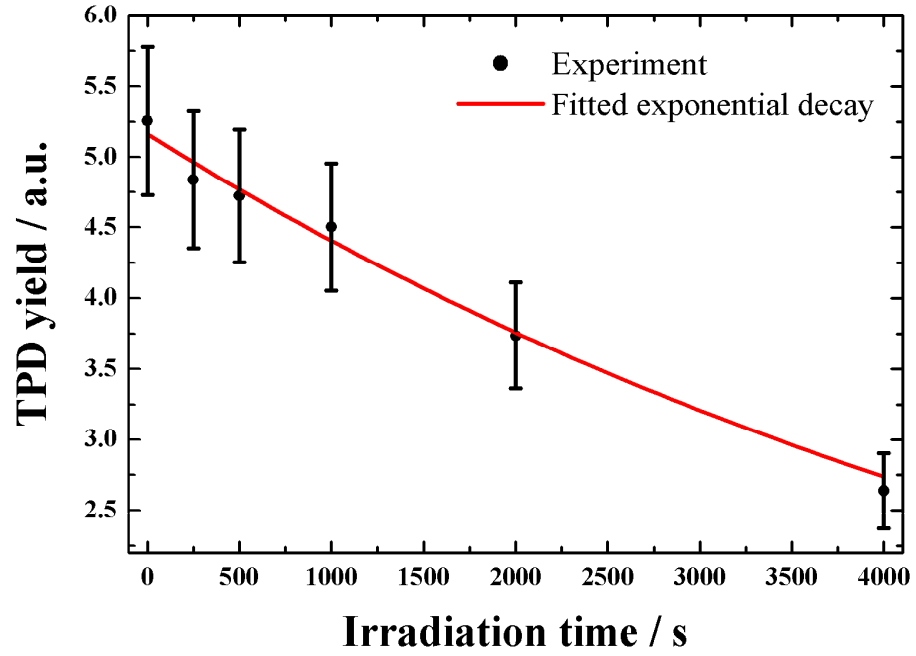

Figure 5.5: Fitted exponential decay for the 10 L C_6H_6 TPD yield decay as a function of electron irradiation time at 250 eV.

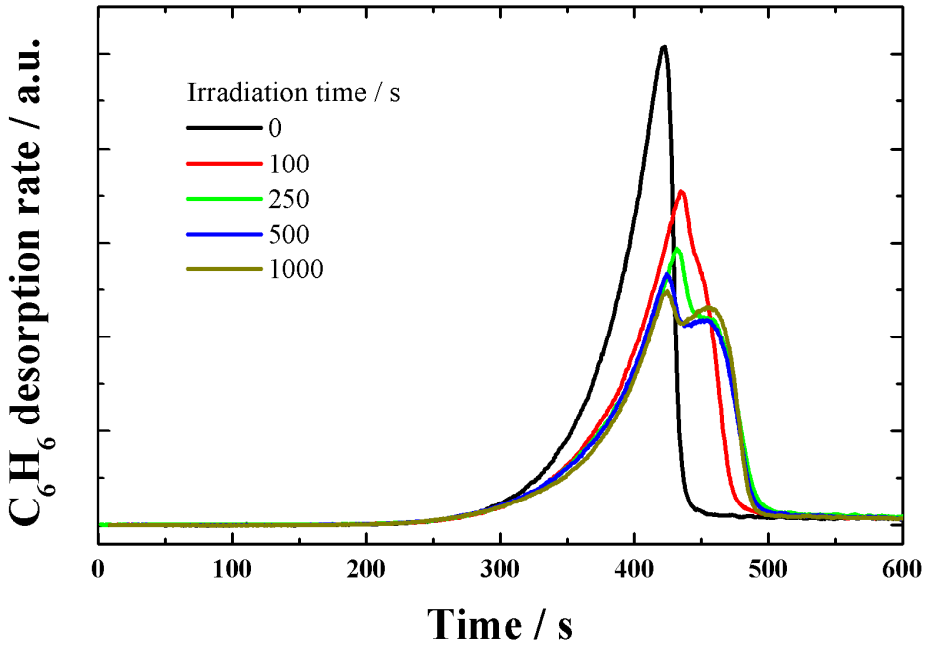

Figure 5.6: TPD traces obtained after irradiation of 50 L of C_6H_6 adsorbed on amorphous SiO_2. An electron energy of 250 eV was used.

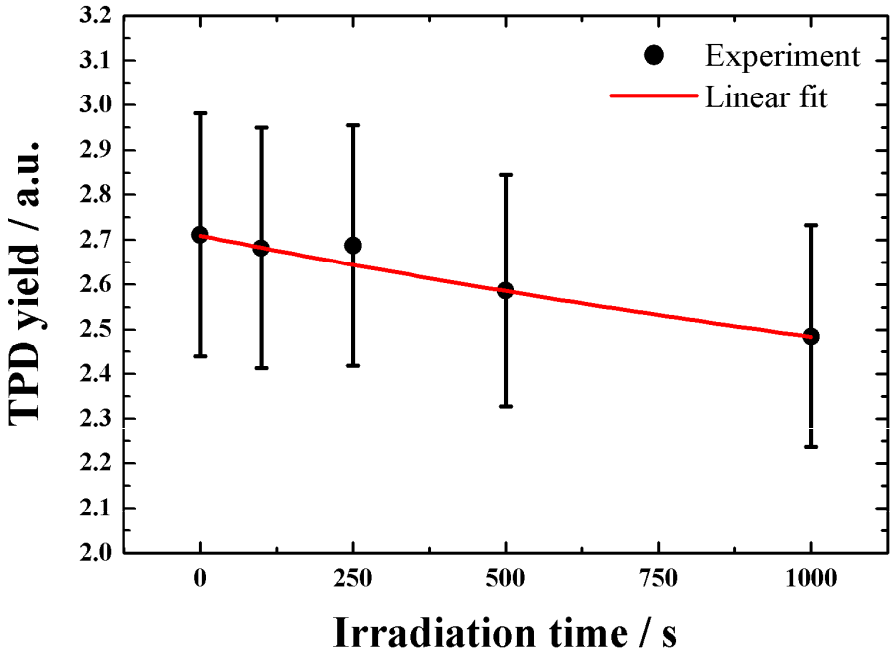

Figure 5.7: Fitted exponential decay for the 50 L C_6H_6 TPD yield decay as a function of electron irradiation time at 250 eV.

5.3.3 Electron irradiation of C_6H_6 adsorbed on ASW

The electron irradiation of C_6H_6 on ASW was considered in significantly more detail. First, the ESD of neutral C_6H_6 upon electron irradiation will be discussed, followed by complementary TPD and RAIRS experiments.

ESD of C_6H_6 adsorbed on ASW

In contrast to the case of C_6H_6 adsorbed directly on the amorphous SiO_2, a significant ESD signal was observed when the C_6H_6 was adsorbed on a thick layer of ASW. In all cases, ASW films were deposited to a thickness sufficient to completely cover the SiO_2 substrate. The results presented here were obtained using either a thick film (200 L) of background dosed ASW, or one deposited using the molecular beam (*ca.*150 L). These film thicknesses are comparable to those used in the experiments described in **Chapter 3** and **Chapter 4**. The substrate temperature used in these experiments was sufficiently high to result in the formation of compact ASW [4]. As a result, no differences were observed in the presented data that could be attributed to film deposition method, in accordance with expectation. Initially, low electron currents of 10-50 nA were used, for comparison with the experiments performed with C_6H_6 adsorbed directly on the amorphous SiO_2 surface. The typical beam currents used and calculated electron fluxes are shown in **Table 5.2**. Beam currents of 100 and 200 nA are included for completeness as they were used in subsequent experiments that will be discussed later. It should be noted that the cross-section calculations utilized the actual beam currents measured using the picoameter. These were averaged over the irradiation time, with the error reflecting the beam stability. The errors quoted for the nominal values in **Table 5.2** correspond to typically observed fluctuations, which were around 10%. The beam current dependence of the ESD signal is examined in **Figure 5.8** for C_6H_6 exposures of 10 and 5 L adsorbed on a thick, multilayer film of ASW. The films were irradiated with 250 eV electrons at the beam currents indicated. The ESD signal displays a peak upon the commencement of irradiation which decays exponentially.

Beam current / nA	Electron flux / electrons cm^{-2} s^{-1}
10±2	$(6.2\pm1)\times10^{12}$
20±3	$(1.2\pm0.2)\times10^{13}$
50±5	$(3.1\pm0.3)\times10^{13}$
100±10	$(6.2\pm0.6)\times10^{13}$
200±20	$(1.2\pm0.1)\times10^{14}$

Table 5.2: Typical beam currents and the corresponding electron fluxes used in the ESD experiments.

This decay does not decay to zero signal, rather a low intensity desorption signal persists until the beam is closed off, as evidenced by a sharp drop in signal. This is visible in one of the plots in **Figure 5.8**, though was also present in the other plots when the beam was closed off at significantly later times. The full desorption timescale is not displayed in order to improve the clarity of the sharp peak. Whilst the shape of the decay is clearly dependent on the C_6H_6 exposure, there are no significant differences between the profiles obtained with the two beam currents. The form of the ESD signal indicates the presence of two desorption channels, one which is very efficient and gives rise to the sharp feature, and a second, much slower process which results in the desorption tail. It is also apparent that the sharp desorption feature displays a faster decay for the 5 L C_6H_6 exposure compared with the 10 L exposure. This layer thickness effect is examined in more detail in **Figure 5.9** which shows the C_6H_6 ESD signals resulting from the 250 eV irradiation of 1, 2, 5, 10 and 20 L exposures of C_6H_6 on ASW. This confirms the decrease in decay rate with increasing C_6H_6 exposure. Although the fast desorption process appears to become less efficient with increasing C_6H_6 film thickness, the tail resulting from the slower process can be seen to increase in intensity. It should also be noted that the most significant change in the fast process occurs for C_6H_6 exposures of *ca*. 5 L and higher. In **Chapter 3** it was shown that multilayer growth begins at exposures in excess of 2 L. It is therefore possible to attribute the sharp desorption feature to the efficient desorption of C_6H_6 adsorbed directly on the ASW surface. The tail feature can be attributed to a much slower desorption process within C_6H_6 overlayers which are not in direct contact with the ASW.

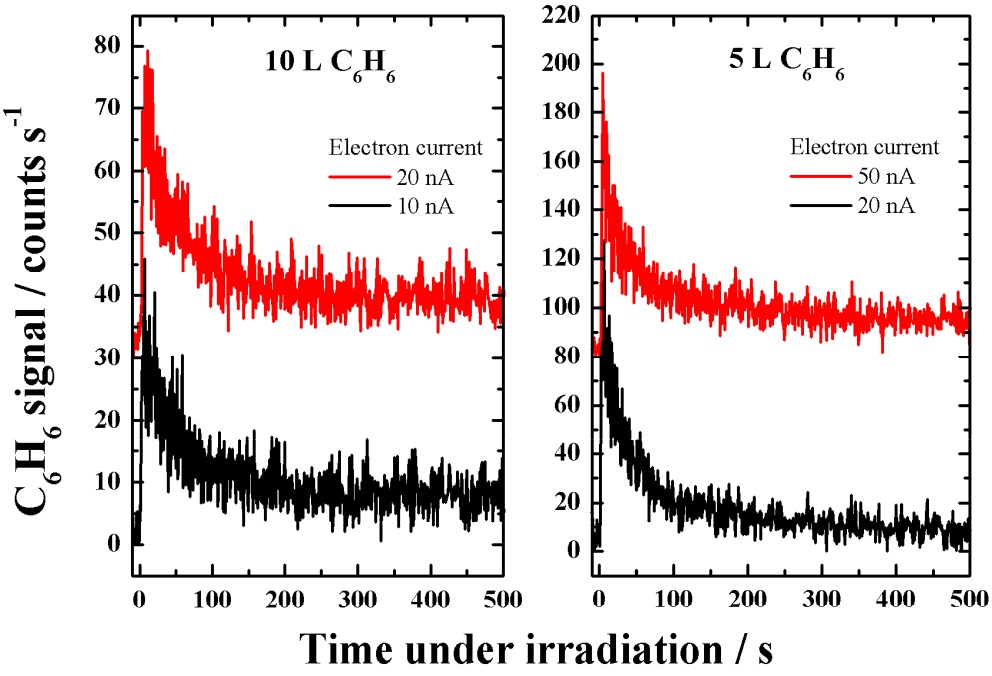

Figure 5.8: C_6H_6 ESD signals for C_6H_6 exposures of 10 and 5 L on ASW for different electron currents and a common electron energy of 250 eV. For each exposure, the two curves have been normalized to a common peak intensity.

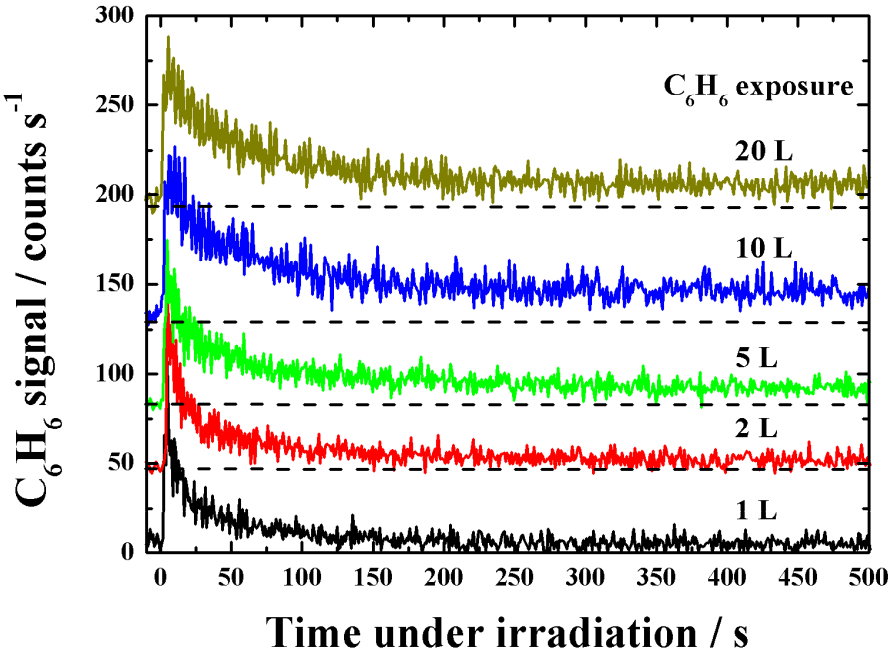

Figure 5.9: C_6H_6 ESD signals for various C_6H_6 exposures on ASW. The electron energy was 250 eV in all cases. All curves have been normalized to a common peak intensity. The dotted lines indicate the baseline for each profile.

In order to make a more quantitative assessment on the effect of film thickness on desorption efficiency, the desorption cross-section was obtained using semilog plots as discussed in **Chapter 4**. As the ESD signals decay to zero, or very close to zero compared to the initial signal, no correction for S_∞ was required. An example of one of these is shown in **Figure 5.10**, with the red line indicating the linear fit used to extract the decay constant. The two linear regions in this plot clearly indicate the presence of two desorption regimes. The cross-sections were calculated using the decay constants and measured beam fluxes, with the error being derived by suitable combination of flux and linear fit uncertainties. The final values for the fast component are shown in **Figure 5.11**. This clearly shows the decrease in cross-section once multilayer growth has begun, although quantitatively this is a relatively small effect. Attempts were made to obtain desorption cross-sections for the slow component, though the poor signal-to-noise ratio in this region made it possible only to suggest an upper limit of 10^{-16} cm^2. The electron energy dependence of the desorption cross-section for the fast desorption component was examined in more detail. In order to minimize the effect of the tail, and to maximise the efficiency of the fast component, a C_6H_6 exposure of 1 L was used. The ESD signals obtained for electron energies of 80, 100, 150, 200 and 250 eV are shown in **Figure 5.12**. The corresponding desorption cross-sections are shown in **Figure 5.13**. The cross-section displays a monotonic increase with electron energy, although this increase is not particularly large over the energy range investigated. Where possible, the cross-section for the slow component was extracted with, as previously, an upper limit of 10^{-16} cm^2 being obtained. There was no apparent energy dependence, though it is likely that this is simply a result of the extremely small signal intensity.

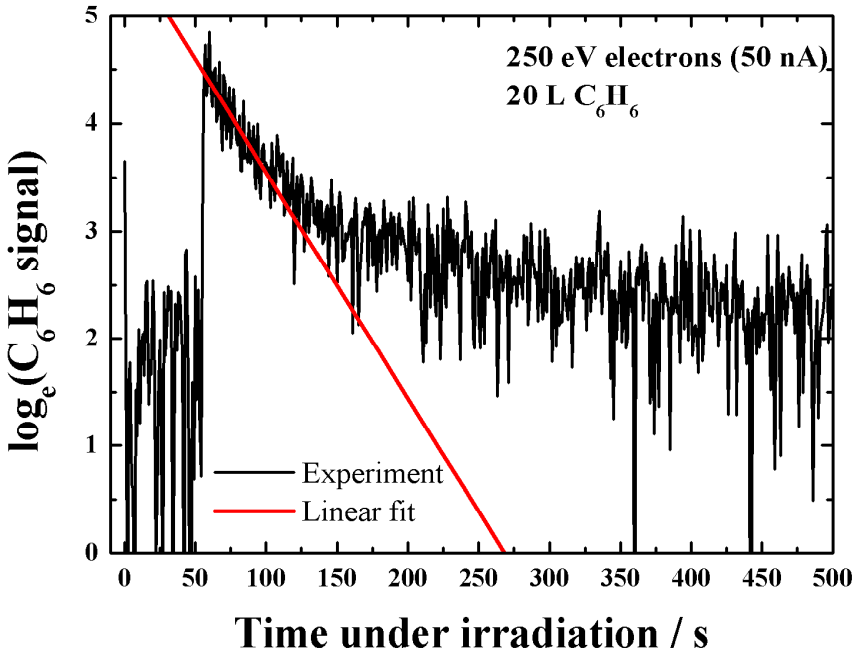

Figure 5.10: Example of a semilog plot for the ESD of C_6H_6 from a 20 L exposure of C_6H_6 adsorbed on ASW. The electron energy and beam current were 250 eV and 50 nA respectively.

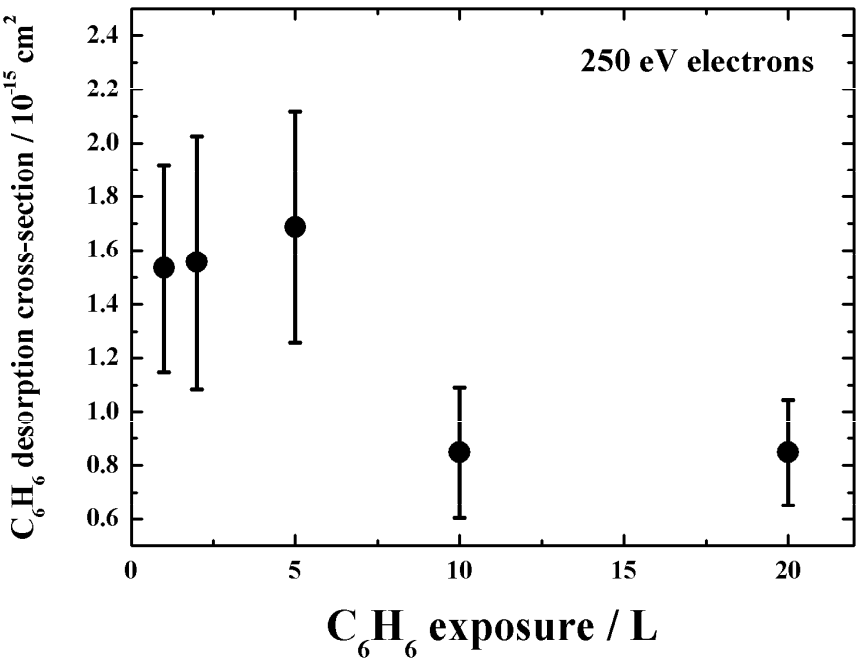

Figure 5.11: C_6H_6 ESD cross-section as a function of C_6H_6 exposure. These values correspond to the fast desorption process that results in the sharp peak at the start of the irradiation period.

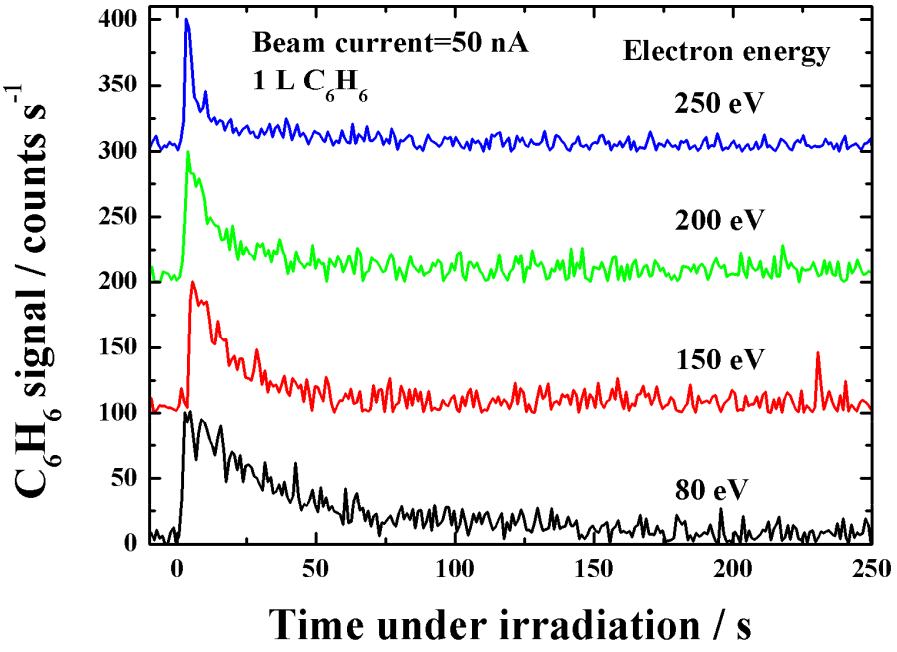

Figure 5.12: C_6H_6 ESD signals for several electron energies. An exposure of 1 L of C_6H_6 on ASW was used in all cases. The curves have been normalized to a common peak intensity and offset for clarity.

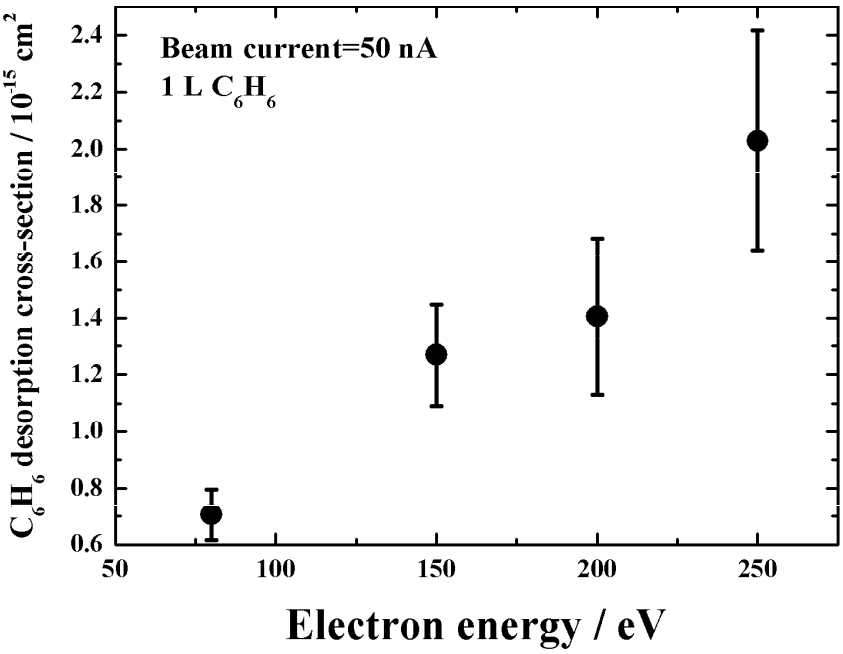

Figure 5.13: C_6H_6 ESD cross-section as a function of electron energy for 1 L of C_6H_6 adsorbed on ASW. These values correspond to the fast desorption process that results in the sharp peak at the start of the irradiation period.

In order to investigate further the slower desorption process, a beam current of 100 nA was used to increase the signal. Retuning of the QMS also resulted in a significant improvement in signal. **Figure 5.14** shows a series of C_6H_6 ESD signals for small exposures (1, 2 and 5 L) of C_6H_6 adsorbed on ASW and irradiated with 200 eV electrons using a beam current of 100 nA. A close-up of the slow desorption process is shown in **Figure 5.15**. The overall features of the ESD curves are in good agreement with those obtained at lower beam currents. The fast decays all appear to be very similar, as seen previously for exposures below 10 L. It should be noted that at this electron flux, this feature is sufficiently fast that the number of points in the decay is significantly reduced. The slow component however decays in a much more reliable fashion with a significantly improved signal-to-noise ratio. A typical semilog plot for this data is shown in **Figure 5.16** for the 2 L C_6H_6 exposure which clearly shows two linear regions associated with the two desorption processes. It should be noted that in obtaining the cross-section, no subtraction of the slow decay was made when determining the slope for the fast decay. It is thought that in this case the slow decay is sufficiently slow compared with the fast decay that the effect is within the uncertainty. The desorption cross-sections obtained for the two processes are plotted as a function of exposure in **Figure 5.17.** There is no apparent strong exposure dependence of either cross-section, though the decrease in going from 3 to 5 L may indicate the start of a gradual decrease in cross-section to the value for a 10 L exposure discussed previously. Mean values of the cross-sections for small exposures of C_6H_6 are found to be $(2.6\pm1)\times10^{-15}$ cm^{-2} and $(2.9\pm1)\times10^{-17}$ cm^2 for the fast and slow components respectively. In both cases, the thickness dependence of the cross-section is relatively minor over the range investigated. However, there is some evidence for a thickness dependence of the amount of C_6H_6 desorbed. Variability in sensitivity made a quantitative assessment of this difficult, but some general trends can be observed. For low coverages of around 1 monolayer the fast component dominates. As the exposure is increased to a few multilayers, the intensity of the fast component decreases whist that of the slow component increases. Limited experiments for thick C_6H_6 layers of 200 L exposure resulted in extremely small signals – in agreement with the lack of observation of C_6H_6 from the pure C_6H_6 ice.

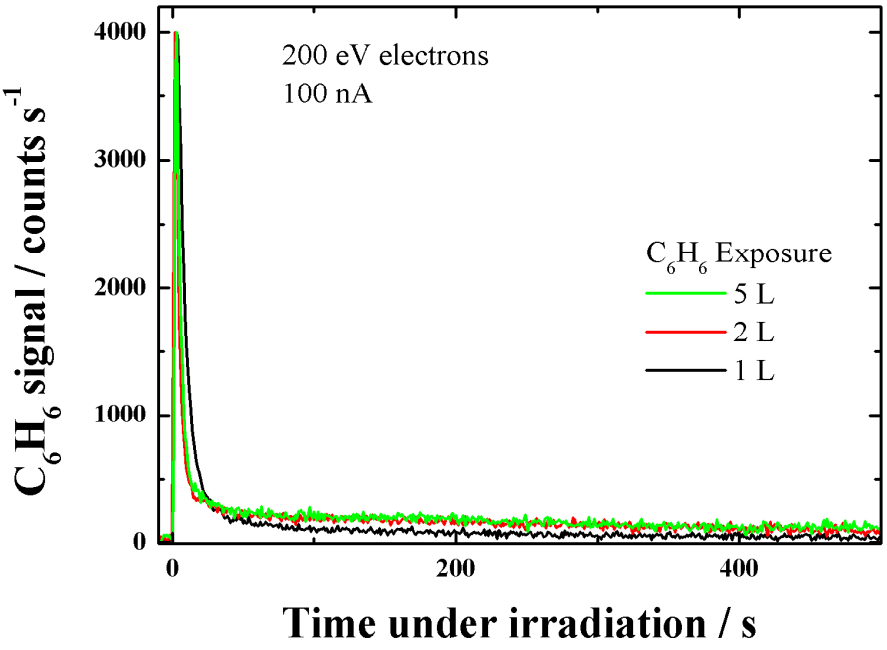

Figure 5.14: C_6H_6 ESD signals for small exposures of C_6H_6 adsorbed on ASW and irradiated with 200 eV electrons at a beam current of 100 nA. All three traces have been normalized to a common peak intensity.

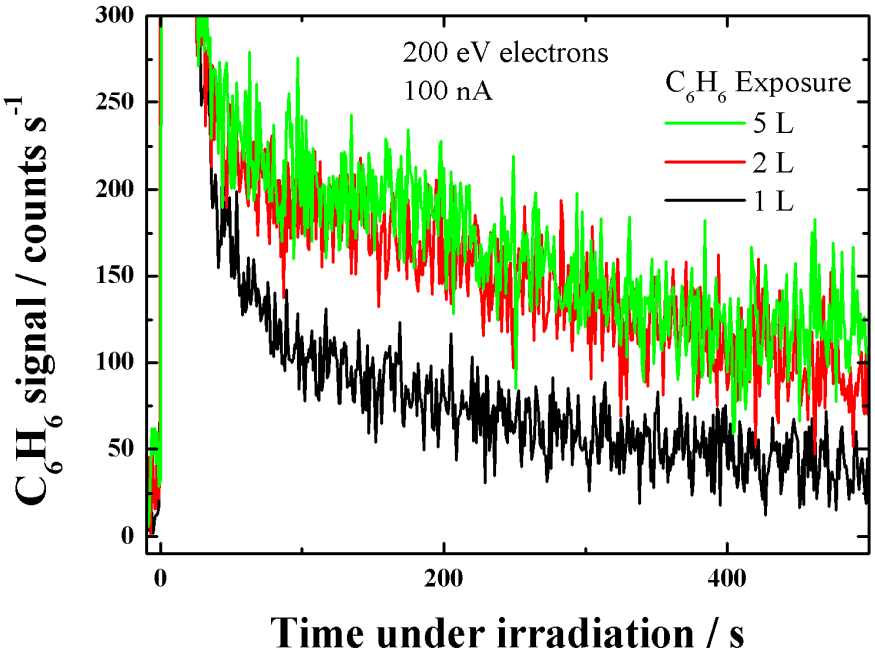

Figure 5.15: C_6H_6 ESD signals for small exposures of C_6H_6 adsorbed on ASW and irradiated with 200 eV electrons at a beam current of 100 nA showing a close-up of the slower decay component.

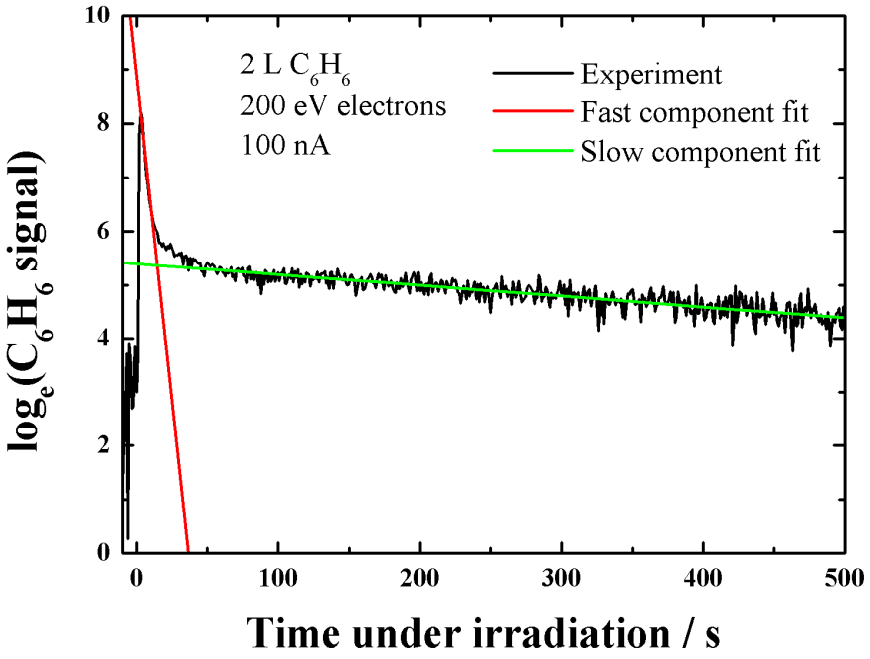

Figure 5.16: Semilog plot for the C_6H_6 ESD from 2 L of C_6H_6 adsorbed on ASW and irradiated with 200 eV electrons at a beam current of 100 nA. Linear fits to the fast and slow component are shown.

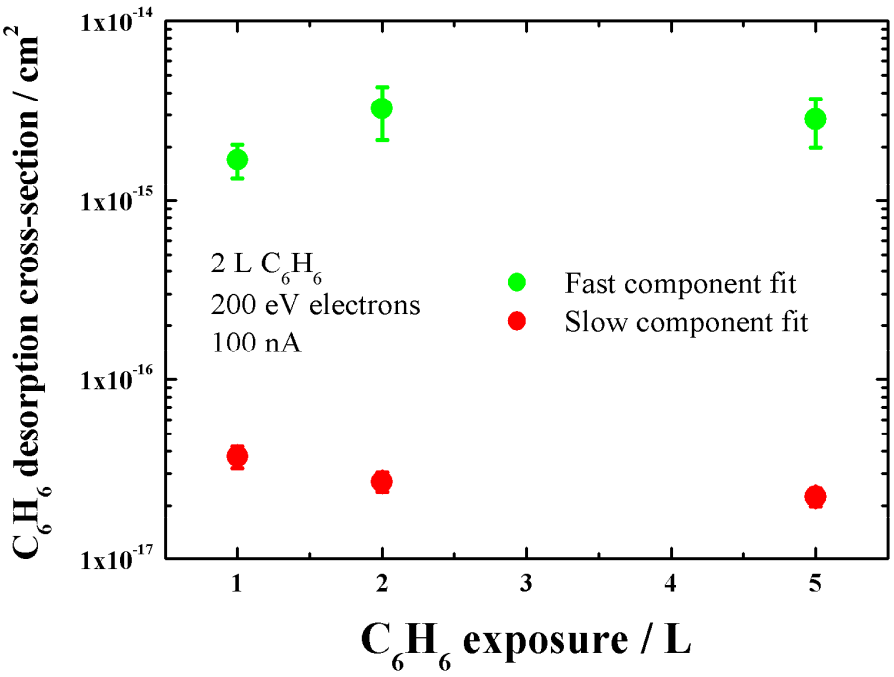

Figure 5.17: C_6H_6 ESD cross-section as a function of C_6H_6 exposure. An electron energy of 200 eV and beam current of 100 nA were used in all cases.

These observations indicate that both of the observed desorption channels are in some way related to the interface between the C_6H_6 and H_2O ice.

A more consistent sensitivity was obtained in experiments performed with a beam current of 200 nA. These were used to obtain further estimates of the desorption cross-sections. **Figure 5.18** shows clearly the intensity variation of the signals with C_6H_6 exposure for film thickness ranging from *ca.* 1 monolayer to a few monolayers. The extremely small signal at an exposure of 0.1 L must result from isolated C_6H_6 molecules on the ASW surface. At this higher beam current, the slow desorption component also exhibits an appearance type region where the desorption signal increases before decaying. This is suggested in some of the profiles obtained at lower beam currents and is probably enhanced here as a result of the increased desorption signal. This suggests that the slow component does not begin at the same instant that the irradiation begins; rather it may rely on some precursor that initially increases in concentration.

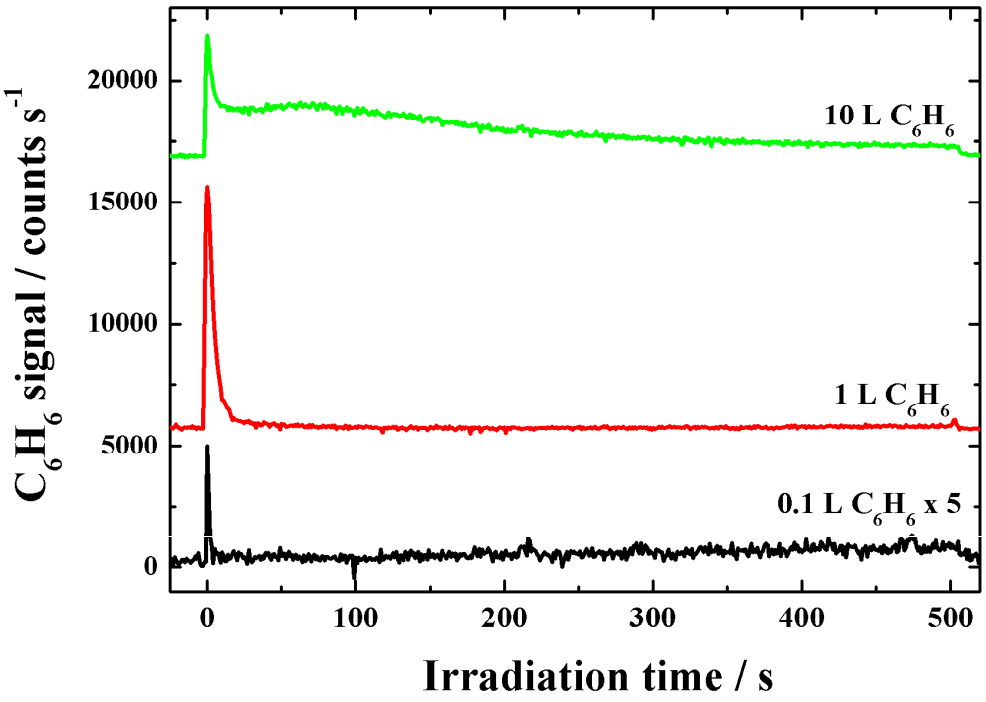

Figure 5.18: C_6H_6 ESD from various exposures of C_6H_6 adsorbed on ASW. A beam current of 200 nA and an electron energy of 250 eV were used.

ESD profiles obtained at a range of electron energies are shown in **Figure 5.19** and **Figure 5.20** for C_6H_6 exposures of 1 and 10 L respectively. The desorption cross-sections for the fast component obtained from the 1 L exposure data are shown in **Figure 5.21**. The values obtained are in good agreement with those obtained at lower beam currents. Extraction of the fast component cross-section from the 10 L data was more difficult as a result of the more complicated nature of the desorption. Semilog plots were fitted for the initial decay, with the obtained decay constant suggesting a reduction in the fast component desorption cross-section by approximately a factor of two. Attempts were made to fit the 10 L ESD profiles with the following functional form which includes a fast decay and a slow decay with an associated appearance:

$$S(t) = A_1 \exp\left[-\frac{t}{\tau_1}\right] + A_2\left(\exp\left[-\frac{t}{\tau_{2d}}\right] - \exp\left[-\frac{t}{\tau_{2a}}\right]\right) \qquad \textbf{Equation 5.3}$$

where A_1 and A_2 are the amplitude and τ_1 and τ_{2d} are the decay constants associated with the two components. τ_{2a} is the time constant associated with the appearance of the second component. The resulting fits reproduced the experimental data well as shown in **Figure 5.22**. A comparison of the cross-sections for the fast component obtained from semilog plots for the 1 L and 10 L exposure experiments and the three component fit for the 10 L experiment are shown in **Figure 5.23**. The errors displayed in all cases are derived from the uncertainty in the flux and the error associated with the fitting procedure employed. A generally monotonic increase from around $(0.7\pm0.2)\times10^{-15}$ cm^{-2} to $(2.2\pm0.5)\times10^{-15}$ cm^{-2} between electron energies of 100 and 300 eV is observed. Cross-sections corresponding to the appearance and slow decay components were extracted, although difficulties were encountered for those plots where no significant rise was observed. The electron energy dependence in the range studied was relatively minor, and approximate cross-sections for the slow decay and associated appearance of $(8\pm2)\times10^{-17}$ cm^2 and $(3\pm2)\times10^{-17}$ cm^2 respectively were obtained. The value for the decay component is in agreement with the estimate of $<10^{-16}$ cm^2 obtained using lower beam currents.

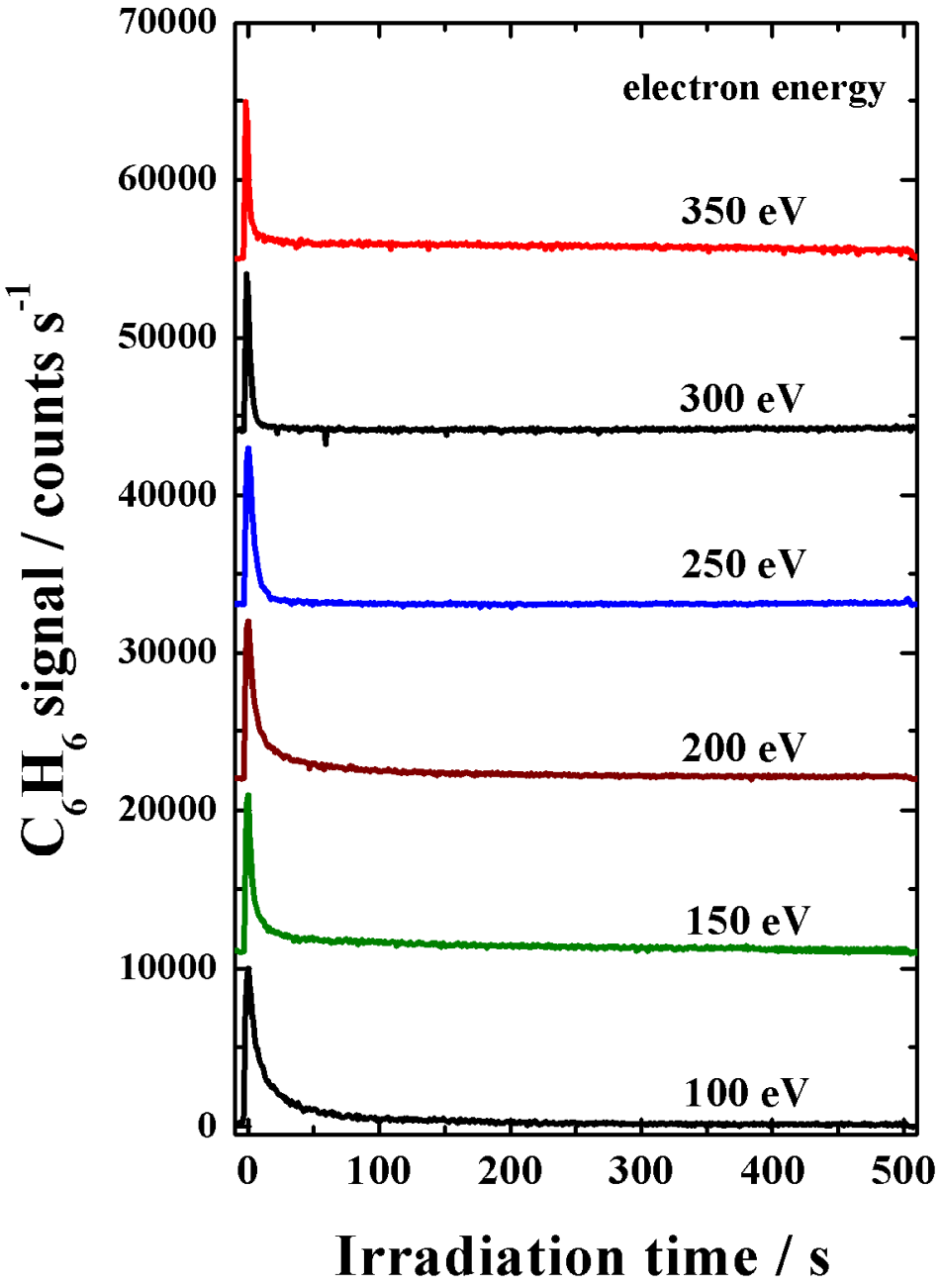

Figure 5.19: C_6H_6 ESD signals obtained from 1 L of C_6H_6 adsorbed on top of ASW for various electron energies. A beam current of 200 nA was used in all cases. The traces have been normalized to a common peak intensity.

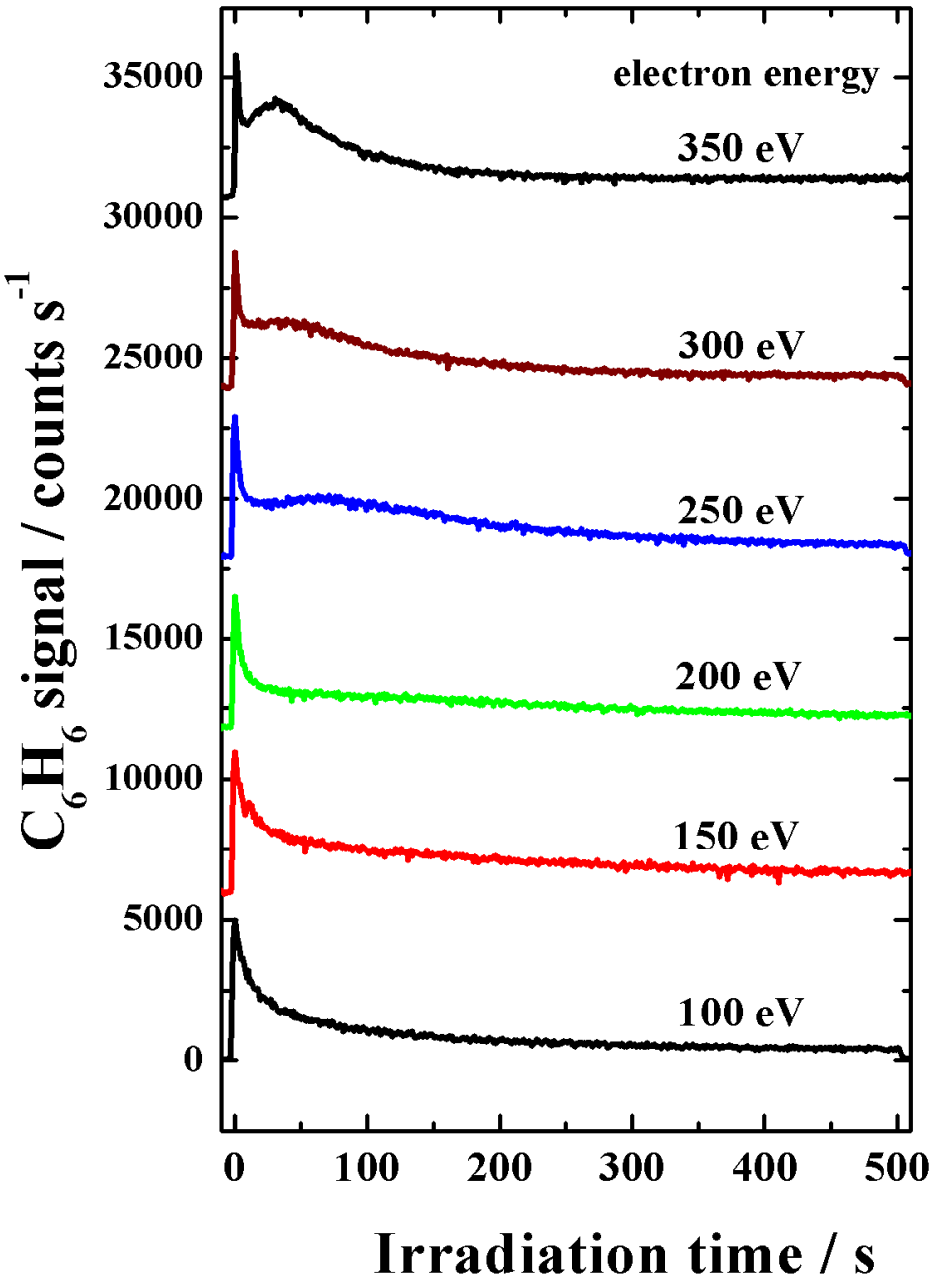

Figure 5.20: C_6H_6 ESD signals obtained from 10 L of C_6H_6 adsorbed on top of ASW for various electron energies. A beam current of 200 nA was used in all cases. The traces have been normalized to a common peak intensity.

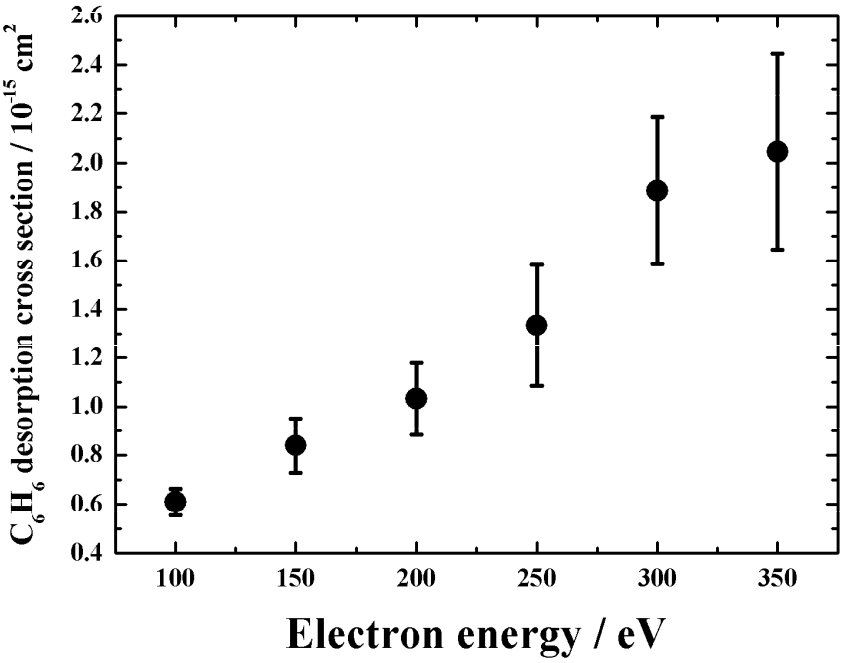

Figure 5.21: C_6H_6 desorption cross-sections for the fast component as a function of electron energy.

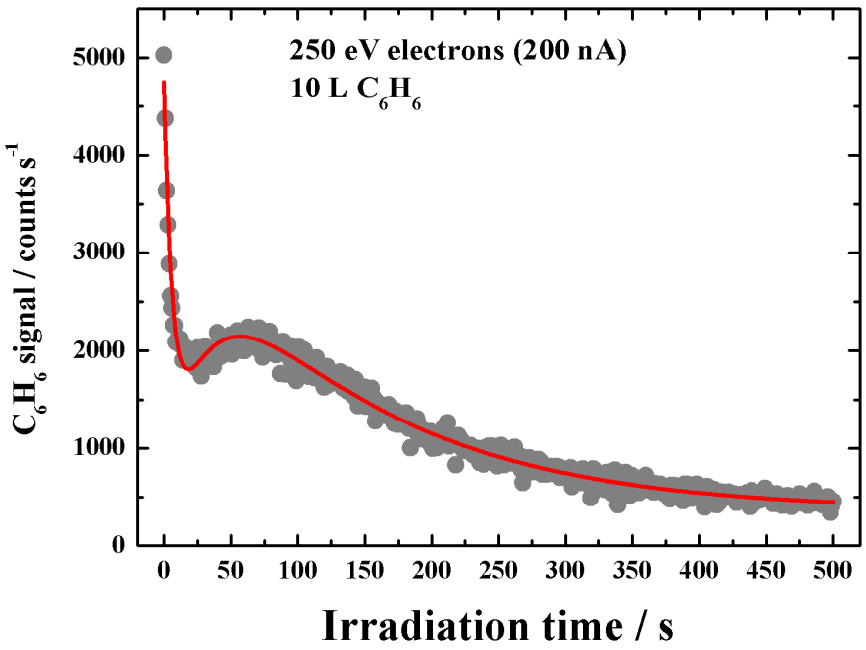

Figure 5.22: Three component fit to the C_6H_6 ESD observed with an electron energy of 250 eV a beam current of 200 nA.

The suggested mechanisms behind the desorption processes will be discussed later. Finally, **Figure 5.24** shows examples of H_2O ESD observed during the irradiation experiments. It can be observed that the H_2O desorption is inhibited by the overlayer of C_6H_6 with the H_2O signal decreasing in intensity as the C_6H_6 film thickness is increased. Measurements of the H_2O desorption cross-sections from pure H_2O films using a combination of ESD, TPD and RAIRS are underway [5].

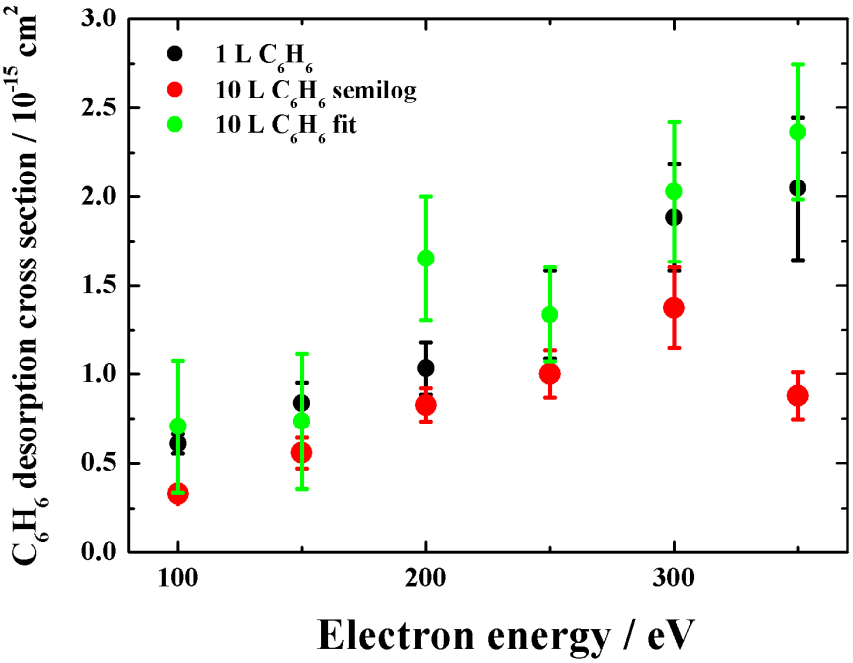

Figure 5.23: Comparison between cross-sections obtained for the fast component using different methods.

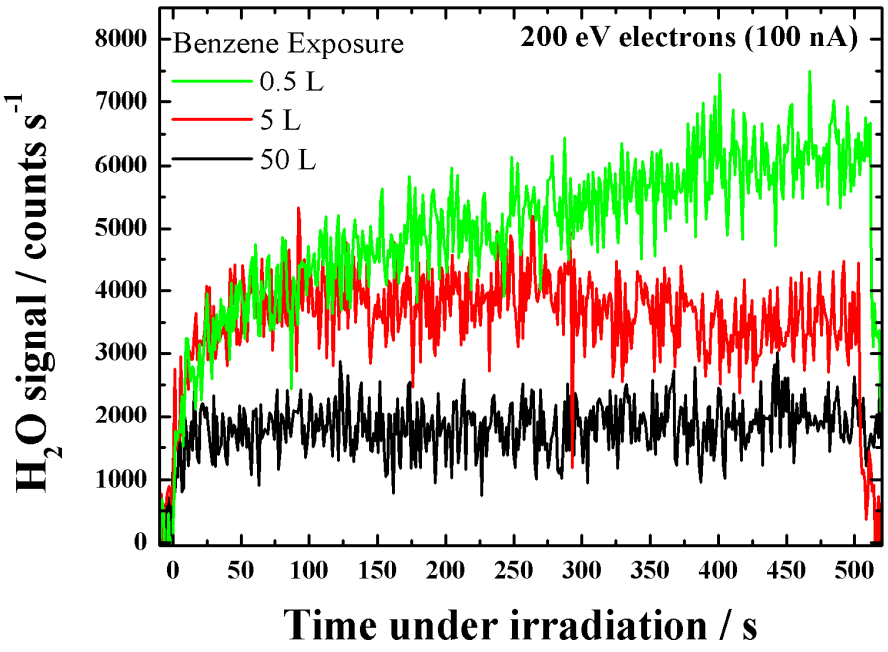

Figure 5.24: Typical H_2O ESD signals observed when different exposures of C_6H_6 are adsorbed on top of ASW.

Loss of C_6H_6 adsorbed on ASW observed through RAIRS

As the electron energy dependence of the observed desorption has been shown to relatively small, experiments were conducted using energies of 250 and 100 eV. For comparison with the experiments performed on the amorphous SiO_2 surface, TPD experiments were also conducted for this system. RAIRS was however found to be a much more reliable method of determining total loss as a full experiment could be performed using the same C_6H_6 sample. With the TPD experiments, difficulties with dose reproducibility and sensitivity made cross-section determination difficult. **Figure 5.25** shows an example of a such an experiment performed at 250 eV using a C_6H_6 of 10 L deposited on top of a thick ASW film. The overall change in shape of the TPD profile with irradiation is in agreement with that obtained on amorphous SiO_2, with an initial decrease in the original peak and the simultaneous growth of a high temperature shoulder, with the overall intensity gradually decreasing as a function of irradiation time. The scatter in the TPD yields made cross-section determination difficult, though an estimate of 2000±500 s for the time constant could be made. This corresponds to a cross-section of $<1\times10^{-17}$ cm^2. The difficulties encountered suggest that the loss process may be more complicated than a simple exponential decay. Without a full understanding of the appearance of the high temperature shoulder, the values obtained here, and for C_6H_6 multilayers on SiO_2 should be regarded as estimates.

Typical RAIR spectra for C_6H_6 are shown in **Figure 5.26** for 20 L of C_6H_6 adsorbed on a thick ASW film. Spectra are shown prior to irradiation, and following 4000 s irradiation with 250 eV electrons using a beam current of 150 nA. C_6H_6 loss was monitored by considering the integrated absorbance, *A*, of the aromatic C-C stretching band at 1477 cm^{-1}. It is clear that a significant amount of H_2O is lost, probably through a combination of desorption and dissociation with subsequent reaction. The H_2O loss was not studied in detail as more detailed investigations are currently in progress [5]. The C-C stretching band for C_6H_6

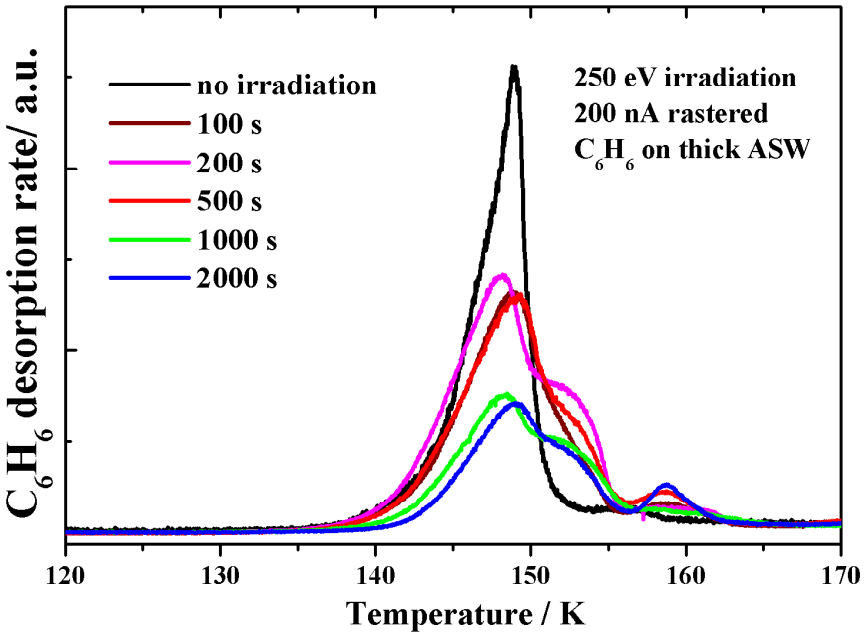

Figure 5.25: TPD profiles obtained prior to and following different irradiation periods with 250 eV electrons using a beam current of 200 nA.

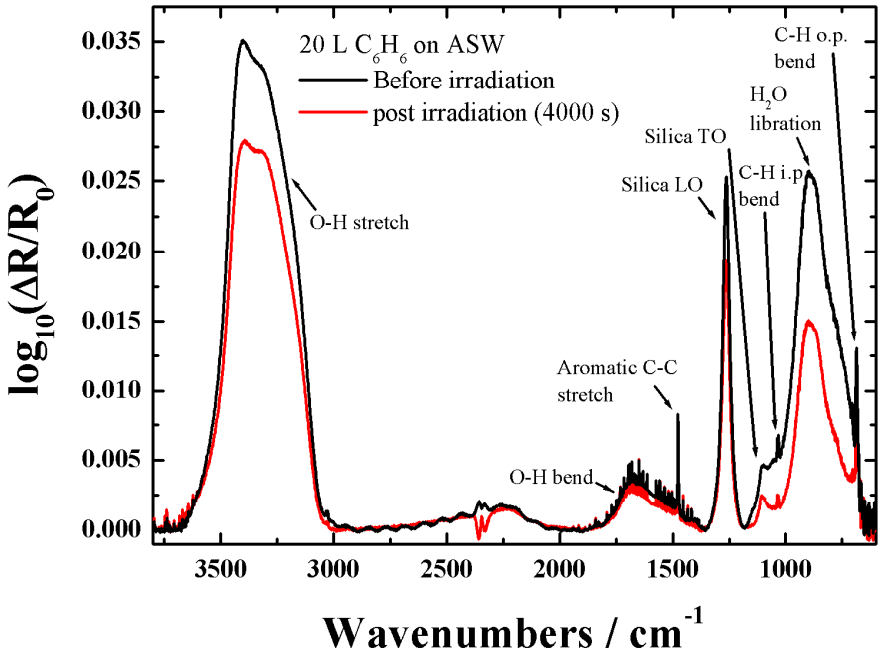

Figure 5.26: RAIR spectra for 20 L of C_6H_6 adsorbed on a thick ASW film prior to irradiation and after 4000 s irradiation with 250 eV electrons using a beam current of 150 nA.

exposures of 10, 20 and 50 L is shown in **Figure 5.27** as a function of irradiation time with 250 eV electrons using a beam current of 150 nA. Corresponding decay curves for the integrated absorbance relative to the unirradiated band (*i.e.* A/A_0) along with single exponential decay fits are shown in **Figure 5.28**. The equivalent spectra and decay curves for experiments using 100 eV electrons are shown in **Figure 5.29** and **Figure 5.30** respectively. Exponential fits were only possible for irradiation times of up to 1000 s and 2000 s for electron energies of 250 and 100 eV respectively. The extra loss observed at longer times possibly arises as a result of thermal desorption occurring during the extended irradiation time. Cross-sections were obtained from the decay constants of the fits. The errors were calculated by considering an error of 1×10^{-4} for the RAIR spectra, resulting in an error of around 1×10^{-3} for the integrated absorbance. The corresponding relative error was combined with that associated with the electron flux. The cross-sections yielded by this analysis are summarized in **Table 5.3** and **Figure 5.31**. Compared to the ESD cross-sections, the fast component with a cross-section of around 2×10^{-15} cm^2 is clearly absent. This is reasonable given that this channel is only efficient for a very small population of C_6H_6 molecules in direct contact with the ASW surface. Whilst this channel is extremely efficient for the desorption of this small amount of C_6H_6, it would not have a significant impact on the total amount of C_6H_6 desorbed. The overall loss cross-sections for the 10 and 20 L C_6H_6 films observed through the RAIRS experiments are around 8×10^{-17} cm^2 and 5×10^{-17} cm^2 for electron energies of 250 and 100 eV respectively. These are comparable to the value obtained for the slow ESD component and likely consist of contributions from both ESD and decomposition of bulk C_6H_6. The ESD component was previously attributed to a second mechanism at the C_6H_6 interface.

No chemical reaction products were observed in any of the RAIR spectra observed. This most likely results from the dominant non-desorption channel being dehydrogenation through the breaking of C-H bonds in which no C-C bonds are cleaved. This is in contrast to studies involving energetic ion irradiation. Strazulla *et al*. [6] observed the formation of products both more and less volatile

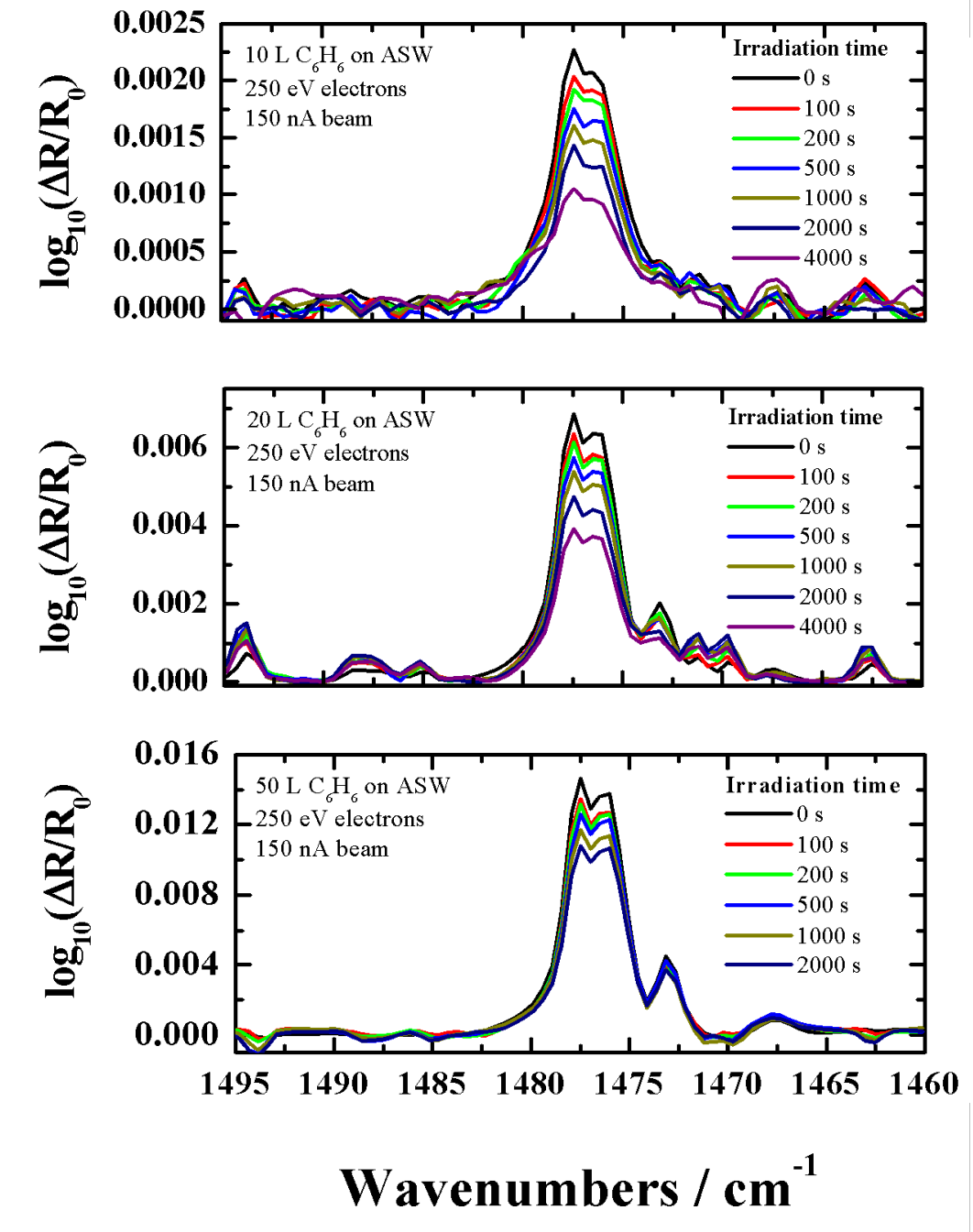

Figure 5.27: C_6H_6 C-C stretching band for 10, 20 and 50 L of C_6H_6 adsorbed on ASW as a function of irradiation time. The electron energy was 250 eV.

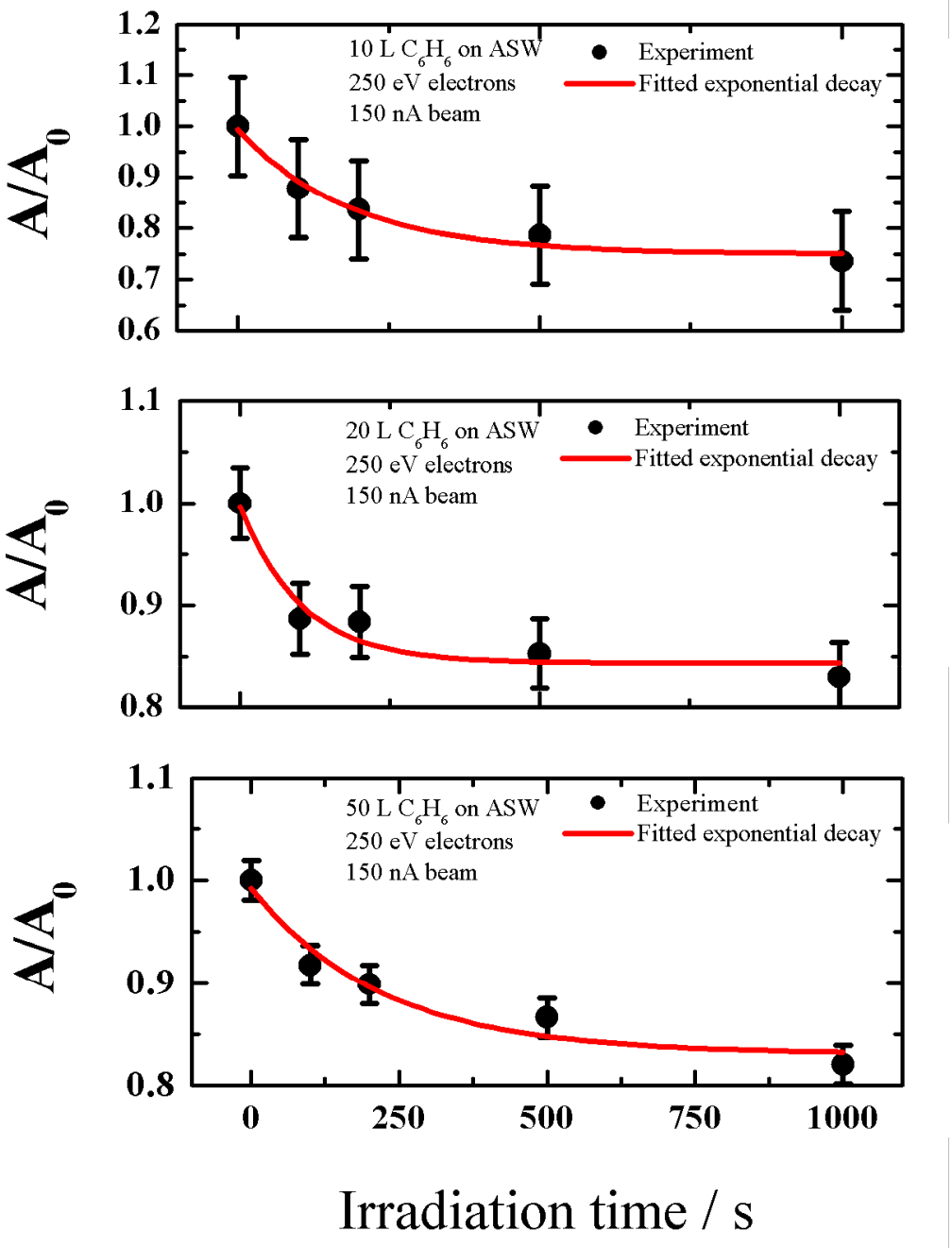

Figure 5.28: Fitted exponential decays for the decay of the C-C stretching band 10, 20 and 50 L of C_6H_6 adsorbed on ASW as a function of irradiation time. The electron energy was 250 eV.

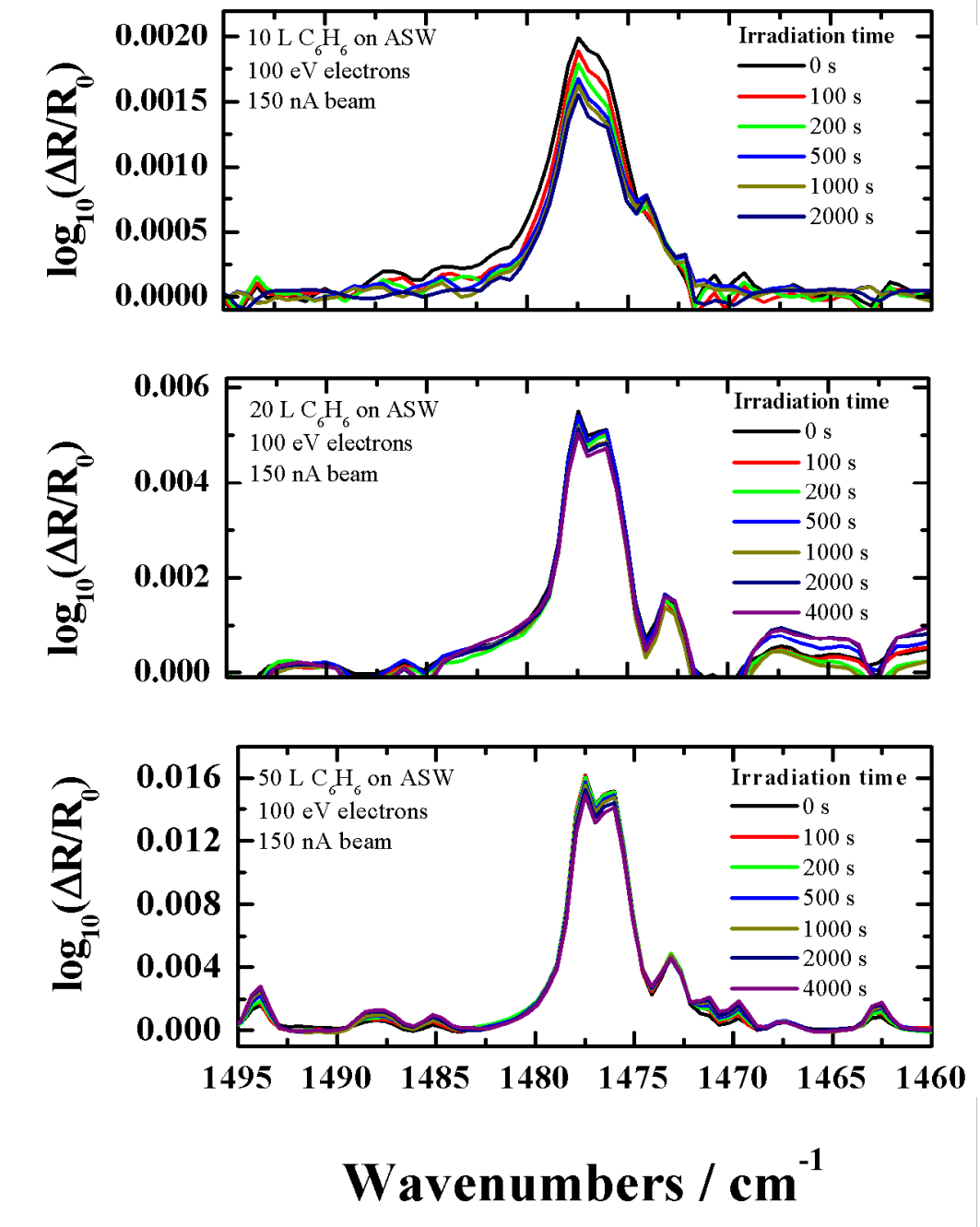

Figure 5.29: C_6H_6 C-C stretching band for 10, 20 and 50 L of C_6H_6 adsorbed on ASW as a function of irradiation time. The electron energy was 100 eV.

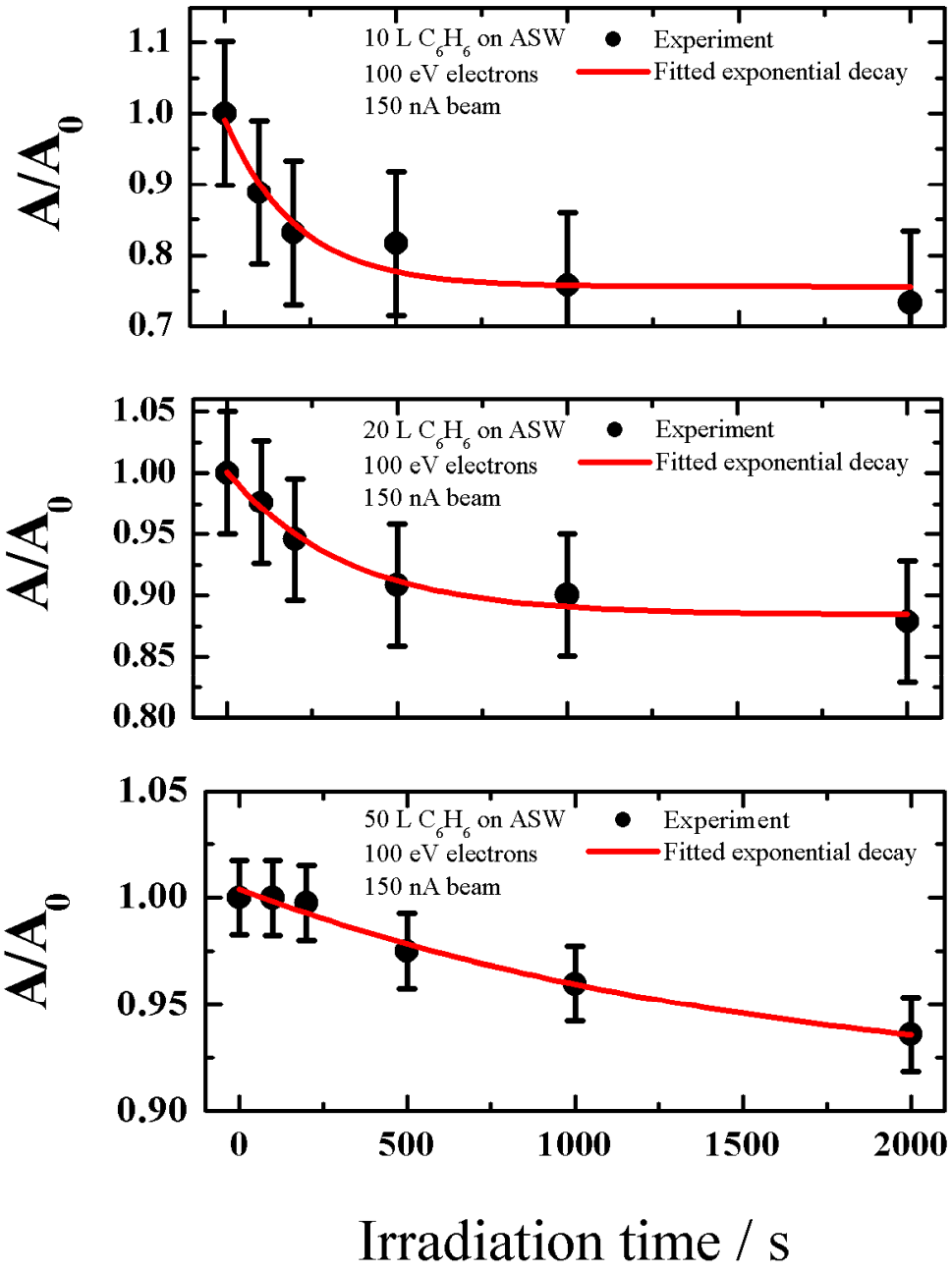

Figure 5.30: Fitted exponential decays for the decay of the C-C stretching band 10, 20 and 50 L of C_6H_6 adsorbed on ASW as a function of irradiation time. The electron energy was 100 eV.

Energy / eV	C_6H_6 exposure / L	Cross-section / 10^{-17} cm^2
250	10	6.6±4
250	20	9.5±5
250	50	3.8±2
100	10	6.5±2
100	20	3.6±1
100	50	0.8±0.1

Table 5.3: Cross-sections for C_6H_6 loss obtained through RAIRS experiments for C_6H_6 exposures of 10, 20 and 30 L and electron energies of 250 and 100 eV.

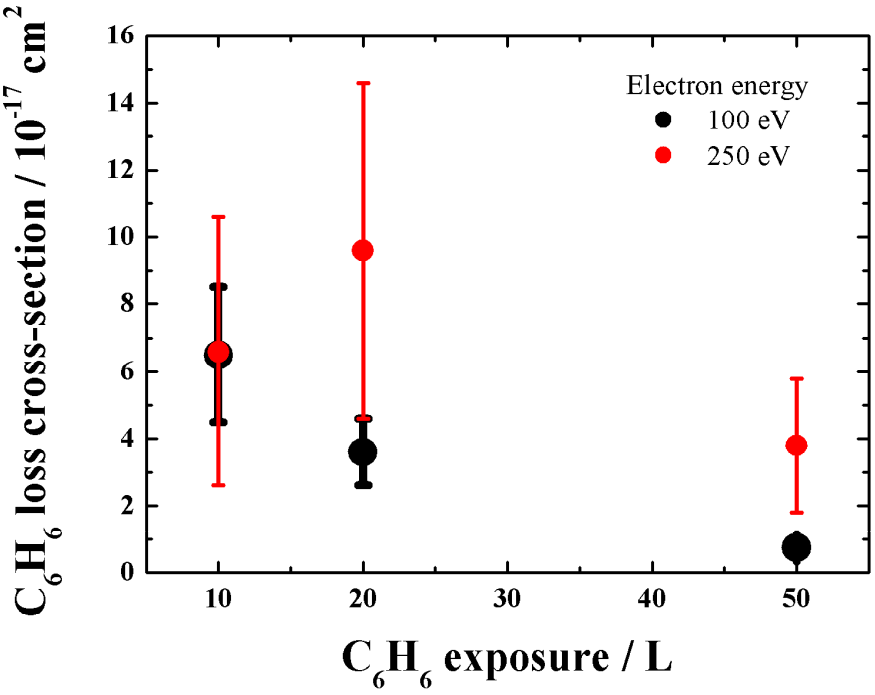

Figure 5.31: Total C_6H_6 loss cross-sections as determined from the RAIRS experiments. The 100 eV points and error bars are plotted with thicker lines for clarity.

than C_6H_6 as a result of irradiation with 3 keV ions. Acetylene (C_2H_2) was observed through three bands at 3232, 1414 and 754 cm^{-1} corresponding to the C-H asymmetric stretch, combination and C-H out-of-plane bend of C_2H_2 respectively. Ruiterkamp *et al.* [7] also observed C_2H_2 formation through the same bands following the irradiation of both pure and Ar matrix isolated C_6H_6

with either 800 keV protons or VUV photons. Any possible reaction products within the C_6H_6 film are best examined by considering the 50 L experiment where limited loss of C_6H_6 was observed. RAIR spectra for the spectral regions where these bands associated with C_2H_2 are shown in **Figure 5.32**. No features that can be attributed to C_2H_2 are visible. The sharp features in the combination region are associated with small fluctuations in the concentration of H_2O vapour in the purge. The deviation between the two spectra in the C-H bend region is an artefact associated with this region being very close to the cut-off of the RAIRS system employed. Whilst no clear evidence of C_2H_2 was obtained, it is worth noting two possibilities. Any C_2H_2 that does form would be expected to desorb at the base temperature of these experiments. Previous studies have demonstrated the desorption of multilayer C_2H_2 is complete by *ca*. 70 K [8]. Any C_2H_2 that is trapped may also recombine on the timescale of these experiments. Phenyl radicals are also a possible product having been observed previously in the 1 MeV electron irradiation of Xe matrix isolated C_6H_6 [9], though this was attributed to a mechanism involving first the ionization of Xe.

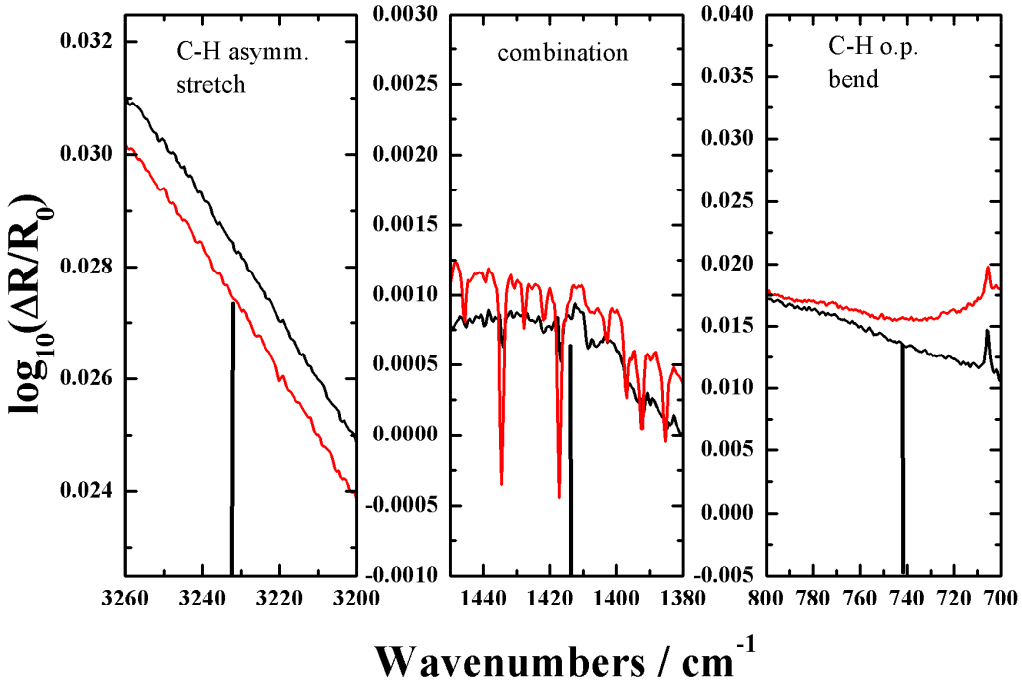

Figure 5.32: RAIR spectra showing the regions where IR bands associated with C_2H_2 would be expected before (black) and after (red) irradiation of 50 L of C_6H_6 on ASW with 250 eV electrons for 2000s. The vertical black lines indicate the location of C_2H_2 bands observed in ion irradiation experiments [6].

Furthermore, these experiments were performed at 16 K and annealing at 45 K resulted in the formation of the cyclohexadienyl radical identified through an IR feature at 618-620 cm^{-1} associated with the C-H out-of-plane band and the CH_2 wagging mode. This frequency is outside the range accessible by the system used in these experiments. However, in the current non-isolated system it seems more likely that reactions are limited to dehydrogenation and simple recombination reactions, reforming benzene along with larger scale carbonaceous deposits. No spectral evidence of any other products within the C_6H_6 were observed. The possibility of reaction at the C_6H_6/H_2O interface involving fragments from H_2O decomposition to form phenol (C_6H_5OH) was also considered. No bands that could be attributed to the O-H stretching mode around 3200 cm^{-1} (hydrogen bonded) or 3600 cm^{-1} (free O-H) [10] were visible, though the presence of the H_2O O-H stretching band would make identification difficult. It is also likely that the concentration of C_6H_5OH formed in the interface region would be below the detection limits. The observed rapid desorption of C_6H_6 from the interface region also indicates that C_6H_5OH would be a minor channel. In summary, despite extensive searches no reaction products could be identified through RAIRS experiments confirming that C_6H_6 loss through desorption and carbonization are the dominant processes. As a result, the origin of the high temperature shoulder on the irradiated multilayer C_6H_6 TPD profiles is uncertain. Physical processing of the bulk C_6H_6 ice would seem the most plausible explanation. The presence of carbonaceous deposits could lead to subtle changes in the C_6H_6 binding energy and effectively trap some C_6H_6 to a higher desorption temperature. Further studies would be required to investigate the origin of this feature, possible with the use of STM to examine the formation of carbon structures on the surface.

Overview of possible mechanisms for C_6H_6 loss

A summary of the signatures of C_6H_6 loss from the experiments discussed in this chapter is presented in **Table 5.4**. The non-desorption loss channel of dehydrogenation has already been discussed, along with the possibility of the formation of reaction products either below the detection limit or that desorb upon formation. The two desorption channels will now be considered in more detail.

Mechanism	Experiment	Cross-section / cm^2	Electron energy / eV	Beam current / nA	Comments
Dehydrogenation	TPD C_6H_6 on SiO_2	$(3\pm1)\times10^{-17}$	250	15	
Desorption (Slow)	ESD C_6H_6 on ASW	$(8\pm2)\times10^{-17}$ $(3\pm1)\times10^{-17}$	250 200	200 100	Decreases with C_6H_6 thickness
	RAIRS C_6H_6 on ASW	$(8\pm4)\times10^{-17}$ $(5\pm3)\times10^{-17}$	250 100	150 150	
Desorption (Fast)	ESD C_6H_6 on ASW	$(2.5\pm1)\times10^{-15}$ $(1.5\pm1)\times10^{-15}$	200 200	100 200	Increases with energy decreased for thick layers

Table 5.4: Summary of C_6H_6 loss processes observed through the experiments discussed in this chapter.

It is important to consider estimates of the electron penetration depth into both C_6H_6 and H_2O ices in understanding the possible desorption mechanisms. An estimate of the mean free path for electrons of energy, E can be calculated from the following expression: [11]

$$\lambda / nm = \frac{538a}{E^2} + 0.41a^{3/2}E^{1/2} \qquad \textbf{Equation 5.4}$$

where a is the mean "atomic" diameter of the scattering material given by:

$$a = \left(\frac{\Omega}{1000 \rho L} \right)^{1/3}$$ **Equation 5.5**

where Ω is the molar mass, ρ the material density and L the Avogadro number. H_2O was considered as a single scattering centre of mass 18 g mol^{-1} and with the density of ice determined in **Chapter 4** (0.87 g cm^{-3}). The major scattering centres for C_6H_6 are the C atoms. Therefore, a was calculated assuming the density of C_6H_6, (1.11 g cm^{-3}) associated with the number density calculated in **Chapter 4** and the atomic mass of carbon. The calculated mean free paths for C_6H_6 and H_2O are shown as a function of electron energy over the range used in these experiments in **Figure 5.33**. The mean free path values at the electron energies of interest can then be used to obtain the ratio of the intensity of the initial electron beam, to that at a distance d in the film, I/I_0 for an angle of incidence, θ [11]:

$$\frac{I}{I_0} = \exp\left(-\frac{d}{\lambda(E)\cos\theta} \right)$$ **Equation 5.6**

This quantity is plotted for C_6H_6 and H_2O in **Figure 5.34** and **Figure 5.35** respectively. It should be noted that the penetration depths have been converted into dose equivalent units in Langmuir using the film thickness calculated for particular doses in **Chapter 4**. These figures will be referred to in the discussion of mechanisms that follows. The ESD data clearly indicate that both of the desorption channels identified are reliant on the presence of H_2O molecules. In particular, the fast desorption channel with a cross-section of *ca.* 1×10^{-15} cm^2 is the only channel present at low coverage. As the coverage is increased towards monolayer saturation, this component increases in intensity. Once multilayers begin to form, this component is gradually reduced in intensity, along with a gradual decrease in cross-section. This desorption is therefore attributed to the desorption of isolated C_6H_6 molecules that are directly in contact H_2O molecules at the vacuum interface. This is analogous to the photon-induced desorption of C_6H_6 from surface bound $C_6H_6(H_2O)_n$ clusters discussed in **Chapter 4**.

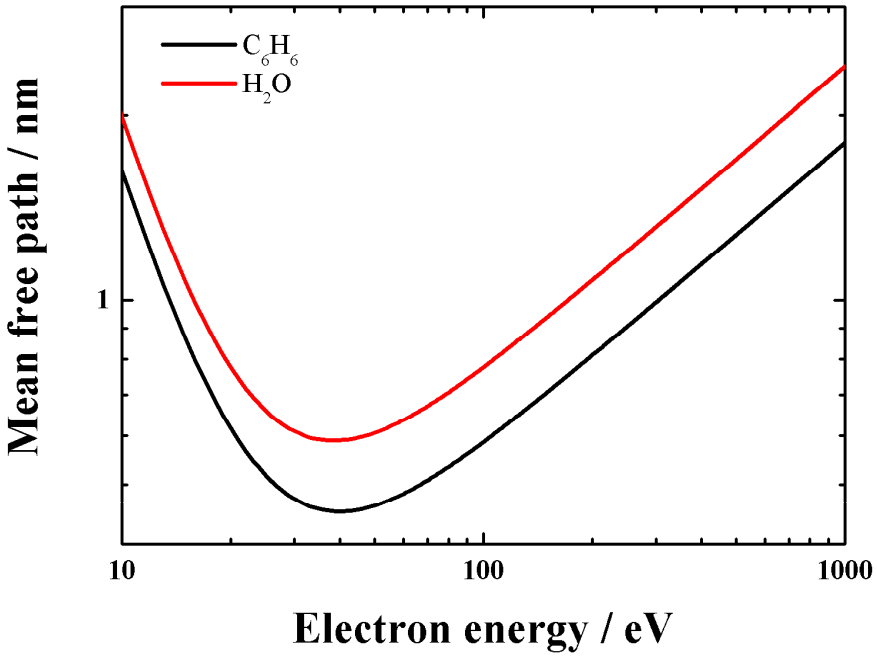

Figure 5.33: Calculated mean free paths for electrons in C_6H_6 and H_2O films.

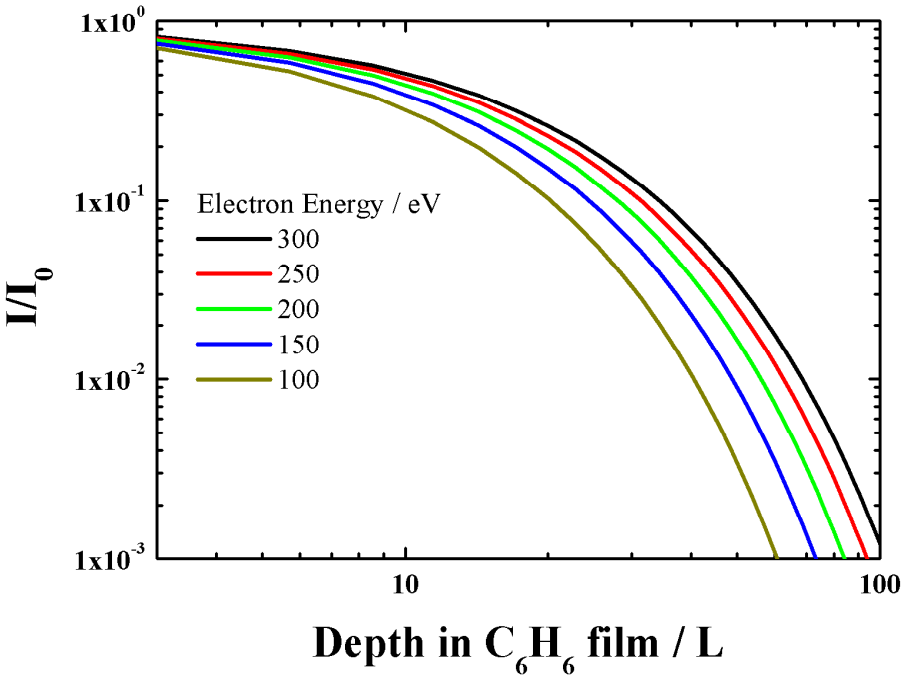

Figure 5.34: Calculated electron penetration through C_6H_6 films for the electron energies used in this work. The penetration depths are reported in dose equivalent units to aid comparison with the previously presented data.

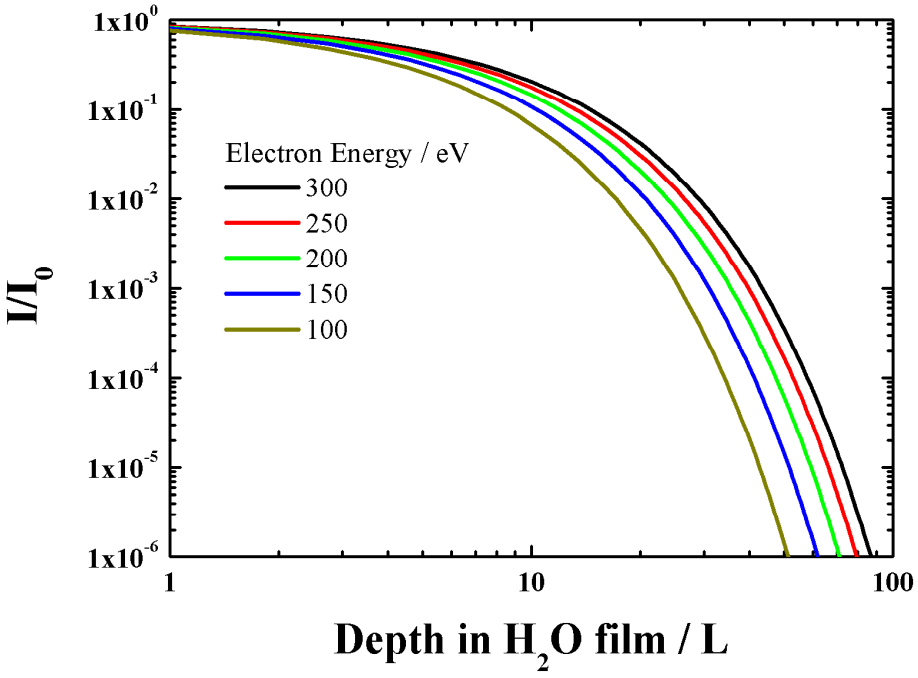

Figure 5.35: Calculated electron penetration through C_6H_6 films for the electron energies used in this work. The penetration depths are reported in dose equivalent units to aid comparison with the previously presented data.

In the case of photodesorption, the photon was absorbed directly by the C_6H_6 molecule, leading to unimolecular decomposition of the cluster and the desorption of C_6H_6 and H_2O molecules. Here, the decomposition of the same surface bound cluster is likely to result in the observed desorption. At the energies used here, the electron scattering cross-section for H_2O is dominated by ionization [12], with electronic excitations also playing an important role. However, the total inelastic scattering cross-section is calculated to be around $1\text{-}2\times10^{-16}$ cm^2 for electron energies of 100-300 eV [13] and ionization of H_2O molecules cannot therefore lead directly to the desorption of C_6H_6 molecules. It is important to note from the electron penetration curve for H_2O that it is likely that very few electrons will completely penetrate the H_2O film corresponding to an exposure of 150 L. It is therefore necessary to consider what happens during the passage of electrons through the H_2O film. Ionization that occurs along the path of an electron passing through the H_2O film will result in a cascade of secondary electrons. This has been calculated for the cascade that results from a 500 eV oxygen Auger electron in H_2O [14] where 25 secondary electrons were found to be generated within 100

fs. The calculations indicated the presence of a large population of electrons with energies of less than 50 eV. The experiments reported here were conducted using electrons with energies below 500 eV and consequently the number of secondary electrons and their average energy is likely to be somewhat smaller. Nevertheless, it is reasonable to assume that a cascade of electrons will be formed in the present case, resulting in an effective amplification of the effect of the primary electron beam. Several possibilities then exist for the transport of these electrons to the surface region where they can lead to the desorption of C_6H_6.

The generation of secondary electrons within H_2O ice will lead to the formation of solvated electrons $e^-(aq)$ and these reactive species have been shown to be important in reactions in CCl_4/H_2O films [15]. It is worth stressing that this alone will have important consequences for chemistry in mixed ices where solvated electrons will readily interact with species present within the ice matrix. These solvated electrons might then diffuse through the ice, with some of them reaching the surface bound $C_6H_6(H_2O)_n$ clusters. Isolated solvated electrons have a microsecond lifetime [16], although in the presence of electron scavengers this is reduced. This suggests that these solvated electrons are likely to play a role only close to the vacuum interface as a result of rapid recombination with hydronium ions, which is thought to be efficient in the bulk [17]. As well as slow secondary electrons becoming solvated directly, it is also necessary to consider the possibility of excitation and dissociation of H_2O molecules [18]. This will result in the formation of ionic products, and a pre-solvated electron. The nature of the pre-solvated electrons depends on the excitation energy and are thought to include pre-solvated conduction band electrons, localized partially solvated electrons, and excited states of H_2O molecules. In particular, excitons, which are bound states of electron-hole pairs, have been proposed for transporting excitation energy from the bulk to the vacuum interface. This mechanism has been used to explain the desorption of D_2 from the vacuum interface region following the 100 eV electron irradiation of ASW [17], an experiment not unlike the present case. The efficient formation of excitons at defect sites within ASW films has also been suggested as a mechanism for the desorption of H_2O from interfacial sites on ASW adsorbed

on graphite [19]. Here, excitons were formed as a result of multi-photon excitation of H_2O molecules, with H_2O desorption showing a 9 eV threshold, compatible with the ice band gap. Migration of the excitons that were formed was again thought to be responsible for the observed H_2O desorption. Bulk excitations and subsequent migration have also been shown to play a role in the formation of O_2 although the actual mechanism by which the migration occurs remains unclear [20]. It therefore seems reasonable that the same mechanism is transporting excitation energy to the vacuum interface in the present case. Upon reaching the vacuum interface, this energy will excite any surface bound clusters, possibly resulting in H_2O and fragmentation product desorption. Decomposition of the cluster and ejection of the weakly bound C_6H_6 molecule is also highly likely. This mechanism is analogous to that discussed for the case of the photon-induced desorption of C_6H_6 from surface bound clusters. Whilst with 250 nm photons the energy enters the system though excitation of the C_6H_6 molecule, with low energy electrons the energy pathway is *via* the H_2O molecules. The large cross-section for the fast desorption component can therefore be ascribed to an effective amplification of the primary electron beam by the formation of multiple secondary electrons and excitations in the ice that leads to the observed desorption.

As the C_6H_6 coverage is increased, the surface concentration of isolated C_6H_6 molecules in surface bound clusters will decrease as a result of island formation. For C_6H_6 exposures of around 10 L, the TPD experiments in **Chapter 3** indicate the presence of 3-dimensional islands on the surface, between which isolated C_6H_6 molecules must also exist. As has been discussed, the initial fast desorption arises as a result of desorption of isolated molecules, resulting in a concentration gradient. Further desorption can only occur as a result of the diffusion of C_6H_6 from the edges of islands to the bare regions. The observed slow desorption is therefore attributed to desorption that occurs *via* the same mechanism as the fast desorption process, but after diffusion of C_6H_6 molecules from the islands to form new surface bound clusters. This also accounts for the observed appearance profile which can be related to the increasing concentration gradient during the

fast desorption. As the initially isolated C_6H_6 molecules desorb, the desorption rate will depend on the diffusion rate of C_6H_6 molecules from the islands. This will be fastest for small islands which will be consumed more rapidly, leading to an overall decay in diffusion rate. This is essentially analogous to Ostwald ripening in colloidal dispersions [21] where large particles tend to grow at the expense of small ones. As the C_6H_6 exposure is increased further, the number of large islands will increase and both desorption channels will be reduced in efficiency as observed experimentally. Furthermore, **Figure 5.35** shows that the overall energy content of electrons reaching the ASW film is much reduced for C_6H_6 exposures of tens of L, reducing the rate of H_2O excitation. For thick films of C_6H_6 the desorption mechanism will therefore be blocked by the presence of the C_6H_6 film itself resulting in the dehydrogenation channel observed in multilayer C_6H_6 films as the only active loss channel. The film morphologies which give rise to these effects are shown schematically in **Figure 5.36**.

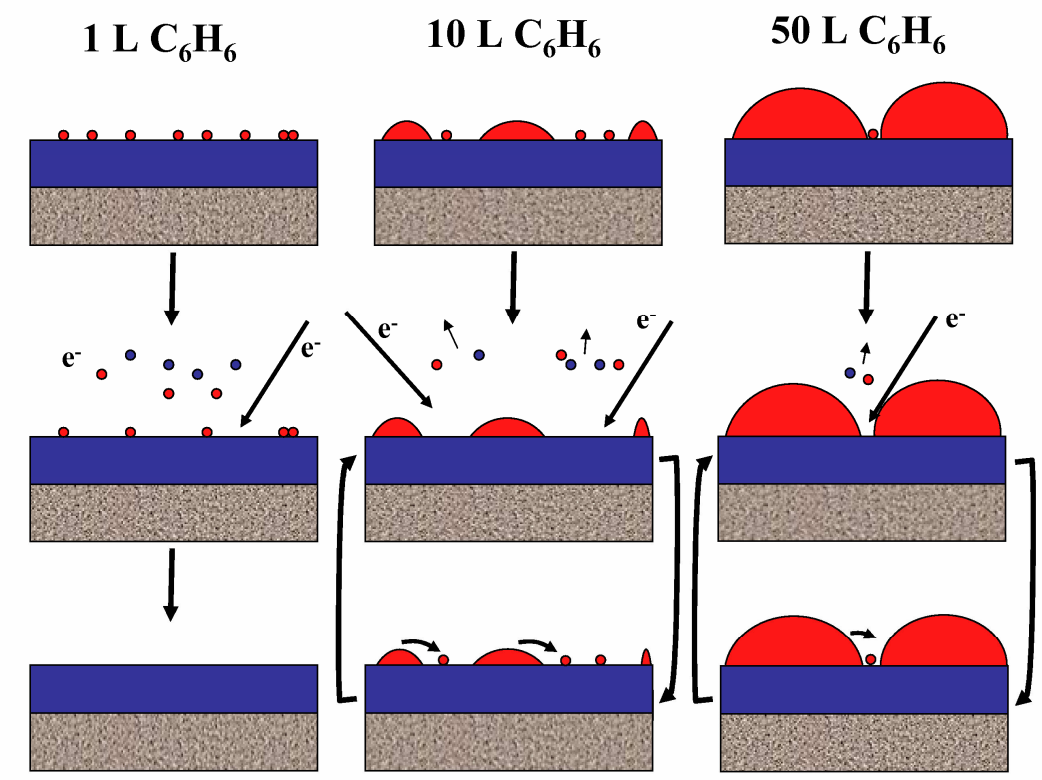

Figure 5.36: Cartoon showing why both fast and slow channels for C_6H_6 desorption from ASW arise. C_6H_6 film thickness plays an important role in the efficiencies of the desorption of pre-existing isolated C_6H_6 molecules, and those that depend on the diffusion of C_6H_6 from islands. Both channels are much reduced in efficiency for thick films.

As has been discussed, the RAIRS experiments reveal only the total loss of C_6H_6 and appear to primarily reflect the slow desorption channel, along with dehydrogenation for thick films. It is clear from the desorption traces that for thick films the limiting value for C_6H_6 loss is around 20%. As well as the effect of not irradiating the full surface area, the accumulated carbon deposits will form a cap that will result in a reduction of further C_6H_6 loss as a result of a reduction in electron beam intensity reaching the unirradiated C_6H_6.

5.4 Astrophysical implications and conclusions

The results in this chapter suggest that the electron-stimulated desorption of species needs to be included in astrochemical models that include the gas-grain interaction. The fast cross-section obtained here for the desorption of C_6H_6 from the surface of an ASW surface is extremely large, indicating a very efficient desorption process. As has been discussed, the mechanism thought to be driving this desorption has previously been shown to result in the formation of both intact H_2O molecules, and H_2 molecules from the vacuum interface region, as well as initiating chemical reaction within the ices. The implication is that the cascade of secondary electrons within H_2O dominated ices that results from the passage of cosmic ray particles through the ice will result in the transport of excitation energy to the vacuum interface region, leading to the desorption of many species from this region. The impact of the H_2O desorption that arises as a result of this will be discussed in **Chapter 6** along with a consideration of the efficiency of this mechanism in an interstellar environment.

The results presented here also further highlight the importance of substrate effects, given that the C_6H_6 desorption relies on the presence of the underlying H_2O substrate. Further experiments are required to study the effect of electron irradiation of C_6H_6 present within the H_2O ice. However, these experiments suggest that electron irradiation of aromatic hydrocarbons, certainly in the energy range studied, is unlikely to result in significant chemical change apart from dehydrogenation. Experiments with larger PAHs would of course be required to

confirm this assertion, though there is no reason to expect the cleaving of C=C bonds in these larger, more stable aromatic systems.

In summary, the experiments discussed in this chapter have revealed an extremely efficient electron-stimulated desorption channel for isolated C_6H_6 molecules adsorbed on an ASW surface. As no C_6H_6 desorption is observed from a multilayer C_6H_6 film the desorption must be the result of a mechanism involving the underlying ASW layer. The formation of excitons and solvated electrons within the ice and their subsequent migration to the vacuum interface has been observed previously and could provide the necessary mechanism to drive the observed desorption. A slower desorption channel is also observed, with this being attributed to the diffusion of C_6H_6 from islands prior to desorption. This results in a diffusion limited desorption channel. An appearance profile associated with this channel can be attributed to the establishment of a concentration gradient during the initial desorption of isolated C_6H_6 molecules.

5.5 References

[1] J. E. Whitten and R. Gomer, *Surf. Sci.*, 1996, **347**, 280.

[2] XPS was perfomed at the University of Nottinhgam Nanotechnology and Nanoscience Centre as part of the Engineering and Physical Sciences Research Council (EPSRC) grant EP/F019750/1 "A Coordinated Open-Access Centre for Comprehensive Materials Analysis"

[3] J. Hrbek, *J. Vac. Sci. Technol. A*, 1986, **4**, 86.

[4] K. P. Stevenson, G. A. Kimmel, Z. Dohnálek, R. S. Smith, and B. D. Kay, *Science*, 1999, **283**, 1505.

[5] A. G. M. Abdulgalil, Ph.D. Thesis, Heriot-Watt University, Edinburgh, in preparation

[6] G. Strazzulla and G. A. Baratta, *Astron. Astrophys.*, 1991, **241**, 310.

[7] R. Ruiterkamp, Z. Peeters, M. H. Moore, R. L. Hudson, and P. Ehrenfreund, *Astron. Astrophys.*, 2005, **440**, 391.

[8] M. P. Collings, M. A. Anderson, R. Chen, J. W. Dever, S. Viti, D. A. Williams, and M. R. S. McCoustra, *Mon. Not. Roy. Astron. Soc.*, 2004, **354**, 1133.

[9] V. I. Feldman, F. F. Sukhov, E. A. Logacheva, A. Y. Orlov, I. V. Tyulpina, and D. A. Tyurin, *Chem. Phys. Lett.*, 2007, **437**, 207.

[10] W. Kemp, *Organic Spectroscopy*, 3rd ed., Macmillan Education Ltd., London, 1991.

[11] G. Attard and C. Barnes, *Surfaces*, 1st ed., Oxford University Press, Oxford, 1998.

[12] M. Dingfelder, A. Travia, R. A. McLawhorn, J. L. Shinpaugh, and L. H. Toburen, *Radiat. Phys. Chem.*, 2008, **77**, 1213.

[13] M. Vinodkumar, K. N. Joshipura, C. G. Limbachiya, and B. K. Antony, *Nucl. Instrum. Methods Phys. Res. B*, 2003, **212**, 63.

[14] N. Tîmneanu, C. Caleman, J. Hajdu, and D. van der Spoel, *Chem. Phys.*, 2004, **299**, 277.

[15] A. J. Wagner, C. Vecitis, and D. H. Fairbrother, *J. Phys. Chem. B*, 2002, **106**, 4432.

[16] T. W. Kee, D. H. Son, P. Kambhampati, and P. F. Barbara, *J. Phys. Chem. A*, 2001, **105**, 8434.

[17] N. G. Petrik and G. A. Kimmel, *Phys. Rev. Lett.*, 2003, **90**, 166102.

[18] D. M. Bartels, D. Gosztola, and C. D. Jonah, *J. Phys. Chem. A*, 2001, **105**, 8069.

[19] J. Bergeld and D. Chakarov, *J. Chem. Phys.*, 2006, **125**, 141103.

[20] N. G. Petrik, A. G. Kavetsky, and G. A. Kimmel, *J. Chem. Phys.*, 2006, **125**, 124702.

[21] D. J. Shaw, *Introduction to Colloid and Surface Chemistry*, 3rd ed., Butterworths, London, 1980.

CHAPTER 6 - Overall Conclusions and Future Work

6.1 Introduction

This chapter presents a more detailed discussion of the astrophysical implications of the observations presented in this thesis. Simulations performed using astrophysical heating rates are used to assess the impact of the different desorption channels that have been revealed. The overall conclusions of this work are summarized, before a discussion of possible future work.

6.2 Astrophysical implications

6.2.1 Adsorption of C_6H_6 on amorphous SiO_2 and ASW

The thermal desorption experiments reported in **Chapter 3** clearly demonstrate the sensitivity of the adsorption of small amounts of adsorbate to the underlying substrate. In an interstellar context, this indicates that the binding of species to bare grain surfaces in warmer astrophysical environments may be significantly stronger as a result of the presence of high energy binding sites on the grain surface. The distribution of binding energies is much smaller on the c-ASW surfaces studied in this work, although previous work has shown this is likely to be important for the adsorption of volatile species at low temperatures in dense clouds [1-3]. These studies indicated that a broader distribution of binding energies is present on p-ASW and, for a full comparison, thermal desorption studies of C_6H_6 adsorbed on this surface are required.

The thermal desorption simulations performed using astrophysical heating rates demonstrate how a broad distribution of binding energies can lead to a significant lengthening of the timescale for desorption of species from the substrate. This is likely to be a general effect, and would be observed for any species that adsorb sufficiently strongly to the surface. Indeed, for more strongly bound species such as larger PAHs, the distribution might be even broader.

The results presented indicate the importance of using realistic grain mimics in experiments investigating processes that occur on bare grain surfaces, where interactions with the grain itself play an important role. However, a detailed understanding of interstellar grains is extremely challenging. As might be expected, the desorption of thick films of ices is relatively unaffected by the nature of the underlying substrate. This may not be the case for photon or electron induced chemistry. At wavelengths where H_2O ice is relatively transparent, a significant photon flux might reach the substrate. For a metallic substrate, the resulting hot electrons may drive chemical and physical processes that would not be relevant in an astrophysical environment. The SiO_2 substrate may then provide an ideal substrate for performing such irradiation experiments.

6.2.2 Non-thermal desorption mechanisms

The photon-induced desorption experiments described in **Chapter 4** have several important implications. The direct-adsorbate mediated desorption of C_6H_6 is observed to be an efficient process at the wavelength used in these experiments. This confirms the importance of photon-induced desorption in astrophysical environments that has been demonstrated previously [4-6]. Furthermore, the desorption of H_2O at a wavelength where H_2O ice is known to be relatively transparent is an extremely important observation. Such mechanisms will increase the overall efficiency of photon-induced desorption.

The C_6H_6 and H_2O molecules that desorb as a result of photon irradiation have high translational energies, suggesting that this may be an important mechanism for the injection of energetic molecules into the gas phase. The simple calculations presented here demonstrated that in the low collision environment of dense clouds, internal energy is likely to be lost through radiative processes, where allowed transitions exist, before collision with another species. However, translational energy will not be lost until collision, when it may allow reaction over activation barriers otherwise insurmountable as a result of the low temperatures of the interstellar environment.

The electron-stimulated desorption (ESD) experiments described in **Chapter 5** demonstrate that, as well as being responsible for inducing chemical change within interstellar ices, physical processing such as desorption must also be considered. The desorption observed for C_6H_6 is extremely efficient, and the proposed mechanism relies on the presence of an ASW layer indicating that this may also be important for other species. The desorption of intact H_2O molecules was also observed and this is currently being investigated in more detail [7].

In order to assess the impact of the non-thermal desorption channels discussed in this thesis, it is necessary to consider the relevant fluxes, as well as the desorption cross-sections. Desorption cross-sections, σ_{des}, can be converted to first order rate constants, k_1, for desorption by considering the associated flux, F, of electrons or photons driving the desorption:

$$k_1 = \sigma_{des} F \qquad \textbf{Equation 6.1}$$

The rate constants obtained can then be used in kinetic simulations performed with astrophysical heating rates. It is therefore necessary to consider the relevant electron and photon fluxes.

Secondary electrons arise as a result of cosmic ray ionization of interstellar ices. The flux of 1 MeV cosmic ray protons is around 1 cm^{-2} s^{-1} [8] within dense interstellar clouds. This value is taken as being representative of the 1-50 MeV region over which the differential proton flux is relatively flat [9] as shown in **Figure 6.1**. The electron flux derived as a result of this proton flux should therefore be considered as a lower limit because the secondary electron yield for higher energy protons will necessarily be higher. The secondary electron yield for 1 MeV protons can be calculated by considering the stopping power for these particles in water ice [10]. This was calculated by using the Stopping and Range of Ions in Matter (SRIM) software [11]. The electronic stopping power for liquid H_2O with the density of c-ASW, as used in calculations in **Chapter 4**, was found to be 19.22 keV μm^{-1}. The other important factor is the so-called W-value which

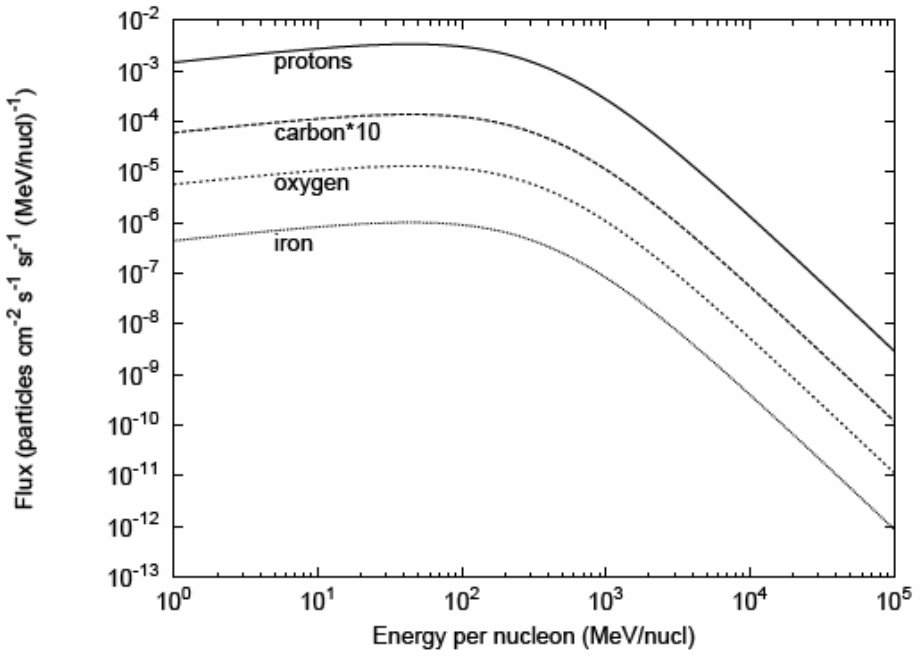

Figure 6.1: Differential cosmic ray fluxes as reported by *Shen et al*. [9]. The integrated flux up to the maximum at 50 MeV is *ca*. 1.5 cm^{-2} s^{-1}.

is the typical energy deposited per ionization event. This value is usually around 2-3 times the ionization potential of the molecule being ionized [12]. For ASW the ionization potential is 11.0 eV [13] which yields a lower limit for the W-value of 22 eV. The number of secondary electrons generated per μm^{-1} can then be estimated from the ratio of the stopping power to the W-value, from which a value of 900 μm^{-1} is obtained. This corresponds to an electron yield of *ca*. 90 electrons per proton along the ion track through an ice film of thickness 100 nm. Given the photon flux this corresponds to an effective electron flux of 90 cm^{-2} s^{-1}. The differential cross-sections for secondary electron generation during the proton irradiation of liquid H_2O for a range of proton energies have been calculated [14]. The fraction of the integrated cross-section as a function of secondary electron energy is shown in **Figure 6.2** for 0.5 MeV protons. This shows that the energy range of 100-300 eV investigated in this work is towards the upper limit of electron energy. However, calculations show that the total inelastic cross-section for H_2O ice does not drop significantly below 100 eV as a result of low energy excitations [15]. This electron flux is therefore a reasonable approximation, within an order of magnitude, for assessing the impact of H_2O ESD.

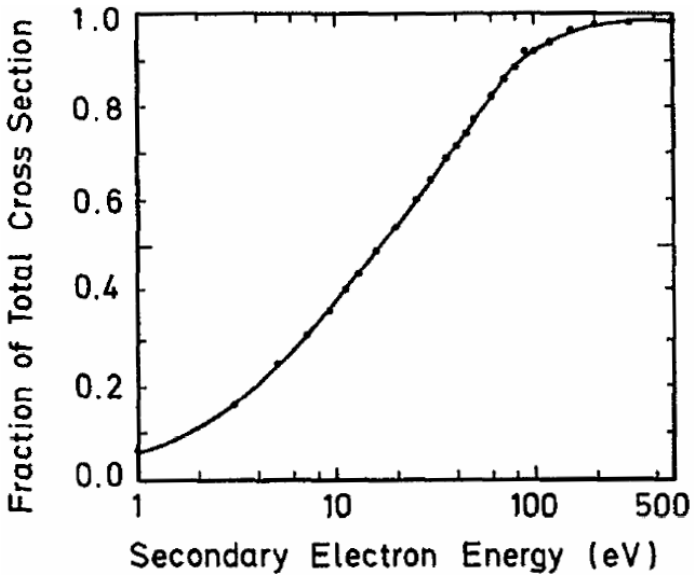

Figure 6.2: Fraction of the total H_2O ionization cross-section as a function of secondary electron energy. From [14].

In terms of the photon flux it is necessary to consider two contributions to the UV field. The interstellar radiation field (ISRF) will be important close to the edge of a dark cloud where A_v values are low. The ISRF field calculated by Mathis *et al.* [16] as shown in **Chapter 1** will be used, with an estimated ISRF photon flux at 250 nm of 10^8 cm^{-2} s^{-1}. Values of 10^6, 10^4 and 10^1 cm^{-2} s^{-1} were estimated for the field at A_v values of 2, 4 and 6 respectively. Within the cloud, the photon flux is dominated by cosmic ray induced fluorescence of H_2, which results in a flux of *ca*. 5×10^3 cm^{-2} s^{-1} [9,17]. This is essentially insensitive to A_v as a result of the penetrating nature of cosmic rays. The spectrum is similar to the output of the broadband hydrogen microwave discharge lamps which have previously been used to study the photon-induced desorption of H_2O in this wavelength region [5]. The spectrum of such lamps is dominated by hydrogen emission features, and they are usually considered to be a reasonable approximation of the UV field at these wavelengths both within the dense clouds and the diffuse ISM. **Figure 6.3** shows an example of the spectra obtained from such lamps compared to that of the diffuse ISM, demonstrating the broad similarity between the spectra.

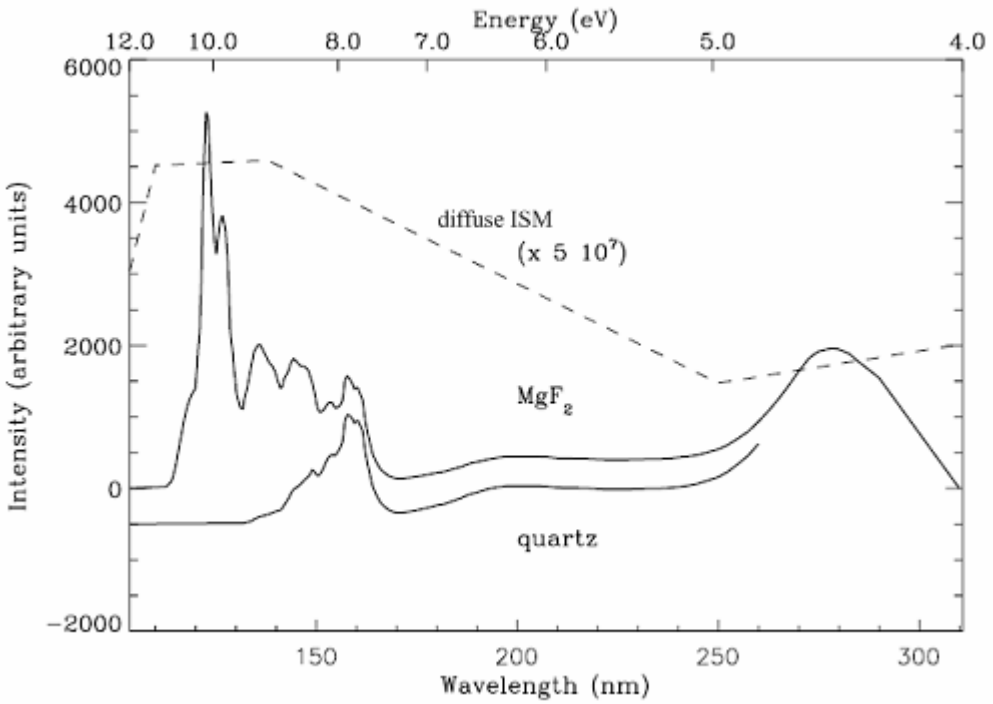

Figure 6.3: Spectrum of broadband hydrogen microwave discharge lamps with quartz and MgF_2 windows compared to the diffuse ISM. From [18].

In order to compare the relative efficiencies of the different desorption channels the desorption of H_2O will be used as an illustrative example. It is therefore necessary to consider the appropriate cross-sections for each of the desorption mechanisms. The direct ESD of H_2O for electron energies in the range 100-300 eV has been found to be $(5\pm2)\times10^{-17}$ cm^2 [7]. Photon-induced desorption of H_2O at wavelengths corresponding to the internal cosmic ray induced field has been shown to occur with a quantum yield of *ca.* 10^{-3} [5] which, combined with the UV photon absorption cross-section at 121 nm of 4×10^{-18} cm^2 [19], yields a desorption cross-section of 4×10^{-21} cm^2. Finally, desorption caused by resonant absorption of photons by other species as demonstrated by the experiments presented in **Chapter 4** of this thesis will be considered. The cross-section for indirect adsorbate-mediated desorption of H_2O of 1×10^{-19} cm^2 will be used. From these cross-sections, along with the estimated photon and electron fluxes, the first order rate constants reported in **Table 6.1** were obtained.

Mechanism	Relevant flux / cm^{-2} s^{-1}		Cross-section / cm^2	k_1 / s^{-1}
H_2O ESD	90 electrons		5×10^{-17}	4.5×10^{-15}
H_2O PSD (internal UV field)	5×10^3 photons		4×10^{-21}	2×10^{-17}
H_2O PSD (indirect mechanism) (ISRF)	A_v=0	10^8 photons	1×10^{-19}	10^{-11}
	A_v=2	10^6 photons		10^{-13}
	A_v=4	10^4 photons		10^{-15}
	A_v=6	1 photon		10^{-19}

Table 6.1: Fluxes, cross-sections and corresponding first order rate constants for the non-thermal desorption of H_2O.

A kinetic model for incorporating these non-thermal desorption mechanisms was built using *CKS* [20,21] as described in **Chapter 3**. The simulations were performed with an initial ASW surface concentration of 3.4×10^{17} cm^{-2} corresponding to a realistic ice film thickness of the order of 10^2 layers. Both steady state simulations, with a constant temperature of 10 K, and those incorporating a heating rate of 1 K / 1000 yr, as justified in **Chapter 1,** were performed. In the latter, the thermal desorption of both ASW and crystalline ice, along with the crystallization of ASW, were considered. The kinetic parameters for these thermal processes were optimized for recent H_2O TPD experiments [7] from those previously reported by Collings *et al*. [22]. Simulations performed with the thermal processes only were included for comparison.

Figure 6.4 and **Figure 6.5** show the simulated desorption traces for the different mechanisms under steady state conditions at 10 K for extinctions of A_v=0 and A_v=6 respectively. For A_v=0, corresponding to the edge of a cloud, desorption induced by the ISRF dominates. This indicates that a full understanding of the potential of the indirect adsorbate-mediate desorption mechanism discussed in **Chapter 4** is required for desorption under such conditions. At high extinctions of A_v=6 and higher, desorption deep within clouds is dominated, not by the photon-induced desorption as a result of the internal field, but by direct ESD of H_2O.

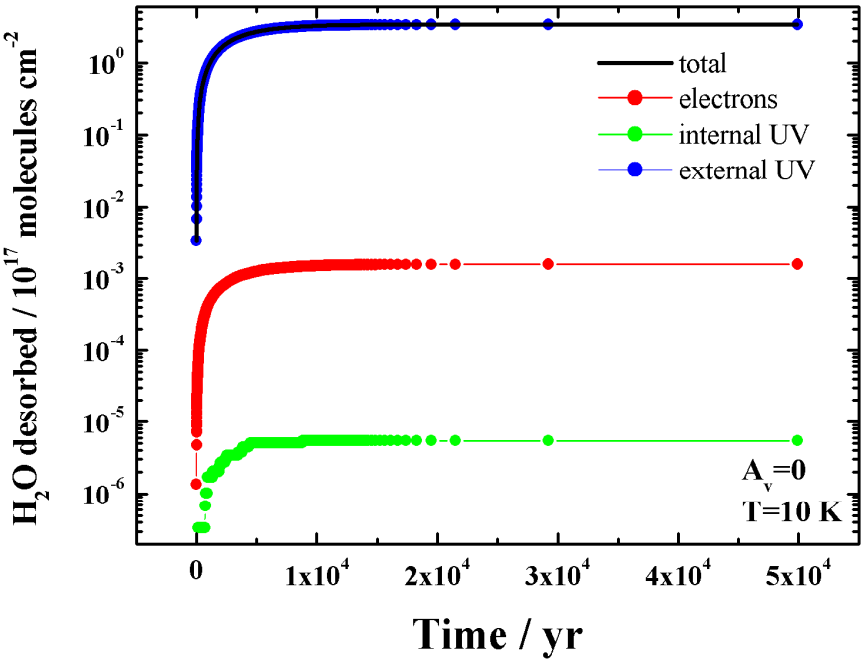

Figure 6.4: Traces showing the desorption of H_2O as a result of non-thermal processing at a steady state temperature of 10 K for A_v=0.

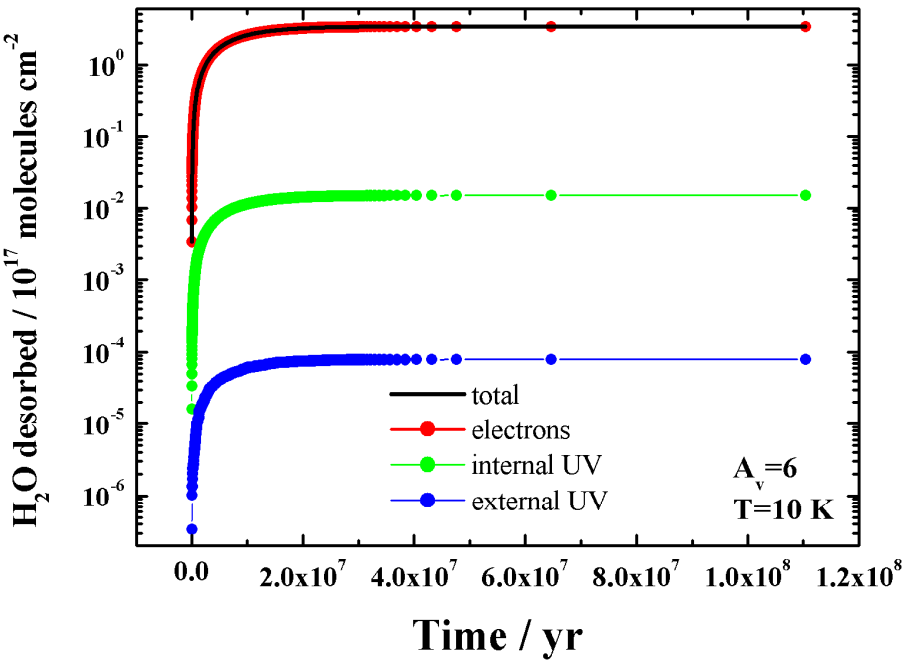

Figure 6.5: Traces showing the desorption of H_2O as a result of non-thermal processing at a steady state temperature of 10 K for A_v=6.

This suggests that this channel, which has not previously been considered in detail, may be an extremely important mechanism for the non-thermal desorption of H_2O and is currently under more detailed investigation [7].

Corresponding desorption traces for the simulations including thermal desorption with a heating rate of 1 K / 1000 yr are shown in **Figure 6.6** and **Figure 6.7** respectively. These indicate that for low A_v values, the photon-induced desorption mechanism may result in the complete desorption of H_2O before the temperature has risen sufficiently for the onset of thermal desorption. This indicates that the inclusion of non-thermal desorption *via* this mechanism into astrochemical models will significantly decrease the time required for H_2O desorption at the edge of a dense cloud. Indeed, this mechanism may play an even greater role than suggested by these simulations. The absorption spectra for larger PAHs are situated towards longer wavelengths [23], a trend seen generally with increasing molecular complexity. The ISRF increases in intensity by as much as an order of magnitude to longer wavelengths. Desorption that results from resonant absorption by such molecules may therefore be extremely important, and relevant laboratory investigations would be desirable to ascertain the true extent of the impact of such mechanisms. Deeper within clouds thermal desorption is the dominant channel, although ESD leads to significant H_2O desorption prior to the temperature being sufficiently high for thermal desorption. This mechanism is again at least two orders of magnitude more efficient than photon-induced desorption as a result of the internal UV field.

To further demonstrate the importance of non-thermal desorption, the fraction of total H_2O desorbed by all of the non-thermal mechanisms is compared to that desorbed thermally as a function of A_v in **Figure 6.8**. Clearly, non-thermal desorption is extremely important under low extinction conditions. Finally, considering only the non-thermal mechanisms, **Figure 6.9** demonstrates that the ISRF driven channel is important up to extinctions as high as A_v=4 whilst **Figure 6.10** confirms the dominance of the direct ESD of H_2O over that driven by the internal UV field for all values of A_v.

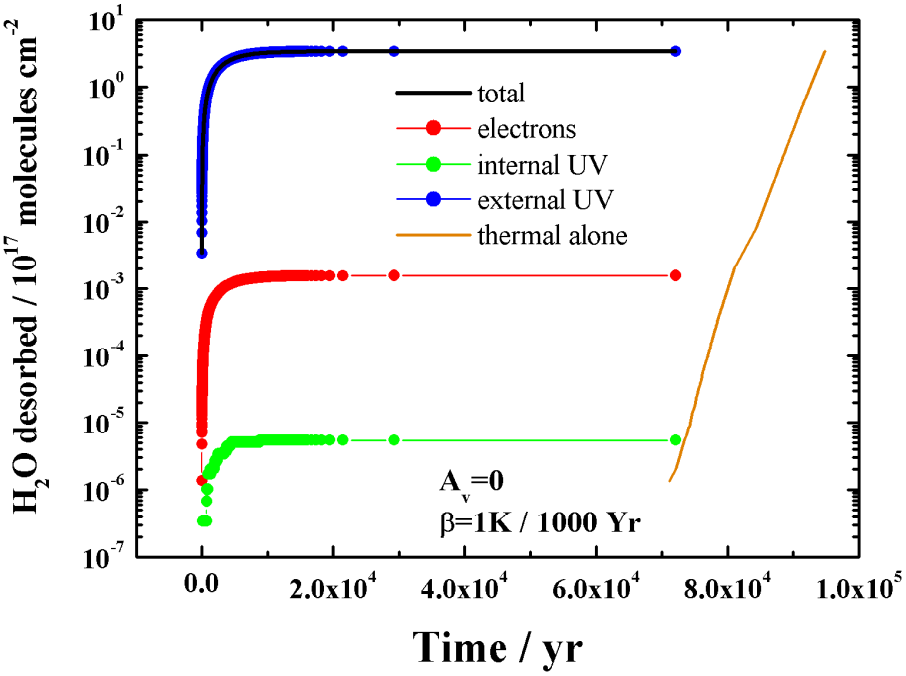

Figure 6.6: Traces showing the desorption of H_2O as a result of thermal and non-thermal processing with a heating rate of 1 K / 1000 yr for A_v=0. No thermal trace is shown as all the H_2O desorbs non-thermally prior to the onset of thermal desorption The orange line corresponds to thermal desorption alone.

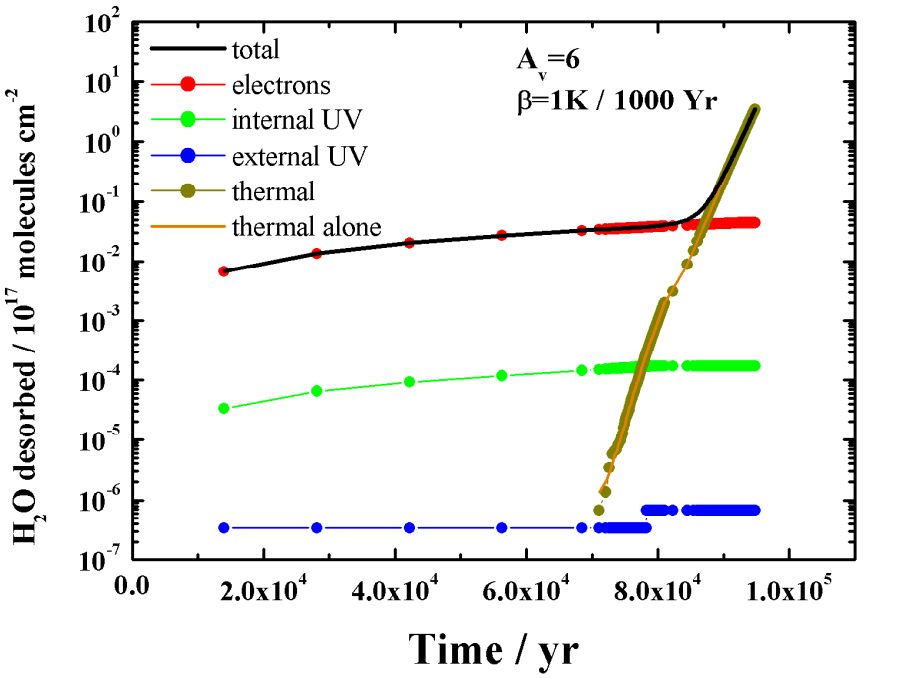

Figure 6.7: Traces showing the desorption of H_2O as a result of thermal and non-thermal processing with a heating rate of 1 K / 1000 yr for A_v=0. The orange line corresponds to thermal desorption alone.

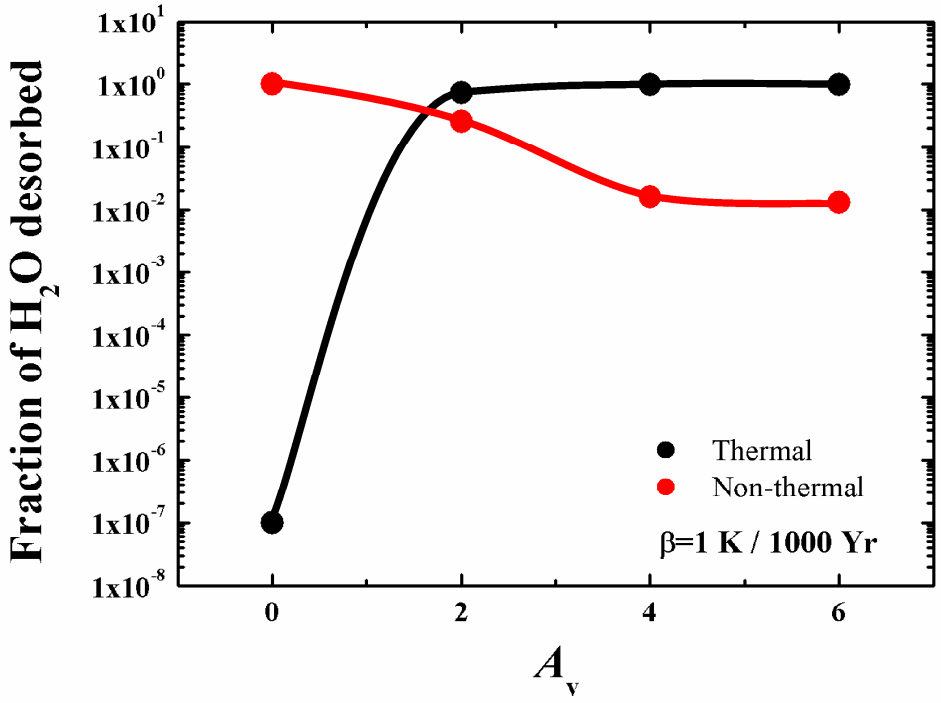

Figure 6.8: Comparison between the fractions of H_2O desorbed thermally and non-thermally as a function of A_v for a heating rate of 1 K / 1000 yr. The smoothed lines are to guide the eye.

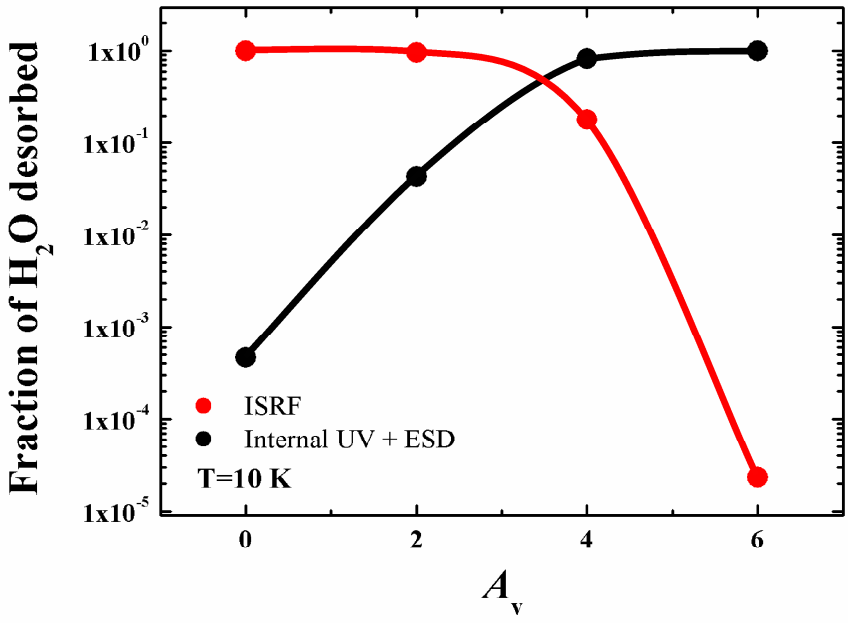

Figure 6.9: Comparison between the fractions of H_2O desorbed by ISRF photons those from the internal UV field along with electrons as a function of A_v at 10 K. The smoothed lines are to guide the eye.

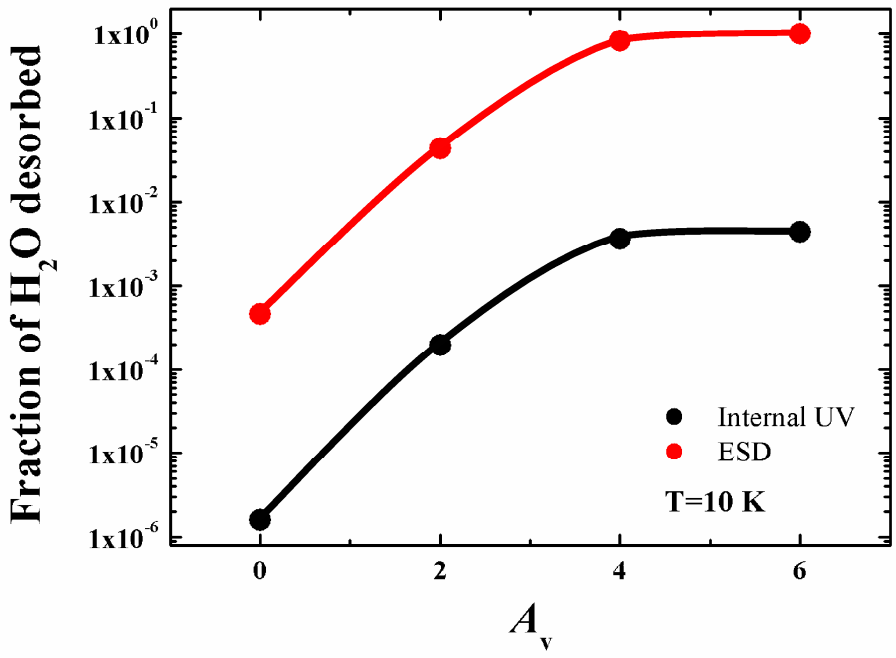

Figure 6.10: Comparison between the fractions of H_2O desorbed by photons from the internal UV field and electron irradiation as a function of A_v at 10 K. The smoothed lines are to guide the eye.

These simulations confirm the importance of the inclusion of non-thermal desorption mechanisms in astrochemical models and, in particular, highlights the impact of including the two mechanisms investigated in this work; indirect adsorbate-mediated desorption induced by the ISRF and direct ESD driven by the secondary electrons produced by cosmic ray ionization of ices.

6.3 Overall conclusions

The work presented in this thesis has provided insight into the thermal and non-thermal desorption of C_6H_6, as a model of larger aromatic hydrocarbons, under a range of interstellar conditions. The thermal desorption experiments reported in **Chapter 3** have indicated the strong dependence for small adsorbate quantities of the desorption kinetics on the nature of the underlying substrate. In the present case, although C_6H_6 is thought to bind to both ASW and amorphous SiO_2 through hydrogen bonding interactions, the observed desorption behaviour is sensitive to the gross morphology of the substrate. A broad distribution of desorption energies

was extracted for the case of the SiO_2 substrate compared to a much narrow distribution for the ASW substrate. Multilayer desorption kinetics were in agreement with previous studies, indicating the relative insensitivity of thick films to the substrate. The RAIR spectra obtained suffered from a lack of sensitivity for submonolayer coverages but did indicate a possible shift that could be attributed to hydrogen bonding interactions on both substrates. Clearly, astrochemical processes that involve direct adsorbate-substrate interactions must be conducted on a relevant substrate. This SiO_2 substrate developed in this work is one possible approach for modelling the interstellar silicate grain population.

Chapter 4 considered the photon-induced desorption of C_6H_6 and H_2O from pure and binary layered ices of the two species. One key observation is the desorption of hot C_6H_6 molecules, as characterised by translational temperatures in excess of 1100 K. The possible importance of the desorption of such energetic molecules in the cold environment of the ISM has been considered. Also of importance was the observation of an indirect adsorbate-mediated desorption channel by which H_2O was desorbed following resonant absorption by C_6H_6 molecules. The observations were consistent with desorption occurring following the unimolecular decomposition of a surface bound $C_6H_6(H_2O)_n$ cluster. Furthermore, the H_2O molecules desorbed were also translationally hot. Desorption cross-sections were obtained which indicated that the desorption of both species was efficient at 250 nm. Typical values for these cross-sections were *ca*. 10^{-19} cm^2.

In **Chapter 5** the focus was on electron-stimulated processing. No C_6H_6 desorption was observed during electron irradiation of either C_6H_6 multilayers, or low coverages of C_6H_6 adsorbed on amorphous SiO_2. In these cases dehydrogenation is thought to be the dominant loss channel. This is in agreement with previous studies. However, significant desorption of C_6H_6 was observed when submonolayer coverages of C_6H_6 were adsorbed on top of a pre-adsorbed c-ASW film. This desorption occurred with an extremely high cross-section of 10^{-15} cm^2 and was attributed to the formation of excitons within the H_2O layer which subsequently migrate to the vacuum interface. Solvated electrons, which arise as a

result of the complete stopping of electrons within the thick ASW film, may also play a role in the desorption. A slower desorption channel with a cross-section of the order of 10^{-17} cm^2 was observed for thin multilayer films which was attributed to the diffusion of C_6H_6 from islands to regenerate the isolated species desorbed *via* the fast mechanism. No evidence for chemical change was observed during irradiation using electrons within the energy range 100-350 eV.

Finally, the impact of non-thermal desorption mechanisms under interstellar conditions has been assessed using kinetic simulations to model the thermal and non-thermal desorption of H_2O. The kinetic model described made use of interstellar fluxes and cross-sections obtained from this work, along with previous studies in the literature. The results of the simulations indicate the importance of including non-thermal desorption mechanisms in astrochemical models. In particular, electron-stimulated desorption may play a far greater role within dense clouds than previously thought. At the edges of dense clouds, and for extinction values of up to A_v=4, the indirect desorption mechanism observed in **Chapter 4** results in significant H_2O desorption; an effect that may be even more efficient for more complex absorbing species.

6.4 Future work

The results of this work have highlighted many possibilities for future research, and some of these will be highlighted here. In order to gain a more fundamental understanding of the impact of the SiO_2 substrate on thermal desorption it would be desirable to use a flat crystalline SiO_2 film which could, in principle, be formed by heating the stainless steel substrate during the evaporation procedure. This would eliminate the complexity of desorption traces that arises as a result of the gross morphology of the film, allowing the typical SiO_2-adsorbate adsorption energy to be obtained. Experiments considering different silanol concentrations would also be useful. Using a flat surface might also result in an increased RAIRS sensitivity allowing a more detailed spectroscopic analysis of the interactions between submonolayer coverages of adsorbate and the substrate. The inclusion of

metal atoms within the film would be required to make the current film more representative of the metallic silicate grains found in the ISM.

From a chemical physics viewpoint, state-resolved studies to determine the internal energy partitioning of molecules desorbed during photon irradiation would be required for a full understanding of energy disposal. In order to further understand the indirect desorption mechanism observed in this work, full ToF experiments allowing the observation of intact $(H_2O)_n$ clusters during the desorption could be performed. Such experiments could reveal the nature of the slow feature observed in the current H_2O ToF traces. From an astrophysical viewpoint, extension of the current experiments to larger PAHs and other complex molecules would be required to fully determine the importance of this indirect photon-induced desorption mechanism in the ISM.

A fuller understanding of the ESD of H_2O molecules from pure ASW is required and, as has been highlighted, such experiments are currently underway. This work could be extended to lower electron energies, around 10 eV where C_6H_6 resonances are likely to exist, to reveal any direct desorption mechanisms. STM experiments would be required to confirm the proposed mechanisms for the ESD of C_6H_6 from ASW surface; particularly in terms of the diffusion limited slow desorption mechanism. Given the extremely large cross-section of the fast mechanism further studies are warranted. It would also be interesting to use ToF measurements to investigate the translational energies of desorbing C_6H_6 and H_2O molecules for comparison with the photon irradiation experiments. Again, from a chemical physics viewpoint, state-resolved studies would provide a fuller understanding of energy partitioning in the system. As with the photon irradiation experiments extension to larger PAHs would also be a longer term goal. Heteroatomic species, such as pyridine, have the potential for more complex binding as a result of the presence of the nitrogen lone pair, along with the π-system, and are also target molecules of the longer term programme of work initiated by that presented in this thesis.

6.5 References

[1] T. Zubkov, R. S. Smith, T. R. Engstrom, and B. D. Kay, *J. Chem. Phys.*, 2007, **127**, 184707.

[2] L. Hornekaer, A. Baurichter, V. V. Petrunin, A. C. Luntz, B. D. Kay, and A. Al-Halabi, *J. Chem. Phys.*, 2005, **122**, 124701.

[3] J.-H. Fillion, L. Amiaud, E. Congiu, F. Dulieu, A. Momeni, and J.-L. Lemaire, *Phys. Chem. Chem. Phys.*, 2009, **11**, 4396.

[4] K. I. Öberg, E. F. v. Dishoeck, and H. Linnartz, *Astron. Astrophys.*, 2009, **496**, 281.

[5] K. I. Öberg, H. Linnartz, R. Visser, and E. F. van Dishoeck, *Astrophys. J.*, 2009, **693**, 1209.

[6] K. I. Öberg, G. W. Fuchs, Z. Awad, H. J. Fraser, S. Schlemmer, E. F. van Dishoeck, and H. Linnartz, *Astrophys. J.*, 2007, **662**, L23.

[7] A. G. M. Abdulgalil, Ph.D. Thesis, Heriot-Watt University, Edinburgh, in preparation

[8] V. Mennella, G. A. Baratta, A. Esposito, G. Ferini, and Y. J. Pendleton, *Astrophys. J.*, 2003, **587**, 727.

[9] C. J. Shen, J. M. Greenberg, W. A. Schutte, and E. F. van Dishoeck, *Astron. Astrophys.*, 2004, **415**, 203.

[10] R. E. Johnson, *Private communication*.

[11] Stopping and Range of Ions in Matter (SRIM) 2006 software, available online at www.srim.org

[12] W. F. Schmidt and E. Illenberger, *Nukleonika*, 2003, **48**, 75.

[13] M. Vinodkumar, K. N. Joshipura, C. G. Limbachiya, and B. K. Antony, *Nucl. Instrum. Methods Phys. Res. B*, 2003, **212**, 63.

[14] K. A. Long and H. G. Paretzke, *J. Chem. Phys.*, 1991, **95**, 1049.

[15] M. Dingfelder, A. Travia, R. A. McLawhorn, J. L. Shinpaugh, and L. H. Toburen, *Radiat. Phys. Chem.*, 2008, **77**, 1213.

[16] J. S. Mathis, P. G. Mezger, and N. Panagia, *Astron. Astrophys.*, 1983, **128**, 212.

[17] S. S. Prasad and S. P. Tarafdar, *Astrophys. J.*, 1983, **267**, 603.

[18] G. M. Muñoz Caro and W. A. Schutte, *Astron. Astrophys.*, 2003, **412**, 121.

[19] N. J. Mason, A. Dawes, P. D. Holtom, R. J. Mukerji, M. P. Davis, B. Sivaraman, R. I. Kaiser, S. V. Hoffmann, and D. A. Shaw, *Faraday Discuss.*, 2006, **133**, 311.

[20] Chemical Kinetics Simulator (CKS), version 1.0, IBM Almaden Research Center, 650 Harry Road, Mailstop ZWX1D1, San Jose, CA, USA. Further information may be obtained from the CKS website at http://www.almaden.ibm.com/st/msim/ckspage.html

[21] F. A. Houle and W. D. Hinsberg, *Surf. Sci.*, 1995, **338**, 329.

[22] M. P. Collings, J. W. Dever, H. J. Fraser, and M. R. S. McCoustra, *Astrophys. Space Sci.*, 2003, **285**, 633.

[23] W. Kemp, *Organic Spectroscopy*, 3rd ed., Macmillan Education Ltd., London, 1991.